Cranfield University

Thomas Charrett

Development of two-frequency Planar Doppler Velocimetry instrumentation

Centre for Photonics and Optical Engineering
School of Engineering

PhD Thesis

Cranfield University

Centre for Photonics and Optical Engineering
School of Engineering

PhD Thesis

2006

Thomas Charrett

Development of two-frequency Planar Doppler Velocimetry instrumentation

Supervisor: Ralph Tatam

Academic Year 2003 to 2006

This thesis is submitted in partial fulfilment of the requirements for the degree of Doctor of Philosophy

ABSTRACT

This thesis describes the development of the two-frequency Planar Doppler Velocimetry (2ν-PDV) flow measurement technique. This is modification of the Planar Doppler Velocimetry (PDV) technique that allows the measurement of up to three components of the flow velocity across a plane defined by a laser light sheet. The 2ν-PDV technique reduces the number of components required to a single CCD camera and iodine cell from the two CCDs in conventional PDV. This removes the error sources associated with the misalignment of the two camera images and polarisation effects due to the beam splitters used in conventional PDV. The construction of a single velocity component 2ν-PDV system is described and measurements made on the velocity field of a rotating disc and an axisymmetric air jet. The system was then modified to make 3D velocity measurements using coherent imaging fibre bundles to port multiple views to a single detector head. A method of approximately doubling the sensitivity of the technique was demonstrated using the measurements made on the velocity field of the rotating disc and was shown to reduce the error level in the final orthogonal velocity components by ~40 to 50%. Error levels of between 1.5ms^{-1} and 3.1ms^{-1} depending upon observation direction are demonstrated for a velocity field of ±34ms^{-1}.

The factors that will influence the selection of a viewing configuration when making 3D PDV measurements are then investigated with the aid of a computer model. The influence of the observation direction, the magnitude of the flow velocity, and the transformation to orthogonal velocity components are discussed. A new method using additional data in this transformation is presented and experimental results calculated using four-measured velocity components are compared to those found conventionally, using only three components. The inclusion of additional data is shown to reduce the final error levels by up to 25%.

Keywords:
PDV, Doppler Global Velocimetry, DGV, coherent fibre bundles

ACKNOWLEDGEMENTS

My thanks go to Ralph Tatam (academic supervisor), David Nobes and Steve Staines for their assistance.

This work was carried out with the support of the Engineering and Physical Science Research Council (EPSRC) under grant GR/S04291.

TABLE OF CONTENTS

TABLE OF FIGURES

TABLE OF TABLES

TABLE OF EQUATIONS

GLOSSARY OF SYMBOLS

Doppler formula and geometry

$\hat{o}$ / $\hat{o}_n$	Observation vector / nth view observation vector
$\hat{\imath}$	Illumination vector
$(\hat{o} - \hat{\imath})$ / $(\hat{o}_n - \hat{\imath})$,	Measured velocity component (sensitivity vector) / nth view sensitivity vector
X, Y, Z	Cartesian unit vector components of the sensitivity vector.
X_n, Y_n, Z_n	Cartesian unit vector components of the sensitivity vector for the n^{th} view.
ϕ	Angle between $\hat{o}$ and $\hat{\imath}$
ν	Frequency of illuminating light
λ	Wavelength of illuminating light
$\Delta\nu$	Doppler frequency shift.
c	Speed of light.
$\hat{V}$	Velocity of scattering object
U_n	Velocity component along sensitivity vector
U, V, W	Orthogonal velocity components, horizontal, vertical and out-of-plane.

Definition of views

T	Rotation (around from Z axis in XZ plane)
P	Elevation (up from XZ plane, varies from -90 to $+90^o$).

Beer-Lambert Law

I	Measured light intensity through molecular filter.
I_0	Initial light intensity.
l	Path length through absorbing medium.
α	Absorption coefficient of medium.

White card correction

SIG	Signal image intensity.
REF	Reference image intensity.
W_{SIG}	White card signal image intensity.
W_{REF}	White card reference image intensity.
$TR_{corr.}$	Corrected transmission ratio.

Calculation of Doppler shift

TR_{pixel}	Transmission ratio of pixel in image
TR_{zero}	Transmission ratio of un-shifted light
ν_0	Frequency of un-shifted light
ν_D	Frequency of Doppler shifted light

Speckle noise

NSR	Noise to signal ratio due to speckle.
m	Magnification ratio.
F	F-number of the optical system.
Δx	Average size of camera pixels.

2ν-PDV linear approximation

I_1, I_2	Recorded Intensities in images one and image two respectively.
Is	Intensity of scattered light.
T_1, T_2	Un-shifted transmission ratios, on falling and rising slope respectively.
ΔT_1	Shift in transmission on falling slope.
TR_1	Normalised transmission ratio on falling slope.
M_1, M_2	Gradients of falling and rising slopes of the iodine absorption line.
$m_2 = \left\| \frac{M_2}{M_1} \right\|$	Ratio of gradient of rising slope to falling slope of iodine absorption line.

Calculation of orthogonal velocity components

$[U_m]$	Column vector of measured components.
$[A]$	Transformation matrix for 3C method.
$[C]$	Inverse of transformation matrix $[C] = [A]^{-1}$.
$[V]$	Velocity written as column vector.
$[J]$	Transformation matrix for 4C methods.
$[w]$	Weighting matrix used for least squares solution for 4C method.

Empirical jet equations

r_0	Radius of jet nozzle.
r_1	Distance from centre line to inner edge of shear layer (outer edge of potential core).
r_2	Distance from centre line to out edge of jet.
b	Distance to half the initial velocity (u_0) from the inner edge of shear layer (outer edge of potential core).
u	Magnitude of velocity.
u_0	Initial jet velocity / exit velocity.
u_1	Magnitude of velocity of ambient fluid.
x	Distance along centre line.
x_0	Distance along centre line the potential core extends to.

Condition number

$\kappa(A)$	Condition of the matrix A calculated:
κ_1	Using the norm based on the largest column sum in A
κ_2	Using the norm based on the largest column value in A
κ_3	Using the norm based on Frobenius-norm of matrix A, $\sqrt{\sum diag(A'.A)}$
κ_4	Using the norm based on the largest row sum in A.

1 Introduction

1.1 Planar Doppler Velocimetry: a flow measurement technique

The ability to measure flow velocities in fluids, is an essential part of the design process for flow systems and in the development of fluid mechanics theory, both as direct measurements of flow phenomena and in comparison to computational fluid dynamics results.

There are several techniques that allow the velocity field to be measured, which can be separated into intrusive, such as hot-wire anemometry and pitot tubes and non-intrusive methods. The non-intrusive methods have the advantage of not disturbing the flow field. Several well established techniques for non-intrusive velocity measurement exist including laser Doppler and laser transit techniques. These are point measurement methods, and would require a scanning apparatus to measure the whole flow field. These scanning systems may be difficult to implement in large wind tunnels, as well as resulting in long, and expensive, run times, in order to provide a suitable resolution of the flow field. However they do provide high temporal and spatial information and these systems are routinely used.

The non-intrusive planar measurement techniques of particle imaging Velocimetry (PIV) and Planar Doppler Velocimetry (PDV), sometimes known as Doppler Global Velocimetry (DGV), have the advantage of being able to capture the whole flow field in a single measurement period. These are both non-intrusive optical techniques that can provide multiple component measurements of the velocity. This thesis concentrates on the recent PDV technique and its development.

1.2 Theory of PDV

Planar Doppler Velocimetry[1,2], also called Doppler Global Velocimetry[3,4] (DGV), is based upon the Doppler principle that light scattered from a moving object is subjected to a frequency shift depending upon the velocity of the object, the direction that the light is incident, and the observation direction, see Figure 1-1. The frequency shift experienced is given by the Doppler formula. A general schematic of a PDV experiment is shown in Figure 1-2.

$$\Delta v = \frac{v(\hat{o} - \hat{i}) \cdot \hat{V}}{c}$$

Equation 1-1

Where $\Delta\nu$ is the Doppler frequency shift of the scattered light from the initial frequency of the light ν, $\hat{V}$ is the velocity of the scattering object and $\hat{o}$ and $\hat{i}$ are unit vectors representing the observation and illumination vectors respectively.

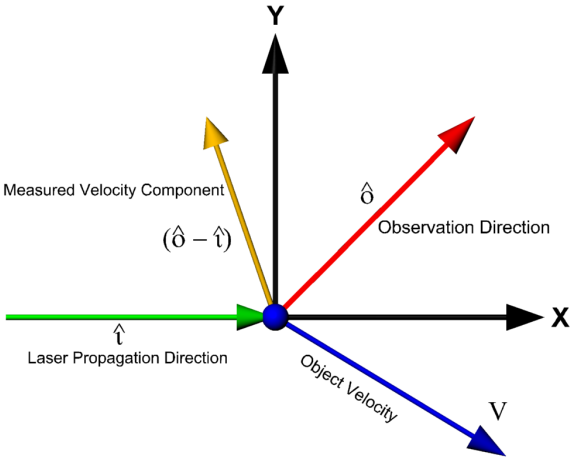

Figure 1-1 The relationship of laser illumination direction and observation direction to the measured velocity component determined from the Doppler equation.

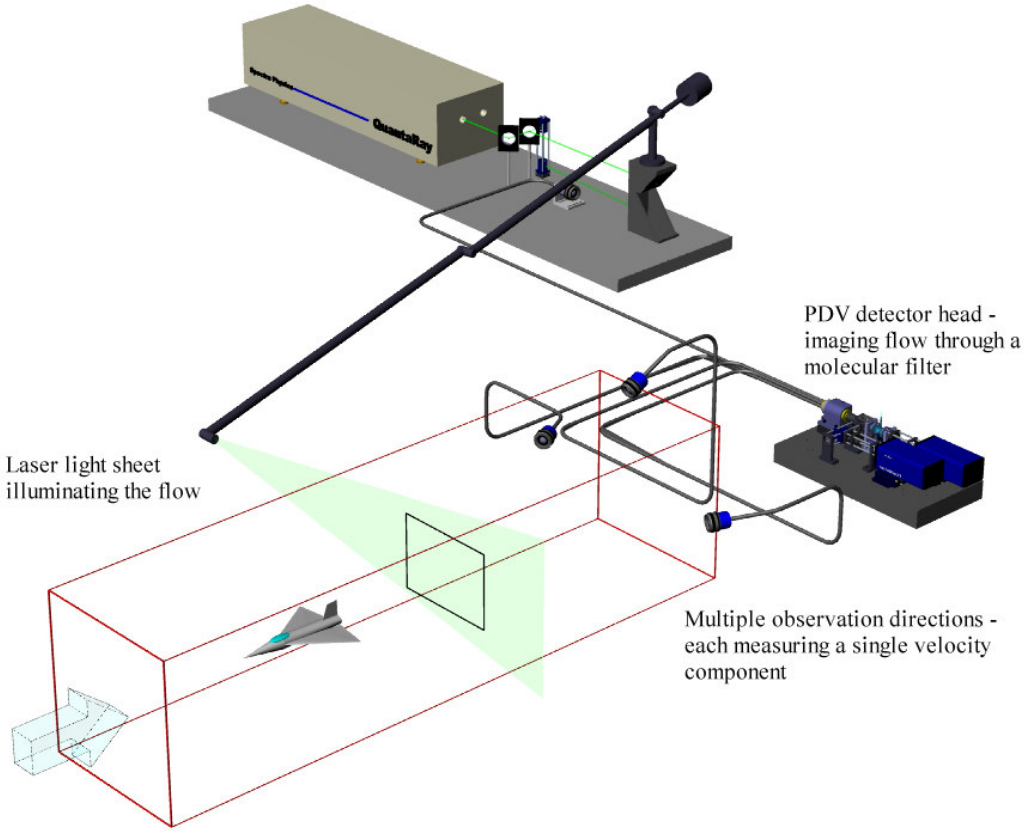

Figure 1-2 Schematic diagram of a PDV system in wind tunnel.

In PDV, a region of the illuminated flow is imaged, through a glass cell containing iodine vapour onto the active area of a CCD camera. Iodine has numerous narrow absorption lines over a large part of the visible spectrum[5]. Figure 1-3(a) shows the absorption spectrum centred about 514.5nm calculated using a theoretical model for a typical iodine cell. There are sufficient lines that one or more fall within the gain curves of several commonly used laser sources. If the laser frequency is chosen to

coincide with one such line, Figure 1-3, then the optical intensity at any position in the camera image is a function of the Doppler shift experienced at the corresponding flow position, via the frequency-dependent iodine absorption.

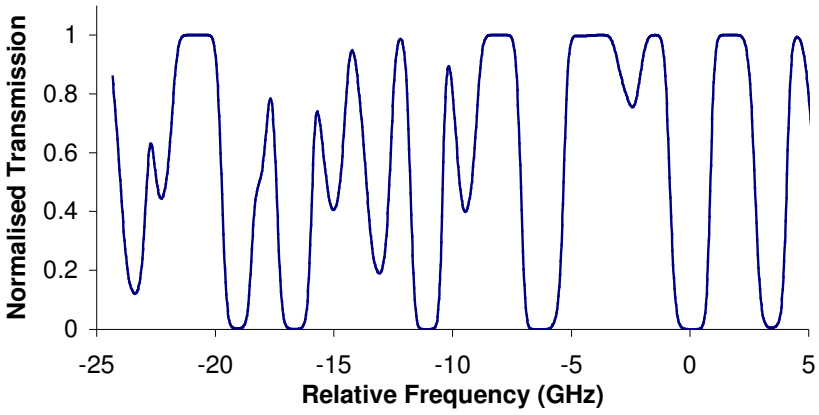

(a)

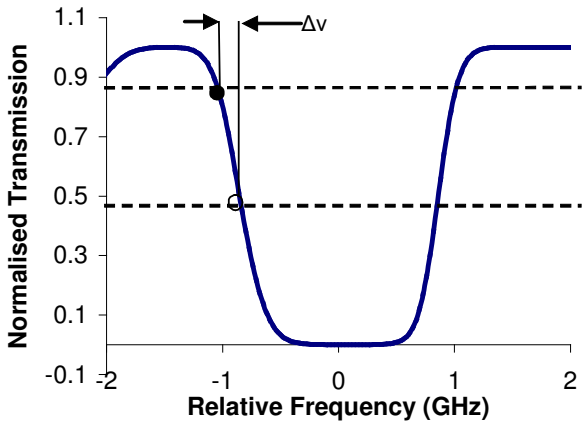

(b)

Figure 1-3 (a) Example of the iodine absorption spectrum centered about 514.5nm, calculated using Forkey's[6] model (b) demonstrating the relationship between intensity and frequency

As well as the frequency of the light passing through the absorption cell the intensity over a PDV image is affected by the intensity profile of the illuminating laser sheet (typically Gaussian), spatial variations of the seeding density within the flow and imperfections in the optical surfaces. These variations are generally of similar amplitude to those resulting from absorption in the iodine cell, and can obscure the information about flow velocity that is contained within the camera image. It is therefore usual to amplitude-divide the image beam onto two cameras; from one of the two imaging paths the iodine cell is omitted, and the resulting image acts as a reference to normalize the signal image carrying the velocity information. A typical arrangement of a single component two camera PDV detector system with associated optical components is shown in Figure 1-4.

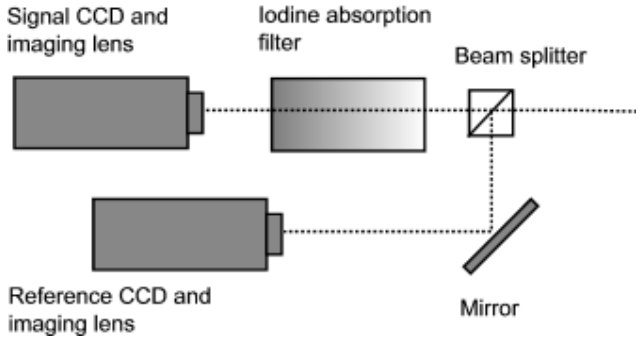

Figure 1-4 Diagram showing the standard PDV detector head arrangement for measurement of a single velocity component

If the initial laser frequency is tuned to be at approximately the 50% transmission point then, zero velocity regions will be recorded as 50% the value of full transmission, whilst any non-zero velocities will be recorded as a change in signal level. The sign of the direction can be determined by the direction of the shift to either lower or higher intensities.

A continuous wave laser can be used to make time averaged measurements[4,7,8], while a pulsed laser can be used to make instantaneous measurements[9-11].

However this approach to PDV has several problems, such as the need to ensure good alignment between the two images, differences between the optical distortions in each optical path, as well as the tendency for even non-polarizing beam splitters to have some polarization sensitivity, that can affect the intensities seen by the cameras.
On top of these problems there is the requirement for two cameras to measure a single velocity component that is a disadvantage when compared to PIV that requires only a single CCD to measure two components of the velocity.

Several groups have proposed systems that reduce the number of CCDs required to one, for example by recombining the two images onto different halves of the same CCD camera, to reduced the amount of equipment required, although with reduced spatial resolution.

The two-frequency PDV technique uses only a single CCD camera in the detector head with the signal and reference images being captured sequentially. A typical two-frequency PDV detector head is shown in Figure 1-5. This method has the potential to avoid the problems of image misalignment and differences in the optical distortions in the optical paths. This is the approach adopted for the work in this thesis and the two-frequency technique is described more completely in chapter 3.

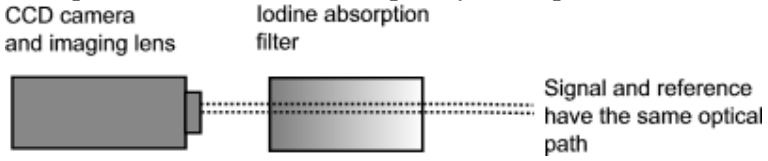

Figure 1-5 Diagram showing a single camera two-frequency PDV detector head arrangement for measurement of a single velocity component

1.3 Contents of thesis

Chapter 2 contains an overview of flow measurement techniques and a detailed review of the current state of the PDV technique. An overview of groups working in the field is followed by descriptions of the different components and methods employed by these researchers in the processing of the data. The causes of errors and ways to minimise them, the procedures used in the experimental set-up and for data capture are then discussed.

Chapter 3 introduces the two-frequency Planar Doppler Velocimetry (2ν-PDV) technique, with a description of the theory and it's potential advantages and disadvantages. There is a description of a potential method to increase the sensitivity of a 2ν-PDV system by using both the rising and falling slopes of the iodine absorption line. This is followed by a more detailed overview of work that has been done previously in PDV on similar related techniques.

Chapter 4 is an overview of the current state of the PDV processing software developed at Cranfield University. It covers both the methods and implementation of the processing that has been developed both for previous PDV projects and how this has been developed for the 2ν-PDV project that is reported in this thesis. This chapter also contains a description of a method of calculating the orthogonal velocity components using four or more velocity components, providing additional data for the transformation than the three velocity components required. If an in-depth knowledge of the processing techniques used is not required then chapter four can be skipped as an overview of the processing used in the experimental work has also been given in those chapters.

Chapters 5 and 6 contain the experimental work undertaken in this project and describe the development of a time averaged 2ν-PDV system based around a continuous wave argon ion laser.

Chapter 5 begins with a description of a beam generation system, using acousto-optic modulators used to produce the two illumination frequencies required. It also includes details on laser frequency stabilisation and light sheet generation.
The imaging head used in the system is described, including analysis of the properties of the CCD camera, imaging optics and the iodine cell. The chapter then concludes with a campaign of measurements made using this 2ν-PDV system. Measurements were made of a single velocity component on both a rotating disc and a seeded axisymmetric air jet with a maximum velocity of $100ms^{-1}$. These are presented along with a comparison with conventional PDV results captured at the same time and with empirical formulas describing the jet.

Chapter 6 describes the extension of the system to make three-dimensional velocity measurements. This was achieved using multiple imaging fibre bundles as an input to the imaging head. Modifications made to both the PDV imaging head and to the illumination system are described with the modifications made to the illumination system allowing measurements to be made using both the normal and increased sensitivity schemes described in chapter 3. A comparison between these two sensitivity schemes is presented using measurements of the velocity field of the

rotating disc, to estimate the magnitude of the velocity errors for both schemes. 3D velocity measurements are then presented for the velocity field of a seeded axisymmetric air jet.

Chapters 7 and 8, concentrate on the process of converting multiple measured velocity components to the orthogonal velocity components for any multi-component PDV system.

Chapter 7 is an analysis of the factors that will affect the selection of a viewing geometry for 3D PDV measurements. The variation of measured velocity component uncertainty with view direction and how this will affect the final level of error in the orthogonal velocity components is discussed. Experimental results from the 2ν-PDV system described in chapter 6 are presented showing this variation. The use of the condition number of the transformation (from measured components to orthogonal components) as a measure of suitability of a viewing configuration is also described. The effect of uncertainty in the sensitivity vector (observation vector minus illumination vector) in this transformation from non-orthogonal to orthogonal velocity components is discussed. Finally, other considerations in the viewing configuration are reviewed; such as optical access and variation in scattered light levels with viewing direction.

Chapter 8 describes an error propagation model that allows viewing configurations to be assessed. The model is initially described which includes the factors described in chapter 7. The model is then used to assess a series of viewing configurations that could be used in a 3D PDV experiment, including several that have been previously reported. How well the condition number of the transformation reflects the final uncertainty levels is also investigated. The benefit of using an additional velocity component in the transformation to orthogonal velocity components is then assessed. The orthogonal components are calculated using the 3C (three component) and 4C (four component) methods, described in chapter 4, for a series of viewing configurations using the error propagation model. The 2ν-PDV measurements made on a rotating disc are also used for a comparison of the experimental results calculated using the 3C and 4C methods. This demonstrates the benefit of using additional velocity components for certain viewing geometries.

Chapter 9 concludes this thesis with a discussion of the main points studied as well as identifying potential areas for future work.

1.4 References

1. Arnette, S.A., Samimy, M., and Elliott, G.S., "Two-component Planar Doppler Velocimetry in the compressible turbulent boundary layer", 1998, *Experiments in Fluids*, Vol. 24, pp 323-332.

2. McKenzie, R.L., "Planar Doppler Velocimetry Performance in Low-Speed Flows", 1997, *35th AIAA Aerospace Sciences Meeting and Exhibit*, Reno, Nevada, AIAA-97-0498.

3. Komine, H., Brosnan, S., Litton, A., and Staepperts, E., "Real-Time Doppler Global Velocimetry", 1991, *AIAA 29th Aerospace Sciences Meeting,* Reno, Nevada, Paper 91-0337.

4. Meyers, J.F. and Komine, H., "Doppler Global Velocimetry: a new way to look at velocity", 1991, *Laser Anemometry*, Vol. 1, pp 273-277.

5. Chan, V.S.S., Heyes, A.L., Robinson, D.I., and Turner, J.T., "Iodine Absorption Filters for Doppler Global Velocimetry", 1995, *Measurement Science and Technology*, Vol. 6, pp 784-794.

6. Forkey, J.N., "Development and Demonstration of Filtered Rayleigh scattering - a Laser Based Flow Diagnostic for Planar Measurements of Velocity, Temperature and Pressure", 1996, *Final Technical Report for NASA Graduate Student Researcher*, Fellowship Grant #NGT-50826, Princeton University.

7. Reinath, M.S., "Doppler Global Velocimeter Development for the Large Wind Tunnels at Ames Research Center", 1997, *NASA*, Technical Memorandum 112210.

8. Roehle, I., Willert, C., Schodl, R., and Voigt, P., "Recent Developments and Applications of Quantitative Laser Light Sheet Measuring Techniques in Turbo machinery Components", 2000, *Measurement Science and Technology*, Vol. 11, pp 1023-1035.

9. Schodl, R., Roehle, I., Willert, C., Fischer, M., Heinze, J., Laible, C., and Schilling, T., "Doppler Global Velocimetry for the analysis of combustor flows", 2002, *Aerospace Science and Technology*, Vol. 6, pp 481-493.

10. Thorpe, S.J., Quinlan, N., and Ainsworth, R.W., "The Characterisation and Application of a Pulsed Neodymium YAG Laser DGV System to a Time-varying High-speed Flow", 2000, *Optics & Laser Technology*, Vol. 32, pp 543-555.

11. McKenzie, R.L., "Measurement Capabilities of Planar Doppler Velocimetry using Pulsed Lasers", 1995, *AIAA 33rd Aerospace Sciences Meeting and Exhibit*, Reno, Nevada, Paper 95-0297.

2 Literature Review

2.1 Overview of flow measurement instrumentation

Experimental techniques to measure the flow velocity can be classed into intrusive and non-intrusive groups. Intrusive techniques are those in which a probe is inserted into the flow in order to make a measurement and have the disadvantage of disturbing the flow. Examples of intrusive flow-measurement techniques include pitot-static probes and hot-wire/film anemometry[1]. These tend to be point measurement techniques and the measurement of multiple points require a rake of probes or scanning apparatus which can be difficult to implement in large wind tunnels and result in long run times.

The second group of techniques are non-intrusive optical techniques. Laser Doppler anemometry (LDA) is one such technique. It relies upon the basic principle that light scattered from a moving particle will experience a Doppler frequency shift. By measuring the frequency shift the component of velocity can be determined. The Doppler shift can be measured directly with a Fabry-Perot interferometer and has been applied to supersonic flows[2] however this is often impractical due to mechanical vibrations and acoustic noise. Practical LDA system can be achieved using two methods, the reference beam technique[3] and the differential Doppler system. In the reference beam technique the scattered light is mixed with a reference beam and the signal recorded by a detector. In the differential Doppler system the input beam is split into two parallel beams that are bought to a common focus by a lens. This creates a pattern of plane interference fringes within the measurement volume. As a particle moves through this region the scattered light detected will vary according to the particles position within the fringes and from this the velocity component perpendicular to the fringes can be found. This can be extended to measure multiple velocity components, by a variety of methods; polarisation multiplexing[4], time division multiplexing[5] and wavelength multiplexing[6]. 3D fibre optic LDA systems are available in commercial packages such as those from TSI[7] and Dantec[8].

Another non-intrusive measurement technique is Laser two-focus (L2F) velocimetry[9]. This is a time-of-flight method where two beams with a known separation illuminate the flow and light scattered from the flow is collected. The velocity can be determined by the time taken for seed particles to cross both beams. This technique can also be expanded to three dimensions[10].

These point measurement techniques are well developed and can provide high accuracy measurements at a high temporal resolution. However they do not allow the simultaneous measurement of velocity at all points across the flow, instead the probe must be traversed making measurements at each point if this is required. As many flows will vary in time it is desirable to be able to make simultaneous velocity measurements at many points. There are several methods described which expand these techniques to measure the velocity at multiple points simultaneously[11] or along a profile[12-14]. Several methods exist that allow the flow to be measured at many points simultaneously including particle imaging velocimetry (PIV), molecular flow tagging and Planar Doppler velocimetry (PDV).

Molecular flow tagging[15] is a method by which a grid or series of lines are written into the flow using a laser to induce a chemical process such as fluorescence or phosphorescence. The tagged molecules are then transported along with the flow. An image captured a know time afterwards will reveal the displacement of these tags and the velocity can be found. However these techniques have a limited spatial resolution due to the original line or grid written into the flow.

Particle Imaging Velocimetry (PIV) is a time of flight method involving the measurement of the displacement of a particle, or group of particles, between two sequential images with a known time interval and is a well-established measurement technique. This simplest form of PIV allows the two in-plane components of the velocity to be measured, however several methods exist that allow the third, out-of-plane component to be measured. Stereoscopic PIV[16] involves the extension of the technique to mimic eyes by adding a second camera. This views from a different perspective and allows the motion of the particle to be triangulated. A further extension of this method is three-dimensional Particle Tracking Velocimetry[17]; here two cameras with an angular separation of 90^{o} view an illuminated volume. Particle tracks introduced into the flow are captured in sequential frames recording the particles motion over time. However this technique is restricted by the difficulty of distinguishing particle tracks, limiting the number that can be used. Three-dimensional scanning PIV[18] can be used to make 3D velocity measurements; here a light sheet is scanning across a volume normal to the plane of the light sheet and images pairs captured at each position. The in-plane velocity components are found by cross-correlation of the image pairs and the out-of-plane by cross-correlation of images from different light sheet positions. Holographic techniques[19] have been used to record particle positions over a volume.

The need to be able to distinguish individual particles in PIV leads to the requirements for high quality optics (at least SLR camera quality), and a limited measurement area (or limited spatial resolution with larger measurement areas), in order that individual particles can be imaged. In contrast PDV is an intensity-based technique so it is not necessary to be able to image individual scattering particles, removing these restrictions. In PIV the spatial resolution is limited by the size of the measurement window used in the cross-correlation process. PDV allows for a much higher spatial resolution, effectively limited to the area imaged onto a single pixel on the CCD. Another potential benefit of the PDV technique over PIV is that the computer processing required is much less than for PIV, with an entire flow field being calculated in tens of seconds or less, rather than the minutes required in PIV, although more recent PIV systems are capable of producing flow fields at kHz rates.

However PDV has some major drawbacks, the most important of which is the velocity resolution of the technique. As PDV relies upon measuring the Doppler frequency shift from changes in image intensity, small Doppler shifts are not easily resolved. This means that PDV is unsuitable for low speed flows (less than $2ms^{-1}$[20]) where PIV is successful. There may however be a successful marriage of the two techniques where PDV is used for rapid large area measurements, followed by ‘zooming in’ on areas of interest using PIV, for example in wind tunnel applications where running time is expensive and a quick overview of the flow may be desirable,

and only smaller areas needing the accuracy or low speed resolution of PIV, however the seeding requirements for the two techniques differ.

An overview of the features of the different flow measurement techniques is shown in Table 2-1. Willert et al [21] include a discussion of the suitability of the PDV and PIV techniques for use in a cryogenic wind tunnel. The main points are shown in Table 2-2 with their conclusion being that the PDV method is the only feasible method for that facility, however PIV should be used where possible with PDV used when this fails or is difficult to implement.

Table 2-1 Overview of flow measurement instrumentation

Technique	Notes
Hotwire	Intrusive, point measurements (Some multipoint using multiple probes) Velocities from a few cms^{-1} to supersonic High temporal resolution, fluctuations up to several hundred kHz High spatial resolution, down to 1 mm or less Up to three velocity components can be measured. Instantaneous velocity information
LDA	Non-intrusive, point measurements (Some multi-point/profile capability) Velocity range from zero to supersonic Up to three velocity components can be measured using 1 or 2 detector heads High spatial and temporal resolution Instantaneous and time averaged
L2F	Non-intrusive, point measurements. Up to 3 components using 2 views Poor for in-line velocity component. 1 – 3000 ms^{-1} velocity range. Good spatial resolution (~200μm).
PIV	Non-intrusive, planar measurements (Some volume techniques e.g. Holographic PIV). Velocity range from zero to supersonic. Up to three velocity components can be measured. 1 view for 1 component, 2 views for 3 components
PDV	Non-intrusive, planar measurements. Velocities greater than ~$2ms^{-1}$. Up to three velocity components can be measured, 1 view per velocity component. Instantaneous or time averaged velocity measurements possible.

Table 2-2 Performance comparison between PIV and DGV (PDV) applications in a cryogenic environment (taken from Willert et al [21])

Particle image velocimetry	Doppler global velocimetry (Planar Doppler velocimetry)
Provides 2-C data, 3-C with increased complexity	Provides 3-C velocity
Unsteady measurement	No unsteady data
Lengthy averaging procedure, but have RMS data (~1 min for 100 recordings)	Fast, time-averaged measurement (<5 s per data set)
Strong sensitivity to main flow vector (requires adjustment of $d\tau$ and light sheet thickness)	All velocity components with similar sensitivity
Good performance in low- to medium-speed flows	Good performance in medium- to high-speed flows
Requires good optical resolving power (=short depth of field), may suffer from temperature-induced refraction changes	Optical distortion tolerable, imaging through flexible fiber bundles
Intrusive installation on sting or similar to get flow-normal velocity components (for 2-C configuration.)	Non-intrusive installation behind tunnel walls
Requires direct light sheet delivery	Fiber-based laser light delivery
Low seeding concentration	Seeding concentrations ~10x higher
Requires >1 μm particles from dedicated seeding generator (possible oil residue)	Works with tiny ice crystals, simple seeding method without residue (accumulation of ice possible)
Medium to low sensitivity to background light (can use high-pass filters)	Strong sensitivity to background light/reflections (requires special treatment of background)
Most PIV hardware and software readily available	Custom designed, complex hardware

2.2 Previous work in PDV

The initial concept for using an atomic line filter as a frequency-to-intensity converter can be found in the 1990 patent by Hiroshi Komine[22], whilst working at the Northrop Corporation, California. This patent describes a basic PDV system with a frequency-controlled laser, formed into a sheet that is incident on a seeded flow. The receiving optics gather the scattered light, splits it into two, with one half being passed through a molecular iodine cell to a camera, and the other half passing straight to a second camera, to provide a reference.

A proof of concept Doppler Global Velocimeter was constructed at NASA's Langley Research centre[23], and analogue and digital processing schemes were evaluated [24]. Since then a large amount of work, on both time averaged and instantaneous measurement systems, has been carried out at the NASA Langley research centre into the technique[25-28]. Work has also been done at the NASA Ames Research centre focusing on time averaged flow measurements in large wind tunnels[29,30].

In Europe a large amount of work has been carried out by Germany's DLR into three component PDV measurements using three orthogonal light sheets and a single viewing direction, to make time averaged and instantaneous measurements,[31-39]. Other groups in Europe include ONERA at Toulouse[40-42], and the Institute of Fluid dynamics, Switzerland[43,44] as well as Oxford [45,46] and Cranfield [47] [48-62]in the UK.

There are also several university groups, in the US, involved in PDV research including West Virginia University[63-67], who have also done work on the related point measurement technique, point Doppler Velocimetry (pDv)[68-70] ,Ohio State University[71-73], Rutgers University[74,75] and Texas A&M University[73,76].
This is not an exhaustive list of all the groups involved in PDV research, and in the following sections I shall give details of work done in the development and assessment of the various parts and processing of a PDV system.

2.3 Lasers in PDV

Samimy and Wernet[71] state that in PDV it is necessary to have a laser operating at a single frequency for the illumination of the flow, also it must have the capability to be tuned to a specific point on the iodine absorption profile, for example the 50% transmission point, and must operate in a frequency range that is convenient for the use of iodine filters. The line width of the laser should also be narrower than the absorption profile to give acceptable results.

The most common choice of lasers for PDV systems are continuous wave Argon Ion lasers, operating at 514.5nm, and frequency doubled Nd:YAG pulsed lasers, at 532nm. Continuous wave (CW) lasers generally have narrower line widths (1-10MHz) than pulsed lasers (~100MHz). The use of CW lasers allows only time-averaged measurements, whilst pulsed systems allow instantaneous velocity measurements to be made.

Another consideration is the need to either control or measure the frequency of the laser so that the Doppler shift, and hence velocity can be found. A good discussion of lasers used in PDV can be found in the review by Elliott and Beutner[74].

2.3.1 Continuous wave lasers

The common choice for continuous wave (CW) systems is the Argon Ion laser, fitted with an intra-cavity temperature controlled etalon, which can be adjusted to allow only a single laser frequency. The laser can be tuned to a particular frequency by adjusting the control voltage applied to the etalon. There has also been some work done using CW dye lasers[77,78], the main advantages being the ability to select an iodine line which has a well resolved shape, and a linear profile which is suitable for the velocity range to be measured. For instance if lower velocities where to be measured then a sharp slope would be chosen. The CW dye laser used by Leporcq et al [77] allowed the laser line to be tuned from 500nm to 700nm and with a narrow bandwidth of 500 KHz.

Argon Ion lasers are affected by frequency drifts, as reported by Meyers[27] and Roehle[31], so some form of active control of the laser frequency (ν_0) is necessary to ensure that the laser frequency remains constant throughout the measurement period. Several groups use a second iodine cell, through which a portion of the laser beam is diverted, and photodiodes to lock the laser to a set transmission ratio. Alternatively Roehle[31] at DLR suggests using the hyperfine structure of iodine to measure frequency even more accurately. For their laser control system they report precision of $\pm$ 1 MHz in the reproducible laser frequency over a range of 2 GHz, with the same level of control in the fast frequency fluctuations.

2.3.2 Pulsed lasers

The alternative laser source for PDV systems is the pulsed Nd:YAG laser, this has the advantage of providing instantaneous images of the velocity field. A typical pulse length would be 5-10ns, Smith[25], allowing temporal features on this scale to be seen. Several problems and difficulties of using Nd:YAG lasers have been noted by groups using them for PDV. Firstly there is considerable pulse-to-pulse frequency variation (~80MHz as reported by Meyers & Lee[26] and Nobes et al[51]), making it essential that the frequency is known at the time of the measurement. As for CW lasers the value of the non-shifted laser frequency, $\nu_{0,}$ is required for the velocity calculation. Again a second iodine cell system can be used to monitor ν_0, which is easier than attempting to stabilize the laser. Although this is desirable for the CW laser it is not as essential, as it can be assumed that the Argon laser has been tuned to a certain frequency and will only drift away from it slowly at approximately 50MHz / ^{o}C [79].

Another problem that has been reported is frequency variation across the pulse. Forkey et al[80], reported a 100MHz variation across the output of a frequency doubled Nd:YAG, this was also observed by Thorpe et al[45] although to the lesser extent of 25MHz. Any gradients in the laser frequency distribution would produce a spurious velocity gradient in measurements.

2.3.3 Frequency monitoring

The simplest approach to determining the laser frequency is to direct a portion of the laser beam onto a stationary object in the field of view, so as to provide a zero velocity reference. An extension of this idea is used by Nobes et al[49], at Cranfield, in their three-component PDV system using imaging fibre bundles. In this approach a portion of the laser beam is scattered off a screen that is viewed by the fourth imaging bundle, whilst the other three provide the three viewing directions necessary for 3D PDV and this allows the same iodine cell to be used for the frequency monitoring and measurements.

In another extension to this method the group at ONERA, in Toulouse[40], use an acousto-optic device to generate a series of five shifted frequencies, which where imaged though the iodine cell, alongside the flow image, to provide a real-time description of the transmission profile.

2.3.4 Laser sheets

The laser sheet itself can be made using either cylindrical optics, or for continuous wave lasers using a beam scanner. This creates a time-averaged sheet of uniform intensity, unlike cylindrical optics that will produce a non-uniform sheet with a Gaussian intensity profile. This is the approach used by Roehle[31] at DLR where the laser is formed using a scanning technique with a modulation frequency of 10 to 20 Hz.

The use of scanning sheets also reduces the problem of a variation in illumination direction across the sheet. Ford and Tatam[47] include a discussion of this with the associated error for a beam divergence of 15^{o} being $2ms^{-1}$.

2.3.5 Flow seeding

Samimy and Wernet[71] include a discussion of the seeding requirements in PDV in which they state several main issues including the particles response to the flow and spatial resolution, as well as a comparison with PIV and LDV. The seeding used in PDV measurements, as for PIV and LDV measurements, must be able to track the flow sufficiently well for measurements to be made. PDV is able to use smaller particles than PIV as it is not necessary to be able to image individual particles. The smaller the particles the better the flow tracking so here PDV has the advantage over PIV. Although some PIV methods exist using the diffraction limited images. PIV also has an upper limit on the number density of particles in the flow, again due to the need to image individual particles, this is not the case for PDV where high number density is preferable due to increased light scattering. However there is a speckle noise associated with seed particles in PDV, which is discussed later. PDV also requires sufficient seeding density so that there is sufficient scattered light to make measurements.

2.4 The PDV imaging head

2.4.1 PDV imaging head arrangement

Intensity gradients other than those caused by a velocity gradient may be present for example due to variations in seeding levels, variations in the laser light sheet power and imperfections in the optics. To account for these it is necessary to normalize the recorded image with a second image that is viewed without passing through the iodine cell, Komine[22]. The original and most commonly used arrangement for capturing the required images is that described by Komine[22] and others uses two cameras, one of which views thought the iodine cell and the other does not, see Figure 2-1.

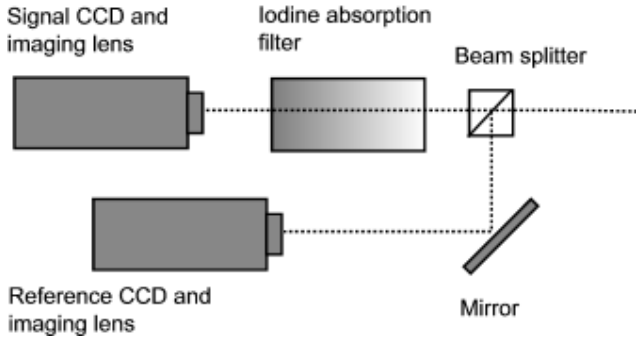

Figure 2-1 Diagram showing the standard PDV head arrangement

This approach requires two cameras, which makes the technique expensive, especially if three dimensional velocity measurements are required, as this would need three separate PDV heads each with two cameras. There are however several simplified PDV systems described in the literature, which use only a single camera to capture both the signal and reference images. Ainsworth et al[46] describe a technique whereby the two images are recorded side by side on the same CCD, by the use of non-polarizing beam splitters and mirrors. See Figure 2-2. Chan[61,81] describe a similar single-camera arrangement using a mirror instead of a beam splitter to combine the two images, this is shown in Figure 2-3 to reduce the number of CCDs to one.

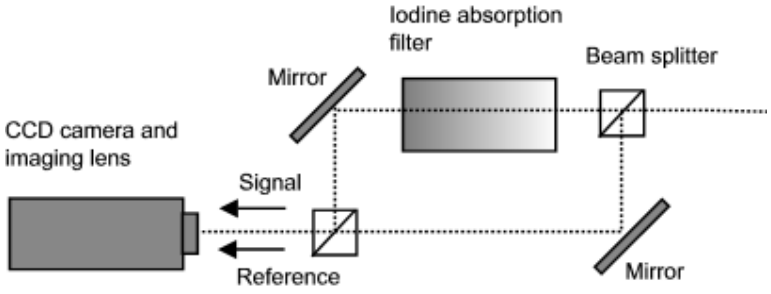

Figure 2-2 Diagram showing the single camera approach used by Ainsworth et al[46]

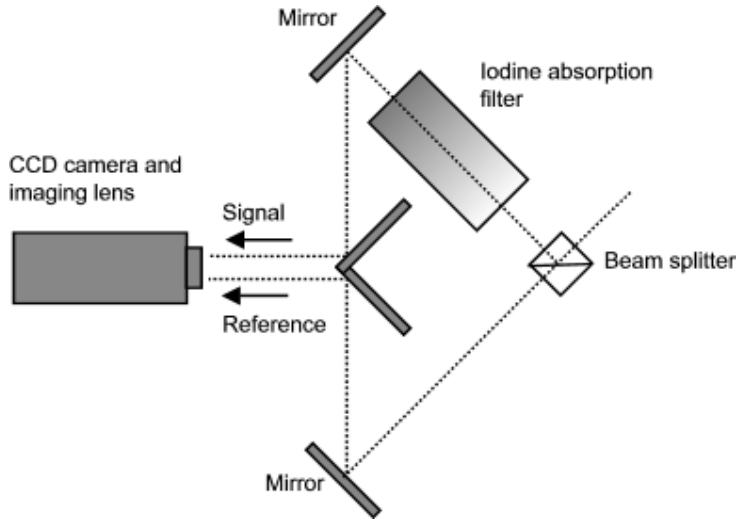

Figure 2-3 Diagram showing the single camera approach used by Chan et al[61,81]

A third, very different approach to the need to record a reference image is the 'two colour' approach, Figure 2-4. In this the flow is illuminated with laser light at two different frequencies, one of which is positioned well away from an absorption line, and the other tuned to a partial transmission point. The frequency that is well away from an absorption line is used as a reference while the second frequency provides the signal image. This technique is discussed further in chapter 3.

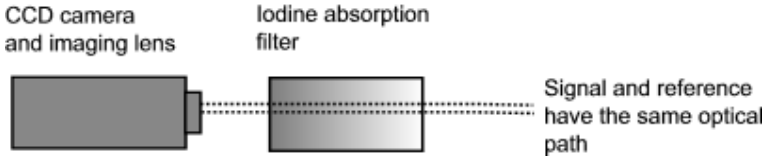

Figure 2-4 showing the two colour approach

2.4.2 Absorption cells

Typically the absorption cell used in PDV contains iodine vapour. Iodine gas has a large number of absorption lines in its spectrum and it is these that are used in PDV to provide the intensity to frequency conversion. The spectra of iodine has been described by Gerstenkorn and Luc[82] and calculated in a model by Forkey[83], with approximately 47000 lines in the 490-670nm range. One of the reasons why Iodine is ideally suited for use in PDV is that it is usually possible to tune the laser to an absorption line whilst remaining inside the gain curve of the laser.

The Beer-Lambert Law describes the absorption process through a medium:

$$\frac{I}{I_0} = \exp(-\alpha l)$$

Equation 2-1

Where l is the path length through the medium, (i.e. the cell length), and α is the absorption coefficient, which is dependent upon frequency and the concentration of the absorbing medium. I represents the measured intensity will I_0 is the initial intensity.

The shape of the absorption line is determined by three broadening process:

1) Natural broadening – Due to the finite lifetime of the energy state
2) Thermal (Doppler) broadening – Doppler shift caused by the thermal motion of molecules
3) Pressure broadening – Due to collisions between particles, foreign non-absorbing gases (Lorentz broadening), molecules of the same kind (Holtsmark broadening) and electrons or ions (Stark broadening).

There is also an additional continuum absorption (due to a transitions in the diffuse $1u(^1\Pi)\leftarrow X$ band and the $A(1u^3\Pi)\leftarrow X$ band[84]) in the 500-600 nm range, which increases with the number density of iodine. Different groups have used a variety of iodine cell designs, but the basic configuration consists of a cylindrical glass chamber with a side arm protruding from one side. In some it is possible to seal of the side arm using a valve.

The temperature of both of the side arm and the main chamber can usually be independently controlled and the chamber itself can be filled with pure iodine vapour or a mixture of iodine and another inert gas that is used to provide pressure broadening of the absorption lines. By keeping the side arm temperature lower than the cell the number density of iodine in the cell can be controlled, as the iodine will condense on the coldest point. This will also prevent condensation on the optical windows that are typically the next coldest point.

Elliot and Beutner[74], Samimy and Wernet[71] and Chan et al[61], provide good reviews of the absorption process and descriptions of how the transmission characteristics of an iodine cell can be varied:

1) Number density of Iodine

As the number density increases the cell goes from optically thin operation to optically thick operation. In the optically thin regime a considerable amount of light is not affected by its passage through the cell, leading to a shallower absorption well. The optically thick regime can be thought of as when at the minimum transmission point absorption is nearly complete. The optically thick regime is preferable as this leads to the greatest transmission curve gradient and hence better velocity resolution. Examples of the sizes of iodine cells used are: 76mm (3") diameter by 69.85mm (2.75") long[29] and 40mm diameter by 50mm long[36].

2) Temperature

The temperature of the cell can be varied to change the amount of Thermal broadening although this also increases the background absorption. Typical temperature ranges used are 50-110^{o}C[36,74].

3) Non-absorbing species (buffer gases)

The introduction of a second non-absorbing species, typically nitrogen, into the cell results in the pressure broadening of the absorption line. This can be used to stretch the feature making it possible to measure over larger velocity ranges.

When the desired characteristics of the cell have been decided upon it is necessary to take care in operating them. Saturated cells are those in which there is still condensed iodine present, as the side arm cannot be sealed off. These require precise control over the temperature of both the side arm and the cell body to ensure that the number density of iodine remains constant, and that the thermal broadening also remains constant.

Starved cells are those in which all the iodine is evaporated at a lower temperature than the operating temperature. This means that the number density will remain constant so long as the temperature is held above the point of total evaporation.
Saturated cells are easier to construct but have the disadvantages of requiring better temperature control to avoid the effect of environmental variations.

It is possible to design systems that work with other molecular filters, which can be selected to have absorption lines at frequencies at which the laser operates. For example Muller et al[85] use a Caesium absorption cell with a Distributed Feedback Reflector (DBR) Laser-diode operating at 852nm.

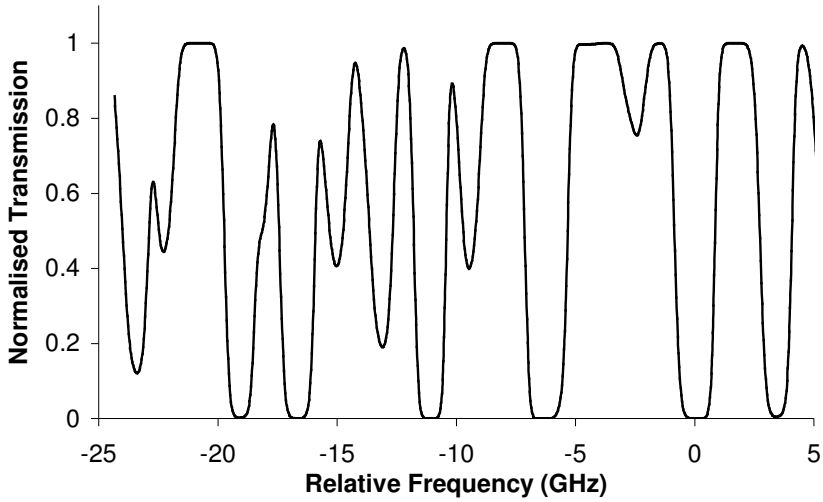

Figure 2-5 Example of Iodine absorption lines centred about 514.5nm, as calculated using the Forkey model[83] for the Cranfield system's iodine cell

2.4.3 CCD cameras

PDV measurements have been made using a variety of different quality cameras, from 8-bit video cameras with interlaced frames, to 16-bit cooled, scientific grade cameras. Elliot & Beutner[74] give a discussion on the advantages and disadvantages of the different cameras, with the following main points.

1) The lower quality camera have the advantage of lower cost, with researchers arguing that the higher quality camera cost cannot be justified with the level of error, from other effects in current PDV systems
2) Scientific grade cameras do reduce the uncertainties due to the measurement of intensities and they also offer a greater well depth. This seems important as for some PDV applications the intensity can vary considerably, with areas on the CCD saturated and others too low to be of use.

2.5 Processing schemes

The initial approach taken for the storage and processing of the data was the use of CCD camera's to capture the image, then analogue division and storage on high quality video cassette, as described in Komine's patent[22].

Meyers and Lee[24] describe and compare, an analogue-processing scheme, in which an analogue divider is used to provide a real-time normalized signal, and a digital scheme. They concluded that the flexibility in providing the capability to adjust for CCD pixel sensitivity, low signal level or saturated pixels and background light corrections, justified the use of a digital approach. It is the digital approach that is now universally favoured.

Although different groups may perform processing steps in a slightly different order, Reinath[29] gives the following as a general sequence of the processing steps, needed to convert raw PDV images into velocity images.

1) Background subtraction – remove ambient light and laser reflections.
2) Correction for pixel sensitivity variations – ensures that all pixels have the same response to a given incident light level.
3) De-warping – Images are warped to provide best possible alignment between signal and reference, as well as alignment between different component views, when more than one component of velocity is to be measured.
4) Normalization / Divide – Calculate the normalized transmission at each pixel, by dividing the signal pixel values by the reference values.
5) Flat-field/ 'white card' correction – Corrects for imaging defects that cause a variation in light levels across the CCD when a uniform scene is imaged.
6) Calculation of velocity image – The Doppler shift is first calculated using the normalized transmission and the zero velocity frequency; this is then converted to velocity using the Doppler equation.

Reinath[29] corrects for the pixel sensitivity variation using a linear correction technique. The actual response of each pixel is measured at two illumination levels, low and high, and then a correction is calculated by setting the corrected response to be the same as the mean response of the detector.

Several groups use a de-warping algorithm in their processing scheme in order to improve the pixel-to-pixel alignment between the signal and reference cameras.
Several authors include a good description of their de-warping algorithms, which are generally similar including Elliot & Beutner[74], Reinath[29] and Naylor[65].

The general principle behind them is the same with an image of a target being obtained before the data collection. The target is a grid of either dots or crosses, which is placed in the field of view. The software identifies the centres of each mark and these marks are used as reference points to 'warp' one image onto the other with each mark aligned to the corresponding mark on the other image. From this the value of each pixel in the de-warped image can be determined using the levels of the nearest pixels, Reinath[29] and McKenzie[86] reported that this improves the alignment to an accuracy of within 0.3 pixels.

The de-warping procedure can correct for image distortions caused by the optics, and the perspective distortion. Nobes et al[55] describe a technique to use the de-warping calculations to correct for variations that may occur in the assumed illumination and viewing vectors as discussed in the error assessment section. In this the viewing direction is calculated for each pixel in the image based upon the de-warping coefficients.

The flat-field, or 'white card', correction is used to correct for imaging defects, it can also correct for intensity variations caused by other effects. The white card correction consists of dividing the normalized pixel values by their respective white card correction pixel values.
In it's simplest from a piece of white card is illuminated uniformly with either white light or the laser sheet itself, in the imaging plane[64] and both signal and reference images are recorded. These are then normalized to produce the correction image.

Meyers[87] uses a variation which is now used by most groups, e.g. Kuhlman et al[88], which corrects for intensity variations caused by other effects. In this the laser is tuned to a position of maximum transmission and the white card images obtained by imaging the flow under measurement conditions. As the laser is tuned off the transfer function any Doppler shifting will not cause a change in transmission, although care must be taken to ensure that the laser frequency is far enough from an absorption feature. The resulting signal and reference camera images can then be divided to create the white card correction.

The correction is then applied by dividing the normalised image by the white card image. The corrected transmission ratio, TR_{corr}, is given in Equation 2-2, where the signal and reference images are *SIG* and *REF* respectively, and the white card signal camera image and reference camera images are given by W_{SIG} and W_{REF}

$$TR_{corr.} = \frac{SIG/REF}{W_{SIG}/W_{REF}}$$

Equation 2-2

After these corrections have been applied the ratio image values can then be converted to frequency shift values and finally to velocity, using the Doppler formula. This is done in two steps; the first step is to calculate the Doppler shift for each pixel in the image. This is done by converting from the transmission ratio to frequency for each pixel, and then subtracting the initial laser frequency, ν_0. The initial laser frequency itself is found from the transmission ratio of a portion of the laser directed into the field of view, or other similar techniques detailed above. Figure 2-6 shows an overview of the conversion from image intensity to the Doppler frequency shift, where TR_{pixel} is the transmission ratio for a pixel in the image, and TR_{zero} is the transmission ratio of the laser frequency reference/ zero velocity reference.

$$\Delta\nu = \nu_D - \nu_0$$

Equation 2-3

As well as these basic processing steps many groups choose to use spatial filters or pixel binning in the image processing to improve the clarity of results, by removing high frequency variations such a speckle noise.

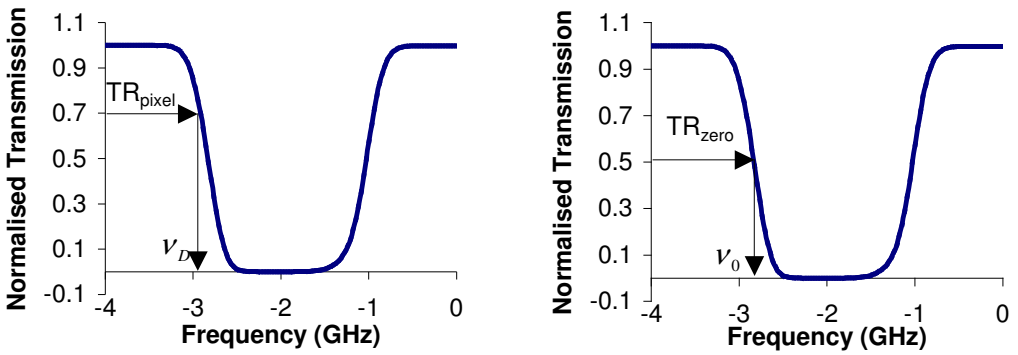

Figure 2-6 Overview of the conversion from transmission ratio to Doppler frequency shift; (a) showing the calculation Doppler shifted frequency ν_D from the transmission ratio TR_{pixel} and (b) the calculation of the zero shift frequency ν_0 from the laser transmission set point TR_{zero}

2.6 Evaluation of error sources in PDV

Elliot and Beutner[74] and Meyers et al[27] include a comprehensive discussions of the error sources found in a generalized PDV system. It is possible to separate the contributions to the uncertainty in PDV measurements, into biases and random errors.

2.6.1 Bias errors

The mechanisms for bias error, which are consistent for measurement-to-measurement, that are considered non-negligible are reported as:

1) Uncertainty in the angle between the incident light and the observation direction, ϕ.
2) Uncertainty in the calculation of frequency from the iodine cell absorption function.
3) Uncertainty in the laser frequency, ν_0, the zero velocity frequency.
4) Uncertainty in the measured transmission ratio.

Elliot and Beutner show that the uncertainty in the velocity, introduced by the angle between the incidence and observation directions is proportional to the velocity itself, Equation 2-4, and that the maximum error is found when the incident and observation directions are close together, going to infinity at ϕ=0, where the system is insensitive to velocity.

$$\Delta U_n = \frac{\partial U_n}{\partial \phi}\Delta\phi = \frac{-U_n}{2\tan(\phi/2)}\Delta\phi$$

Equation 2-4

Also as the illumination beam may be divergent, this angle will vary across the image; using large cylindrical optics or a scanned beam sheet can reduce this. The more divergent the sheet the larger the error, for a beam divergence of 15° Ford and Tatam[47] quote an error of 2ms^{-1},over 100ms^{-1} range, rising to 6ms^{-1} for a divergence of 30°. This can probably be ignored if the divergence is kept small or large optics or beam scanners are used.

A similar effect also discussed by Ford and Tatam[47] is that the observation vector will vary over the field of view, and they have calculated the typical effect this has upon normalized transmission. The effect is found to be greatest towards the edges of the image and can rise to above 0.01 of normalized transmission, or 2ms^{-1}, at greater than 5 degrees out from the centre of the field of view.

The uncertainty in velocity associated with the calculation of frequency from the iodine absorption function, has two sources, the accuracy in which the transmission profile was measured and any changes in the cells operating conditions between calibration and measurements. Several researchers smooth their measured profiles either by fitting to a Boltzmann Distribution or to theoretical absorption curves. The second effect, changes in the operating conditions of the iodine cell, such as temperature variations or leaks, will cause changes in the absorption profile. This can

be minimised by careful design of the cell and cell oven to isolate the molecular filter from environmental changes. The use of starved cells reduces the effect of the variation in cell temperature to only the thermal broadening of the absorption line.

Any error in the measurement of the laser zero-velocity frequency will cause a bias in the measured velocity as the Doppler shifts are measured relative to this frequency. There are two main causes of error in this zero-velocity frequency. The first is frequency chirp, the spatial variation in frequency across a pulse. This affects pulsed Nd:YAG lasers, as reported by Forkey[80], and can be reduced to less than 4MHz, by using only the centre of the beam, or careful alignment of the seed laser. The second source is long-term frequency drift, caused by thermal variations in the laser-operating environment.

Clancy[89] and Elliot et al[28] suggest that by careful selection of three viewing directions any effect of this laser frequency variation can be eliminated from two of the three orthogonal velocity components in the transformation stage. It is also suggested this can be extended to allow all three components to be independent of any frequency variation, by adding a fourth measured component which can be used to eliminate any laser frequency variation from the remaining orthogonal velocity component. However this may not always be possible due to optical access limitations.

Uncertainties arising from the measurement of the transmission ratio can come from several sources. Firstly there is camera non-linearity, the behaviour of the CCD to varying light levels. Scientific grade CCD cameras are generally linear. Willert et al[39] report non-linearity of up to several percent, towards the higher signal levels, which can be generally be ignored. The next error source is due to the image processing and includes changes in the background light level or camera movement since calibration.

An error can also be introduced due to secondary scattering effects from seeding particles. This can cause additional light to be scattered from surfaces biasing the background that was measured during calibration. Also secondary light scattering causes a change in the incident light direction as well a possible Doppler shift in addition to that cause by the primary scattering. Finally any scattering off surfaces may cause regions of the CCD to become saturated, this can be avoided by experimental design and/or discarding the affected regions.

2.6.2 Random errors

These are errors that fluctuate from measurement to measurement, and can be reduced by averaging. The main random errors are due to the measurement of the laser frequency, ν_0, the zero velocity frequency, and the measurement of the transmission ratio.

The random error in the zero velocity frequency depends upon the type of laser used as well if frequency monitoring is used. For Nd:YAG lasers the random uncertainty in the seed laser frequency is generally quoted by manufacturers as ~10-20MHz, which can rise to 150MHz if there is large variations in ambient temperature, or any vibrations acoustic noise.

For Argon Ion lasers the random fluctuation in frequency is about 10 MHz [46], but as mentioned previously there is also a long-term drift and also mode hops, which can be monitored and controlled. The error when frequency monitoring is used depends on the method of monitoring. For example Roehle[31] at DLR report precisions of ±1 MHz in their frequency monitoring system using the hyperfine structure in the iodine absorption spectrum.

The final source of random error is in the measurement of the transmission ratio. There are three main sources that contribute to the error in transmission, these are.

1) Radiometric noise from the CCD cameras.
2) Laser speckle noise.
3) Image alignment uncertainties.

The CCD radiometric noise has been investigated by McKenzie[84] and can be divided into three main contributions, photon statistical noise of the detection process, the circuit noise of the detector, which includes the read-out noise and the dark current noise, and the truncation of the signal when it is digitised. In this analysis a typical error in a velocity measurement, using scientific grade cameras, is calculated to be less than 2MHz (~1.5ms^{-1}). He also discusses the effect of varying the digital resolution of the cameras. Figure 2-7 show the effect of digital resolution on the random uncertainty in the Doppler shift. Using 8-bit cameras significantly worsens the uncertainty across the full range. In conclusion he states that 8-bit cameras are only suitable in high-speed flows where all the velocity components are significantly greater than 10ms^{-1}.

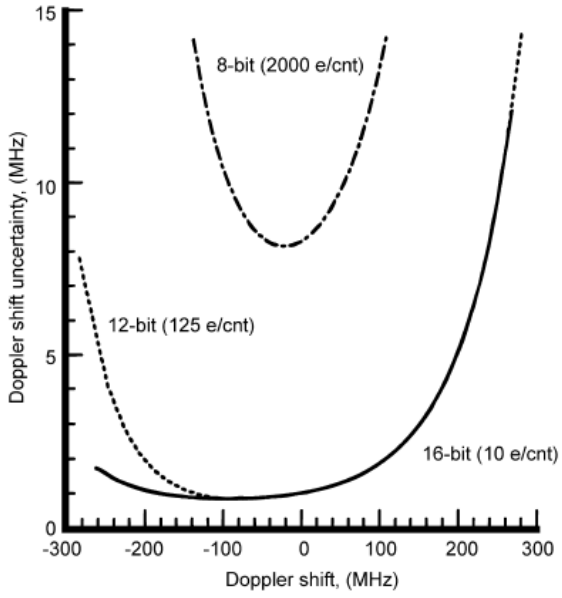

Figure 2-7 The effect of digital resolution on Doppler shift uncertainty, from McKenzie[84]

For instantaneous PDV measurements there is a major component of random uncertainty in the measurement of the transmission ratio caused by laser speckle. Speckle noise is introduced by interference patterns in light scattered off a surface or

from a cloud of particles. As PDV relies upon a ratio of the signal and reference images if the speckle pattern is not identical in both images then major errors can be introduced at this ratio stage. The speckle pattern is not the same in both images due to slight image alignment differences, and small differences in path length between the signal and reference. McKenzie[86] and Smith[90] give similar equations for the noise-to-signal ratio due to speckle, Equation 2-5, where F is the f-number of the optical system, m is the magnification ratio and Δx is the average size of the camera pixels.

$$NSR = \frac{1.2(1+m)\lambda F}{\Delta x}$$

Equation 2-5

This leads to the conclusions that to reduce the speckle noise, a small f-number (large camera aperture), small magnification and larger CCD pixels should be used. As magnification tends to be small for PDV experiments reducing the f-number is the most effective method of reducing the speckle noise.

Any error in the alignment between the signal and reference images will lead to an error in the normalisation stage. This is particularly important for areas with a high intensity gradient. Thorpe et al[91] discuss the assessment of the alignment error and quote a value of 0.1 of a pixel as a typical misalignment. They then go on to calculate the velocity error caused by this and give a figure of ± 5ms^{-1} as a pessimistic estimate.

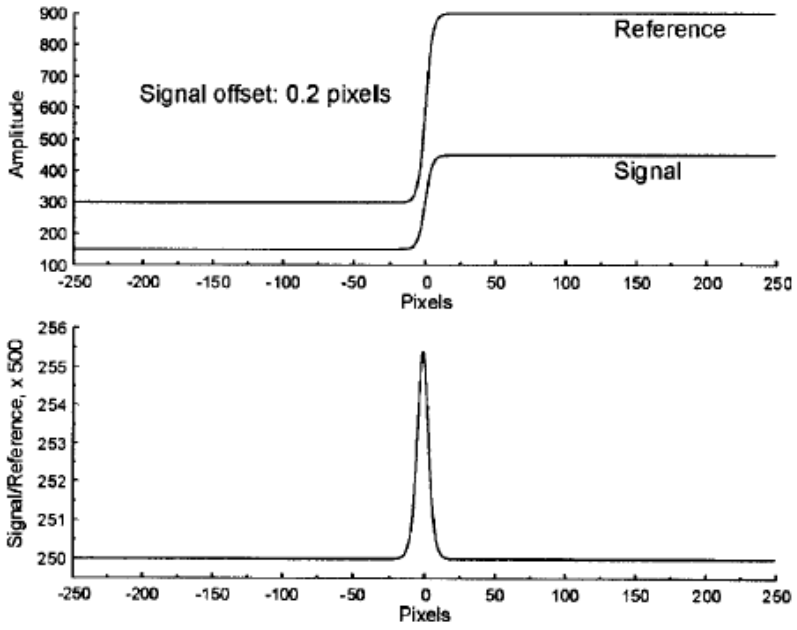

Figure 2-8 Simulated misalignment of the signal image with the reference image to determine the effect on the normalized results. From Meyers and Lee[26]

Meyers and Lee[26] also describe a technique to determine the level of misalignment between the signal and reference images. In this they compare the characteristics of the edge of some PDV data of a rotating wheel, with some theoretical edges for which the image misalignment was known. They choose to use a hyperbolic tangent function, Figure 2-8, for the theoretical transition from high to low signal levels, which simulated the edge of the disc. The resultant normalised signal is an impulse function when the images are misaligned, and by comparing the shape of this impulse with similar impulses seen in the PDV data the image misalignment could be estimated. Figure 2-9 shows the PDV data that they used with the 5-pixel wide impulses caused by the misalignment labelled.

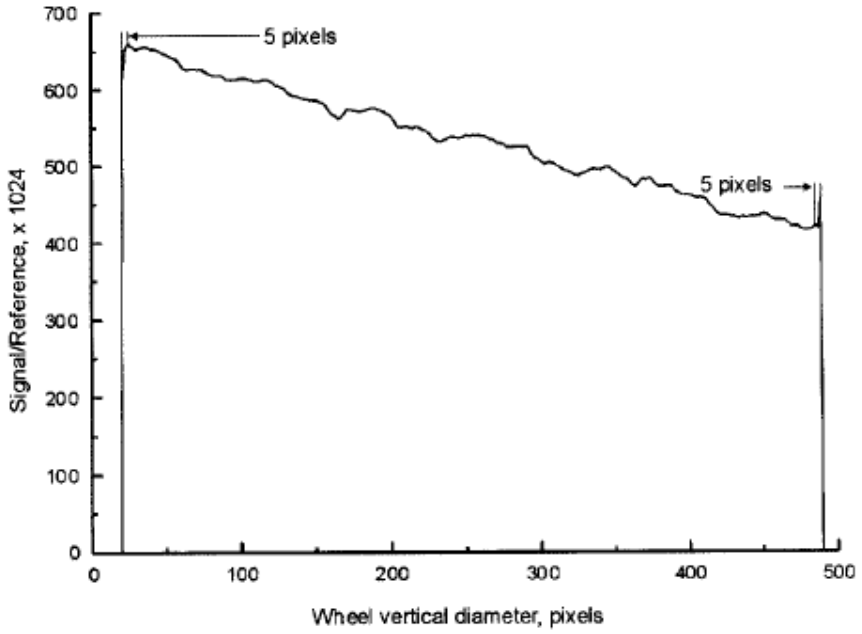

Figure 2-9 Normalized signal amplitude along the vertical axis of a rotating wheel indicating a misalignment of the signal and reference images. From Meyers and Lee[26]

Elliot and Beutner[74] report some values for the current level of bias and random error from various investigators. This is shown in Table 2-3.

Table 2-3 Reported bias and random error levels from various experiments, from Elliot and Beutner[74]

Velocity (m/s)	Bias Error (m/s)	Random Error (m/s)	Reference
600	30	30	[72]
18.9	1.0-1.51	0.35-0.95	[92]
20.2	0.5	1.3	[93]
500	25	40-80	[94]
-83 - 83	10	15	[95]
380	15	32	[96]
500	35	<20	[97]
60	2-5	2	[86]
-50 - 50	1	3.6	[98]
0.115-20	2.3		[99]
14.2	1.7	3.8	[100]
20.2	0.5	3.0	[100]
260	7	6	[100]
59	5	4	[66]
42	4	4	[66]
60	0.4-0.7	4-7	[29]
40-130	3		[101]

2.7 Experimental set-up and procedure

The viewing and illumination vectors should be chosen to maximize, the velocity component of the flow to be measured, however it not always possible due to restrictions in the optical access which is of particular importance when looking at internal flows such as in DLR's work [33,39].

One method that has been investigated for use in internal flows is the use of borescopes, Nobes et al[51], to make measurements in the wake region of a rotor stage on Cranfield University's Low speed research compressor. This is made possible by the use of imaging fibre bundles to transfer the images. Schodl et al[33] made use of endoscopes for PDV measurements in an engine inlet duct of a 1:10 scale model aircraft.

Another important issue that can affect choice of viewing directions is the Mie scattering geometry, where stronger scattering can be observed in the forward scattering direction and in some cases can result in low and high scattering intensities at particular viewing angles.

2.7.1 Three-dimensional velocity measurement

When the system is to measure 3D velocities it is necessary to measure three velocity components and then convert these to the orthogonal velocity components. This can be achieved in several different ways; by having three separate PDV heads, with three different viewing directions as done by Reinath[30], with three different illumination directions and a single PDV head, as has been done at DLR [31-34,36-39] or using multiple imaging fibre bundles, as used at Cranfield, to port multiple views to a single PDV imaging head[21,51].

The three-illumination approach is only suitable for time averaged velocity measurements as it necessary to illuminate from each direction at different times, where as with three views it is possible to make measurements simultaneously.

The third approach to measuring three components of velocity has been used by Nobes et al[51] this involves using only one PDV detector head but using multiple imaging fibre bundles, with four bundles delivering their views to a single end, split into quadrants. Light from the bundle can then enter the PDV head. The first three views are used to deliver the three viewing directions, with the fourth view being used to measure the intensity transmission of the un-shifted laser frequency. The four bundles come together at the detector head to produce a view that is spilt into four quadrants. Willert et al have also adopted a similar approach[21].

The three measured components will not usually be the same as the coordinate system used in the experiment; therefore it is necessary to convert the measured velocity components to those used in the experiment. A derivation of the method for this is given in Reinath[29] as well as an analysis of the uncertainty in the final components. From this it can be seen that the choice of the three measured components will affect the errors propagating into the calculated components in the experiments coordinate system. The ideal case would be for three mutually orthogonal components to be measured, although this is difficult to achieve with the restrictions on optical access and scattering geometry, as discussed below.

One approach to optimising 3D PDV systems is to use the condition number of the matrix defining the transformation to the orthogonal components from the measured components. This provides a measure of how uncertainties are amplified/propagated from the measured components to the orthogonal components. Elliott et al[28] include a discussion about the optimisation of a multi-component PDV by minimising the condition number for the special case-viewing configuration where laser frequency fluctuations will be cancelled out in the calculation.

Another consideration with 3D PDV systems is that it is necessary to have the same measurement area from each view. This can be obtained by careful set-up and the use of the de-warping process to map all the views to a common view. This then allows the calculation of the orthogonal components to proceed.

2.7.2 Combined PDV and particle imaging velocimetry (PIV)

Several groups[43,44,102,103] have also reported work using a combined PDV and PIV approach. A pulsed laser is combined with double frame PIV cameras viewing the light sheet perpendicularly. Here the in plane velocities are measured using PIV

(using both recorded frames) and the out of plane velocity component measured using PDV (using both cameras). Wernet[103] reports a demonstration of such a system on the measurement of a seeded air jet and makes a comparison with stereo PIV measurements made on the same flow. Here he reports errors of 2.1, 3 and 5.3ms^{-1} for the U, V and W components respectively with improved accuracy being possible with modifications to the injection seeded laser used.

2.7.3 Combined point Doppler Velocimetry (pDv) and Laser-two-focus (L2F) velocimetry

Forster et al[10] describe a combined Laser-two-focus (L2F) and Doppler velocimeter, capable of making point three component velocity measurements. The probe consisted of three parallel beams with different frequencies, two for the L2F method (at 488nm and 496nm) and the third at 514nm to find the Doppler shift. The collected light from particles passing through these beams is collected and separated according to its wavelength. Two components of the velocity are found using the signal from the scattered light at 488nm and 496nm and commercial L2F signal processors. The pulse of light from the third beam is separated and split into two using a non-polarising beam splitter. One beam is guided through an iodine cell to a photomultiplier tube, and provides the signal light pulses while the other is guided through an optical fibre delay line to the same photomultiplier. This provides the reference light pulse, separated from the signal pulse by 645ns. The third velocity component can then be calculated by the ratio of the intensities of each pulse.

2.7.4 Coherent detection in PDV using streak cameras

Coupland and Lawson [104,105] describe a related technique which they called multi-point Laser Doppler Anemometry (MPLDA). Here the flow is illuminated with a set of parallel propagating laser beams, the light scattered by particles seeded in the flow is collected and mixed with a reference beam. A streak camera is then used to record the periodic fluctuation in intensity at the Doppler frequency, from which the velocity can be determined along a profile. By using multiple beams and limiting the streak camera translation multiple velocity profile can be found corresponding to multiple beams in the flow. A frequency shift in the reference beam is used to avoid direction ambiguity. They present low speed results on a rotating disc, over a velocity range <3mms^{-1}, using a rotating mirror to streak the images. A system using an electronic streak tube was then demonstrated on a water spray with a velocity of ~9ms^{-1}.

2.8 Summary

The aim of this chapter was to give an overview of flow measurement instrumentation and the relevance of the PDV technique. Previous work in the PDV field was then reviewed with the components and methods used reviewed along with the main issues, including:

- The laser illumination, frequency monitoring and stabilisation and flow seeding requirements.
- The detector head including the arrangement, cameras and molecular filters.
- Processing applied to the captured data.
- Evaluation of error sources
- Experimental set-up and procedure including requirements for 3D measurements and combined methods using PDV with other techniques.

2.9 References

1. Stainback, P.C. and Nagabushana, K.A., "Review of Hot-wire Anemometry Techniques and the range of their applicability for various flows", 1997, *Electronic Journal of Fluids Engineering, Transactions of the ASME.*

2. Jackson, D.A. and Paul, D.M., "Measurement of supersonic velocity and turbulence by laser anemometry", 1971, *J. Phys. E: Sci Instrum.*, Vol. 4, No. 3, pp 173-177.

3. Yeh, Y. and Cummins, H.Z., "Localized flow measurements with a HE-Ne laser spectrometer", 1964, *Applied Optics*, Vol. 4, No. 10, pp 176-178.

4. Nakatani, N., Tokita, M., and Yamada, T., "LDV using polarisation-preserving optical fibers for simultaneous measurement of two velocity components", 1984, *Applied Optics*, Vol. 23, pp 1686-1687.

5. Lockey, R.A. and Tatam, R.P., "Multi-component time-division multiplexed optical fibre Doppler anemometer", 1997, *IEE Proc. Optoelectron.*, Vol. 144, pp 168-175.

6. James, S.W., Tatam, R.P., and Elder, R.L., "Design considerations for a three-dimensional fibre optic laser Doppler Velocimeter for Turbomachinery applications", 1997, *Review of Scientific Instruments*, Vol. 8, pp 3241-3246.

7. TSI website", 2006, http://www.tsi.com.

8. Dantec website", 2006, http://www.dantecdynamics.com/.

9. Schodl, R., " Method of and apparatus for measuring flow vectors in streams of gas", 1983, *GB patent*, GB2109548.

10. Forster, W., Karpinsky, H., Krain, H., Rohle, I., and Schodl, R., "3-Component-Doppler-Laser-Two-Focus Velocimetry applied to a transonic

centrifugal compressor", 2000, *10th International Symposium on Applications of Laser techniques to Fluid Mechanics*, Lisbon, Portugal, Paper 7-2.

11. Nakatani, N., Nishikawa, T., and Yamada, T., "LDV optical system with multifrequency shifting for simultaneous measurement of flow velocities at several points", 1980, *J. Phys. E: Sci Instrum.*, Vol. 13, pp 172-173.

12. Czarske, J., "Laser Doppler velocity profile sensor using chromatic coding", 2001, *Measurement Science and Technology*, Vol. 12, pp 52-57.

13. Buttner, L. and Czarske, J., "Spatial resolving laser Doppler velocity profile sensor using slightly tilted fringe systems and phase evaluation", 2003, *Measurement Science and Technology*, Vol. 14, pp 2111-2120.

14. Pfister, T., Buttner, L., and Czarske, J., "Laser Doppler profile sensor with sub-micrometre position resolution for velocity and absolute radius measurements of rotating objects", 2005, *Measurement Science and Technology*, Vol. 16, pp 627-641.

15. Stier, B. and Koochesfahani, M., "Molecular Tagging Velocimetry (MTV) measurements in gas phase flows", 1999, *Experiments in Fluids*, Vol. 26, pp 297-304.

16. Arroyo, M.P. and Greated, C.A., "Stereoscopic Particle Image Velocimetry", 1991, *Measurement Science and Technology*, Vol. 2, pp 1181-1186.

17. Kent, J.C., Trgui, N., Choi, W.-C., Guezennec, Y.G., and Brodkey, R.S., "Photogrammetric calibration for improved three-dimensional particle tracking velocimetry", 1993, *Proc. SPIE Optical Diagnostics in Fluid and Thermal Flow*, Vol. 2005, pp 400-412.

18. Brucker, C., "3D scanning PIV applied to air flow in a motored engine using digital high speed video", 1997, *Measurement Science and Technology*, Vol. 8, pp 1480-1492.

19. Hinsch, K.D., "Holographic particle image velocimetry", 2002, *Measurement Science and Technology*, Vol. 13, pp R61-R72.

20. McKenzie, R.L. and Reinath, M.S., "Planar Doppler Velocimetry Capabilities at Low Speeds and its Application to a Full-Scale Rotor Flow (Invited)", 2000, *AIAA 21st Aerodynamic Measurement Technology and Ground Testing Conference*, Denver, Colorado, Paper 2000-2292.

21. Willert, C., Stockhausen, G., Beversdorff, M., klinner, J., Lempereur, C., Barricau, P., Quest, J., and Jansen, U., "Application of Doppler Global velocimetry in cryogenic wind tunnels", 2005, *Experiments in Fluids*, Vol. 39, pp 420-430.

22. Komine, H., "System for measuring velocity field of fluid flow utilizing a laser-Doppler spectral image converter", 1990, *United States Patent*, Number 4,919,536.

23. Meyers, J.F. and Lee, J.W., "Proof of concept test of the Doppler Global Velocimeter", 1991, *Spaceborne Photonics: Aerospace Applications Of Lasers And Electro-optics*, Newport Beach, CA,

24. Meyers, J.F. and Lee, J.W., "Signal processing schemes for Doppler Global Velocimetry", 1991, *14th International Congress on Instrumentation in Aerospace Simulation Facilities*, Rockville, Maryland,

25. Smith, M.W., "Application of a Planar Doppler Velocimetry System to a High Reynolds Number Compressible Jet", 1998, *36th AIAA Aerospace Sciences Meeting and Exhibit*, Reno, Nevada,

26. Meyers, J.F. and Lee, J.W., "Investigation of Measurement Errors in Doppler Global Velocimetry", 1999, *SAE World Aviation Congress and Exposition*, San Francisco, California, Paper 1999-01-5599.

27. Meyers, J.F., Lee, J.W., and Schwartz, R.J., "Characterization of Measurement Error Sources in Doppler Global Velocimetry", 2001, *Measurement Science and Technology*, Vol. 12, pp 357-368.

28. Elliott, G.S., Crafton, J., Beutner, T.J., Carter, C.D., Baust, H.D., and Tyler, C., "Evaluation and optimisation of a Multi-component Planar Doppler Velocimetry System", 2005, *AIAA 43rd Aerospace Sciences Meeting and Exhibit*, Reno, Nevada, AIAA 2005-35.

29. Reinath, M.S., "Doppler Global Velocimeter Development for the Large Wind Tunnels at Ames Research Center", 1997, *NASA*, Technical Memorandum 112210.

30. Reinath, M.S., "Doppler Global Velocimeter Development for Large Wind Tunnels", 2001, *Measurement Science and Technology*, Vol. 12, pp 432-441.

31. Roehle, I., "Three-dimensional Doppler Global Velocimetry in the flow of a fuel spray nozzle and in the wake region of a car", 1996, *Flow Measurement Instrumentation*, Vol. 7, No. 3/4, pp 287-294.

32. Willert, C., Blumcke, E., Beversdorff, M., and Unger, W., "Application of Phase-Averaging Doppler Global Velocimetry to Engine Exhaust Flows", 2000.

33. Schodl, R., Willert, C., Roehle, I., Heinze, J., Foerster, W., Fischer, M., and Beversdorff, M., "Optical diagnostics Techniques in Turbomachinery", 2002, *22nd AIAA Aerodynamic Measurement Technology and ground testing conference*, St. Louis, Missouri, AIAA 2002-3038.

34. Forstermann, M. and Buterfisch, K.A., "Experimental Investigations on Vortex Breakdown over Delta Wings with Doppler Global Velocimetry", 1999, *18th International Congress on Instrumentation in Aerospace Simulation Facilities*, Toulouse, France,

35. Fischer, M., Heinze, J., Matthias, K., and Roehle, I., "Doppler Global Velocimetry in Flames Using a newly Developed, Frequency Stabilized

Tunable, Long Pulse Nd:YAG Laser", 2000, *11th International Symposium on Applications of Laser techniques to Fluid Mechanics*, Lisbon, Portugal,

36. Roehle, I., Willert, C., Schodl, R., and Voigt, P., "Recent Developments and Applications of Quantitative Laser Light Sheet Measuring Techniques in Turbo machinery Components", 2000, *Measurement Science and Technology*, Vol. 11, pp 1023-1035.

37. Roehle, I. and Willert, C., "Extension of Doppler Global Velocimetry to Periodic Flows", 2001, *Measurement Science and Technology*, Vol. 12, pp 420-431.

38. Schodl, R., Roehle, I., Willert, C., Fischer, M., Heinze, J., Laible, C., and Schilling, T., "Doppler Global Velocimetry for the analysis of combustor flows", 2002, *Aerospace Science and Technology*, Vol. 6, pp 481-493.

39. Willert, C., Roehle, I., Schodl, R., Dingel, O., and Seidel, T., "Application of Planar Doppler Velocimetry within Piston Engine Cylinders", 2002, *Proceedings 11th International Symposium on Applications of Laser Techniques to Fluid Mechanics*, Lisbon, Portugal, Paper No. 38-2 (engines).

40. Mignosi, A., Lempereur, C., Barricau, P., Mathe, J.-M., and Buchet H., "Development and Qualification of a new Doppler Global Velocimeter", 2001, *19th International Congress on Instrumentation in Aerospace Simulation Facilities*, pp 386-396.

41. Lempereur, C., Barricau, P., Mathe, J.-M., and Mignosi, A., "Doppler Global Velocimetry: Accuracy Tests in a Wind Tunnel", 1999, *18th International Congress on Instrumentation in Aerospace Simulation Facilities*, Toulouse, France,

42. Barricau, P., Lempereur, C., Mathe, J.-M., Mignosi, A., and Buchet H., "Doppler Global velocimetry : Development and Wind Tunnel Tests",

43. Boemmels, R. and Roesgen, T., "Components for a three-component velocimeter using Doppler global velocimetry (DGV) and PIV", 2002, *Proc. Appl. Math. Mech.*, Vol. 1, pp 250-251.

44. Boemmels, R. and Roesgen, T., "Development of a planar three component velocimeter using Doppler Global Velocimetry and PIV", 2001, *19th international Congress on Instrumentation in Aerospace Simulations Facilities*, pp 211-218.

45. Thorpe, S.J. , Quinlan, N., and Ainsworth, R.W., "The Characterisation and Application of a Pulsed Neodymium YAG Laser DGV System to a Time-varying High-speed Flow", 2000, *Optics & Laser Technology*, Vol. 32, pp 543-555.

46. Ainsworth, R.W., Thorpe, S.J., and Manners, R.J., "A New Approach to Flow-Field Measurement - A View of Doppler Global Velocimetry", 1997, *Int. J. Heat and Fluid Flow*, Vol. 18, pp 116-130.

47. Ford, H.D. and Tatam, R.P., "Development of Extended Field Doppler Velocimetry for Turbomachinery Applications", 1997, *Optics and Lasers in Engineering*, Vol. 27, pp 675-696.

48. Ford, H.D., Nobes, D.S., and Tatam, R.P., "Acousto-optic Frequency Switching with Fibre-optic Delivery for Single Camera Planar Doppler Velocimetry", 2003, *16th International Conference on Optical Fiber Sensors*, Nara, Japan, Tu3-5, pp 226-229.

49. Nobes, D.S., Ford, H.D., and Tatam, R.P., "Instantaneous, Two Camera, Three Dimensional Planar Doppler Velocimetry using Imaging Fiber Bundles", 2001, *SPIE Proceedings, Optical Diagnostics for Fluids, Solids and Combustion*, San Diego, Vol. 4448, pp 72-83.

50. Nobes, D.S., Ford, H.D., and Tatam, R.P., "Planar Doppler Velocimetry Measurements of Flows using Imaging Fiber Bundles", 2003, *Proc. SPIE*, 5191, pp 122-133.

51. Nobes, D.S., Ford, H.D., and Tatam, R.P., "Three Component Planar Doppler Velocimetry Using Imaging Fibre Bundles", 2004, *Experiments in Fluids*, Vol. 36, No. 1, pp 3-10.

52. Ford, H.D., Nobes, D.S., and Tatam, R.P., "Acousto-optic Frequency switching for single-camera planar Doppler Velocimetry", 2001, *SPIE proceedings, Optical Diagnostics for Fluids, Solids and Combustion,* San Diego, CA, Vol. 4448, pp 272-282.

53. Charrett, T.O.H., Ford, H.D., Nobes, D.S., and Tatam, R.P., "Dual Illumination Planar Doppler Velocimetry using a Single Camera", 2003, *Optical Diagnostics for Fluids, Solids, and Combustions II, Proceedings of the Society of Photo-optical Instrumentation Engineers (SPIE)*, San Diego, CA, paper 5191, pp 113-121.

54. Ford, H.D. and Tatam, R.P., "Imaging System Considerations in Doppler Global Velocimetry", 1995, *Proc. SPIE*, San Diego, CA, 2546, 454-464.

55. Nobes, D.S., Wieneke, B., and Tatam, R.P., "Determination of View Vectors from Image Warping Mapping Functions", 2004, *Optical Engineering*, Vol. 43, No. 2, pp 407-414.

56. Charrett, T.O.H., Ford, H.D., Nobes, D.S., and Tatam, R.P., "Two frequency Planar Doppler Velocimetry (2υ-PDV)", 2004, *Review of Scientific Instruments*, Vol. 75, No. 11, pp 4487-4496.

57. Charrett, T.O.H., Ford, H.D., Nobes, D.S., and Tatam, R.P., "Two-Frequency Planar Doppler Velocimetry (2υ-PDV)", 2004, *12th International symposium on the application of Laser Techniques to fluids*, Lisbon,

58. Charrett, T.O.H., Ford, H.D., and Tatam, R.P., "Single camera 3D planar velocity measurements using imaging fibre bundles and two frequency Planar Doppler Velocimetry (2ν-PDV) ", 2005, *17th Conference on Optical Fibre Sensors (OFS)*, Bruges, Belgium, Proc SPIE 5855, pp924-927.

59. Charrett, T.O.H., Ford, H.D., and Tatam, R.P., "Single Camera 3D Planar Doppler Velocity Measurements using Imaging Fibre Bundles", 2005, *Second international conference on Optical and Laser Diagnostics (ICOLAD)*, City University, London,

60. Charrett, T.O.H. and Tatam, R.P., "Single camera three component planar velocity measurements using two frequency Planar Doppler Velocimetry (2n-PDV) ", (In press), *Measurement Science and Technology*.

61. Chan, V.S.S., Heyes, A.L., Robinson, D.I., and Turner, J.T., "Iodine Absorption Filters for Doppler Global Velocimetry", 1995, *Measurement Science and Technology*, Vol. 6, pp 784-794.

62. Chan, V.S.S., Robinson, D.I., and Turner, J.T., "A simplified Doppler Global Velocimeter", 1995, *Laser Anemometry ASME*, FED-Vol 229.

63. Kuhlman, J., Naylor, S., James, K., and Ramanath, S., "Accuracy Study of a 2-component Point Doppler Velocimeter (PDV)", 1997, *AIAA 28th Fluid Dynamics Conference*, Snowmass Village, Colorado, AIAA-97-1916.

64. Naylor, S. and Kuhlman, J., "Accuracy Studies of a Two-Component Doppler Global Velocimeter (DGV)", 1998, *36th AIAA Aerospace Sciences Meeting and Exhibit*, Reno, Nevada.

65. Naylor, S., "Development and Accuracy Determination of a Two-Component Doppler Global Velocimeter (DGV)", 1998, *West Virginia University*, PhD Dissertation.

66. Naylor, S. and Kuhlman, J., "Results for a Two-Component Doppler Global Velocimeter", 2000, *AIAA Journal*, Vol. 38, No. 5, pp 835-842.

67. Kuhlman, J., Collins, P.M., and Scarberry, T., "Two-Component Point Doppler Velocimetry Data in Circular Jets", 2001, *Measurement Science and Technology*, Vol. 12, pp 395-408.

68. Webb, D.L., "Development of and Measurements Using a Point Doppler Velocimetry (PDV) System", 1998, *West Virginia University*, MSc Thesis.

69. Collins, P.M., "Point Doppler Velocimetry measurements in Circular Jets", 2000, *West Virginia University*, MSc Thesis.

70. Kuhlman, J. and Scarberry, T., "Improved Point Doppler Velocimeter (pDv) Turbulence Data in Circular Jets", 2001, *39th AIAA Aerospace Sciences Meeting and Exhibit*, Reno, Nevada,

71. Samimy, M. and Wernet, M.P., "Review of Planar Multiple-Component Velocimetry in High-Speed Flows", 2000, *AIAA Journal*, Vol. 38, No. 4, pp 553-574.

72. Arnette, S.A., Samimy, M., and Elliott, G.S., "Two-component Planar Doppler Velocimetry in the compressible turbulent boundary layer", 1998, *Experiments in Fluids*, Vol. 24, pp 323-332.

73. Thurow, B., Hileman, J., Samimy, M., and Lempert, W., "Progress towards a real-time quantitative measurement technique for high-speed flows", 2001, *31st AIAA Fluid Dynamics Conference and Exhibit*, Anaheim, California, AIAA-2001-2985.

74. Elliott, G.S. and Beutner, T.J., "Molecular Filter Based Planar Doppler Velocimetry", 1999, *Progress in Aerospace Sciences*, Vol. 35, pp 799-845.

75. Arnette, S.A., Elliott, G.S., and Mosedale, A.D., "Two-colour planar Doppler Velocimetry", 2000, *AIAA Journal*, Vol. 38, No. 11, pp 2001-2006.

76. Morrision, G.L. and Gaharan, C.A., "Uncertainty estimates in DGV Systems due to Pixel Location and velocity Gradients", 2001, *Measurement Science and Technology*, Vol. 12, pp 369-377.

77. Leporcq, B., Le Roy, J.F., Pinchemel, B., and Dufour, C., "An Improvement in Doppler Global Velocimetry The Use of a CW Dye Laser", 1996, *8th International Symposium on Application of Laser Techniques to Fluid Mechanics*, Lisbon, Portugal,

78. Leporcq, B., Le Roy, J.F., Pinchemel, B., and Dufour, C., "Interest of a CW Dye Laser in Doppler Global Velocimetry", 1996, *1996 ASME Fluids Engineering Division Conference*, San Diego, CA,

79. Chehura, E. and Tatam, R.P., "In-line Laser Doppler Velocimeter using fibre-optic Bragg grating interferometric filters", 2003, *Measurement Science and Technology*, Vol. 14, pp 724-735.

80. Forkey, J.N., Lempert, W.R., and Miles, R.B., "Observation of a 100-MHz frequency variation across the output of a frequency-Doubled injection-seeded unstable-resonator Q-switched Nd:YAG laser", 1997, *Optics Letters*, Vol. 22, No. 4, pp 230-232.

81. Chan, V.S.S., "Particle Based Velocimetry Techniques for Measurement in Reciprocating Engines", 1999, *University of Manchester*, PhD Thesis.

82. Gerstenkorn, S. and Luc, P., " Atlas du Spectre d'Absorption de la Molecule d'Iode 14800-200 cm^{-1} Complement: Identification des Transitions du Systeme (B-X)", 1986, Editions du Centre Nationale de la Recherche Scientifique, Paris, France, ISBN

83. Forkey, J.N., Lempert, W.R., and Miles, R.B., "Corrected and calibrated I_2 absorption model at frequency-doubled Nd:YAG laser wavelengths", 1997, *Applied Optics*, Vol. 36, No. 27, pp 6729-6738.

84. McKenzie, R.L., "Measurement Capabilities of Planar Doppler Velocimetry using Pulsed Lasers", 1995, *AIAA 33rd Aerospace Sciences Meeting and Exhibit*, Reno, NV, Paper 95-0297.

85. Muller, H., Eggert, M., Pape, N., Dopheide, D., Czarske, J., Buttner, L., and Razik, T., "Time resolved DGV based on laser frequency modulation", 2004, *12th International symposium on the application of Laser Techniques to*

fluids, Lisbon, Portugal.

86. McKenzie, R.L., "Planar Doppler Velocimetry Performance in Low-Speed Flows", 1997, *35th AIAA Aerospace Sciences Meeting and Exhibit*, Reno, Nevada, AIAA-97-0498.

87. Meyers, J.F., "Evolution of Doppler Global Velocimetry data processing ", 1996, *8h International Symposium on Applications of Laser Techniques to Fluid Mechanics*, Lisbon, Portugal,

88. Kuhlman, J., Burton, L., and Scarberry, T., "Doppler Global Velocimetry data in circular jets", 2002, *Measurement Science and Technology*, Vol. 13, pp 1154-1162.

89. Clancy, P.S., Samimy, M., and Erskine, W.R., "Planar Doppler Velocimetry: Three Component velocimetry in Supersonic Jets", 1999, *AIAA Journal*, Vol. 37, No. 6, pp 700-707.

90. Smith, M.W., "The Reduction of Laser Speckle Noise in Planar Doppler Velocimetry Systems", 1998, *20th AIAA Advanced Measurement and Ground Testing Technology Conference*, Albuquerque, NM, AIAA 98-2607.

91. Thorpe, S.J., Ainsworth, R.W., and Manners, R.J., "The Development of a Doppler Global Velocimeter and its Application to a Free Jet Flow", 1995, *ASME / JSME Fluids Engineering and Laser Anemometry Conference and Exhibition*, Hilton Head, SC, USA,

92. Beutner, T.J., Elliott, G.S., Mosedale, A.D., and Carter, C.D., "Characterization and applications of Doppler Global Velocimetry", 1999, *37th AIAA Aerospace Sciences Meeting and Exhibit*, Reno, NV, AIAA-1999-266.

93. Beutner, T.J., Elliott, G.S., Mosedale, A.D., and Carter, C.D., "Doppler global velocimetry applications in large scale facilities", 1998, *20th AIAA Advanced measurement and ground testing technology conference*, Albuquerque, NM, AIAA-1998-2608.

94. Clancy, P.S., "Development and application of three-component planar Doppler velocimetry for high speed flows", 1997, *The Ohio State University*, Ph.D. Dissertation.

95. Elliott, G.S., "The study of compressible free shear layers using laser based diagnostic techniques", 1993, *The Ohio State University*, Ph.D. Dissertation.

96. Elliott, G.S. and Samimy, M., "A molecular filter based velocimetry technique for high speed flows", 1994, *Experiments in Fluids*, Vol. 18, pp 107-18.

97. Elliott, G.S., Mosedale, A.D., Gruber, M.R., Nejad, A.S., and Carter, C.D., "The study of a transverse jet in a supersonic cross-flow using molecular filter based diagnostics", 1997, *33rd AIAA/ASME/SAE/ASEE Joint Propulsion Conference and Exhibit*, Seattle, WA, AIAA-1997-2999.

98. Meyers, J.F. and Komine, H., "Doppler Global Velocimetry: a new way to look at velocity", 1991, *Laser Anemometry*, Vol. 1, pp 273-277.

99. Morrision, G.L. and Gaharan, C.A., "On the development of a Doppler planar velocimeter", 1998, ASME Paper FEDSM98-5283.

100. Mosedale, A.D., Elliott, G.S., Carter, C.D., and Beutner, T.J., "On the use of planar Doppler velocimetry ", 1998, *29th Fluid Dynamics Conference*, Albuquerque, NM, AIAA-98-2809.

101. Roehle, I. and Schodl, R., "Evaluation of the accuracy of the Doppler Global velocimetry technique", 1994, *Proceedings in Heat and Fluid Flow*, London, UK, 155-161.

102. Wernet, M.P., "Planar Particle Imaging Doppler velocimetry, A 3-Component Velocity Measurement Technique", 2004, *42nd AIAA Aerospace Sciences Meeting and Exhibit*, Reno, Nevada, AIAA 2004-22.

103. Wernet, M.P., "Planar Particle Imaging Doppler velocimetry, a hybrid PIV/DGV technique for three-component velocity measurements", 2004, *Measurement Science and Technology*, Vol. 15, pp 2011-2028.

104. Coupland, J., "Coherent Detection in Doppler Global Velocimetry: A simplified method to measure subsonic fluid flow fields", 2000, *Applied Optics*, Vol. 39, No. 10, pp 1505-1510.

105. Coupland, J. and Lawson, N., "The Development of Multi-point Laser Doppler Anemometry (MPLDA): A New method to estimate Fluid Flow Statistics", 2004, *12th International symposium on the application of Laser Techniques to fluids*, Lisbon.

3 Two-frequency Planar Doppler Velocimetry

3.1 Introduction

This chapter contains an explanation of the two-frequency Planar Doppler Velocimetry (2ν-PDV) concept, including a description of the two approaches for the positioning of the illumination frequencies. The advantages and disadvantages of the technique are discussed along with a review of other similar techniques in the Doppler Velocimetry field.

3.2 The theory of Two-frequency Planar Doppler Velocimetry (2ν-PDV)

In the two-frequency Planar Doppler Velocimetry (2ν-PDV) technique the signal and reference images are acquired sequentially, on the same CCD camera, Figure 3-1, by the use of two illumination frequencies. There are two approaches to the positioning of the illumination frequencies relative to the iodine absorption line, the normal and increased sensitivity schemes.

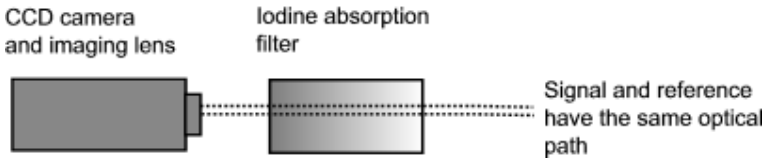

Figure 3-1. Two frequency PDV, single CCD camera imaging head.

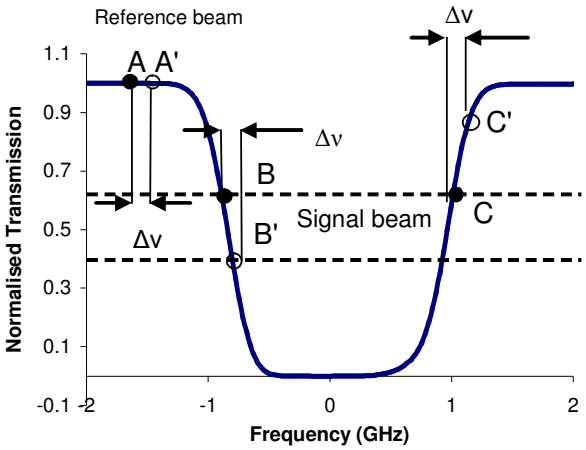

Figure 3-2. Relative positions of the laser frequency, and the shifted frequency on a typical absorption feature for 2ν-PDV (A and B/C denote the position of the illumination frequencies and A' and B'/C' the Doppler shifted frequency)

3.2.1 Normal sensitivity scheme

The first approach, the normal sensitivity scheme, is similar to conventional PDV, where signal and reference images are acquired. In conventional PDV these are acquired simultaneously using two CCD cameras, however, as mentioned above, here they are acquired sequentially on a single CCD camera.

The first illumination frequency is tuned just off the low frequency side of an absorption line to lie in a zero absorption region of the iodine transfer function (Figure 3-2, point A). With the flow illuminated by this beam any Doppler frequency shifts will cause no change in the level of light transmitted through the iodine cell, so long as the reference beam frequency is positioned on a flat portion of the transmission spectrum and that this region extends beyond the range of the Doppler frequency shift. An image taken with this illumination will have no sensitivity to the velocities in the flow, and can provide a reference image.

The second illumination frequency is positioned on the absorption line, typically at approximately midway (50%) on the iodine cell transfer function (Figure 3-2, point B). The flow is illuminated with this beam and similar to normal PDV a signal image, which is sensitive to the velocities in the flow, can be acquired.

The two images can then be processed as in conventional PDV, by dividing the two images to produce a normalised transmission image that is then used to calculate the frequency, Doppler shift and finally the velocity.

3.2.2 Increased sensitivity 2v-PDV

The second approach increases the sensitivity of the system by tuning the two frequencies to the positions shown as B and C in Figure 3-2. With one source tuned onto the falling slope and the other on the rising slope, a constant Doppler shift will result in the further attenuation of one image to a lower signal level and the rise in the signal level in the other image. Dividing the difference of the images by the sum, and taking into account any difference in the gradients will give a result that has approximately double the sensitivity of the current PDV methods. In practice the gradient of either side of the iodine absorption line will be different so this will have to be taken into account.

The initial (un-shifted) transmission ratio of each frequency and the relative gradients of each slope of the iodine absorption line can be taken into account using the following analysis.

If the flow is illuminated using with two frequencies of laser light, which are tuned to opposite sides of the iodine absorption line, as shown in Figure 3-2, (points B and C), then the Doppler shift expressed in terms of the change in transmission ratio (for the first beam), ΔT_1, can be obtained.

If the intensity of the light scattered from the flow at any point is given by, I_s, then this can be assumed to be the same under both illuminations, if the time interval between them is short and the seeding conditions remain constant, as the difference in

the Mie scattering for the closely spaced frequencies will be negligible (discussed further in section 3.3).

The intensity recorded at a pixel on the CCD will depend upon this scattered intensity and the absorption that occurs in the iodine cell, which is dependent upon the frequency of the illuminating light.

Under the illumination of the first frequency, ν_1, the recorded intensity, I_1, will be given by:

$$I_1 = (T_1 + \Delta T_1) I_s$$

Equation 3-1

Likewise under the illumination of the second frequency, ν_2, the recorded intensity, I_2, will be given by:

$$I_2 = (T_2 - \Delta T_1 m_2) I_s$$

Equation 3-2

Where:

I_1, I_2	Recorded intensity at any pixel on the CCD under the illumination of ν_1 and ν_2
I_s	The intensity of the light scattered from any point in the flow.
T_1, T_2	Initial (un-shifted) transmission ratios of the illumination frequencies, ν_1 and ν_2
ΔT_1	Change in transmission ratio (on the negative gradient slope of the iodine absorption line.)
M_1, M_2	Gradients functions of the two sides of the iodine absorption line
$m_2 = \left\| \frac{M_2}{M_1} \right\|$	Ratio of gradients of positive gradient side to the negative side of the iodine absorption line.

By rearranging and equating (3.2) and (3.3) the change in transmission is given by:

$$I_1(T_2 - \Delta T_1 m_2) = I_2(T_1 + \Delta T_1)$$

Equation 3-3

$$\Delta T_1 = \frac{(I_1 T_2 - I_2 T_1)}{(I_2 + m_2 I_1)}$$

Equation 3-4

This shift can then be added to the initial transmission ratio, T_1, of the first illumination frequency to find the normalised transmission, TR_1, as found in conventional PDV using a signal divided by a reference. Alternatively the Doppler frequency shift can be calculated directly from ΔT_1 using the gradient of the first (negative gradient) slope of the absorption line.

$$TR_I = T_I + \Delta T_I$$

Equation 3-5

This method assumes that both sides of the iodine absorption line are linear over the range of Doppler shifts to be found in a measurement. An alternative method of realising the increased sensitivity technique would be to directly calculate the Doppler shift from the intensity values in the two images using a look-up table approach. This would allow the non-linear portion of the absorption line to be used increasing the velocity range of the system, although the increase in the sensitivity of the system will depend upon the relative gradients of the two slopes.

3.3 Advantages / disadvantages of 2ν-PDV

The main motivation for this work is the removal of the beam splitter and the second CCD camera from the imaging head. This will remove the problems associated with image misalignment and polarisation effects.

Superposition of the reference and signal images to sub-pixel accuracy is essential if errors in the calculated velocities are to be minimized, for example Thorpe et al[1] assess the impact of image misalignment, on the velocity field of a rotating disc. For an image misalignment of 0.1 pixels, they give an estimate of this error as ± 5ms^{-1}. Errors due to poor image registration can become particularly troublesome if large velocity gradients are present in the region imaged. The main causes of poor image registration are differences between the optical aberrations and magnifications of the two imaging paths. Thus errors tend to be worse towards the outside edges of the images, where these factors are largest. However, as the signal and reference images, in the two-frequency technique, are now captured on the same CCD camera, the image alignment will now be automatic.

Another potential source of error in a conventional PDV system is introduced by the use of a beam splitter. Ideally this would be completely insensitive to the polarisation state of the scattered light, splitting the incoming light 50:50 between the signal and reference cameras. However even “non-polarising” beam splitters retain a slight sensitivity to polarisation, this can result in differing split ratios for different polarisations of light causing significant errors in the calculated velocities[2]. For example non-polarizing beam splitters are often quoted as ±3% variation in the split ratio for S and P polarised light, leading to typical velocity errors of ±7ms^{-1}. Again this will be avoided in the two-frequency technique, as the beam splitter is no longer required in the imaging head optics.

The two-frequency method also simplifies the system and reducing the hardware required for a PDV measurement. The need for a reference image means that in normal PDV a second CCD camera is required. By capturing the signal and reference images sequentially this is no longer necessary, reducing the costs and complexity of the PDV system.

The technique does however introduce several new issues that have to be taken into account. The first of these is the fact that the two images are no longer captured simultaneously. For steady-state flows this is not a major difficulty, provided that the seeding is relatively dense and the seeding distribution remains essentially unchanged during the time taken to acquire the two image frames. The extent to which this condition is satisfied will depend upon the flow situation.

The optical frequency difference between the two beams should be sufficiently small so that there will be minimal change between the scattered light intensity for the two illumination beams. Figure 3-3 shows the percentage difference in scattered light intensity for two frequencies separated by 2GHz, for a 5μm particle. Table 3-1 shows the differences in scattered light intensity for a range of particle sizes, from this it can be seen that the maximum expected difference in scattered light intensity for the two illumination frequencies would only be 0.35%. This would only occur if a view was located at a precise angle and the mean change is less than five hundredths of a percent. From these calculated differences in scattering light intensity it can be seen that the Doppler shift error this would introduce is negligible, with a peak value of 17.3kHz and a mean value of 2.24kHz. This is much smaller than the line width of the laser frequency and for the smaller particles typically used the effect is even smaller.

Table 3-1 The effect of using different illumination frequencies due to Mie scattering differences

	Size of scattering particle (μm)				
	0.1	0.2	1.0	2.0	5.0
Maximum % change in scattered light intensity[1]	0.0047	0.0056	0.013	0.060	0.35
Mean % change in scattered light intensity[2]	0.0020	0.0020	0.0034	0.012	0.045
Estimated max. Doppler shift uncertainty (kHz)[3]	0.23	0.28	0.65	2.98	17.3
Estimated mean Doppler shift uncertainty (kHz)[3]	0.099	0.097	0.17	0.61	2.24

[1]Maximium percentage change in Mie scattering intensity between ν1 and ν2 (=ν1+2GHz)
[2]Mean percentage change in Mie scattering intensity ν1 and ν2 (=ν1 + 2GHz)
[3]Estimated Doppler shift uncertainty assuming absorption slope goes from 0-100% over 500MHz

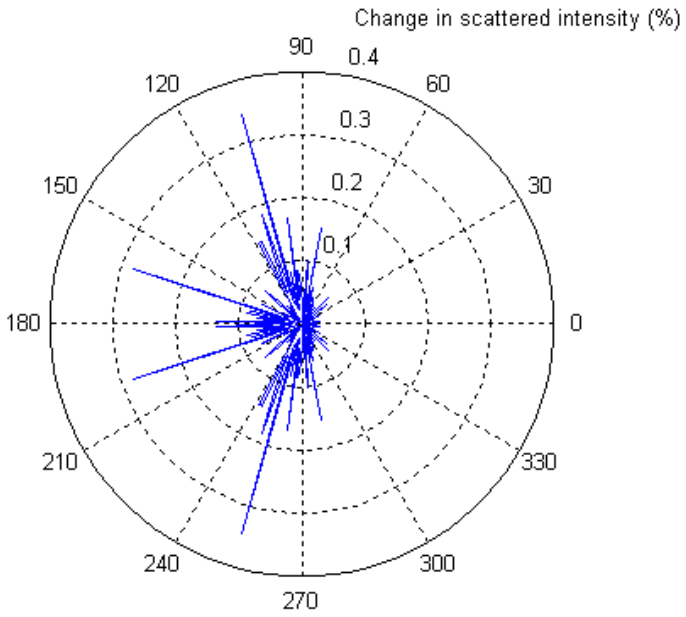

Figure 3-3 Showing the percentage change between the scattered light intensity from a 5µm particle for two illumination frequencies separated by 2GHz.

The position of the reference beam on the absorption function is also important when using the normal sensitivity approach. Not only does the reference frequency have to be positioned far enough from any absorption line so that Doppler shifts produce no change in intensity; we also have to know that this region is completely flat at 100% transmission. Any variation in the transmission will result in the reference image being slightly sensitive to the velocity introducing errors, so it is necessary to check this region at any potential operating frequencies.

3.4 Previous work on similar or related techniques

The idea for two-colour or two-frequency PDV has been suggested by several researchers including Chan[3], in which it was proposed to use a single colour CCD camera, using the composite colour output to record the red, green and blue images separately. It was proposed to use two lasers to produce light in the red and green spectrum to provide the reference and signal images respectively.

The first reported system to employ the idea was implemented by Arnette et al[4]. They used a single colour CCD detector and two laser illumination frequencies: one tuned onto the slope of an iodine absorption band at 532nm (from an Nd:YAG laser) and a reference source from a Nd:YAG pumped dye laser at 618nm. The two signals were captured in one image on a single colour CCD camera. Here each data point is made up from the signal from a group of three pixels, one measuring each of the red, blue and green colours. The signal was collected on the green pixels while the reference was collected by the red pixels in each group. However the arrangement of pixels in a colour camera would imply that there is an image offset of at least one and possible two pixels between the signal and reference image.

They also found that "signal bleed" of the scattered intensity from one pixel to another led to significant errors. The absorption bands in the region of the 618nm reference beam were not reported either experimentally or theoretically and it is not clear what effect this would have on the reference image and no account was taken of the potentially differing responses of the CCD at the two wavelengths.

The effects of different scattering efficiencies of the particles at 532 and 618nm were not taken into account with the Mie scattering from widely spaced wavelengths potentially being very different. For example Figure 3-4 shows the Mie scattering from a 0.8μm particle for these wavelengths with significantly differences in the Mie scattering at these wavelengths.

The use of two separate lasers not only increased the cost and complexity of the system but also requires that care must be taken to ensure that the two laser light sheets are well matched both in alignment and power distribution.

Thompson et al[5] have also described another similar system, which they called spectral-line-filtered Velocimetry (SLFV). Although this is not a planar measurement technique it operates on the same principle as PDV, but with the intensity levels being recorded using a photo-multiplier tube rather than a CCD, allowing only a point measurement. In this system a He-Ne laser provides an illuminating frequency in the red, whilst an argon ion laser was used to provide the green frequency. However unlike the work carried out by Arnette et al[4] an acousto-optic tuneable filter (AOTF) was used to select whether the signal or reference scattering intensity is being recorded. This leads to the temporal separation of the signal and reference intensities. In their analysis they conclude that the light will be scattered off the same particle if the switching is fast enough. The separation of the signal and reference images in time removes the misalignment problems associated with use a colour CCD chip, although the system will still have the other issues associated with the use of widely separated wavelengths, as in the Arnette et al set-up.

To avoid the problems with widely separated wavelengths Ford et al[6,7] describe a two-frequency approach that also uses a temporal separation of the signal and reference data. In this system instead of filtering out one frequency at the point of detection, the flow was illuminated with each frequency sequentially. In this technique an acousto-optic modulator is used to shift the frequency of an Argon Ion laser, to provide a second frequency that is close to the original but shifted enough so that one is positioned on an absorption line while the other is not. In this system the reference beam was always present, resulting in an image pair, consisting of signal plus reference and reference only. As the signal was always combined with the reference this was not ideal. Further work[8] separated the signal and reference frequencies completely.

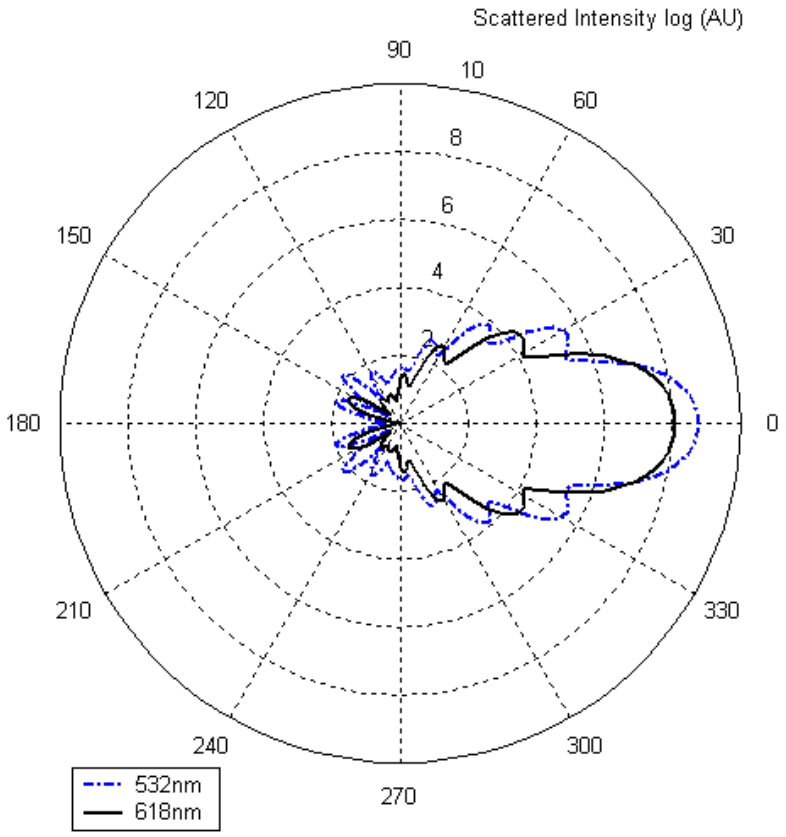

Figure 3-4 Relative Mie scattering intensities for 532nm (top) and 618nm (bottom) light and a 0.8μm particle

Muller et al [9] described a similar method using a frequency modulated Distributed Bragg Reflector (DBR) laser diode (852.6nm, 100mW) and a Caesium absorption cell. Here they initially used a profile sensor, constructed of 25-avalanche photo diodes (APD) arranged linearly to measure linear velocity profiles. In this system instead of using two distinct frequencies the illumination light is frequency modulated about the minimum of an absorption line. As the laser frequency is modulated, so the transmission will also modulate, see Figure 3-5, if a Doppler shift is applied to the laser frequency this transmission modulation will change. By taking the quotient of the amplitudes of the first and second harmonics in the photodiode signal the frequency shift can be determined. Also fluctuations in the scattered light will not effect the calculation so an additional reference detector is not necessary. If a Doppler shift is applied to the light the recorded amplitude modulation will change, and the frequency shift can be determined by taking the quotient of the amplitudes of the first and second harmonics in the photodiode signal. The method was then modified to make planar measurements using a CCD camera to capture three sequential images at different points of the frequency modulation cycle. This was demonstrated with velocity measurements of a rotating disc.

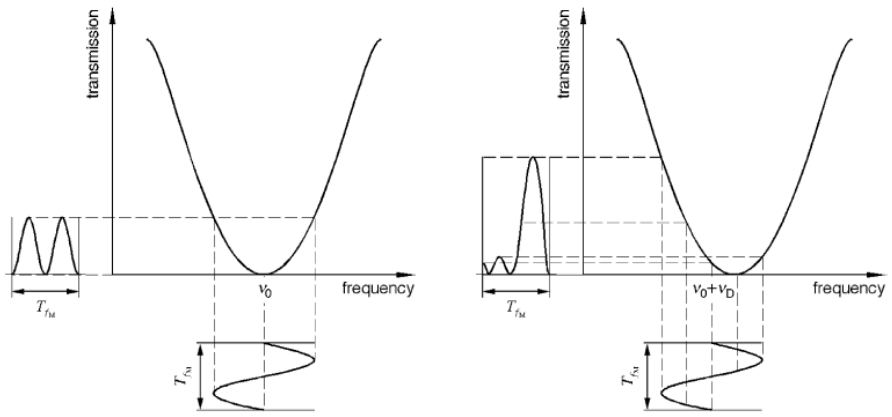

Figure 3-5 Absorption cell transmission for the frequency modulation system described by Muller et al[8]. Showing the 1st and 2nd harmonics of the modulation frequency, for two centre frequencies ν_0 and $\nu_0+\nu_D$

3.5 Summary

In this chapter two different sensitivity schemes that are possible using the 2ν-PDV technique have been described. The first, the normal sensitivity scheme is similar to conventional PDV, where one images contains the velocity information and the second is used as a reference to remove scattered light intensity variations. In the second, the increased sensitivity scheme, both images contain velocity information and the sensitivity of the system is approximately doubled over that of conventional PDV.

The following advantages and disadvantages of the technique were identified:

- Removal of signal/reference image misalignment errors typically resulting in velocity errors of ± 5ms^{-1}.
- Removal of beam splitter polarisation errors, typically resulting in velocity errors of ±7ms^{-1}.
- In 2ν-PDV the images are no longer acquired simultaneously which could result in seeding levels changing between images. The suitability of the technique will depend upon the flow situation.
- Mie scattering may be different for the two frequencies of illuminating light, however this will not be an issue if the frequencies are closely spaced, ~1GHz.

3.6 References

1. Thorpe, S.J., Ainsworth, R.W., and Manners, R.J., "The Development of a Doppler Global Velocimeter and its Application to a Free Jet Flow", 1995, *ASME / JSME Fluids Engineering and Laser Anemometry Conference and Exhibition*, Hilton Head, SC, USA,

2. Meyers, J.F. and Lee, J.W., "Identification and Minimization of Errors in Doppler Global Velocimetry Measurements", 2000, *10th International Symposium on Applications of Laser techniques to Fluid Mechanics*, Lisbon, Portugal,

3. Chan, V.S.S., "Particle Based Velocimetry Techniques for Measurement in Reciprocating Engines", 1999, *University of Manchester*, PhD Thesis.

4. Arnette, S.A., Elliott, G.S., Mosedale, A.D., and Carter, C.D., "A Two-Color Approach to Planar Doppler Velocimetry", 1998, *36th Aerospace Sciences Meeting and Exhibit*, Reno, Nevada, AIAA-98-0507.

5. Thompson, B.E., Friess, W.A., and Ramada, K., "time-Resolved spectral-line-filtered velocimetry", 2001, *Experiments in Fluids*, Vol. 31, pp 179-185.

6. Ford, H.D., Nobes, D.S., and Tatam, R.P., "Acousto-optic Frequency switching for single-camera planar Doppler Velocimetry", 2001, *SPIE proceedings, Optical Diagnostics for Fluids, Solids and Combustion,* San Diego, CA, Vol. 4448, pp 272-282.

7. Ford, H.D., Nobes, D.S., and Tatam, R.P., "Acousto-optic Frequency Switching with Fibre-optic Delivery for Single Camera Planar Doppler Velocimetry", 2003, *16th International Conference on Optical Fiber Sensors*, Nara, Japan, Tu3-5, pp 226-229.

8. Charrett, T.O, Ford H,D., Nobes, D.S. and Tatam, R.P., “Dual illumination Planar Doppler Velocimetry using a single camera”, 2003*, Optical Diagnostics for fluids, Solids and Combustion II, Proceedings of the society of Photo-optical Instrumentation engineers (SPIE),* San Diego, CA, paper 5191, pp 113-121.

9. Muller, H., Eggert, M., Pape, N., Dopheide, D., Czarske, J., Buttner, L., and Razik, T., "Time resolved DGV based on laser frequency modulation", 2004, *12th International symposium on the application of Laser Techniques to fluids*, Lisbon, Portugal.

4 Review of PDV processing

4.1 Introduction

In this chapter the techniques and implementation of the PDV processing used at Cranfield are described, this includes detail on previous work as well as software written during the course of this work.

The methods used in the calculation of the measured velocity components, for both conventional PDV and 2ν-PDV are described. Also the methods used in the transformation to orthogonal components used in 3D PDV measurements are described. A new method of calculating the orthogonal components using four or more velocity components as opposed to the three usually used is also presented here.

The chapter is organised into the order that each processing stage would typically be carried out, beginning with an overview and description of the software packages used and the interface that has been developed in the course of this work for PDV processing. This is followed by a description of the implementation of each stage of the processing.

4.2 The PDV processing software

The majority of the code was written in a scripting language (Cl), similar to the C language, which is a propriety language developed for the Davis image processing software provided by LaVision. The Davis software is an image-processing package that allows the easy operation of CCD cameras and other data capture hardware along with image processing tools. All the functions of the package are accessible via a graphical user interface (GUI) or via the Cl scripting language that also allows the design and implementation of custom GUIs. For more CPU intensive functions a dynamic link library (dll) written in C can be called from within the Cl code. Some other functions and tools were written in the Matlab scientific computer language package to take advantage of the built-in mathematical functions and for displaying results.

Image capture is performed using a custom dialog displayed within the Davis package. This enables the control of the CCD cameras as well as the display of the captured images. It is used both in the experimental set-up and to capture images during measurements.

The processing of captured data is performed in the Davis package, using a custom interface, written for this project, that allows the processing scheme to be changed quickly and easily, making the interface suitable for use with different experiments. The main interface consists of a window in which the various operations are displayed as a flow diagram. Each item performs a single operation on its inputs and produces outputs, which can be linked to the inputs of the next operation. An example of this screen is shown in Figure 4-1. Clicking the button for each item opens a dialog window containing the settings for the operation, for example for a filtering operation the settings might contain the size of filter, the number of runs as well as the inputs and output settings. Where the same settings are required for a process several times,

such as filtering several images, then additional channels can be added to the item, allow the process to run multiple times with different inputs and outputs but with the same settings.

All the settings used in an experimental processing scheme can be saved so that the settings can be reloaded at a later date and the processing performed as saved. The saved file is in a text file format that can be easily edited outside of the software.

The following sections will give detail of the different stages of the processing used in PDV and describe their implementation in the flow diagram system. Table 4-1 shows the processing items implemented in the flow diagram system, along with a brief description of their purpose and action, where applicable the section detailing the operation is also shown.

Table 4-1. Processing items implemented within the Davis PDV processing software.

Item name	Description	Described in section
[Raw image]	Loads a saved image buffer, such as experimental data.	4.4
[Deframe]	Splits the two frames of a double camera image into two separate images	4.4
[Split]	Cuts out four areas defined by rectangles into separate output buffers.	4.4
[Mask]	Takes an input buffer and applies a mask, setting values to zero in regions of the image that are to be ignored.	4.4
[Filter]	Filters the input image buffer.	4.5
[Binning]	Bins pixels of an input buffer to create a smaller (in pixels) output buffer	4.5
[Threshold]	Applies a threshold to an input buffer, setting all pixels below the threshold value to zero.	4.5
[De-warp]	Performs image de-warping on an input buffer	4.6
[Calc(O-I)]	Takes the images size from the input buffer and generates the observation direction unit vectors for each pixel in the image based upon the image de-warping	4.6
[Divide]	Divides, on a pixel by pixel basis the two input buffers	4.8
[Doppler]	Takes a ratio image buffer and observation direction buffers as inputs and calculates first the Doppler shift and then the measured velocity component.	4.8
[IncDiv]	Takes two images as input and performs the normalisation for the 2ν-PDV increased sensitivity scheme as described in chapter 3. The output is then a suitable ratio image for use with the Doppler item.	0
[IncSens]	Takes two images as input and calculates the Doppler shift and velocity component using a look-up table method for the increased sensitivity 2ν-PDV method.	0
Cl command	Performs any other entered Cl script command.	-

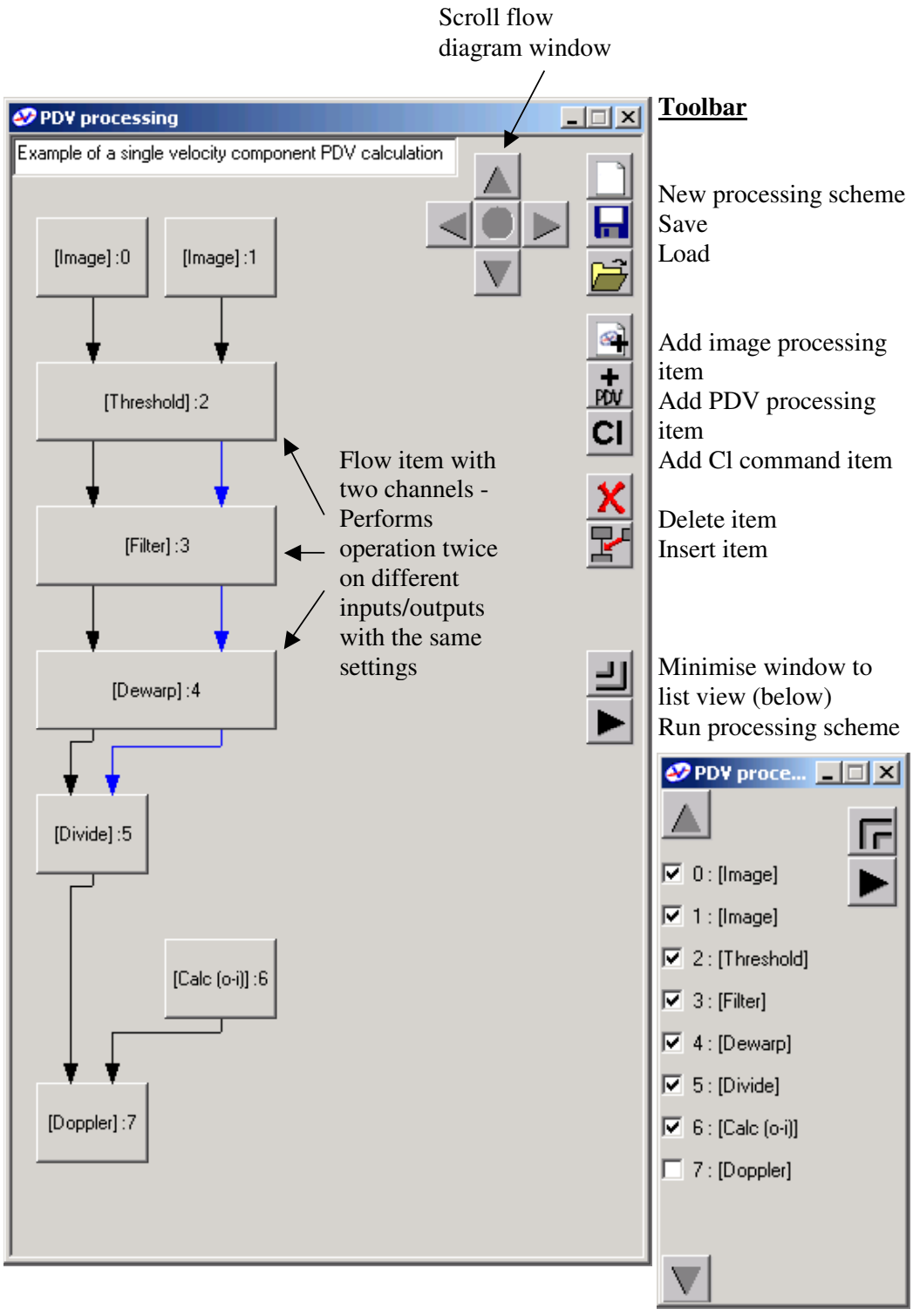

Figure 4-1. Screenshots showing the interface of the PDV processing software running within the Davis image processing package.

4.3 Image capture and background subtraction

As mentioned the images are captured using a separate dialog, this is shown in Figure 4-2. This allows the control of the exposure time and display of the captured image. For two-camera PDV imaging heads, both camera images can be displayed along with the division and sum of the two images (used for alignment between the two cameras). A single image can be captured or images can be captured continuously.

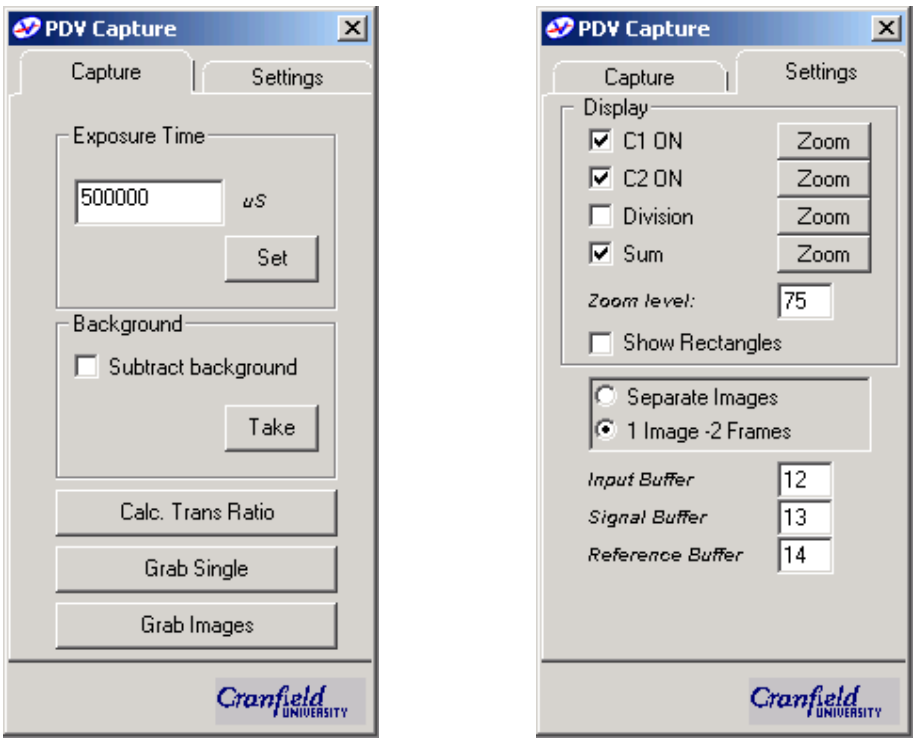

Figure 4-2 Screenshot of the image capture dialog.

The background image subtraction is performed at the image capture stage by the Davis software. The image to be subtracted is obtained by averaging multiple background images, taken shortly before the data acquisition and using the same CCD integration time. As the stored data images have the background subtracted automatically by the image capture software there is no need to implement this in the flow processing software.

4.4 Loading / preparing captured images with the processing software

The flow item [Raw Image] simply loads a specified image file into the output image buffer and provides a starting point for the processing. If multiple cameras are used, Davis software stores both CCD images as a single image with two frames, to process this further it is necessary to split this into two separate image buffers the flow item [Deframe] carries out this operation.

Similarly if the images consist of multiple images captured on a single CCD, such as is the case when using multiple channel imaging fibre bundles then each view must be placed into a separate buffer for processing. The [Split] flow item cuts out four defined rectangles from the input image and outputs these to separate buffers. It also provides the options of flipping, either vertically or horizontally any of the outputs. This is useful when a view is on the opposite side of the light sheet. The [mask] flow item provides a method of removing unwanted regions from the images by setting these areas to zero using a predefined image mask, containing ones and zeros.

4.5 Image filtering, binning and thresholding

Filtering and binning can both be used to increase the signal-to-noise at the expense of spatial resolution. The image filtering, implemented in the [filter] flow item, is a modified smoothing filter that includes a threshold value. Filter sizes of 3x3, 5x5 and 7x7 can be used, with the centre value receiving the average of all the pixels with values greater than the threshold value. The filter can also be applied multiple times using the runs setting in the [filter] dialog.

The binning function, implemented with the [Binning] flow item, takes the sum of 4,9 or 16 pixels and places that value into a new super-pixel with the resulting image having a smaller image size.

Thresholding is used to remove pixels with dubious (either low values dominated by camera noise, or high values outside the linear region of the CCD response) values from the image by replacing then with zero value. The flow item [Threshold], allows a lower and an upper intensity limit to be set; pixels with values outside these limits are then set to zero. For example regions of low light intensity will have reduced signal-to-noise and should be excluded. Likewise pixels with intensity values close to the maximum may by saturated and led to incorrect Doppler shift values.

4.6 Image de-warping and calculation of observation, illumination and sensitivity vectors

As the component of the velocity that a PDV system is sensitive to depends upon the observation and illumination directions used, the image of the light sheet may well be distorted. Image de-warping can be used correct each view to a common field-of-view as if viewing the sheet perpendicularly. When making multiple component or 3D measurements it is necessary to overlay each view to allow the calculation of the orthogonal velocity components and the de-warping can be used to achieve this.

The de-warping algorithm used is a built in function in the Davis image processing software and was designed for use in Particle Imaging Velocimetry (PIV) applications, however previous work by Nobes et al[1] has expanded upon this to allow the calculation of the observation vector based upon the information gathered in the image de-warping process. To perform image de-warping a target must be placed in the region of interest, this consists of a black background with dots marked in a regular grid pattern. An image is captured of this target and this is then processed

using the built-in dialogs within the Davis software package. This allows up to six views to be de-warped to a common field of view. The dialogs allow the definition of an origin in the image, which is used to both align all the de-warped images and to calculate scaling information defining each pixels X and Y co-ordinates within the light sheet. Once this process has been performed the result is a mapping function for each view with 20 coefficients. The de-warping can then be preformed using a built-in Cl function. This has been implemented in the flow diagram system using the [Dewarp] item. This takes an input image and performs the correction using the given de-warping coefficient set.

The method of calculating the viewing direction from the de-warping coefficients has been implemented in the flow item [Calc(O-I)] which in turn calls the C functions used to perform the calculations described in Nobes et al[1] using the set of de-warping co-efficient defined in the dialog box. Alternatively the observation direction can be specified in vector form in the [Calc(O-I)] dialog box. The laser illumination direction is also specified here and this is used in the calculation of the sensitivity vector. The output of the [Calc(O-I)] flow item consists of four image buffers, the first three contain the components of the sensitivity vector, and the fourth contains the magnitude of the sensitivity vector that is used later in the calculation of the measured velocity component.

4.7 Determining the iodine cell transmission spectrum

The shape of the iodine absorption line is first determined by experimentally scanning the laser frequency over the frequency range to be used. This was done using a Cl script to control the laser frequency (for the argon ion laser), capture images and calculate the transmission. This experimental scan, for the case of the argon ion laser used for the experimental work presented here is in terms of transmission vs. etalon voltage, therefore the first stage is to compare the shape of the scanned region with a theoretical model of the absorption spectrum of iodine. Forkey[2,3] has developed a model of the iodine absorption spectrum, and this is used to provide a theoretical spectrum for the iodine cell in use. This allows the relevant portion of the spectrum to be identified. Next the experimental curve is scaled and fitted to this model to provide a reference for the conversion from etalon voltage to frequency. The Forkey code is run from within a Matlab program that then also performs the scaling/fitting process.

The next stage is to fit polynomials to each slope of the iodine absorption line that will be used. As explained below in section 4.8, one fitted curve for the transmission-to-frequency conversion is required for the calculation of the Doppler shift, however four polynomials are required if the look-up table method for the 2ν-PDV increased sensitivity method is to be implemented. These are a frequency-to-transmission conversion curve for both the rising and falling slopes of the absorption line and transmission-to-frequency conversion curves for both slopes. The coefficients of these fitted curves are then output to a data file for use in the Davis processing software. This stage is also performed in Matlab to take advantage of the built in curve fitting functions.

4.8 Calculation of Doppler shift and velocity in conventional PDV processing

The calculation of the Doppler shift and the measured velocity component can be broken down into several stages. Initially a normalised transmission image must be calculated. In this image the value of every pixel corresponds to proportion of light that is transmitted through the iodine cell. This calculation at it's simplest consists of a division, on a pixel-by-pixel basis, of the signal image by the reference image. A more complicated processing arrangement is required if either a white card correction or a pixel sensitivity correction is applied. Both corrections are similar and are applied in the same way, Figure 4-3 shows the processing required to form the normalised transmission image, for (a) no corrections applied and (b) a white card or pixel sensitivity correction applied.

The white card correction corrects for differences in the imaging paths of both images. It consists of a second set of signal and reference images for which there should be no variation in intensity other than the effect of these differences. Initially this was achieved by imaging a piece of card illuminated with a white light source. However the images are now more usually captured using the laser frequency tuned to 100% transmission and under the flow conditions to be measured, because of this it is sometimes also referred to as the green card correction. White card corrections are currently captured in this way.

The pixel sensitivity correction is similar but corrects for the different sensitivity of individual pixels in the CCD cameras. If both cameras were identical the differences in pixel sensitivity would have no effect due to the normalisation stage. However the sensitivity of a pixel in one CCD can be different than the same pixel in the second CCD, resulting in an error. To correct for this images are captured with the CCDs illuminated by a uniform light source. The [Divide] flow item is used to perform these stages in the processing.

Once the normalised transmission image has been found the next stage is to convert from the transmission values to frequency, this is achieved by evaluating the 9th order polynomial that has been fitted to the iodine cell transmission as in section 4.7. This is done for each pixel in the normalised transmission image. The Doppler shift is then found by subtracting the laser frequency, which is also calculated using the known un-shifted transmission and the iodine cell transmission fitting polynomial.

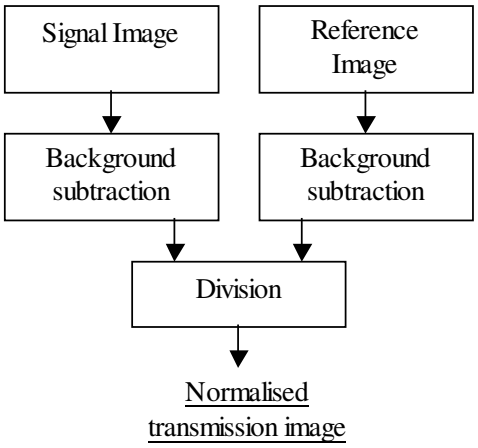

(a)

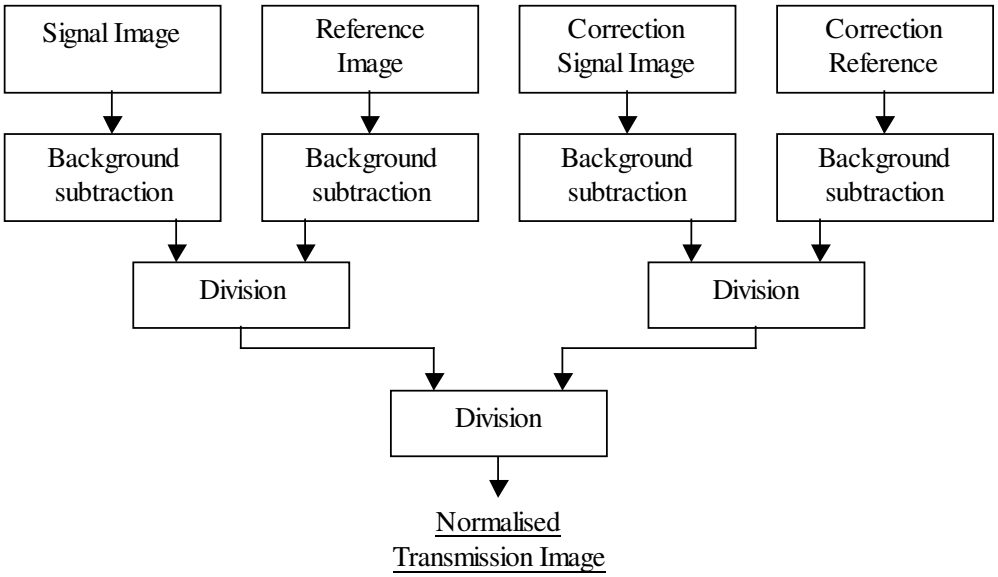

(b)

Figure 4-3 Flow diagram detailing a simple processing scheme for (a) calculating the normalised transmission image (b) calculating the normalised transmission image using an additional correction (either a white card or pixel sensitivity correction) .

Once the Doppler shift for each pixel has been calculated the magnitude of the measured velocity component is calculated using the Doppler formula, rewritten as:

$$\left|U_n\right| = \frac{\Delta\nu.c}{\nu\left|(\hat{o}-\hat{i})\right|}$$

Equation 4-1

Here the direction of the measured velocity component, U_n, is given by the sensitivity vector *(ô-î)*, *c* is the speed of light and ν is the un-shifted laser frequency, which is calculated from the un-shifted transmission value using the fitting polynomial described above.

All of these calculations, shown in Figure 4-4 are performed using [Doppler] flow item. The components of the sensitivity vector are provided as inputs, in the form of four image buffers containing the *X, Y, Z* and length of the sensitivity vector at each pixel in the image. The output of the flow item [Calc O-I] described in section 4.6 is used to generate these images.

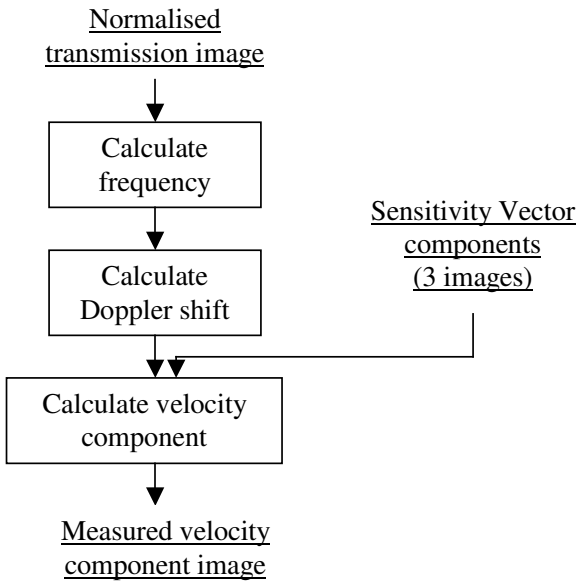

Figure 4-4 Flow diagram showing the stages of processing preformed by the [Doppler] flow item in the calculation of the measured velocity component from a normalised transmission image.

4.9 Calculation of Doppler shift and velocity in 2ν-PDV processing

4.9.1 Normal sensitivity method

The calculation of the Doppler shift and measured velocity component for the normal sensitivity 2ν-PDV method is identical to that used in conventional PDV processing except the division stage is performed using the images captured sequentially under two different illumination frequencies rather than simultaneously on two CCDs.

4.9.2 Increased sensitivity method – normalisation

To calculate the Doppler shift and measured velocity component using the increased sensitivity method, described in chapter 3, the normalised transmission image must be calculated using equations 3-4 and 3-5. The flow item [IncDiv] implements this with the output being a normalised transmission image required as the input for the [Doppler] item. The processing is then preformed in the same way as for conventional PDV described in section 4.8.

4.9.3 Increased sensitivity method – Lookup table

The second way of implementing the increased sensitivity method is to use a look-up table to directly find the Doppler shift from the ratio of the intensities in the two images. Here the ratio of the intensities in the two images is compared with values calculated for known Doppler shifts. Figure 4-5 shows the process in which a look-up table to compare the value of this ratio to known Doppler shifts can be generated. In order to perform this operation it is necessary to fit polynomials to the shape of the iodine absorption line, for both the falling and rising slopes and for both the conversion from transmission-to-frequency and frequency-to-transmission.

It is assumed that the un-shifted transmissions of both illumination frequencies are known. The first stage is to calculate the un-shifted frequency of each illumination frequency using the fitted polynomial. Next the frequency limits for each slope are determined; this is the range over which measurements can be made, i.e. between full transmission and the minimum transmission of each slope. When this frequency range is known the range of valid Doppler shifts can be calculated, as the starting un-shifted frequencies are known. This is the range over which Doppler shifts will exceed the range of the iodine absorption line.

From the Doppler shift range the Doppler shift increment to be used in the look-up table can be found. Next the frequencies of each illumination beam at each value of Doppler shift are found, and then the corresponding transmission values are calculated using the frequency-to-transmission fitting polynomials for each slope. Finally the ratio of the transmission is calculated for each value of the Doppler shift. An alternative method of generating a look-up table directly from the iodine cell transmission values has also been considered although this has not yet been implemented.

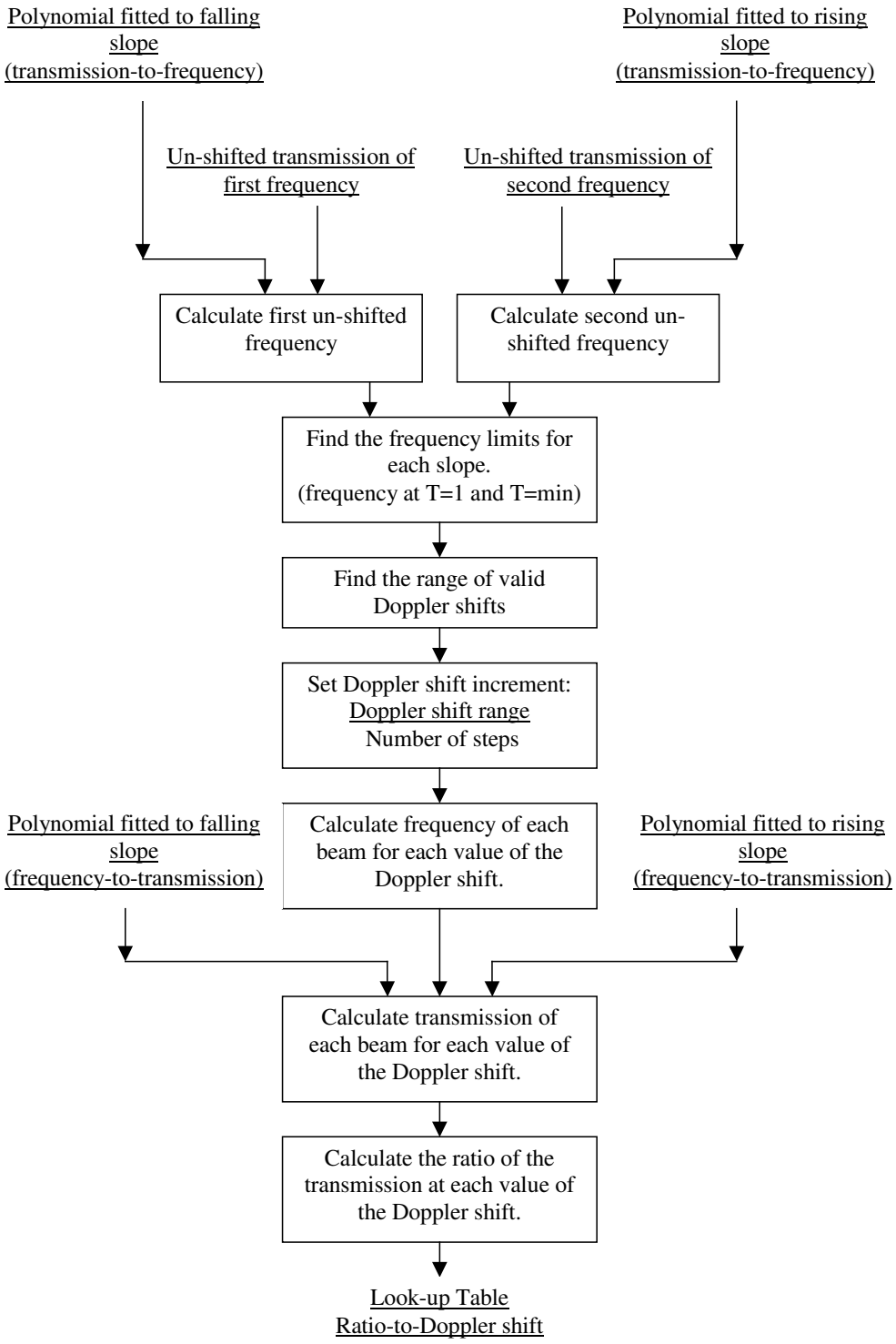

Figure 4-5 Flow diagram showing the generation of a look-up table to convert from intensity ratio to Doppler shift.

Figure 4-6 shows the how the velocity component is calculated using the look-up table method, initially the two images are acquired; the ratio of intensities is then calculated. Then for each pixel in this ratio image, the value is looked up in the table and the upper and lower bounds for the Doppler shift are found. A linear interpolation is then performed between these two values to find the Doppler shift for that value of the ratio. Finally the measured velocity component is calculated using this value for the Doppler shift and Equation 4-1. This method for calculating the velocity component has been implemented in the [IncSens] flow item, which takes a ratio image as an input, generates the look-up table and performs the calculation of the velocity component.

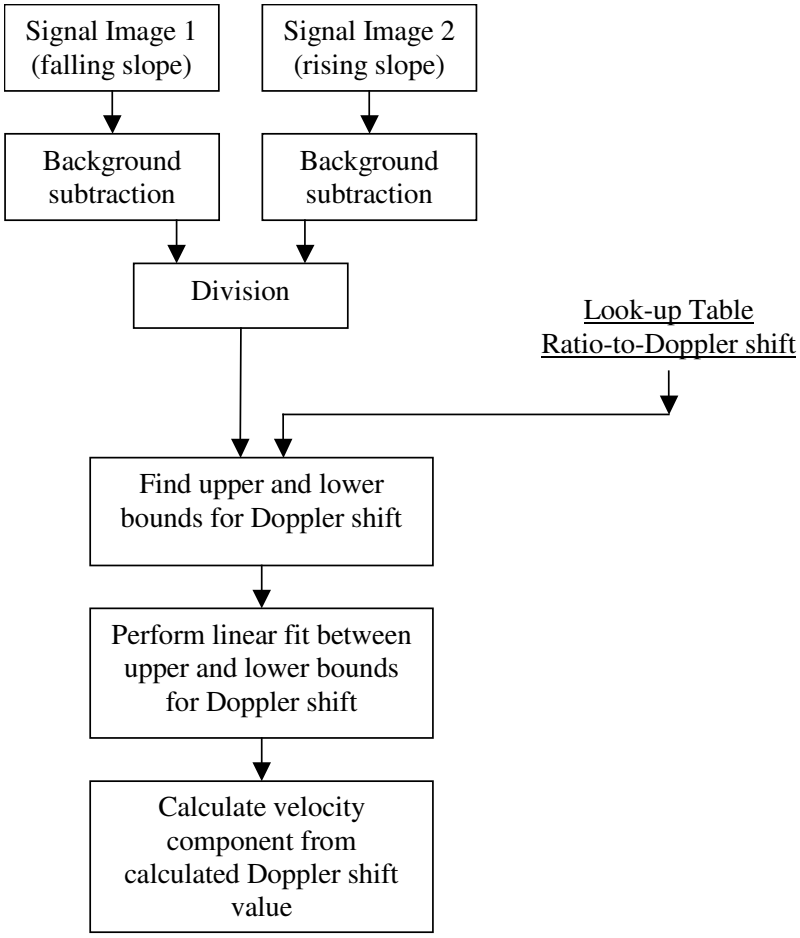

Figure 4-6 Flow diagram showing the calculation of a measured velocity component using a look-up table to implement the increased sensitivity 2ν-PDV method.

4.10 Calculation of orthogonal velocity components

For a 3D PDV velocity measurement at least three velocity components must be measured and these must then be transformed to an orthogonal co-ordinate system. In this chapter the methods for transforming the measured velocity components to orthogonal velocity components are discussed and a method for using additional (to the three) velocity components in the calculation is described.

Throughout previous work in PDV, researchers have concentrated upon either making single velocity component measurements or three-dimensional velocity measurements using three measured components. These velocity components are then converted to the orthogonal velocity components, U, V and W using the equations given by Reinath[4] and presented here in section 4.10.1.

As part of the PDV programme at Cranfield University, multi-component measurements have been made using imaging fibre bundles to port multiple views to a single PDV measurement head[5]. The imaging fibre bundles presently in use have four arms allowing the measurement of an additional velocity component and are described in more detail in chapter 6. A method to use this additional component in the calculation of the orthogonal velocity components the method is given in section 4.10.2 and the benefits of using method are investigated in chapter 8.

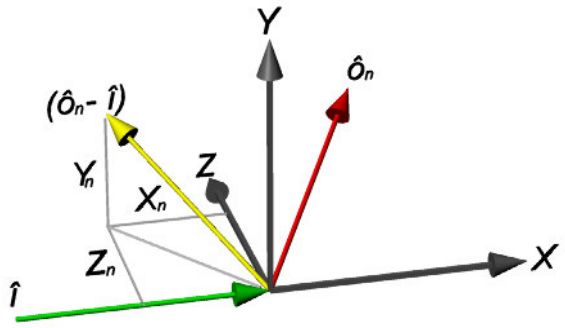

Figure 4-7 Diagram showing the definitions used in the conversion from measured velocity components to the orthogonal components. Here $\hat{o}_n$ is the observation direction of the nth view and $\hat{i}$ is the laser illumination direction; X_n, Y_n and Z_n are the Cartesian components of the measured velocity $(\hat{o}_n - \hat{i})$ component.

4.10.1 Conversion of three non-orthogonal measured velocity components to the three orthogonal components: the three-component (3C) method.

Reinath[4] presents a solution for the calculation of the three orthogonal components by solving the system of simultaneous equations. If $[U_m]$ represents the magnitudes of the measured non-orthogonal velocity components, written as a column vector, and $[V]$ is the required Cartesian components of velocity, then a transformation matrix $[A]$ may be written so that.

$$[U_m] = [A][V]$$

Equation 4-2

Where [A] is independent of the velocity measurements and is only a function of the geometry, hence:

$$[V] = [C][U_m]$$

Equation 4-3

Where $[C]$ is the inverse transformation to $[A]$. It can be seen that the three equations to be solved are:

$$X_1.U + Y_1.V + Z_1.W = |U_1|$$

Equation 4-4

$$X_2.U + Y_2.V + Z_2.W = |U_2|$$

Equation 4-5

$$X_3.U + Y_3.V + Z_3.W = |U_3|$$

Equation 4-6

Where:

$(\hat{o}_1 - \hat{\imath})$	Measured component from camera view 1 $(\hat{o}_1)$
$(\hat{o}_2 - \hat{\imath})$	Measured component from camera view 2 $(\hat{o}_2)$
$(\hat{o}_3 - \hat{\imath})$	Measured component from camera view 3 $(\hat{o}_3)$
$\|U_1\|$	Magnitude of the measured component from camera view 1
$\|U_2\|$	Magnitude of the measured component from camera view 2
$\|U_3\|$	Magnitude of the measured component from camera view 3
X_1, Y_1, Z_1	Unit vector components defining the direction of $(\hat{o}_1 - \hat{\imath})$
X_2, Y_2, Z_2	Unit vector components defining the direction of $(\hat{o}_2 - \hat{\imath})$
X_3, Y_3, Z_3	Unit vector components defining the direction of $(\hat{o}_3 - \hat{\imath})$
U, V, W	Orthogonal velocity components, horizontal, vertical and out-of-plane respectively.

Or in the form of Equation 4-2

$$\begin{bmatrix} |U_1| \\ |U_2| \\ |U_3| \end{bmatrix} = \begin{bmatrix} X_1 & Y_1 & Z_1 \\ X_2 & Y_2 & Z_2 \\ X_3 & Y_2 & Z_3 \end{bmatrix} \begin{bmatrix} U \\ V \\ W \end{bmatrix}$$

Equation 4-7

Using Equation 4-3 and $[C] = [A]^{-1}$ which can be found by

$$[C] = [A]^{-1} = \frac{1}{\det([A])} adj([A])$$

Equation 4-8

Where the determinate can be written as:

$$\det([A]) = X_1Y_2Z_3 + Y_1Z_2X_3 + Z_1X_2Y_3 - Z_1Y_2X_3 - X_1Z_2Y_3 - Y_1X_2Z_3$$

Equation 4-9

And the inverse can be expressed as:

$$[C] = \frac{\begin{bmatrix} \begin{vmatrix} Y_2 & Z_2 \\ Y_3 & Z_3 \end{vmatrix} & -\begin{vmatrix} Y_1 & Z_1 \\ Y_3 & Z_3 \end{vmatrix} & \begin{vmatrix} Y_1 & Z_1 \\ Y_2 & Z_2 \end{vmatrix} \\ -\begin{vmatrix} X_2 & Z_2 \\ X_3 & Z_3 \end{vmatrix} & \begin{vmatrix} X_1 & Z_1 \\ X_3 & Z_3 \end{vmatrix} & -\begin{vmatrix} X_1 & Z_1 \\ X_2 & Z_2 \end{vmatrix} \\ \begin{vmatrix} X_2 & Y_2 \\ X_3 & Y_3 \end{vmatrix} & -\begin{vmatrix} X_1 & Y_1 \\ X_3 & Y_3 \end{vmatrix} & \begin{vmatrix} X_1 & Y_1 \\ X_2 & Y_2 \end{vmatrix} \end{bmatrix}}{\det([A])}$$

Equation 4-10

Substituting Equation 4-9 and Equation 4-10 into Equation 4-3 and separating out the individual terms for the three orthogonal velocity components gives:

$$U = \frac{1}{\det([A])}\left[|U_1|(Y_2Z_3 - Y_3Z_2) - |U_2|(Y_1Z_3 - Y_3Z_1) + |U_3|(Y_1Z_2 - Y_2Z_1)\right]$$

Equation 4-11

$$V = \frac{1}{\det([A])}\left[-|U_1|(X_2Z_3 - X_3Z_2) + |U_2|(X_1Z_3 - X_3Z_1) - |U_3|(X_1Z_2 - X_2Z_1)\right]$$

Equation 4-12

$$W = \frac{1}{\det([A])}\left[|U_1|(X_2Y_3 - X_3Y_2) - |U_2|(X_1Y_3 - X_3Y_1) + |U_3|(X_1Y_2 - X_2Y_1)\right]$$

Equation 4-13

These equations can then be used to calculate the orthogonal components, as the unit vectors defining the direction of the measured components are known, as well as the magnitude of the measured components.

4.10.2 Conversion of four non-orthogonal measured velocity components to the three orthogonal components: Four-component (4C) method.

As an extension to this work the effect on the propagation of errors of calculating the orthogonal velocity components using additional data, provided by adding a fourth observation direction, and thus a fourth measured velocity component has been investigated. This can be readily achieved in practical systems using the imaging fibre bundle approach[5]. Again it is necessary to solve a system of simultaneous equations, however this time for an overpopulated system. This can be solved using the least squares method. The system of equations to be solved is:

$$\begin{bmatrix} |U_1| \\ |U_2| \\ |U_3| \\ |U_4| \end{bmatrix} = \begin{bmatrix} X_1 & Y_1 & Z_1 \\ X_2 & Y_2 & Z_2 \\ X_3 & Y_3 & Z_3 \\ X_4 & Y_4 & Z_4 \end{bmatrix} \begin{bmatrix} U \\ V \\ W \end{bmatrix}$$

Equation 4-14

This is equivalent to:

$$[U_m] = [J][V]$$

Equation 4-15

The general least squares solution for linear equations[6] is given by:

$$[V] = ([J]^T [w][J])^{-1} [J]^T [w][U_m]$$

Equation 4-16

Here w is the weighting matrix, which allows each equation to be ranked, with larger values indicating greater importance, where w_1 etc are the relative weightings [w] has the form:

$$[w] = \begin{bmatrix} w_1 & 0 & 0 & 0 \\ 0 & w_2 & 0 & 0 \\ 0 & 0 & w_3 & 0 \\ 0 & 0 & 0 & w_4 \end{bmatrix}$$

Equation 4-17

This produces a result that attempts to minimise the difference between what would be calculated from the answer and what was measured by each equation. i.e. we will

calculate a 'best' value for *U*, *V* and *W* although this may mean that is not true. Therefore the system we are actually solving is:

$$\begin{bmatrix} |U_1| \\ |U_2| \\ |U_3| \\ |U_4| \end{bmatrix} \approx \begin{bmatrix} X_1 & Y_1 & Z_1 \\ X_2 & Y_2 & Z_2 \\ X_3 & Y_3 & Z_3 \\ X_4 & Y_4 & Z_4 \end{bmatrix} \begin{bmatrix} U \\ V \\ W \end{bmatrix}$$

Equation 4-18

$$[U_m] \approx [J][V]$$

Equation 4-19

Solving Equation 4-16 for the orthogonal velocity gives:

$$\begin{bmatrix} U \\ V \\ W \end{bmatrix} = L \begin{bmatrix} (df - ee)g + (ce - bf)h + (be - cd)j \\ (ce - bf)g + (af - cc)h + (bc - ae)j \\ (be - cd)g + (bc - ae)h + (ad - bb)j \end{bmatrix}$$

Equation 4-20

Where:

$$a = \sum_n X_n^2 w_n \qquad b = \sum_n X_n Y_n w_n \qquad c = \sum_n X_n Z_n w_n$$

$$d = \sum_n Y_n^2 w_n \qquad e = \sum_n Y_n Z_n w_n \qquad f = \sum_n Z_n^2 w_n$$

$$g = \sum_n X_n w_n U_n \qquad h = \sum_n Y_n w_n U_n \qquad j = \sum_n Z_n w_n U_n$$

$$L = \frac{1}{a(df - ee) - b(bf - ce) + c(be - dc)}$$

Although the above analysis only uses four velocity components, the general solution given in Equation 4-20 is expandable to more than four components.

4.10.3 Implementation in PDV processing software

In the flow processing system, the flow item [Calc3D] implements both methods of calculating the orthogonal velocity components. Here the flow item takes image buffers containing the measured velocity components, and buffers containing the X, Y and Z components of the sensitivity vector as it's input and returns a velocity vector buffer (for vector display in the Davis software package) along with the three orthogonal velocity components, U, V and W as separate image buffers. The items dialog box has three options for the method used in the calculation 3C, 4C and 4C with weighting (4Cw). The 3C method is that described in section 4.10.1, the 4C method uses the method described in section 4.10.2 with the weighting values all equal to one (equal weighting), the 4Cw method uses the weighting values defined in the dialog during the calculation.

4.11 Summary

A description of the processing software developed at Cranfield has been presented including a description of the user interface, which is implemented as a flow diagram system.

The method and calculations used at each stage of the processing have been described including methods of calculating the Doppler shifts for conventional PDV as well as for both 2ν-PDV sensitivity schemes. Two alternative methods for calculating the Doppler shift using the 2ν-PDV increased sensitivity scheme have been described, one using the linear approximation derived in section 3.2.2, and the other using a look-up-table approach.

Two different methods to calculate the orthogonal velocity components, U V and W, in a 3D PDV system have been described. The approach used by researchers to date has been to measure three different velocity components from three different viewing directions and convert these to the orthogonal components using the first method, called here the 3C method.

However with the introduction of multiple branch imaging fibre bundles to 3D PDV systems[5,7-9] the cost of measuring additional velocity components is no longer prohibitive. The 4C method described above allows the calculation of the orthogonal components using this additional data.

The benefits of using the 4C method in the calculation of the orthogonal velocity components will be investigated in chapter 8.

4.12 References

1. Nobes, D.S., Wieneke, B., and Tatam, R.P., "Determination of View Vectors from Image Warping Mapping Functions", 2004, *Optical Engineering*, Vol. 43, No. 2, pp 407-414.

2. Forkey, J.N., Lempert, W.R., and Miles, R.B., "Corrected and calibrated I_2 absorption model at frequency-doubled Nd:YAG laser wavelengths", 1997, *Applied Optics*, Vol. 36, No. 27, pp 6729-6738.

3. Forkey, J.N., "Development and Demonstration of Filtered Rayleigh scattering - a Laser Based Flow Diagnostic for Planar Measurements of Velocity, Temperature and Pressure", 1996, *Final Technical Report for NASA Graduate Student Researcher*, Fellowship Grant #NGT-50826, Princeton University.

4. Reinath, M.S., "Doppler Global Velocimeter Development for the Large Wind Tunnels at Ames Research Center", 1997, *NASA*, Technical Memorandum 112210.

5. Nobes, D.S., Ford, H.D., and Tatam, R.P., "Three Component Planar Doppler Velocimetry Using Imaging Fibre Bundles", 2004, *Experiments in Fluids*, Vol. 36, No. 1, pp 3-10.

6. Arbenze, K and Wohlhauser, A, " Advanced Mathematics for Practicing Engineers", 1986, Artech House, Norwood, MA, USA, ISBN 0-089006-189-0,

7. Nobes, D.S., Ford, H.D., and Tatam, R.P., "Instantaneous, Two Camera, Three Dimensional Planar Doppler Velocimetry using Imaging Fiber Bundles", 2001, *SPIE Proceedings, Optical Diagnostics for Fluids, Solids and Combustion*, San Diego, Vol. 4448, pp 72-83.

8. Nobes, D.S., Ford, H.D., and Tatam, R.P., "Planar Doppler Velocimetry Measurements of Flows using Imaging Fiber Bundles", 2003, *Proc. SPIE*, 5191, pp 122-133.

9. Willert, C., Stockhausen, G., Beversdorff, M., klinner, J., Lempereur, C., Barricau, P., Quest, J., and Jansen, U., "Application of Doppler Global velocimetry in cryogenic wind tunnels", 2005, *Experiments in Fluids*, Vol. 39, pp 420-430.

5 Development of a single velocity component time-averaged Two-frequency PDV (2ν-PDV) system

5.1 Introduction

This chapter describes the development of a single velocity component 2ν-PDV system based around a continuous wave argon ion laser. The system is capable of making time-averaged velocity measurements. It includes a description of the equipment and components used in the system as well as a description of the processing schemes that were applied. Experimental results are then presented for single velocity component measurements on both a rotating disc and a seeded air jet. The jet measurements are compared both with conventional PDV results and with a theoretical jet flow.

5.2 Two-frequency Illumination system

The two required optical frequencies where generated using a combination of two acousto-optic modulators and an argon-ion laser operating at 514.5nm. Figure 5-1 shows the configuration and operation of the dual illumination system.

Figure 5-1 (a) shows the beam path for the generation of the reference beam. The fundamental laser beam passes first through a half-wave plate (HWP) to adjust the polarization azimuth and then through an acousto-optic modulator (AOM1), which is an 85MHz frequency shift device. When AOM1 is switched on, the second order beam experiences a frequency shift of 170 MHz and is deflected through twice the Bragg angle. There is some loss of power (typically ~13%) as the process is not 100% efficient. Beam steering optics then redirect this beam into a position from which it can be coupled into an optical fibre. The second half-wave plate, orientated so as to rotate the polarization azimuth through 90^o, is necessary to achieve reflection of the beam at the polarizing beam splitter cube (PBS).

Conversely, when AOM1 is switched off, Figure 5-1(b), the signal beam is generated. The fundamental laser beam passes through with no frequency shift or angular deflection, and is incident upon a second mirror, which directs it into an alternative beam path. The beam passes through the active area of AOM2 and the optical frequency is shifted by 260MHz. The shifted beam is then retro-reflected by a mirror, making a double pass through a quarter wave plate (QWP), which rotates the polarization state by 90^o. The beam makes a second transit through AOM2, doubling the optical frequency shift to a total of 520MHz. It is then recombined with the reference beam path at the output PBS and is coupled into the same optical fibre as the reference beam.

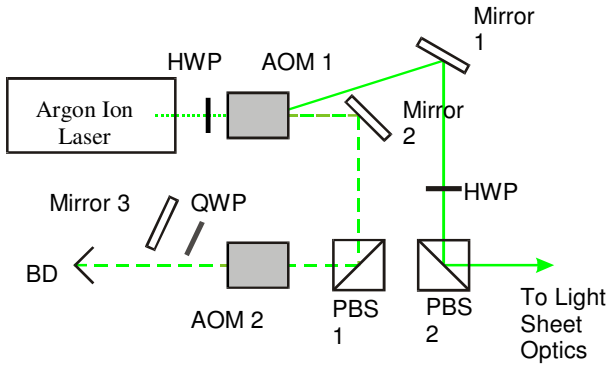

(a)

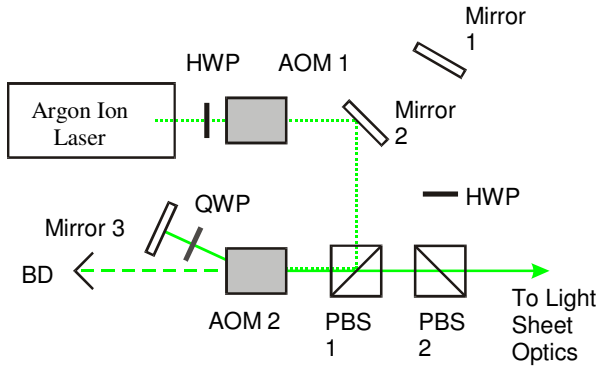

(b)

Figure 5-1 The configuration and operation of the dual illumination system for (a) reference beam generation and (b) signal beam generation

Laser Beam ····· **Shifted Laser beam** ——— **Un-shifted Laser Beam** - - -

5.2.1 Laser & Laser frequency locking system

The light source was a tuneable argon-ion laser (Spectra Physics Beamlok 2060), incorporating a temperature-stabilized etalon to ensure single-mode operation at 514.5 nm. The single-mode line width was about 2MHz. The optical frequency stability was ~3 MHz, plus a long-term drift with ambient temperature of ~50 MHz K^{-1}[1].

In order to overcome this long-term drift the laser was used in conjunction with custom frequency stabilisation system. This uses a second iodine cell, combined with two photodiodes to monitor the transmission ratio of a beam passing through this iodine cell, and hence control the frequency of the laser. Chehura et al[1] had previously designed and constructed an active feedback stabilization system for this laser. The photodiodes are connected to a custom designed PID (Proportional, Integral, Derivative) electronic controller consisting of two stages; the first normalised the two detector signals to remove laser intensity fluctuations, and the second generates an error signal. This is fed back to the laser via the existing z-lock controller, which generates a voltage to either heat or cool the etalon adjusting the cavity length and controlling the laser frequency.

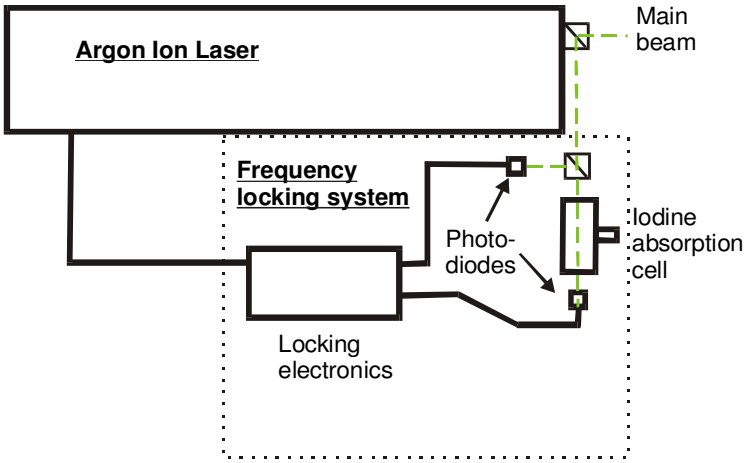

Figure 5-2 Diagram showing the configuration of the laser frequency locking system

The cell used in the locking system is a saturated cell, 100mm in length, which is held in a temperature controlled oven at 30°C. Although the absorption spectrum of this cell is not identical to that used in the PDV imaging head a comparison can be made using the Forkey[2] model for both this cell and the imaging head cell. This is shown in Figure 5-3 although not identical the absorption is very close over the frequency range the locking cell will operate at. By using the predicted absorption spectrum for these cells the transmission ratio through the imaging head cell can be determined for the set transmission through the locking cell.

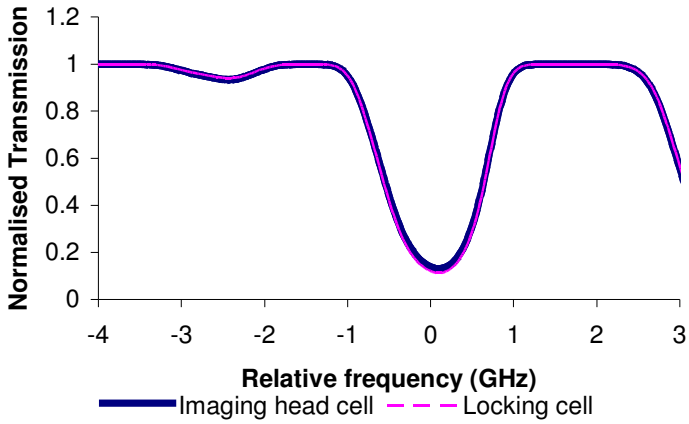

Figure 5-3 Overlaid absorption spectrum for the frequency locking system cell and PDV imaging head cell, calculated using the Forkey model[2].

5.2.2 Acousto-optic modulators

The acousto-optic modulators that were used were Isomet devices. AOM1, an Isomet 1205C device has a Lead Molybdate ($PbMo0_4$) crystal and has a centre frequency of 85MHz. This was combined with a tuneable RF driver the Isomet D301B-856. This allowed the first order shift frequency to be varied between 60 and 105MHz by varying a tuning voltage applied to the driver. Figure 5-4 shows the measured calibration of tuning voltage to frequency shift for this device.

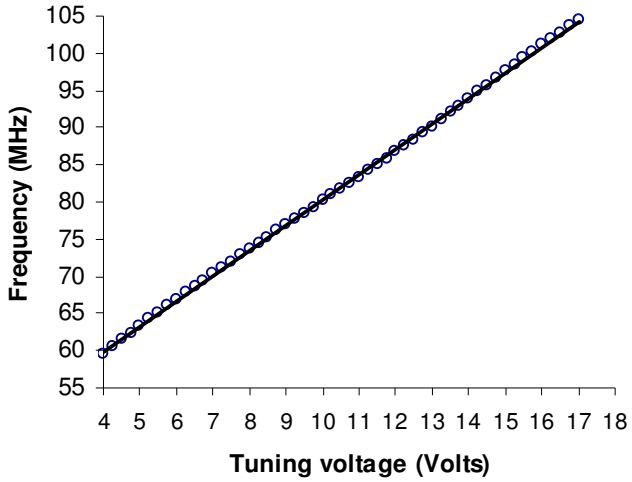

Figure 5-4 The tuning voltage to shift frequency calibration for the Isomet D301B-856 AOM driver.

The second device was an Isomet 1250C-829A, which has a Tellurium Dioxide (TeO_2) crystal. This has a centre frequency of 260MHz and was driven by a fixed frequency 260MHz driver (driver model 226A-1). This is operated by a TTL signal to turn the device on/off.

5.2.3 Beam delivery and Sheet forming optics

In previous work carried out at Cranfield[3] the beams were transported to the measurement region by a single-mode polarisation-preserving optical fibre. When the output of this fibre was formed into a light sheet using a combination of cylindrical lenses, the resulting light sheet had a Gaussian intensity profile, implying reduced intensity away from the centre axis of the sheet. This can lead to a reduction in the signal-to-noise ratio away from the centre of the sheet.

In this work the beams were coupled into a 10μm core fibre, supplied by DLR in Germany, and transported to the sheet forming optics. At 514.5nm this fibre supported a few (~22) modes[4]. In this case the laser sheet was formed using a beam-scanning device, again supplied by DLR. This scans the collimated beam rapidly across the region of interest, resulting in an ideal 'top-hat' intensity profile and avoiding the diffraction artefacts previously caused by imperfections in the sheet-forming optics[5].

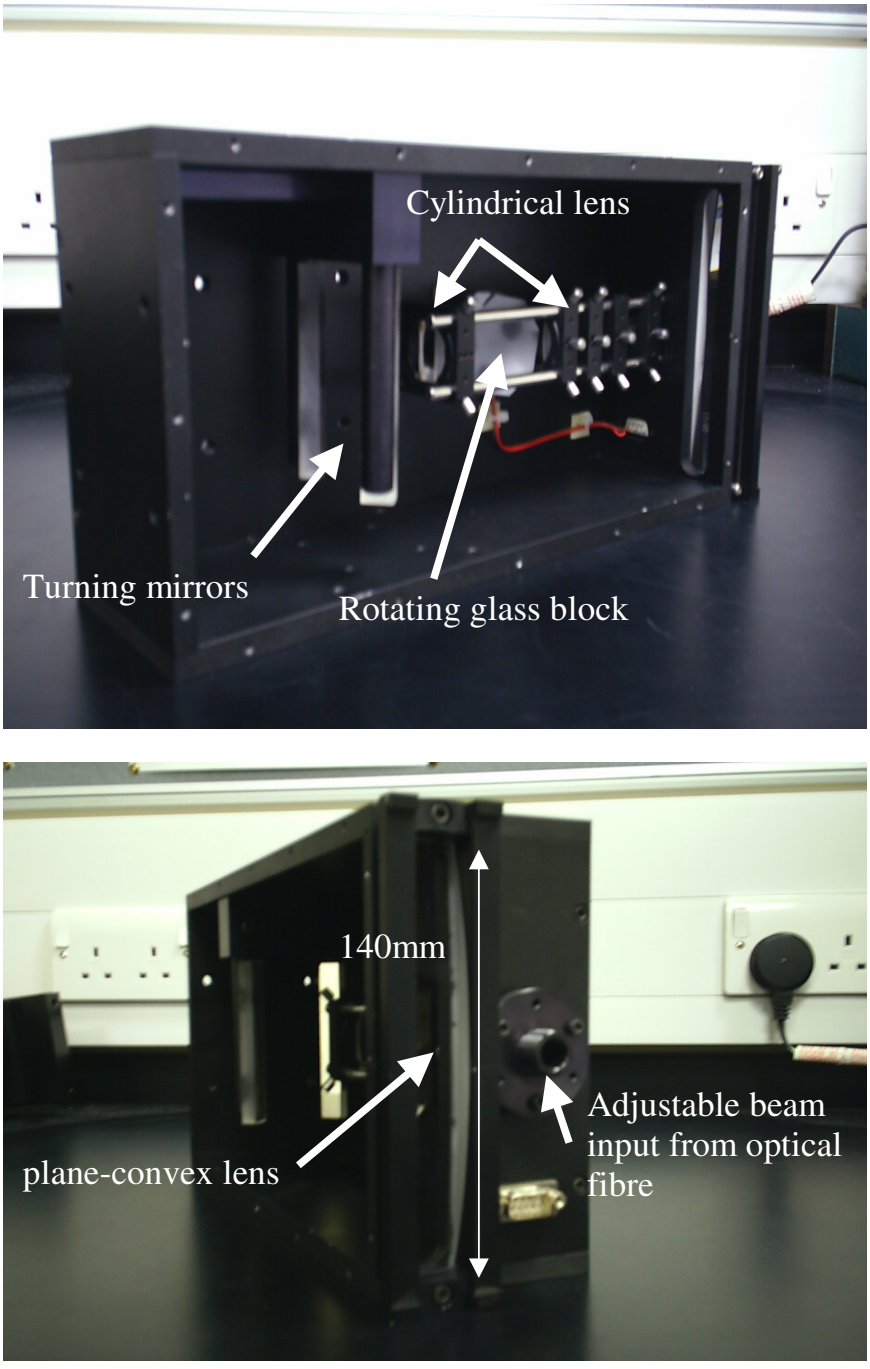

Figure 5-5 The beam scanning device, supplied by DLR, used to form the laser sheet

5.3 PDV imaging head arrangement

For this initial single velocity component work the second camera and the beam splitter where left in place, allowing the simultaneous measurement of both 2ν-PDV data, using only the signal camera, and conventional PDV data, using both the signal and reference cameras.

The PDV imaging head that was used in this work consisted of a conventional PDV imaging arrangement, with two CCD cameras arranged as show in Figure 5-6. The imaging head optics consisted of an infinity-corrected microscope-imaging set-up. An image is collected at the input optics to the imaging head this then falls on a microscope objective (Olympus, PlanApo, 1.25x magnification, infinity corrected) the image is then transferred through the system and refocused onto the CCD chips using matching tube lens (180mm focal length).

The cameras used for image capture were 'Imager Intense' cameras supplied by LaVision. These are digital cameras with 12 bit A/D conversion on a Peltier-cooled chip (-15^{o}C), with a 1376 by 1040 image resolution. The pixel size is 6.7μm by 6.7μm. Dedicated image acquisition and processing software (DaVis) is used to control the camera and to calculate and display normalized intensity maps. The integration time of the camera can be varied between 1 ms and 1000 s, depending on the scattered light intensity.

The PDV imaging head optics allow either a camera lens or the end of an imaging fibre bundle to be located at the front end, this allows either single component measurements to be made, or three component measurements using the arms of the imaging fibre bundle. This is discussed further in the section on 3D measurements in chapter 6.

Initially the system was set-up to measure a single velocity component, with a 35mm SLR camera lens as the input to the imaging head optics, this allowed only a single viewing direction and hence a single measured velocity component. Although there were limitations on the viewing angles that could be chosen, due to the inability to tilt the imaging head optics in the vertical axis, this was unimportant when only considering a single velocity component.

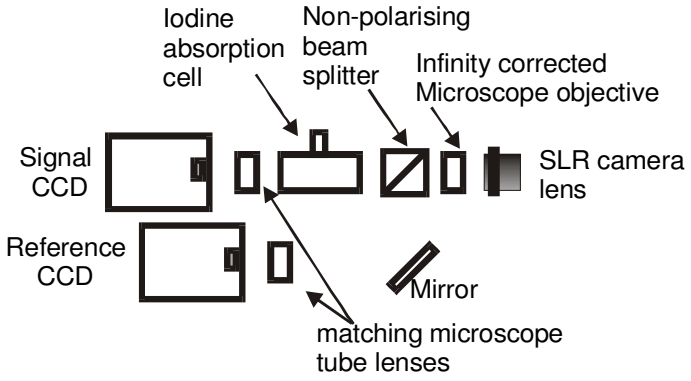

Figure 5-6 Arrangement of the PDV imaging head.

5.3.1 CCD dark current

The capability for long exposure times with these CCD cameras, means that it is possible to collect data from large areas, or when using low laser powers or low seeding levels. However an important factor is the camera noise characteristics under these conditions, especially important is the accumulation of dark current noise. This was investigated, by covering the CCD so that no light was collected in the integration period. An average for the dark current noise was then obtained over many integration periods. This was then repeated for different integration times. The dark current noise was found to be relatively constant over the investigated integration times and Figure 5-7 shows the dark current to be typically 40 to 60 counts.

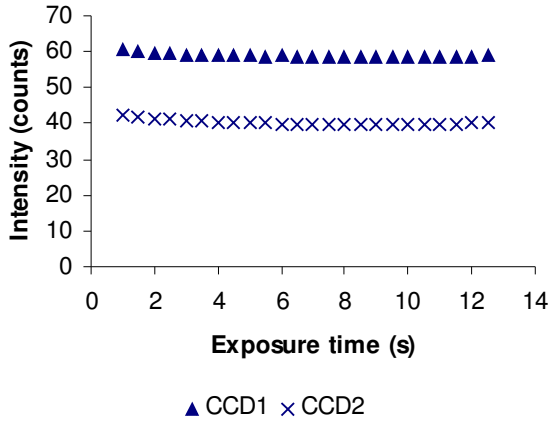

Figure 5-7 A graph showing that the CCD dark current remains relatively constant with varying integration times.

5.3.2 CCD linearity

Another important characteristic of the CCD is the camera linearity. The manufacturer's camera specifications quote the cameras as having a non-linearity of less than 1%. This was investigated by illuminating the CCDs with a uniform light source, by imaging a piece of card illuminated with the expanded beam from the argon ion laser. Images were then captured for varying integration times. An average was taken over many pixels in each collected image, and then again for multiple images with the same integration times. The results, Figure 5-8, show that the cameras are linear over 90% of full range. The remaining non-linear portion can be avoided by discarding flow measurement intensities over a certain threshold, typically >3800 counts.

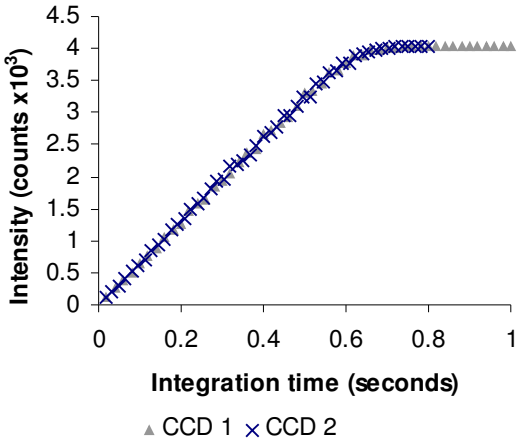

Figure 5-8 A graph showing the results of the investigation into the CCD camera linearity

5.3.3 Iodine cell properties

The iodine cell used in this work, Figure 5-9, operates as a starved cell[6], is 25 mm in diameter and 50 mm long, and incorporates a cold finger that was used to determine the starvation temperature. The use of a starved cell means that the control of the cell temperature can be less stringent, as above the starvation temperature all the iodine is in vapour form, so the characteristics of the absorption will not vary greatly with temperature. The operating temperature should not be too much greater than the starvation temperature of the cell, otherwise thermal broadening of the absorption lines will alter the cell characteristics[7]. The starvation temperature of the cell used is 40^{o}C. The cold finger is held above this temperature using a Peltier element in a feedback loop, and the cell body is contained in an oven held at the same temperature (50^{o}C). The cell diameter is much smaller than those typically used in PDV (50-100mm[5,8]), due to the use of the imaging fibre bundles, helping to maintain a constant temperature throughout the cell volume.

Accurate velocity measurements using PDV require an exact knowledge of the shape of the iodine absorption line as a function of frequency. This was obtained by frequency scanning the laser and monitoring the intensity of a low-power beam scattered off a stationary surface and viewed using the PDV imaging head.

The Spectra-Physics argon-ion laser used allows the optical frequency to be scanned by applying a voltage ramp to an input that controls the etalon temperature. Because the optical frequency change is temperature based, it must be carried out slowly to avoid instability and mode hopping. An uninterrupted scan is generally difficult to achieve, so successive scans were compiled to cover the full range.

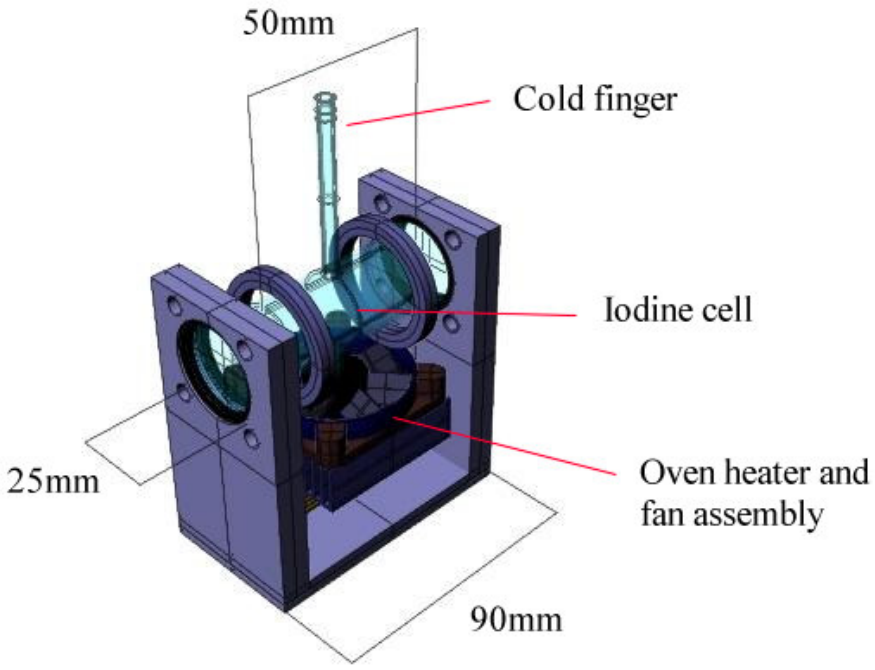

Figure 5-9 Schematic of the iodine cell and oven with covers removed

By passing the laser beam through an AOM and imaging the resultant different order beams, it was possible to measure the transmission at several frequencies simultaneously, and with a frequency spacing that is known. This allowed the easy identification of any mode hops, as well as providing a reference for the conversion from etalon voltage to frequency. This is similar to a frequency monitoring system used by Mignosi et al[9] where the different frequencies produced by an AOM were imaged alongside the flow being measured.

The resultant compiled scan is shown in Figure 5-10, overlaid with the theoretical absorption spectrum, calculated using the Forkey[2] model for our iodine cell. Figure 5-10(a) shows the position of the absorption line being used while Figure 5-10(b) shows this region enlarged.The near-linear region between the normalized absorption values of 0.2 and 0.8 corresponds to a frequency range of about 300 MHz. For practical illumination and viewing geometries, this typically allows measurement of flow velocities from a few meters per second up to a few hundred meters per second.

An important consideration that is unique to 2ν-PDV is the shape of the absorption line in the region of zero absorption. As the reference image is captured using light with a shifted frequency, coinciding with the full transmission portion, any Doppler shifts caused by scattering in the flow, should cause no change in the level of light that is transmitted, for this reference to be true. The scans of the iodine cell show that the zero absorption region is constant, at full transmission, for approximately 0.8 GHz which would require typical velocity shifts of several hundred meters per second for the reference intensity to be affected by the iodine vapour.

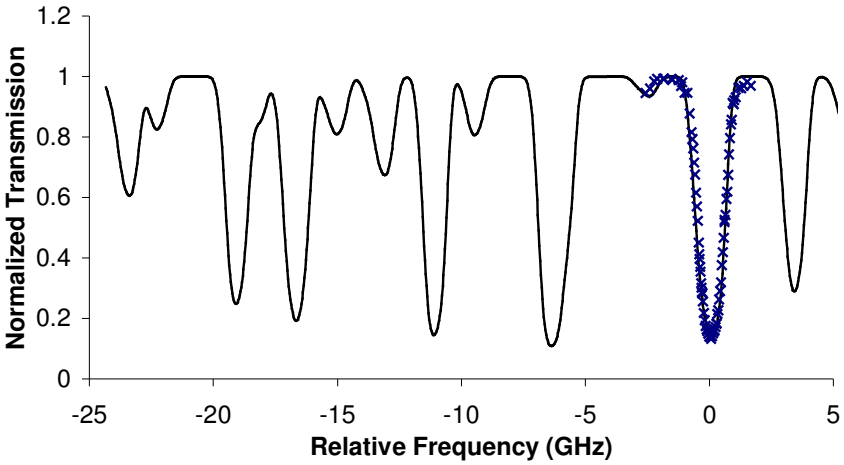

(a)

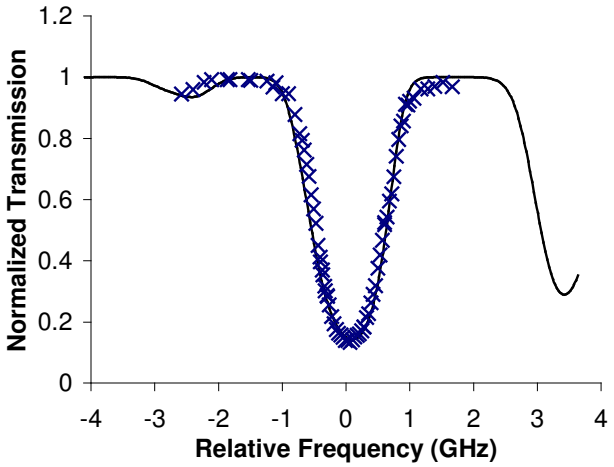

(b)

Figure 5-10 (a) The compiled scan of the PDV imaging head iodine cell overlaid with the theoretical absorption spectrum calculated using the Forkey model [2]. (b) An enlarged region showing the absorption line used in this work.

5.4 Processing scheme

Due to limitations on the optical frequency shift that could be achieved using the available acousto-optic modulators, only measurements made using the normal sensitivity 2ν-PDV scheme where possible, as there was insufficient frequency shift to tune the two illumination frequencies to positions on either side of the iodine absorption line.

The processing required to calculate the velocity maps for a single velocity component, using the 2ν-PDV technique and the normal sensitivity scheme is relatively simple.
In its simplest form, shown as a flow diagram in Figure 5-11, processing the images would consist of a background subtraction to remove ambient scattered light and camera dark current. This is followed by division of the signal image by the reference image, producing the normalized transmission image, which should contain the intensity variations caused by the Doppler shifts. Velocity is then calculated by de-convolution using the iodine absorption curve. Alongside are the relevant processing items used in the flow diagram processing system that is described in chapter 4 which also includes a complete description of each stage.

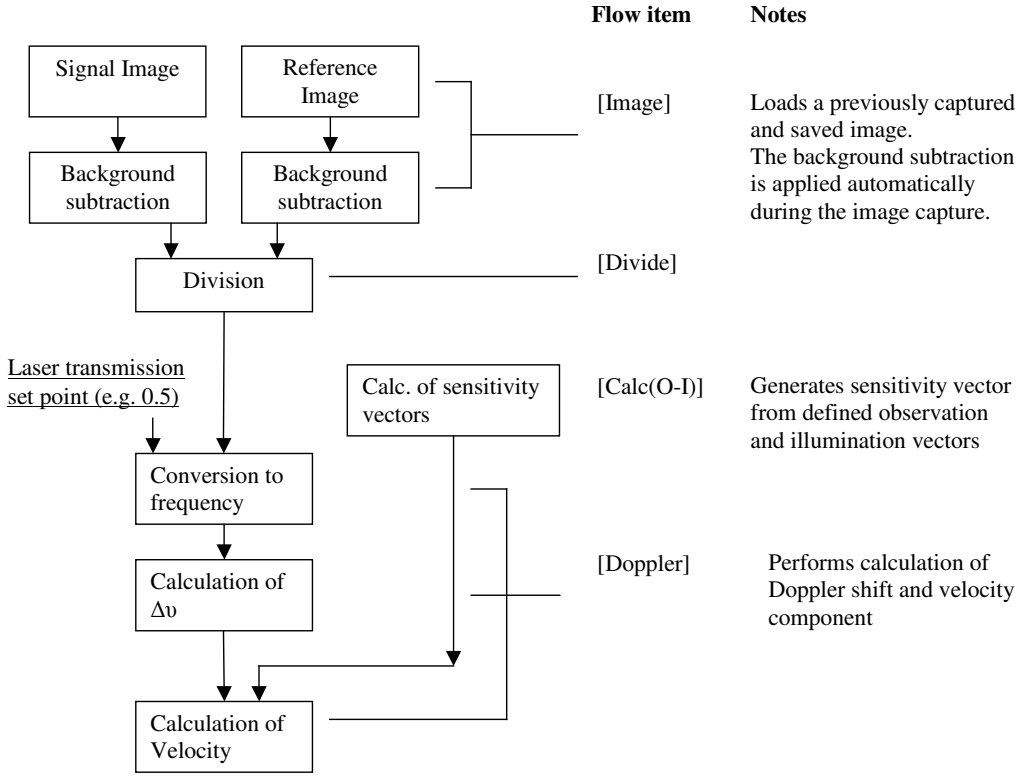

Figure 5-11 Flow diagram detailing a simple processing scheme for a single velocity component measurement.

The background subtraction is obtained by averaging multiple background images, taken shortly before the acquisition of the raw data. This ensures that the ambient light level, geometry and laser power are identical to those during the data collection.

It is also important to take background images for each illumination beam independently, because of the difference in the ambient scattered light caused by the different optical paths in generating the beams. The background is automatically subtracted at the image capture stage using the Davis software package.

Image de-warping is not essential, since image registration is automatic, and only a single view of the flow is captured so there is no need to de-warp multiple views to a common view. However if the viewing geometry chosen produced a very distorted image it may be desirable to include a de-warping stage, to produce a more understandable result although this was not applied to these results.

Typically, the reference and signal illumination beams will be of different power, so a normalization factor was included to account for this in taking the ratio between the signal and reference images. This factor was found by taking the ratio of the measured power in the signal and reference beams.

As an additional stage the recorded images had a threshold applied to remove pixels with levels below, or above those that where considered reliable, for example to remove saturated pixels, outside the linear region of the CCD response, or those in which the signal level was too low to be reliable, typically <100 counts.

Also low pass filtering or binning can be used to reduce high frequency noise in the measurements at a cost to the spatial resolution of the measurements. Both of these stages are applied after the background subtraction, and identical schemes need to be applied to both the signal/reference and white card image pairs.

As, detailed in section 5.3, the conventional PDV head arrangement was retained the collected data consists of two image pairs, one pair is collected when the flow is illuminated by the signal beam and the other when the flow is illuminated with the reference beam. Each pair consists of one image captured on the signal CCD, which views through the iodine cell, and one image captured on the reference CCD, which views directly and would not normally be present in a 2ν-PDV imaging head.

The first image from each pair, captured on the signal CCD, is used in the 2ν-PDV processing, whilst both the images in the pair captured under signal beam illumination can be used to process conventional PDV results. The collection and use of the data is shown in Figure 5-12.

The processing of the conventional PDV data, for comparison purposes, required a more complex processing scheme involving an additional “white card” correction stage and is shown in Figure 5-13. This correction stage was also necessary in the processing of 2ν-PDV measurements made on a rotating disc, which is discussed in more detail later.

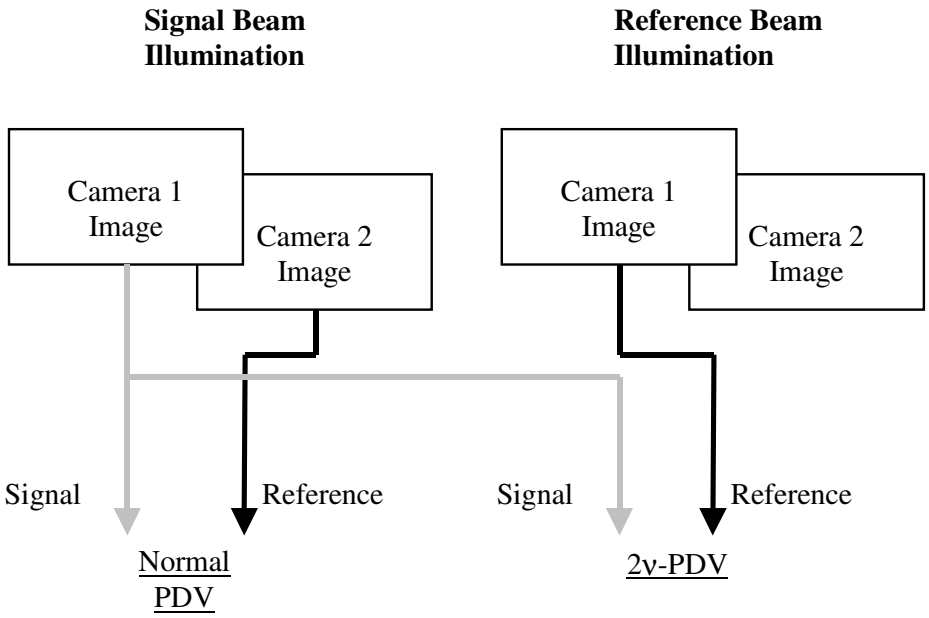

Figure 5-12 Diagram showing the collection and use of the data in this work.

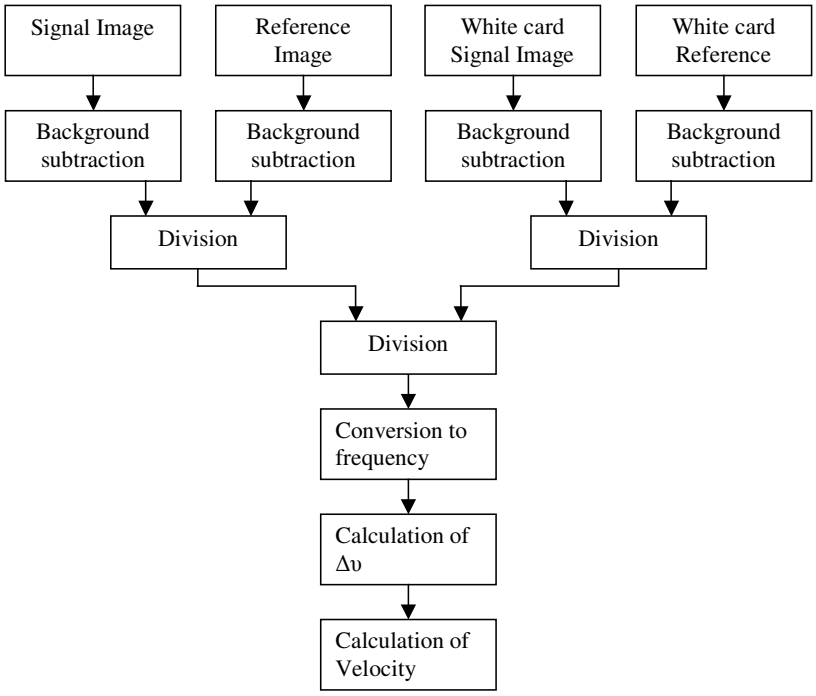

Figure 5-13 Flow diagram detailing a simple processing scheme for a single velocity component measurements with the additional "white card" correction

5.5 Single velocity component measurements on a rotating disc

The first test object used to assess the system was a Perspex disc 150mm in diameter, coated with matt white paint, intended to give a near uniform reflection, and mounted centrally on the spindle of a rotary motor. The aim of this experiment was to investigate a known velocity field. The maximum circumferential velocity of the disc was $31ms^{-1}$, which was measured using an optical tachometer.

5.5.1 Experimental arrangement

Figure 5-14 shows a representation of the experimental arrangement including the swept light sheet generator and the Perspex disk. The observation direction was at an angle of 26^{o} to the illumination direction from the centre of the disc to the centre of the CCD. The geometry was chosen to have a high sensitivity to the horizontal component of rotational velocity, which is expected to vary linearly along any vertical line through the disc.

While the illumination direction (î) is constant over the whole region, the observation direction is different for each pixel in the CCD array. This can cause significant errors for points more than 5^{o} out from the centre of the field of view [10]. This was not the case for this experimental arrangement where the maximum difference in the field of view was ~3^{o}.

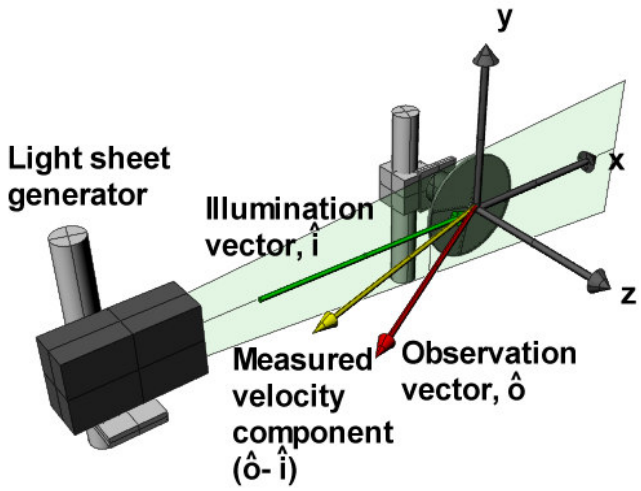

Figure 5-14 Diagram showing the experimental arrangement for measurements on a rotating disc

5.5.2 Results

Sets of image pairs were stored for both anticlockwise and clockwise rotation of the disc, as viewed from the front, at the maximum rotation speed. The power available at the output of the multimode fibre was about 4-8mW from a laser output of about 700mW, which although inefficient, was sufficient for making measurements with integration times 10 seconds. A significant amount of power is lost because the optical arrangement described in section 5.2, includes many surfaces, few of which are anti-reflection coated at 514nm. The major losses however occur in the acousto-optic modulators used. For example the 260 MHz AOM has a very small aperture and a first-order efficiency of less than 50%, and two passes are made through this component. This led to pixel intensity counts of around ~400 counts for the signal images and ~800 in the reference images.

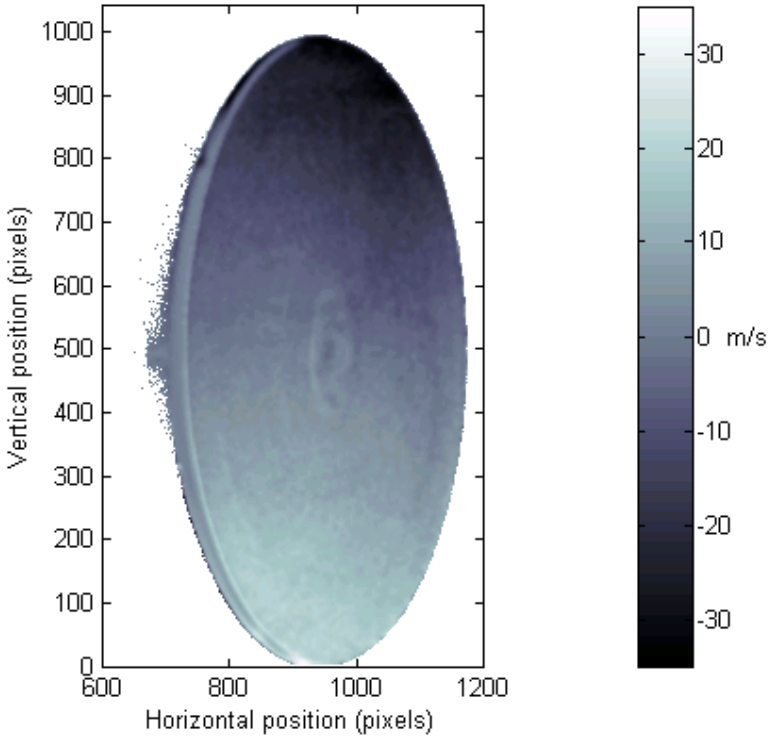

Figure 5-15 A typical calculated velocity field, using the 2ν-PDV system

A typical processed velocity field is shown in Figure 5-15. Profiles of the greyscale value were taken vertically through the smoothed images passing close to the centre of the disc. The profiles, for both clockwise and anticlockwise rotation, are shown in Figure 5-16, along with the theoretical velocity gradient calculated from measurements made with an optical tachometer. As expected, the velocity gradient is negative for the first plot, and positive for the second, corresponding to the reversal in the sense of rotation. The velocity error for these plots is around ±2 ms^{-1}.

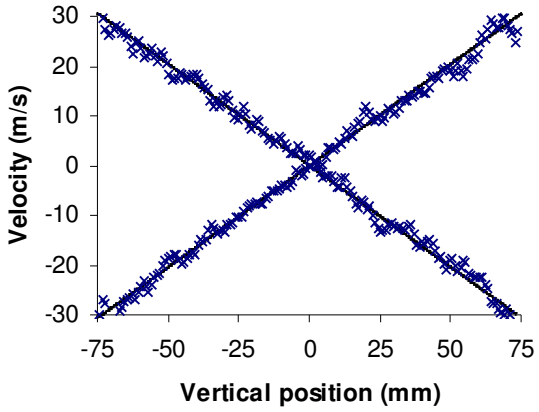

Figure 5-16 Profiles taken through the centre of the disc for clockwise and anticlockwise rotation

Both beams exiting the two-frequency illumination system are coupled into the same fibre for delivery to the sheet forming optics. However this coupling was not ideal for both beams resulting in significantly different populations of propagating modes, giving different output beam power distributions. This is shown in Figure 5-17 where the far-field output of the fibre for each beam was imaged. Because of these differing intensity profiles, a further processing step was required; a "white card" image was taken for each illumination beam. These are images capture under the normal flow conditions, in this case light scattered from the disc, with the laser tuned to a position off the absorption line at 100% transmission. The two white card images are then used to make a correction image by the division of the two. This is then applied to the measurements as described in section 5.4.

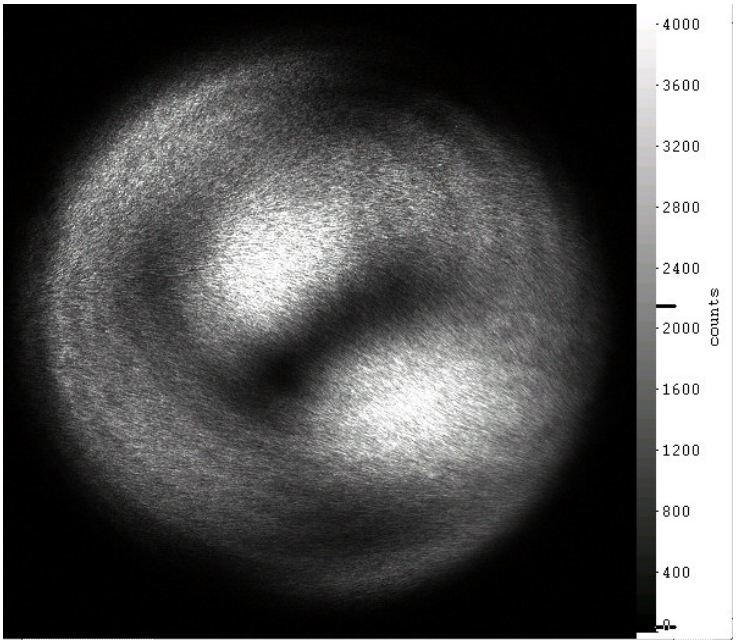

(a)

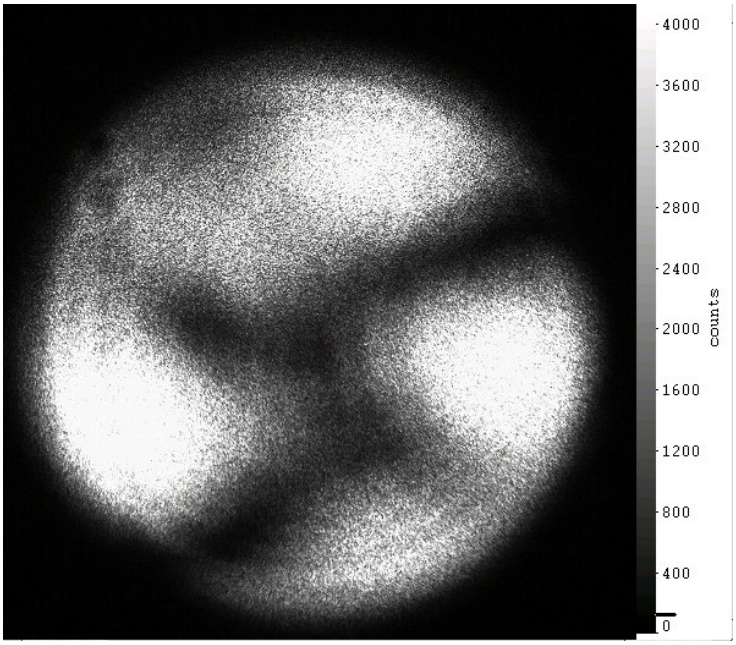

(b)

Figure 5-17 The far-field output of the fibre supplied by DLR, showing the difference in the beam coupling between the (a) signal and (b) reference beams.

5.6 Single velocity component measurements on an axis-symmetric air jet

The next test measurement was made on a seeded air jet, as this allowed the system to be assessed in a situation more closely matching those of the techniques intended applications.

5.6.1 Experimental arrangement

Measurements were carried out on an axis-symmetric air jet, with a 20mm diameter smooth contraction nozzle. The air intake to the jet was seeded using a Concept Engineering ViCount compact smoke generator, which produces particles in the 0.2-0.3μm diameter range. The jet has a theoretical exit velocity of $94ms^{-1}$, which was calculated from measurements of the nozzle pressure ratio.

Figure 5-18 shows the experimental arrangement with the main flow direction of the jet perpendicular to the laser sheet. The observation direction was placed in forward scatter where scattering intensities are greatest; this results in a measured velocity component that is ~20^{o} from the main jet velocity component.

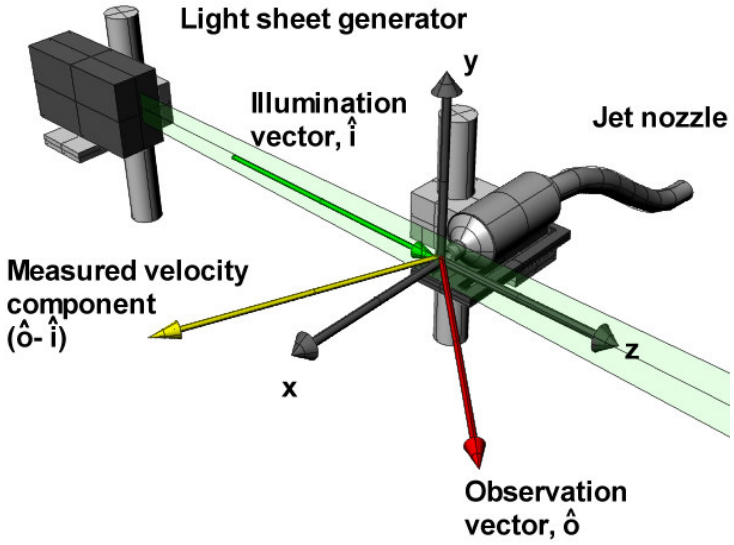

Figure 5-18 Diagram showing the experimental arrangement for measurements on an axis-symmetric air jet.

5.6.2 Results

Sets of image pairs were captured at various locations downstream from the nozzle; this was achieved by moving the nozzle position, in the x direction, relative to the laser sheet. Again the optical power at the output of the optical fibre was about 4-8mW as discussed in section 5.5.2 and the integration time on the cameras was 10 seconds.

The velocity field at each position, 1.5, 2.5, 3.5 and 4.5 nozzle diameters downstream are shown as a 3-dimensional representation in Figure 5-19. Differences in illumination intensity profiles for the reference and signal illumination beams were again present but as the laser sheet used for the jet was small and well-focused, compared to the thick sheet used with the disc, it was no longer necessary to apply the 'white card' correction.

The 2ν-PDV results were compared with a conventional two-camera arrangement by using the second camera in the PDV head to simultaneously capture standard PDV data, Figure 5-20. This was processed using images captured when the signal beam was illuminating the flow, with the second camera providing the reference image. When the conventional PDV data was processed it was necessary to apply a “white card” correction that is common in conventional PDV processing to account for image misalignment.

A comparison of profiles through the centre of each slice, for the 2ν-PDV and conventional PDV jet measurements can be seen in Figure 5-21 and the difference between the two is shown in Figure 5-22. The results from the two techniques agree well to within ~ $\pm 5 ms^{-1}$ over most of the jet diameter. These differences would be expected due to the additional sources of error in the conventional PDV results, where the quality of the pixel matching between the signal and reference images will cause errors in the calculated velocities. Likewise the polarisation sensitivity of the polarising beam splitter will also cause velocity errors in the calculation of the conventional PDV results. Neither of these issues will affect the two-frequency PDV results.

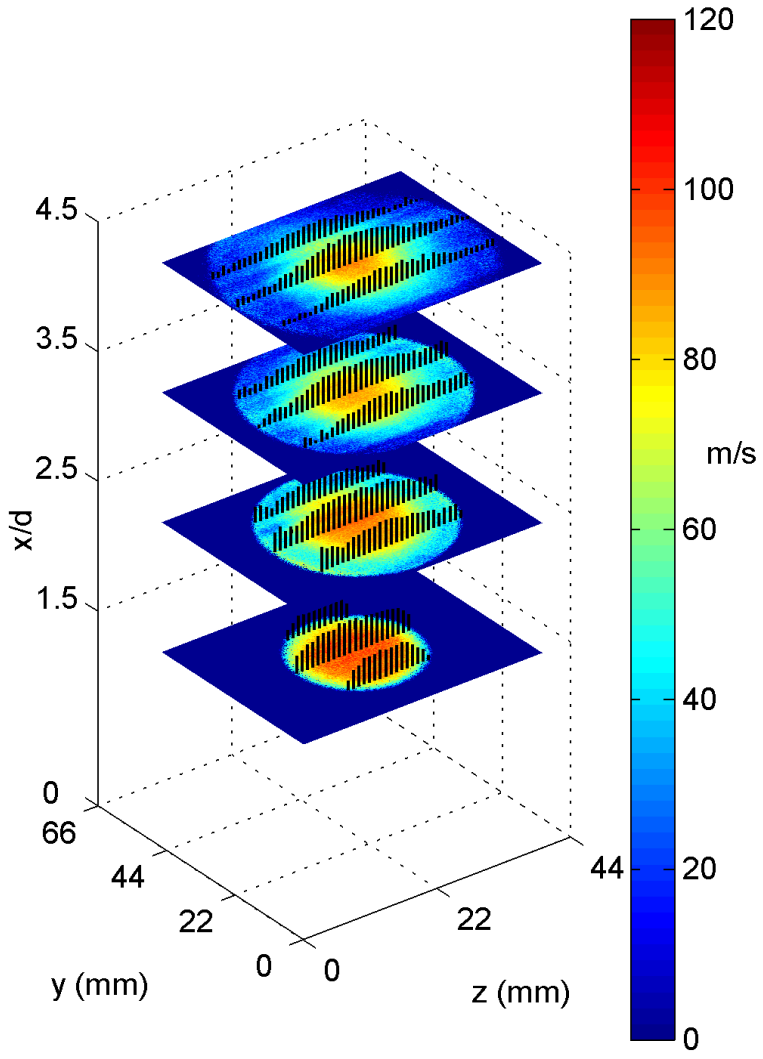

Figure 5-19 The velocity field of an axisymmetric air jet calculated using the 2v-PDV (single CCD) system. Measurements were taken at 1.5, 2.5, 3.5 and 4.5 diameters downstream from the nozzle. Overlaid are vectors showing the magnitude of the velocity at various points (arrow heads have been removed for clarity)

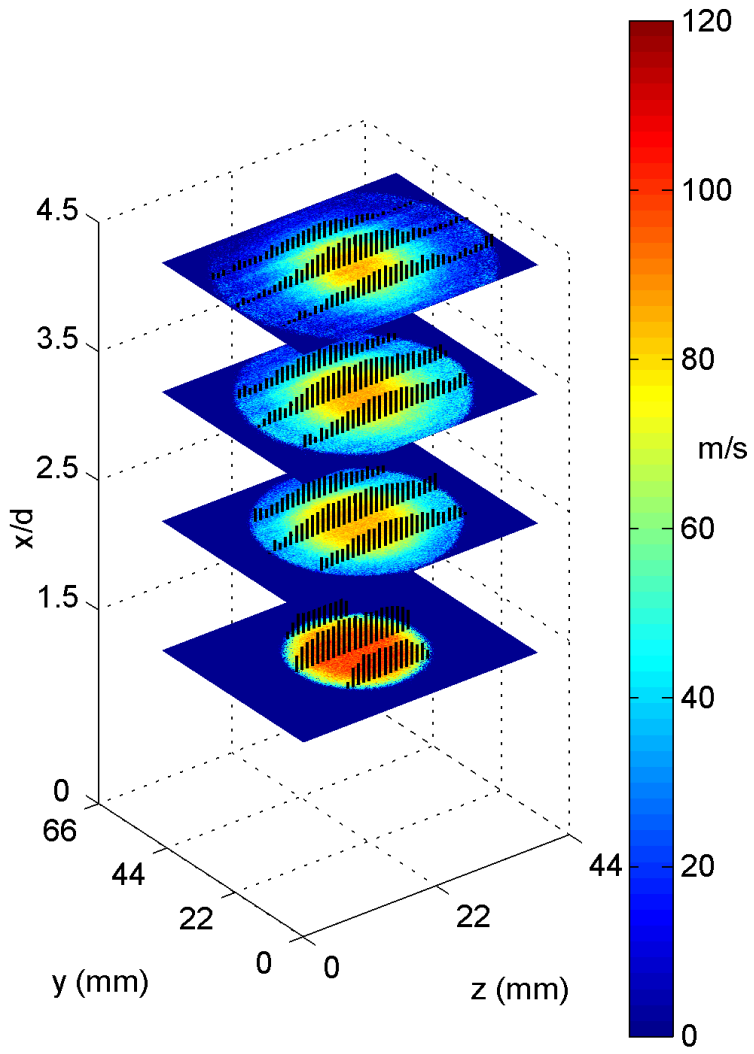

Figure 5-20 The velocity field of an axisymmetric air jet calculated using the standard (two CCD) PDV technique. Measurements were taken at 1.5, 2.5, 3.5 and 4.5 diameters downstream from the nozzle. Overlaid are vectors showing the magnitude of the velocity at various points (arrow heads have been removed for clarity)

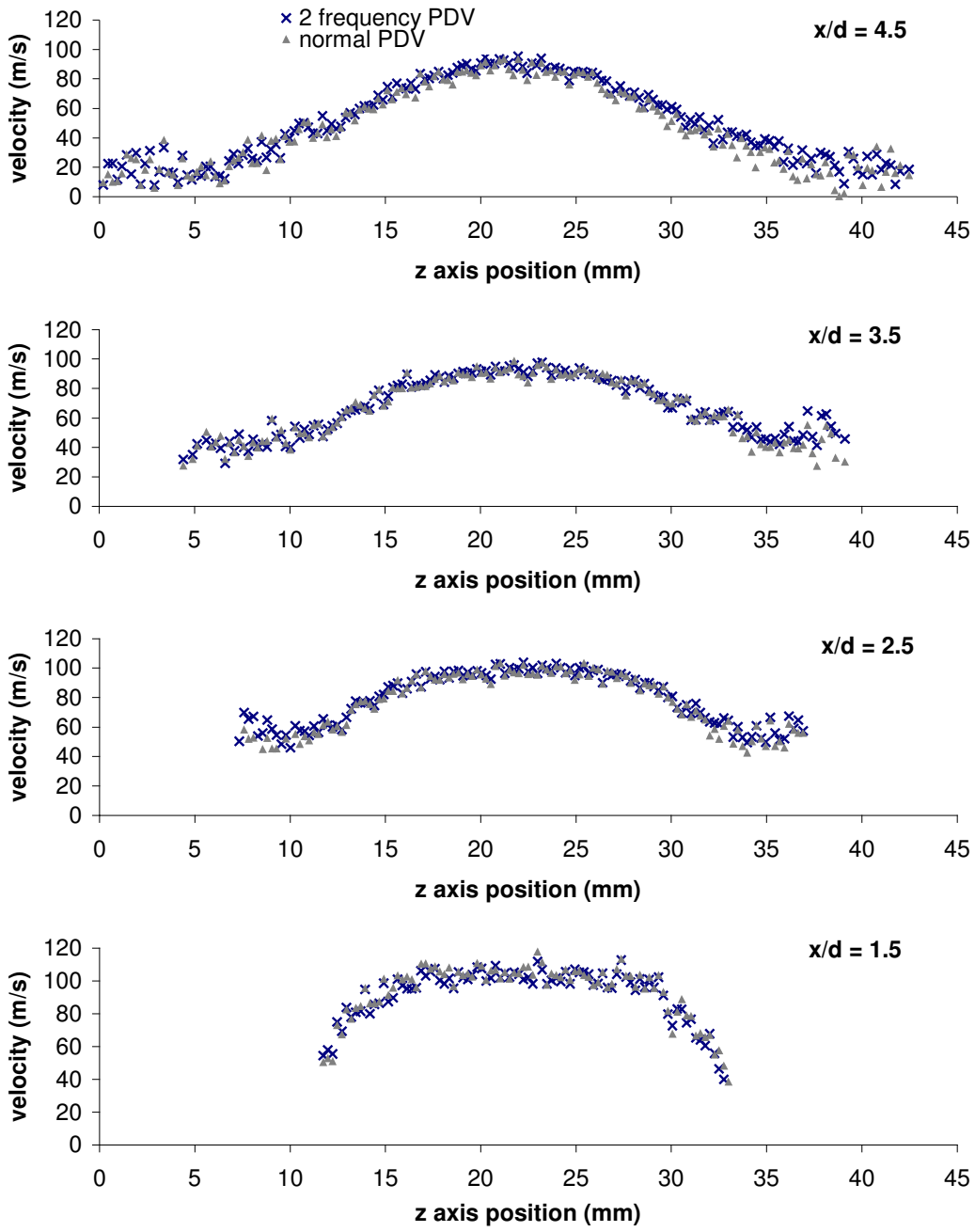

Figure 5-21 A comparison between profiles, taken through the centre of the air jet at 1.5, 2.5, 3.5 and 4.5 diameters downstream, for the 2ν-PDV (single CCD) and standard (two CCD) PDV results (every 5th point shown).

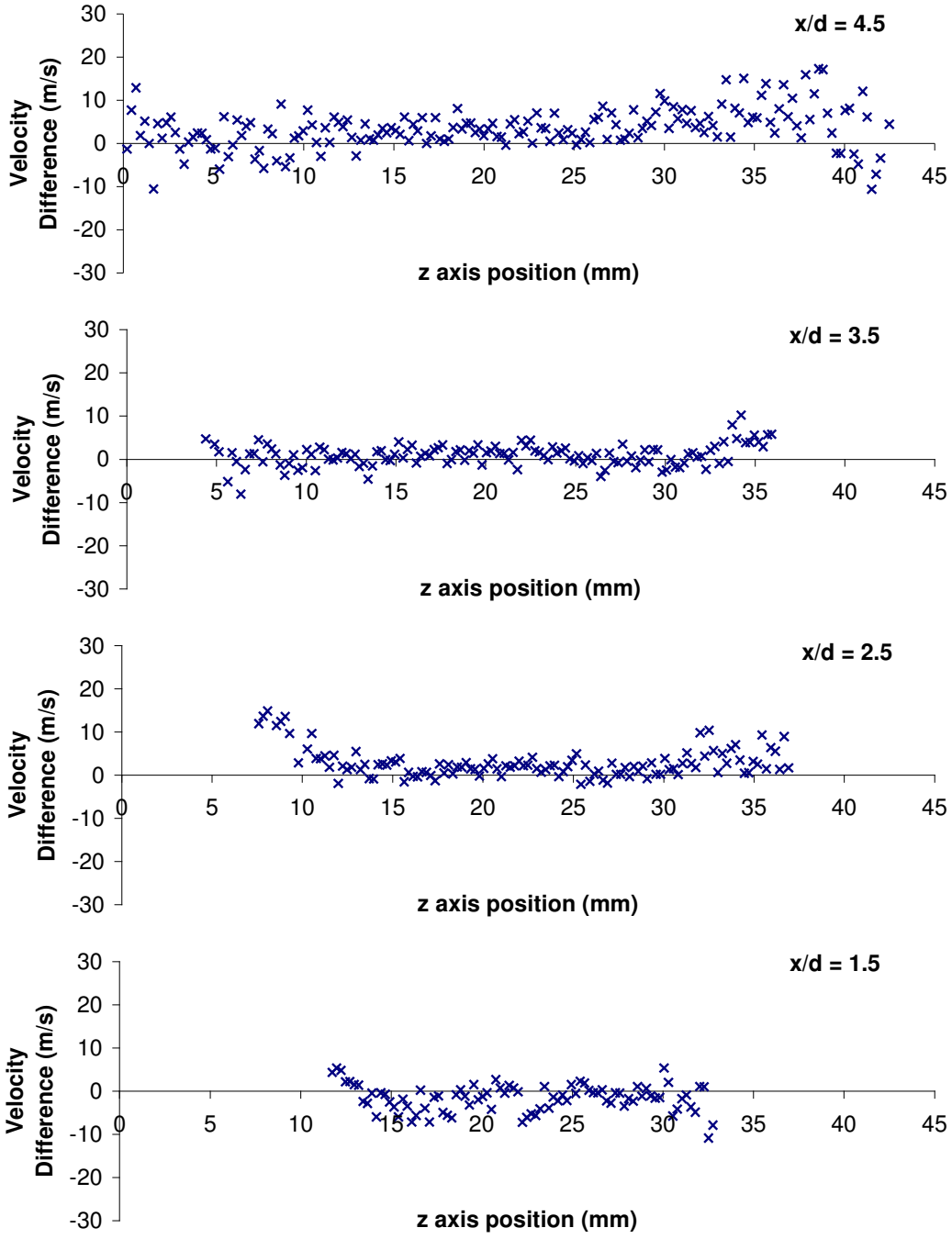

Figure 5-22 The difference between the 2ν-PDV (single CCD) and standard (two CCD) PDV results for the profiles shown in Figure 5-21

A comparison was made between the velocity profiles obtained in Figure 5-21 and profiles calculated from measurements of the nozzle pressure ratio. The profiles were calculated using simple empirical equations to describe the development region of a circular air jet given by Rajaratnam[11] as:

$$r_1/r_0 = 0.95 - 0.097\, x/r_0$$

Equation 5-1

$$b/r_0 = 0.10 + 0.111\, x/r_0$$

Equation 5-2

$$r_2/r_0 = 1.07 + 0.158\, x/r_0$$

Equation 5-3

$$\frac{u - u_1}{u_0 - u_1} \approx \frac{u}{u_0} = 0.5\left[1 - \cos(\pi\varsigma)\right]$$

Equation 5-4

$$\varsigma = \frac{r_2 - r}{r_2 - r_1}$$

Equation 5-5

Where

r	Radial distance from centre line
r_0	Radius of nozzle
r_1	Distance from centre line to inner edge of shear layer (outer edge of potential core)
r_2	Distance from centre line to outer edge of jet
b	Distance to half initial velocity (u_0) point from the inner edge of shear layer (outer edge of potential core)
u	Magnitude of velocity
u_0	Initial jet velocity
u_1	Magnitude of velocity of ambient fluid
x	Distance along centre line (downstream from nozzle)
x_0	Distance along centre line the potential core extends to

Figure 5-23 shows the geometry used in these calculations. The potential core is the triangular region extending from the jet nozzle where the jet's velocity remains constant at the exit velocity. As the jet expands it mixes with the surrounding air producing the shear layer across which the velocity varies from u_0 at the inner edge to zero at the outer edge. It also shows the positions of various key points taken from the profiles shown in Figure 5-21, compared to where the empirical formulas suggest they should be. These include the position in each profile where the potential core ends, and the half of maximum velocity point.

As can be seen these agree well with the theory, except for the extent of the jet measurement, however this can be explained by noting that the jet was seeded through the air intake, which lead to low seeding levels towards the outside of the jet flow, which in turn leads to low levels of scattered light. Velocities where not calculated for these regions as a threshold was applied to remove regions with low signal levels.

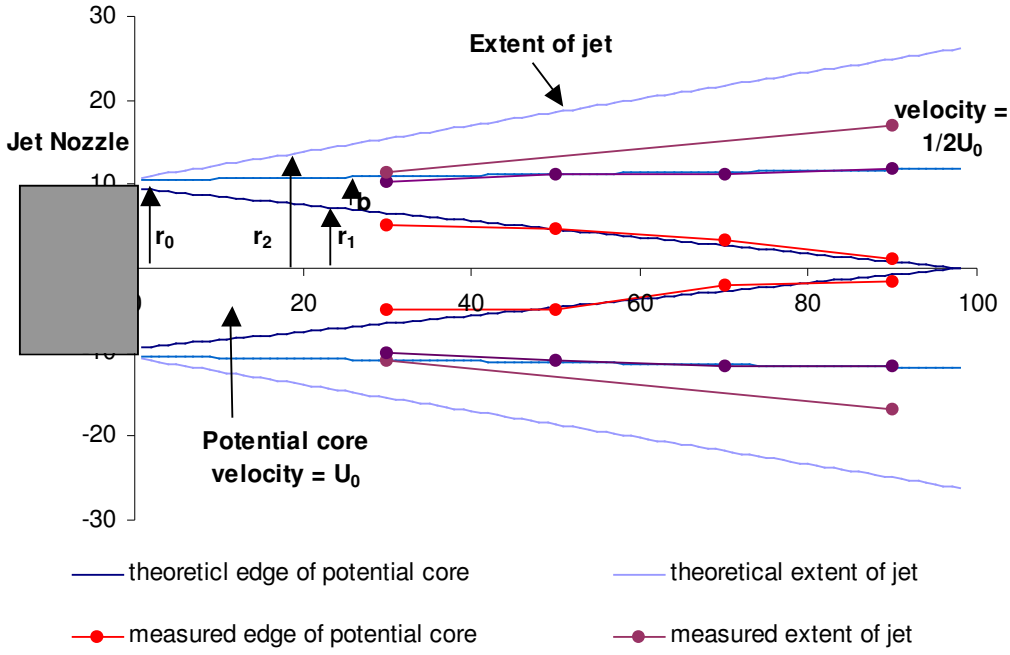

Figure 5-23 Diagram showing the geometry used to calculate the jet profiles and corresponding points measured from the profiles shown in Figure 5-21

Profiles calculated using Equation 5-1 to Equation 5-5, are plotted along with the 2ν-PDV results in Figure 5-24. Again it can be seen that there is good agreement between the two, in terms of the overall profile of the flow. The magnitudes differ between the two but this can be explained by the simple empirical equations used to calculate the theoretical profiles and the possible variations between the flow produced by jet used and a theoretical jet flow. Again lower seeding levels in the regions towards the outside of the jet flow can account for the noticeable differences in these regions.

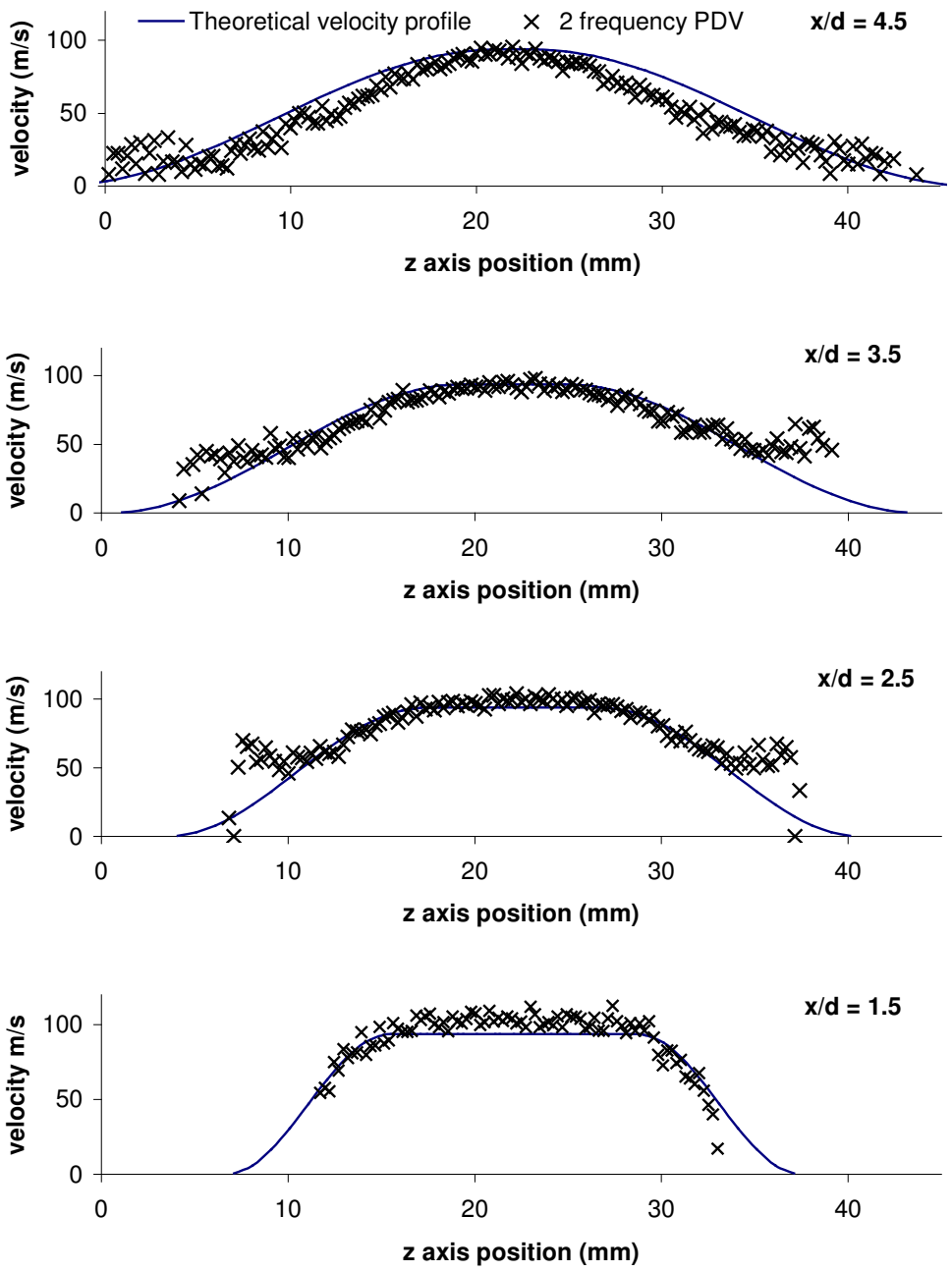

Figure 5-24 A comparison between profiles, taken through the centre of the air jet at 1.5, 2.5, 3.5 and 4.5 diameters downstream, for the 2ν-PDV (single CCD) and profiles calculated using empirical equations described by Rajaratnam[11]

5.7 Discussion

The processing of data is made extremely straightforward in the 2ν-PDV system, by the avoidance of any pixel-matching requirement between the signal and reference images. This can be demonstrated by the fact that a 'white card' correction was not necessary when processing 2ν-PDV results for the seeded flow, but was necessary when processing the conventional, two camera PDV results for the same flow, collected simultaneously.

The differing output beam coupling caused particular problems when using the beam-scanning device to illuminate the surface of a rotating disc, making it necessary to use the “white card” correction used commonly in normal PDV. The effect was less noticeable, and the correction was no longer necessary, when using a small well-focused sheet on a real flow, as was the case in the measurements on a seeded air jet.

The power available at the output of the multimode fibre is currently about 4-8 mW from a laser output of about 700 mW, which although inefficient, is sufficient for making measurements at integration times of a few tens of seconds. A significant amount of power is lost because the optical arrangement includes many surfaces, few of which are anti-reflection coated at 514 nm. Efficiency would be improved by substituting coated optics. The major losses however occur in the particular AOMs used. The 260 MHz AOM has a very small aperture and a first-order efficiency of less than 50%, and two passes are made through this component. Up to ten times more power is available in the reference beam path, since the 85 MHz AOM has a much larger aperture and is more efficient. Components are now available with improved efficiencies and offering larger optical frequency shifts, so we expect to be able to improve the available power from the system to a level more usable in real flows. For example, using two 350 MHz AOMs in single pass configuration, at least an order of magnitude improvement in delivered power would be expected; possibly up to two orders of magnitude, which would result in 100-200 mW in the measurement volume.

5.8 Summary

A 2ν-PDV system capable of making time-averaged, single velocity component measurements has been described. The system was only capable of making normal sensitivity 2ν-PDV measurements due to limitations on the frequency shift achievable using the available acousto-optic modulators.

Measurements on a rotating disc and a seed air jet have been presented along with a comparison with conventional PDV results capture simultaneously. Comparisons of the velocity measurements on the rotating disc with the theoretical velocity indicate a velocity error in these measurements of $\sim\pm 2 ms^{-1}$. This is currently limited by:

- Low illumination light levels from the two-frequency generator.
- Differences in the population of propagating modes in the optical fibre for the two illumination frequencies.

Measurements made on a seeded air jet were compared with results made using conventional PDV simultaneously. This was achieved by using a conventional two camera PDV imaging head to make the measurements, with only the camera viewing through the iodine filter being used in the 2ν-PDV calculations. The measurements on the seeded air jet have also been compared with a simple empirical model describing the jet with good agreement between the two regarding the radius and length of the potential core of the jet.

It has been found the use of a white card correction is no longer necessary for 2ν-PDV measurements made on seeded flows. The correction is still necessary for measurements on the rotating disc, but the differing output beam coupling for the two laser frequencies can explain this. As the light sheet used to illuminate the face of the disc was poorly focussed this caused significant differences in the illumination laser sheets used for the two images. This was not the case when a well-focussed light sheet was used for measurements in real flows.

5.9 References

1. Chehura, E. and Tatam, R.P., "In-line Laser Doppler Velocimeter using fibre-optic Bragg grating interferometric filters", 2003, *Measurement Science and Technology*, Vol. 14, pp 724-735.

2. Forkey, J.N., "Development and Demonstration of Filtered Rayleigh scattering - a Laser Based Flow Diagnostic for Planar Measurements of Velocity, Temperature and Pressure", 1996, *Final Technical Report for NASA Graduate Student Researcher*, Fellowship Grant #NGT-50826, Princeton University.

3. Ford, H.D., Nobes, D.S., and Tatam, R.P., "Acousto-optic Frequency Switching with Fibre-optic Delivery for Single Camera Planar Doppler Velocimetry", 2003, *16th International Conference on Optical Fiber Sensors*, Nara, Japan, Tu3-5, pp 226-229.

4. Syms, R. and Cozens, J., " Optical guided waves and devices", 1992, McGraw-Hill, Maidenhead, England, ISBN

5. Roehle, I., Willert, C., Schodl, R., and Voigt, P., "Recent Developments and Applications of Quantitative Laser Light Sheet Measuring Techniques in Turbo machinery Components", 2000, *Measurement Science and Technology*, Vol. 11, pp 1023-1035.

6. Quinn, T.J. and Chartier, J.-M. , "A New Type of Iodine Cell for Stabilized Lasers", 1993, *IEEE Transactions on Instrumentation and Measurement*, Vol. 42, pp 405-406.

7. Chan, V.S.S., Heyes, A.L., Robinson, D.I., and Turner, J.T., "Iodine Absorption Filters for Doppler Global Velocimetry", 1995, *Measurement Science and Technology*, Vol. 6, pp 784-794.

8. Reinath, M.S., "Doppler Global Velocimeter Development for Large Wind Tunnels", 2001, *Measurement Science and Technology*, Vol. 12, pp 432-441.

9. Mignosi, A., Lempereur, C., Barricau, P., Mathe, J.-M., and Buchet H., "Development and Qualification of a new Doppler Global Velocimeter", 2001, *19th International Congress on Instrumentation in Aerospace Simulation Facilities*, pp 386-396.

10. Ford, H.D. and Tatam, R.P., "Imaging System Considerations in Doppler Global Velocimetry", 1995, *Proc. SPIE*, San Diego, CA, 2546, 454-464.

11. Rajaratnam, N., "Turbulent Jets", 1976, Elsevier, Amsterdam, Oxford, New York.

6 Development of a time averaged, 3D 2ν-PDV system

6.1 Introduction

This chapter describes the development of a time averaged, 3D 2ν-PDV system. The single velocity component system described in chapter 4 was modified using imaging fibre bundles allowing the measurement of multiple velocity components and the calculation of 3D velocity. The imaging fibre bundles and their application are described, followed by details of an alternative two-frequency illumination system that allows both the normal and increased sensitivity schemes to be used. Finally 3D velocity measurements made using the system are presented. These include measurements made on a rotating disc that are used to characterise the system and the performance of the two sensitivity schemes and measurements made on a seeded axis-symmetric air jet.

6.2 Modification of the 2ν-PDV system to allow 3D measurements

Viewing the flow from a single observation direction allows a single component of the flow velocity to be measured; therefore to make three-dimensional measurements a minimum of three viewing directions are necessary. Conventional methods use a separate PDV imaging head (with two cameras and an iodine cell in each) to measure each of the three velocity components. Alternatively multiple light sheets can be used to vary the illumination direction and hence the measured velocity component. However the approach described by Nobes et al[1-4] was used in this work. Here multiple branch imaging fibre bundles are used to port multiple views to a single imaging head.

6.2.1 Imaging fibre bundles

The use of imaging fibre bundles, pioneered at Cranfield University[2-4] considerably simplifies the system by allowing multiple velocity component measurements to be made using a single PDV imaging head. This approach has since been adopted by DLR[5], NASA[6] and Oxford University[7].

As described in chapter 5, the PDV imaging head arrangement allows either a SLR camera lens or the output of an imaging fibre bundle to be used as the input into the imaging head, here the second approach was used. Although the numerical aperture of the imaging system (0.04) is not well matched to the bundles (~0.6[8]) the optics were chosen to produce high quality flat field images on the CCD chip.

The imaging fibre bundles in use at Cranfield are a coherent array of fibres spilt into four channels (Figure 6-1a). Each channel is 4m long, and has 600x500 fibres that have 8μm core diameters and are positioned at 10μm centres. The other end of each channel viewed the region of interest using 35mm SLR camera lenses coupled to the fibre using custom mounts. Cross talk between fibres is minimised by the use of interstitial

absorbers between fibres[8]. The losses through the bundle are ~50% for the 4m length used[8]. These views are combined at the detector head, with each occupying a quarter of the CCD image (Figure 6-1b). The ends of the fibre bundles are secured in aluminium housings for which custom mounts have been made to allow the bundles to be with standard SLR camera lenses and borescopes. An example of the image formed is shown in Figure 6-2. This is a view of a calibration target used to de-warp the image to a common view and determine the observation directions for each view[9]. Figure 6-3 shows the result after this de-warping process (discussed in chapter 4 and further in section 6.3); here all four views have been overlaid for demonstration purposes.

The use of imaging fibre bundles combined in this way make three-component measurements possible with just a single PDV imaging head arrangement, compared with the multiple imaging head arrangement previously required. Another advantage to using the imaging fibre bundle approach is the flexibility this offers in the positioning of viewing directions as well as the ability to isolate the imaging head from the test environment and the wide variety of imaging optics to which the bundle can be coupled.

In previous work[4] using the imaging fibre bundles only three of the four views have been used to view the flow, with the fourth imaging a portion of the laser beam. This fourth view was used to determine the un-shifted laser transmission on the iodine absorption line, and hence the initial laser frequency itself to be calculated. In this work however it was decided to use the fourth view to measure a fourth velocity component, as the laser frequency could be determined using the laser locking system described in section 5.2. The additional fourth measured component could then be used to assess the impact of using over-sampled data in the calculation of the orthogonal velocity components. A method for this has been described in chapter 4 and the benefits will be discussed further in chapter 8.

(a)

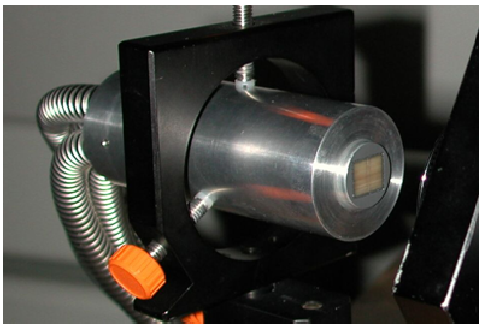

(b)

Figure 6-1 (a) Photograph of the individual channel of the imaging fibre bundle (b) the combined end of the fibre bundle.

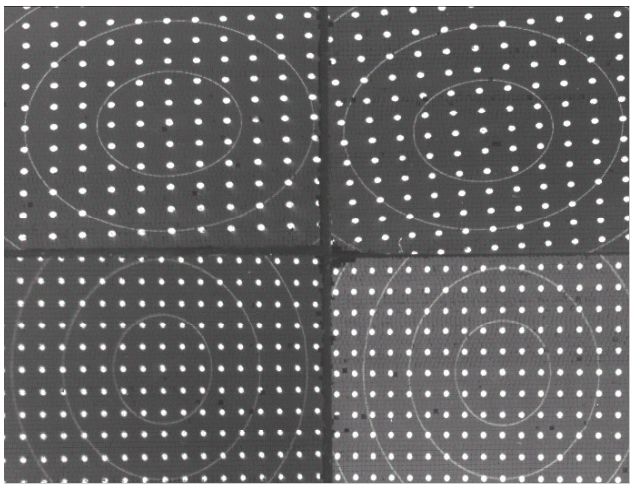

Figure 6-2 An example image of a view through the imaging bundles of a calibration target (field of view ~100 x 100 mm) the white dots are 2.5mm in diameter and spaced on a regular grid of 10mm.

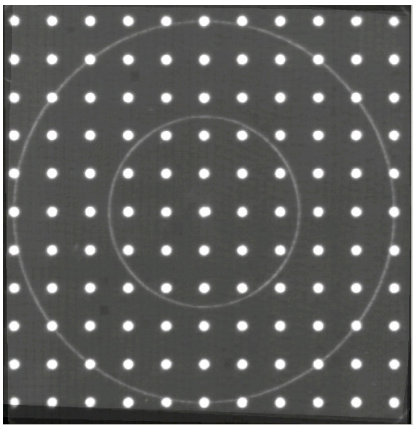

Figure 6-3 An example of the 'de-warped' views, showing all four views overlaid

6.2.2 2ν-PDV imaging head

In the single component velocity measurements described in chapter 5 a conventional PDV imaging head was used, this allowed the simultaneous measurement of conventional PDV results. However as one of the initial motivations for the 2ν-PDV technique was the removal of the beam splitter and the associated polarisation sensitivity problems it was decided to remove the beam splitter and second CCD camera from the imaging arrangement for this work. This would allow 3D velocity measurements to be made using only the 2ν-PDV technique and only a single CCD camera. A further advantage of this was that the intensity of light reaching the signal CCD chip would be approximately doubled, as the light is no longer split into two imaging paths.

6.2.3 Illumination system

For the single velocity component system described in chapter 5 a combination of acousto-optic modulators (AOMs) were used to shift the optical frequency of an argon-ion laser to provide two illumination frequencies separated by approximately 700MHz. This set-up allowed rapid switching between the two illumination frequencies, however this system proved to be light inefficient due principally to multiple passes through a high frequency AOM. This resulted in low illumination powers and low scattered light intensities being received at the CCD. When this set-up was combined with the use of the imaging fibre bundles, which have an optical efficiency of approximately 50%, this resulted in low scattered light levels being collected on the CCD, because of this the experimental arrangement was modified to allow greater illumination power. A schematic diagram of this new experimental arrangement can be seen in Figure 6-4.

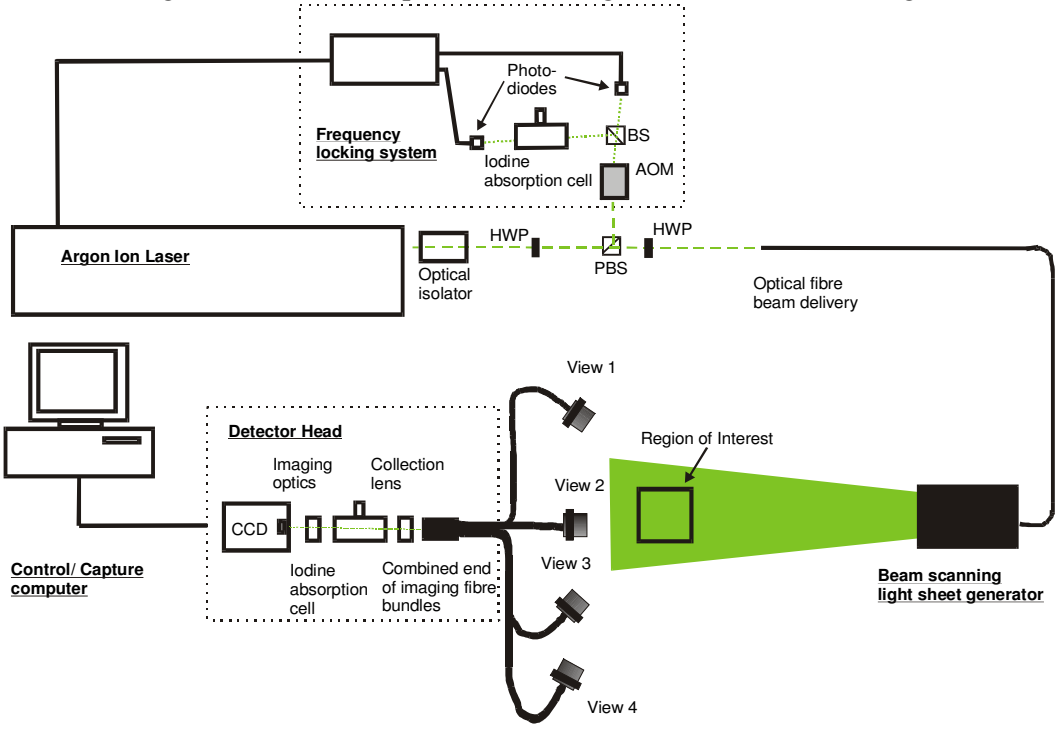

Figure 6-4 Schematic showing the experimental arrangement used for 3D velocity measurements.

As before the light source was a tuneable Argon-ion laser (Spectra Physics Beamlok 2060), incorporating a temperature-stabilized etalon to ensure single-mode operation at 514.5 nm. The output beam from the laser first passes through an optical isolator to prevent back reflections entering the laser cavity. The polarisation is then adjusted using the first half wave plate to set the intensity of light entering the frequency locking system, described in section 5.2.1. The second half wave plate is used to adjust the polarisation for coupling into optical fibre used to guide the light to the beam scanning light sheet generator. The fibre used to transport the beam to the light sheet generator; previously a few-mode fibre supplied by DLR, was replaced with high birefringent single-mode polarisation-maintaining fibre (York VSOP 2253-01F). This was in an attempt to avoid the issue of different mode propagation between the two frequency beams as noted in chapter 5.

The laser frequency was now selected by changing the optical path length of the intra-cavity etalon and then stabilized using the locking system[10]. The locking system (described in chapter 5) consists of an iodine cell, signal and reference photodiodes and locking electronics that adjusts the laser etalon temperature to ensure that the laser frequency is stable. The frequency of the locking beam was shifted using an acousto-optic modulator, so that the locking system can still operate when the laser frequency is tuned to 100% transmission. The locking beam was shifted onto the absorption line so that any frequency fluctuations will result in an associated transmission fluctuation seen by the photodiodes, which can then be corrected for. The acousto-optic modulator (AOM) used here was the 260MHz device described in section 5.2.2 (Isomet 1250C-829A). The locking system can also be used to determine the location of the laser frequency on the iodine absorption line by monitoring the photodiode voltages.

It should be noted that although this arrangement increased the illumination power the images would now be captured with a separation of minutes rather than seconds, due to the time taken to stabilise the laser frequency at each new position on the absorption line.

As well as providing increased beam powers, it is now possible to tune both illumination frequencies to coincide with either side of the absorption line allowing 2ν-PDV measurements to be made using the increased sensitivity approach, described in section 3.2.2. This was not possible using the combination of AOMs used in the single velocity component system, described in chapter 5, as a frequency separation of greater than 700MHz is required to span the absorption line, and this was not achievable with the AOMs available.

6.3 Processing required for 3D 2ν-PDV measurements

The processing required to calculate 3D velocity fields is a little more complicated than for a single velocity component as multiple velocity components must be calculated and then these must be converted to the orthogonal velocity components. Additionally it is now necessary to de-warp each view to a common field of view, to allow the calculation of these orthogonal velocity components.

The general processing scheme used for 3D velocity measurements is shown in Figure 6-5. Each of the four views defined by the imaging fibre bundle channels are split into separate images. It may also be necessary to horizontally flip views that are located on the opposite side of the light sheet so that all four appear to be viewed from the same side. These views are then de-warped to a common field of view. Next each view is processed individually, as in single velocity component measurements, yielding the four non-orthogonal measured velocity components. The final stage is to convert from non-orthogonal to orthogonal velocity components that are aligned with the experiment.

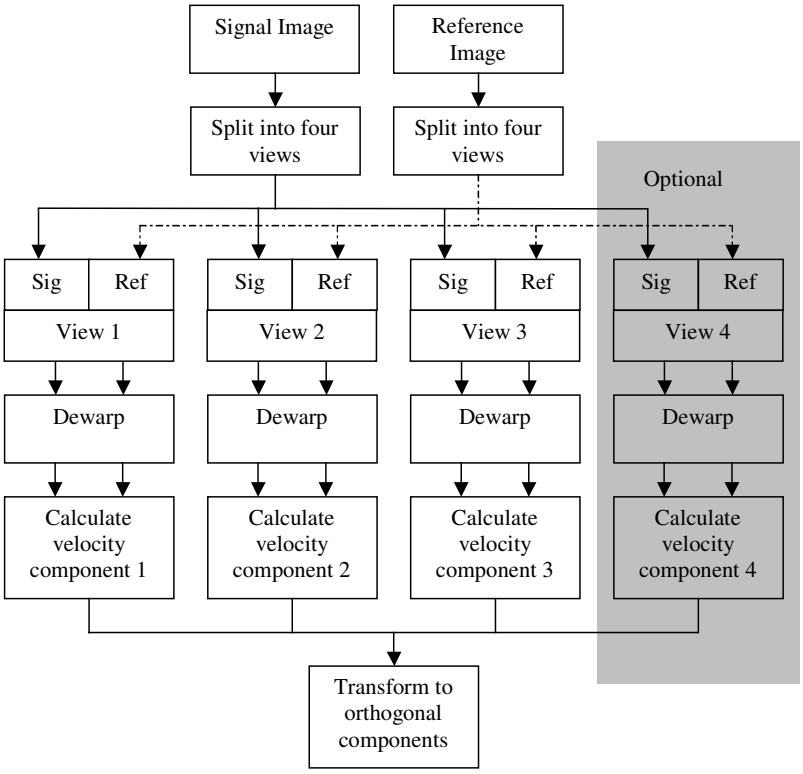

Figure 6-5 Flow diagram detailing the general processing scheme for a 3D PDV measurement.

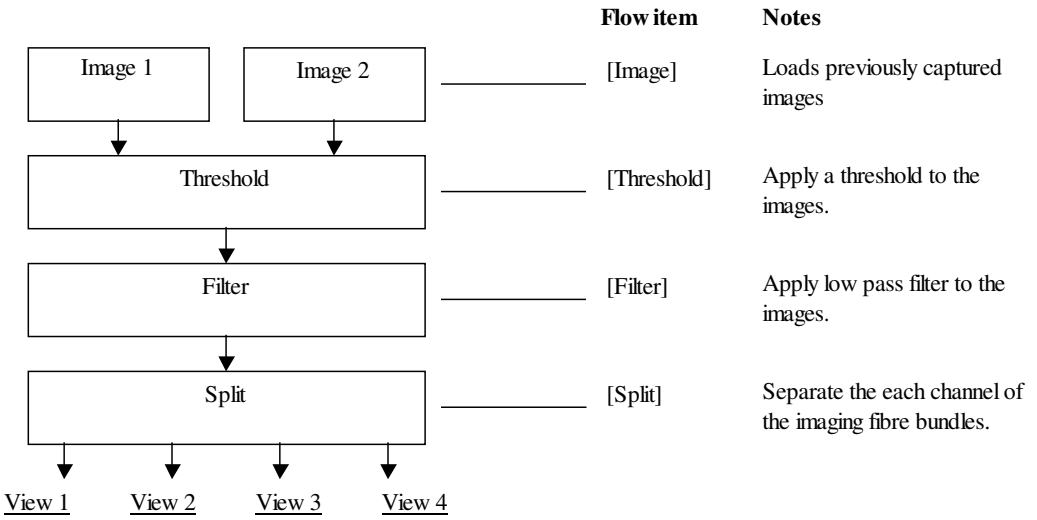

Figure 6-6 Flow diagram showing the common processing applied for both sensitivity schemes.

Using the modified system, described in section 6.2.3 it was possible to make measurements using both 2ν-PDV sensitivity schemes identified in chapter 3. Although the processing used in the calculation of the velocity components for each sensitivity scheme is different the initial processing applied is the same for each method. This is shown in Figure 6-6 along with the processing flow items used in the flow diagram processing software that was described in chapter 4. Initially the captured images are loaded, these have already had the background subtracted, which is performed at the image capture stage. The images then have a threshold applied to remove pixels with levels below, or above those that where considered reliable, for example to remove saturated pixels, outside the linear region of the CCD response, or those in which the signal level was too low to be reliable, typically <100 counts. Additionally a low-pass filter can be applied next to reduce high frequency noise, although for the results presented later this was not used.

6.3.1 Normal sensitivity 2ν-PDV

Figure 6-7 shows a flow diagram of the processing used in the calculation of each velocity component using the normal sensitivity 2ν-PDV method. Alongside are the relevant processing items used in the flow diagram processing system (described in chapter 4). The processing is similar to that described in chapter 5 for a single velocity component, with the notable difference being the use of the de-warping algorithm to calculate the observation direction[9] on a pixel-by-pixel basis and overlay the views to a common view.

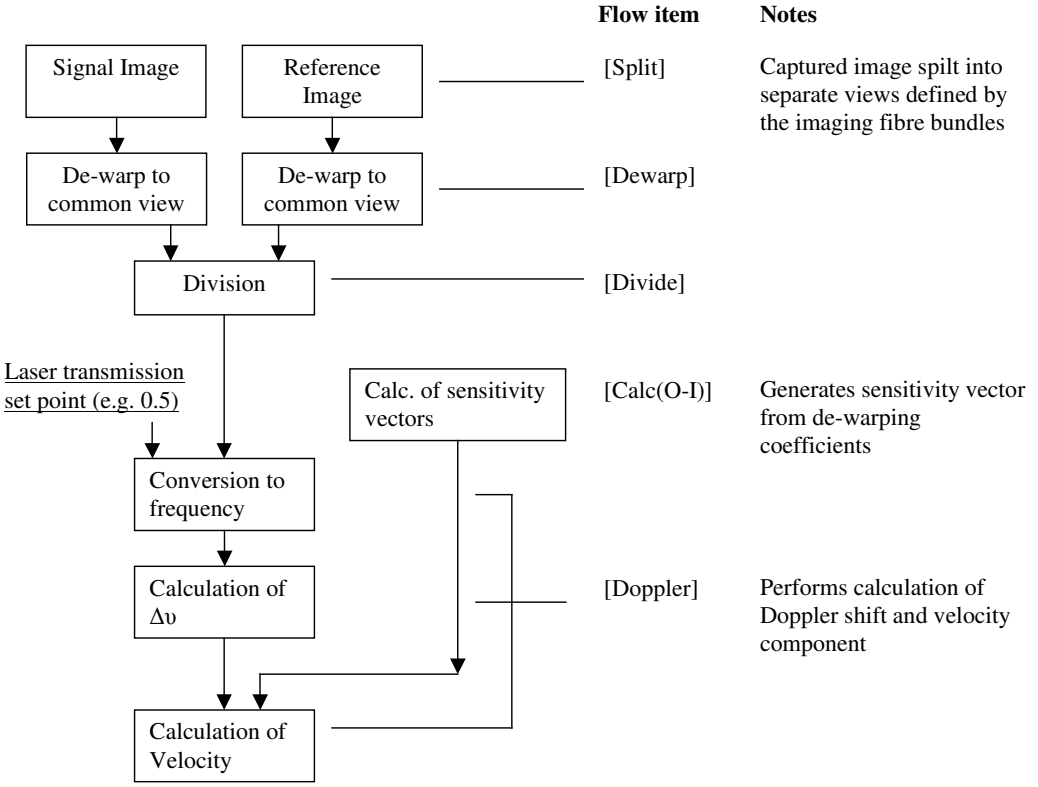

Figure 6-7 Flow diagram detailing the processing used in the calculation of each velocity component for the normal sensitivity 2ν-PDV scheme.

6.3.2 Increased sensitivity 2ν-PDV

As discussed in chapter 3 there are two approaches to the processing of increased sensitivity method measurements. The first uses the approximation that each side of the iodine absorption line used is linear, or at least the region used is linear. With this assumption it is then possible to calculate a normalised transmission image using equations 3-4 and 3-5. Figure 6-8 shows a flow diagram of the processing used in the calculation of each velocity component using the increased sensitivity 2ν-PDV method using this linear approximation. As before the relevant processing items used in the flow diagram processing system are shown alongside. Once this normalised transmission image has been found the processing is the same as for the normal sensitivity method described above.

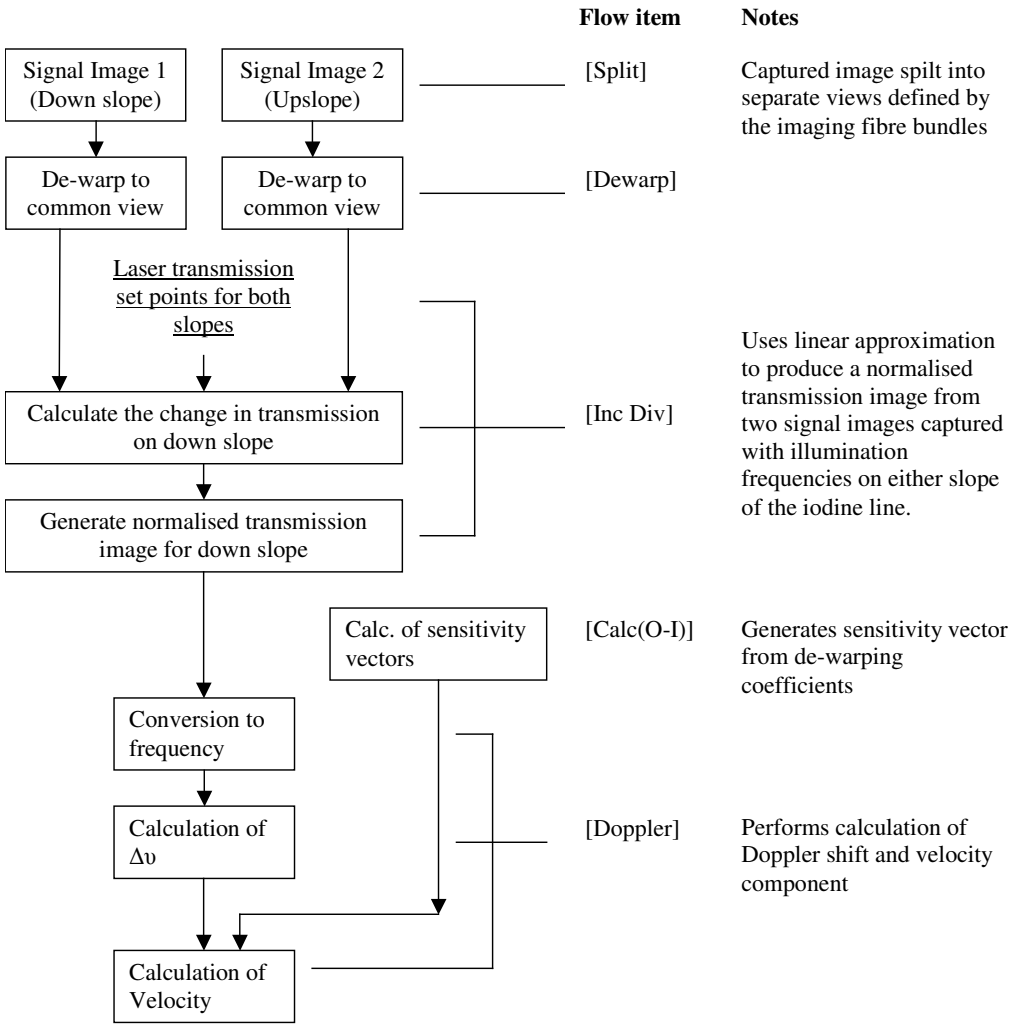

Figure 6-8 Flow diagram detailing the processing used in the calculation of each velocity component for the increased sensitivity 2ν-PDV scheme, using the linear approximation.

The second method involves the use of a look-up table to directly compare values of the ratio of the intensities in each image with those for a known Doppler shift. The processing using this method is shown in Figure 6-9. In both methods the de-warping was again used to calculate the observation directions[9].

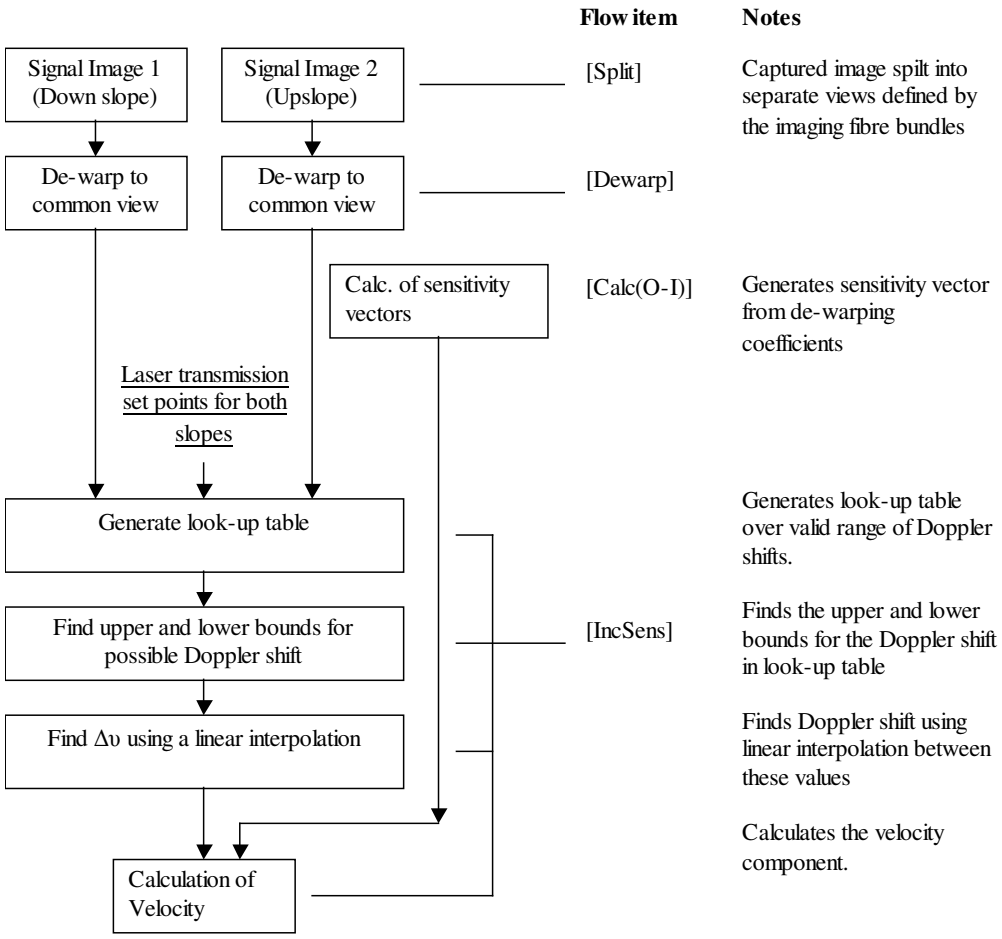

Figure 6-9 Flow diagram detailing the processing used in the calculation of each velocity component for the increased sensitivity 2ν-PDV scheme, using a look-up table.

6.3.3 Conversion to orthogonal velocity components

Once the measured velocity components have been calculated they must be converted to an orthogonal co-ordinate system. This is performed using one of three methods described in chapter 4. Three velocity components can be transformed to the orthogonal components U,V and W (3C method, section 4.10.1) alternatively all four can be used with or without weighting the components (4C and 4Cw method, section 4.10.2). This is done using the processing item [Calc3D].

6.4 3D Velocity measurements on a rotating disc

As with the single velocity component measurements a rotating disc was used to provide a well-defined velocity field with which to characterise the performance of the system. The disc was 200mm in diameter, although the common field-of-view of each observation direction after de-warping was an approximate disc 100mm in diameter. The rotation of the disc was measured using an optical tachometer giving a maximum velocity in the field of view of ~±34ms^{-1}.

6.4.1 Experimental arrangement

Two different viewing configurations were used to make measurements on the rotating disc; these are shown in Figure 6-11 with the viewing angles (defined in Figure 6-10) shown in Table 6-1. The light sheet was propagating in the positive X direction with the four channels viewing the face of the disc as indicated. All four views were located on the same side of the light sheet as only one face of the disc can be illuminated.

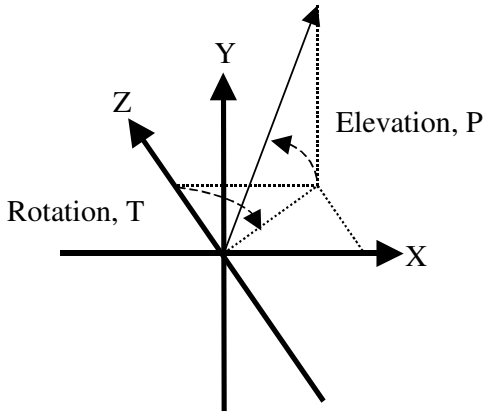

Figure 6-10 Definitions of viewing angles used to describe experimental viewing geometries. Rotation, T (0-360^o) and elevation, P (±90^o)

Table 6-1 Definitions of viewing angles used for measurements on a rotating disc.

Configuration	View Angles (^{o})	1	2	3	4
A	T	180	180	-135	167.7
	P	20.75	-20.75	0	0
B	T	135	135	-135	144
	P	21.9	-21.9	0	0

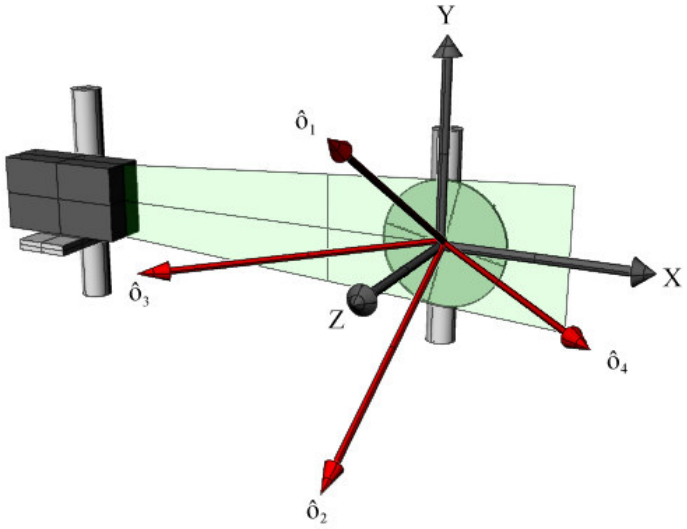

Configuration A

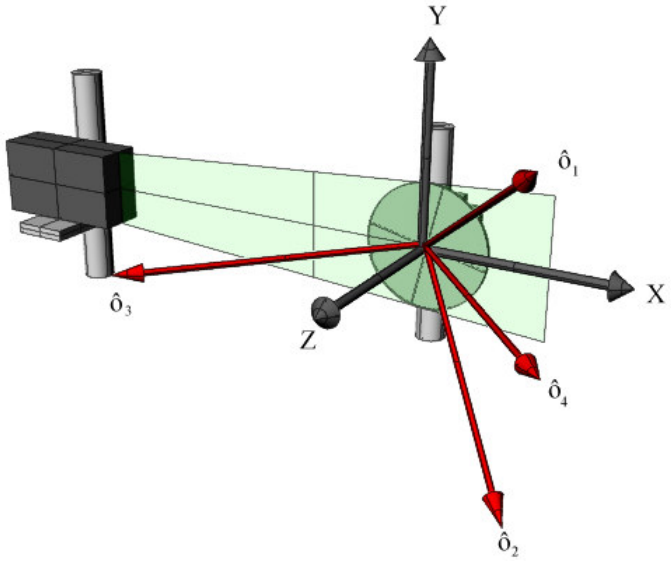

Configuration B

Figure 6-11 Diagram showing the viewing geometry used when making measurements on the rotating disc. $\hat{o}_1$, $\hat{o}_2$, $\hat{o}_3$ and $\hat{o}_4$ are the observation directions for each arm of the imaging fibre bundles.

6.4.2 Results – comparison between the normal and increased sensitivity 2ν-PDV methods.

Images were captured under illumination at three different frequencies located at 100% transmission, ~50% transmission on the falling slope of the iodine absorption line and at ~50% on the rising slope. The optical power at the output of the fibre was ~100mW and the CCD camera integration time was five seconds. This led to pixel intensity counts in the region of 1500-3500 counts depending upon observation direction. The use of single mode fibre to deliver the beam to the light sheet forming optics avoided the differences seen previously in the light sheets for the different frequencies when illuminating the face of the disc. This meant that there was no need to apply the white card correction necessary in chapter 5.

The processed measured (non-orthogonal) velocity components for each observation direction are shown in Figure 6-13 to Figure 6-16 for viewing configuration A and Figure 6-17 to Figure 6-20 for viewing configuration B. Parts (a), (b) and (c) in these figures show the computed velocity component for each method described in section 6.3, normal sensitivity, increased sensitivity (linear approximation) and increased sensitivity (look-up table) respectively.

In order to assess the benefit of the increased sensitivity scheme, a theoretical velocity component was generated, for all points on the wheel, for each view. At each point this was subtracted from the calculated component and a histogram of this variation over the image was plotted. This process is shown in Figure 6-12(a). Part (d) shows this histogram of the remaining error, when the theoretical velocity component is subtracted from the calculated velocity component.

From the velocity field shown in parts (a), (b) and (c) it can be seen that the velocity components calculated using the increased sensitivity schemes are visibly less noisy than those captured using the normal sensitivity scheme. This is confirmed when looking at the histograms, in part (d) of the figures, where the error distribution is significantly narrower. The standard deviations for each of these plots are shown in Table 6-2 (configuration A) and Table 6-3 (configuration B). It can be seen that there is approximately a 30 to 40% reduction in the level of error when using the increased sensitivity scheme over the normal sensitivity scheme.

The two methods of processing the increased sensitivity scheme data generally produce much the same results as would be expected if the linear approximation were true. There are slight differences between the error levels observed for the two methods, for several computed velocity components, e.g. configuration A, view 3 and configuration B, views 3 and 4. There are several possible explanations for this; the first is due to the way in which the look-up table is calculated. As several polynomials are used to convert from frequency to transmission and vice versa an error is introduced into the calculation. For example if the same polynomials were used to first find the frequency for a value of transmission of say 50% and this frequency was then converted back to a transmission value, the answer would not be exactly 50%. This would mean that the look-up table calculated would not be precise leading to errors in the calculated velocity component. This could potentially be avoided by using an alternative method of

calculating the look-up table, for example by directly calculating these values from the measured absorption profile of the iodine cell. The other possible explanation is that the linear approximation used in the first method was sufficiently not true, this may be the case for view 3 in both configurations. This view has larger expected Doppler shifts so the section of the iodine cell absorption line used may have exceeded the linear portion.

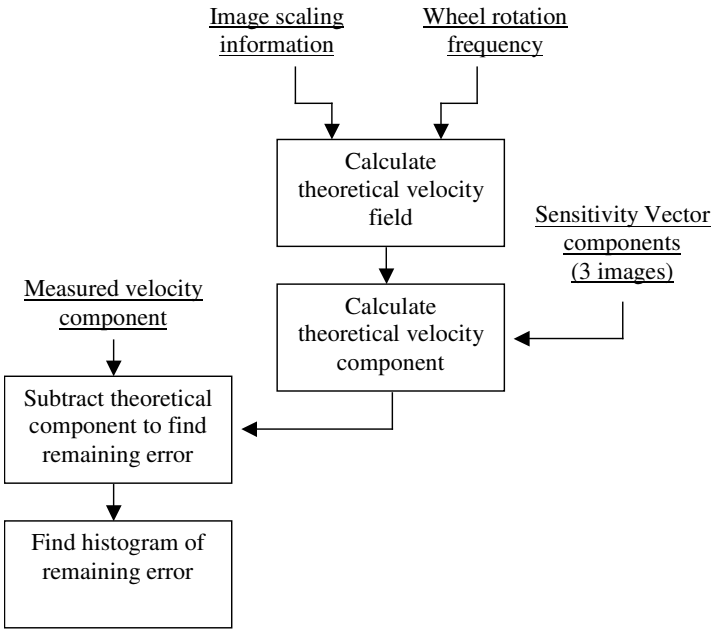

(a)

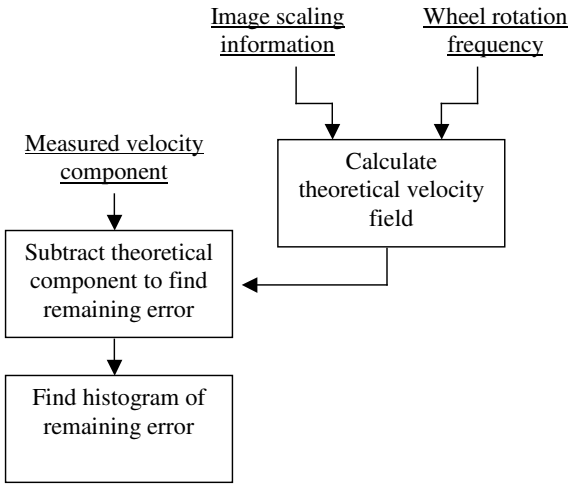

(b)

Figure 6-12 Process used to calculate the error in experimental measurements on a rotating disc for; (a) a measured (non-orthogonal) velocity component and (b) a measured orthogonal velocity component.

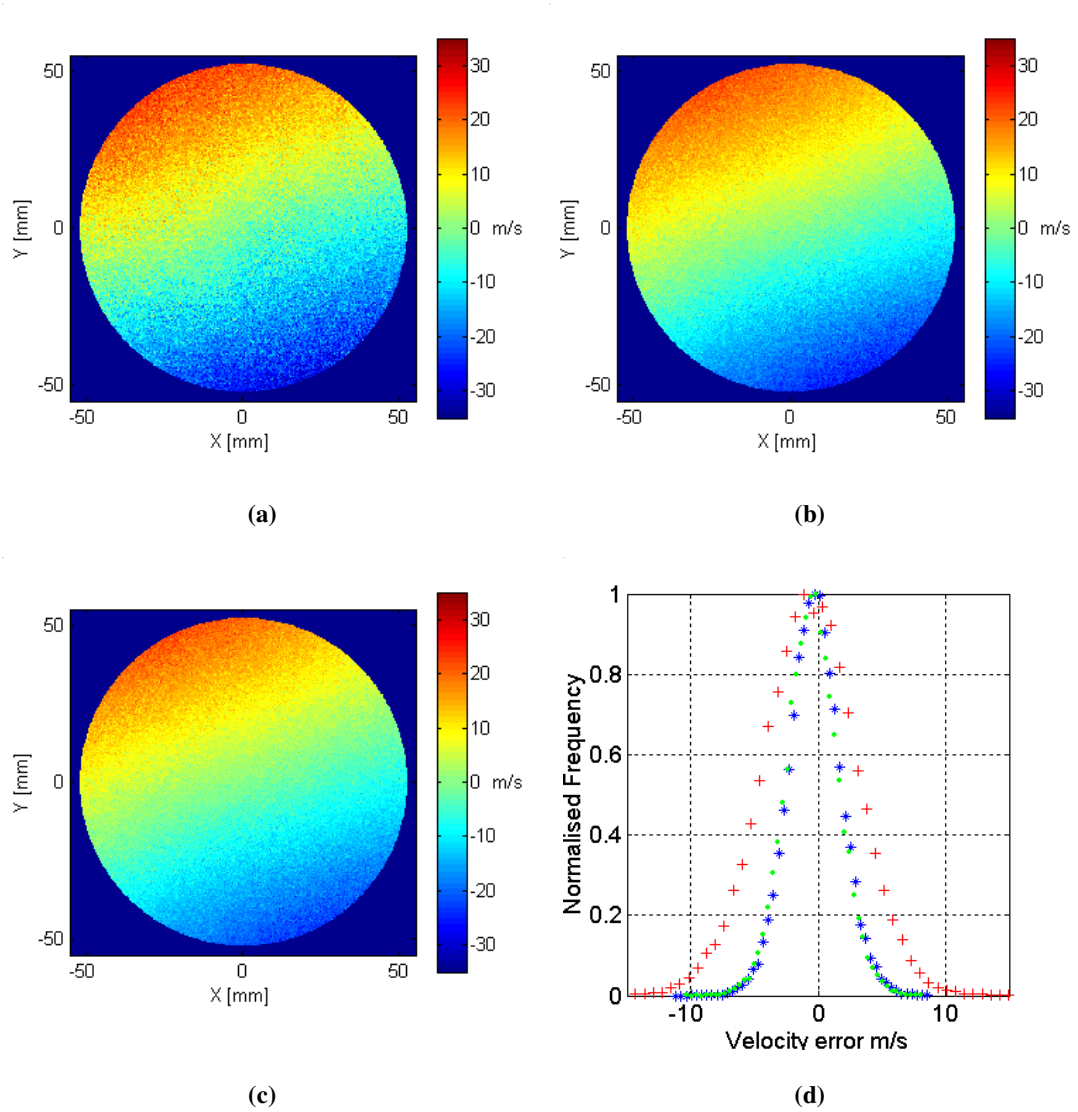

Figure 6-13 Computed measured velocity component for configuration A, view 1 calculated using

(a) Normal sensitivity 2ν-PDV method; (b) Increased sensitivity 2ν-PDV (linear approximation) method; (c) Increased sensitivity 2ν-PDV (look-up table) method. (d) Histogram of the error residual (difference between calculated and theoretical velocity component) where:

+Normal sensitivity 2ν-PDV technique;

***Increased sensitivity 2ν-PDV technique (linear approximation);**

·Increased sensitivity 2ν-PDV (look-up table)

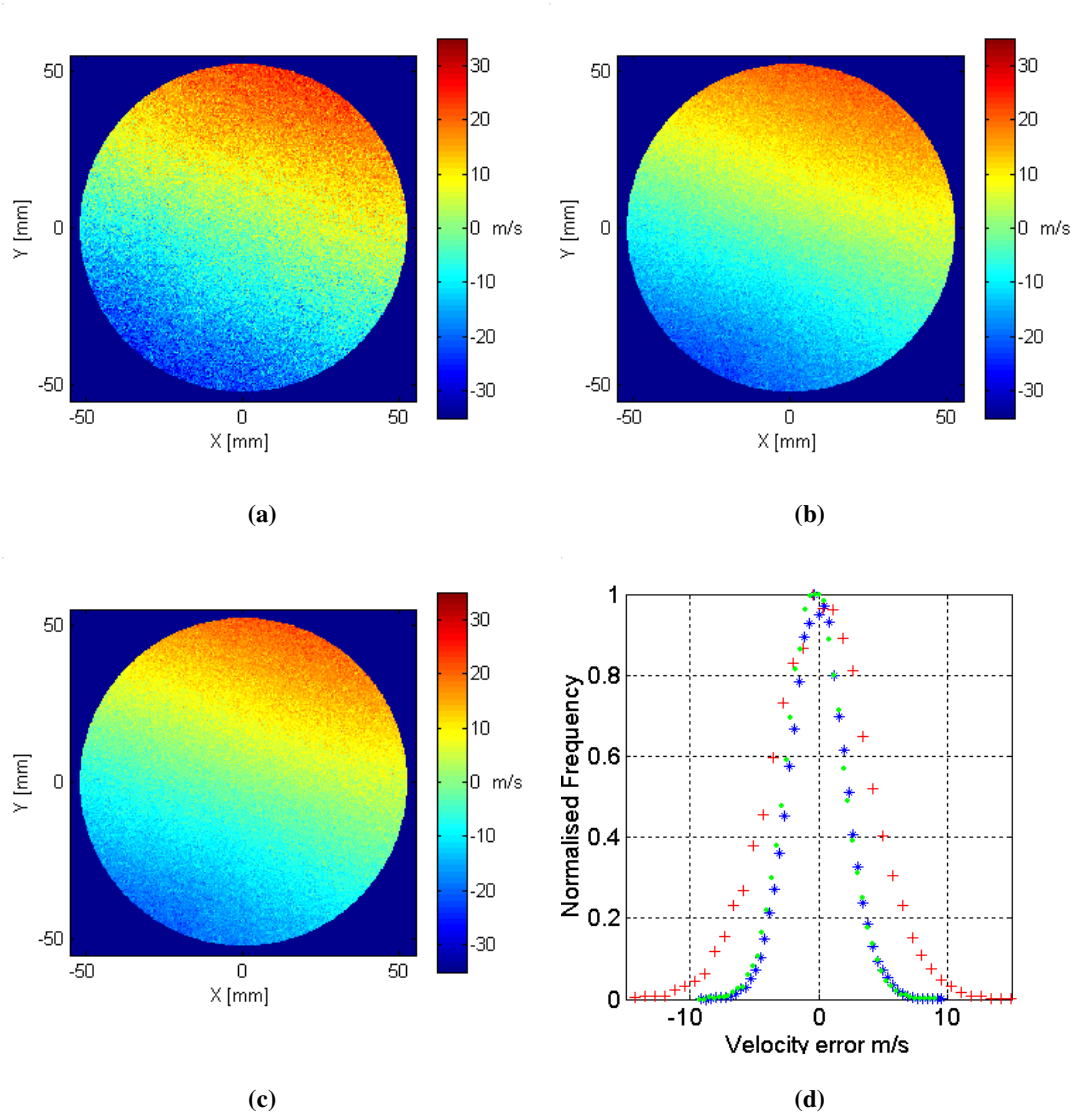

Figure 6-14 Computed measured velocity component for configuration A, view 2 calculated using

(a) Normal sensitivity 2ν-PDV method; (b) Increased sensitivity 2ν-PDV (linear approximation) method; (c) Increased sensitivity 2ν-PDV (look-up table) method. (d) Histogram of the error residual (difference between calculated and theoretical velocity component) where:

+Normal sensitivity 2ν-PDV technique;

***Increased sensitivity 2ν-PDV technique (linear approximation);**

·Increased sensitivity 2ν-PDV (look-up table)

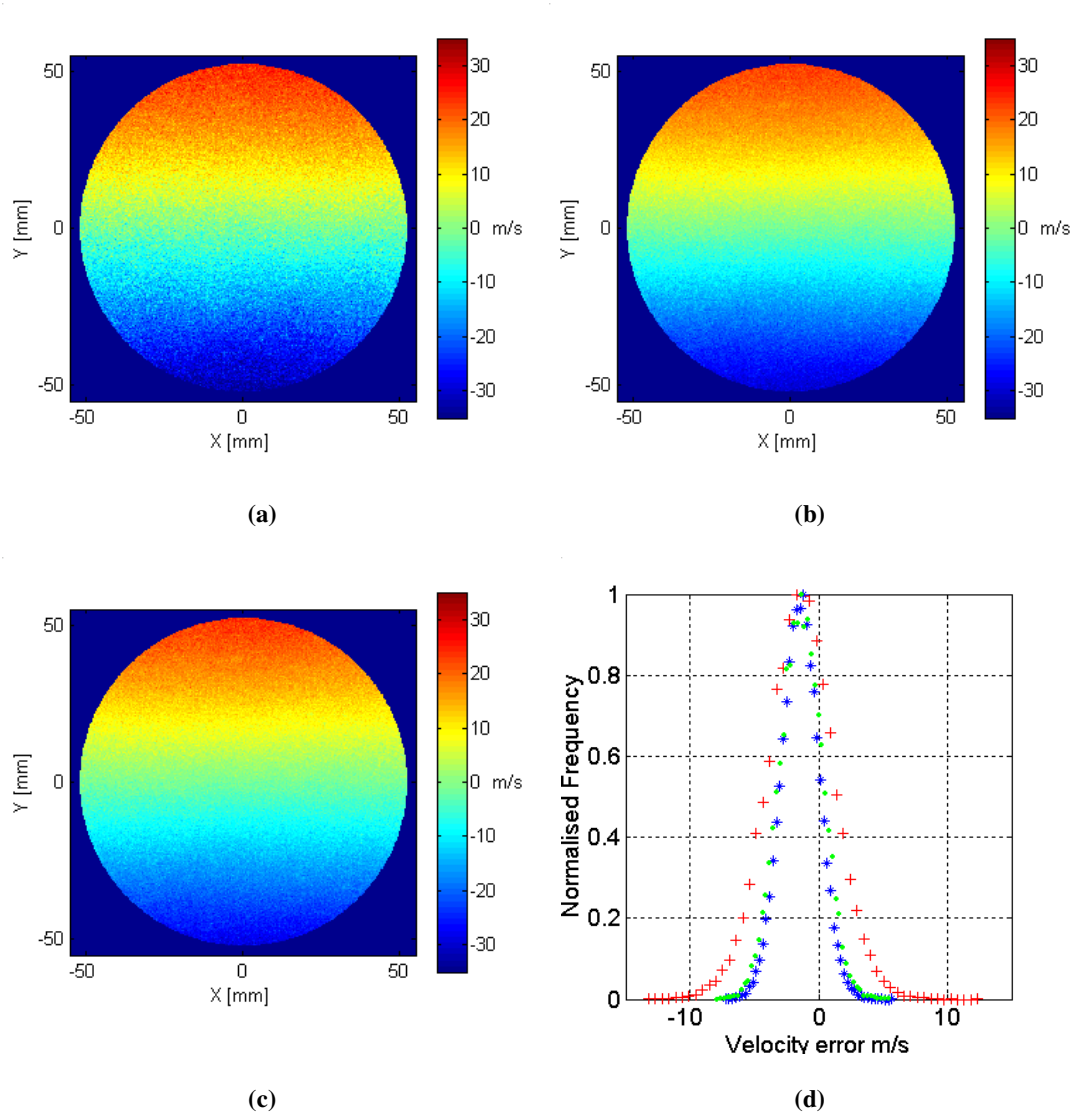

Figure 6-15 Computed measured velocity component for configuration A, view 3 calculated using

(a) Normal sensitivity 2ν-PDV method; (b) Increased sensitivity 2ν-PDV (linear approximation) method; (c) Increased sensitivity 2ν-PDV (look-up table) method. (d) Histogram of the error residual (difference between calculated and theoretical velocity component) where:

+Normal sensitivity 2ν-PDV technique;

***Increased sensitivity 2ν-PDV technique (linear approximation);**

·Increased sensitivity 2ν-PDV (look-up table)

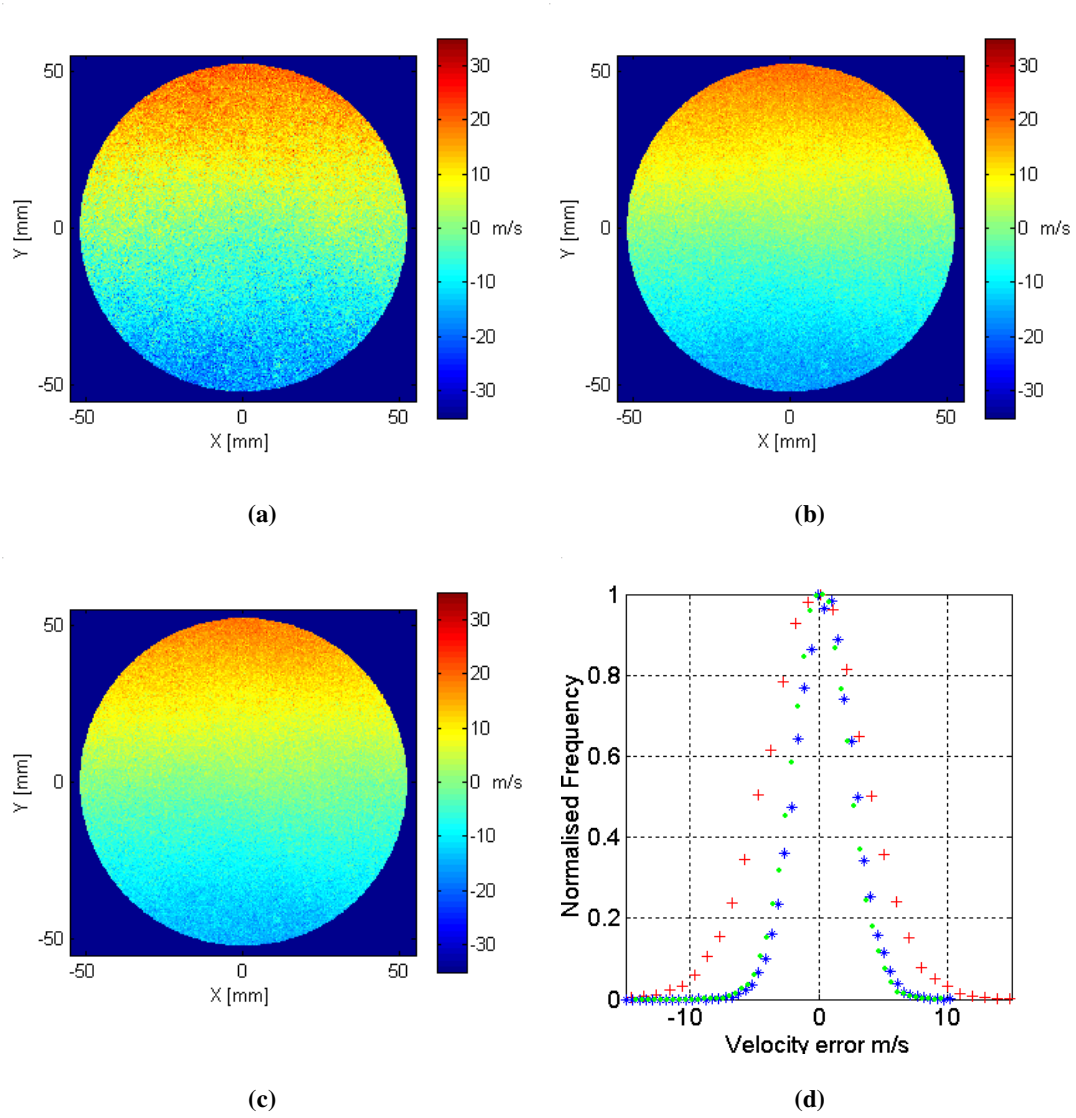

Figure 6-16 Computed measured velocity component for configuration A, view 4 calculated using

(a) Normal sensitivity 2ν-PDV method; (b) Increased sensitivity 2ν-PDV (linear approximation) method; (c) Increased sensitivity 2ν-PDV (look-up table) method. (d) Histogram of the error residual (difference between calculated and theoretical velocity component) where:

+Normal sensitivity 2ν-PDV technique;

***Increased sensitivity 2ν-PDV technique (linear approximation);**

·Increased sensitivity 2ν-PDV (look-up table)

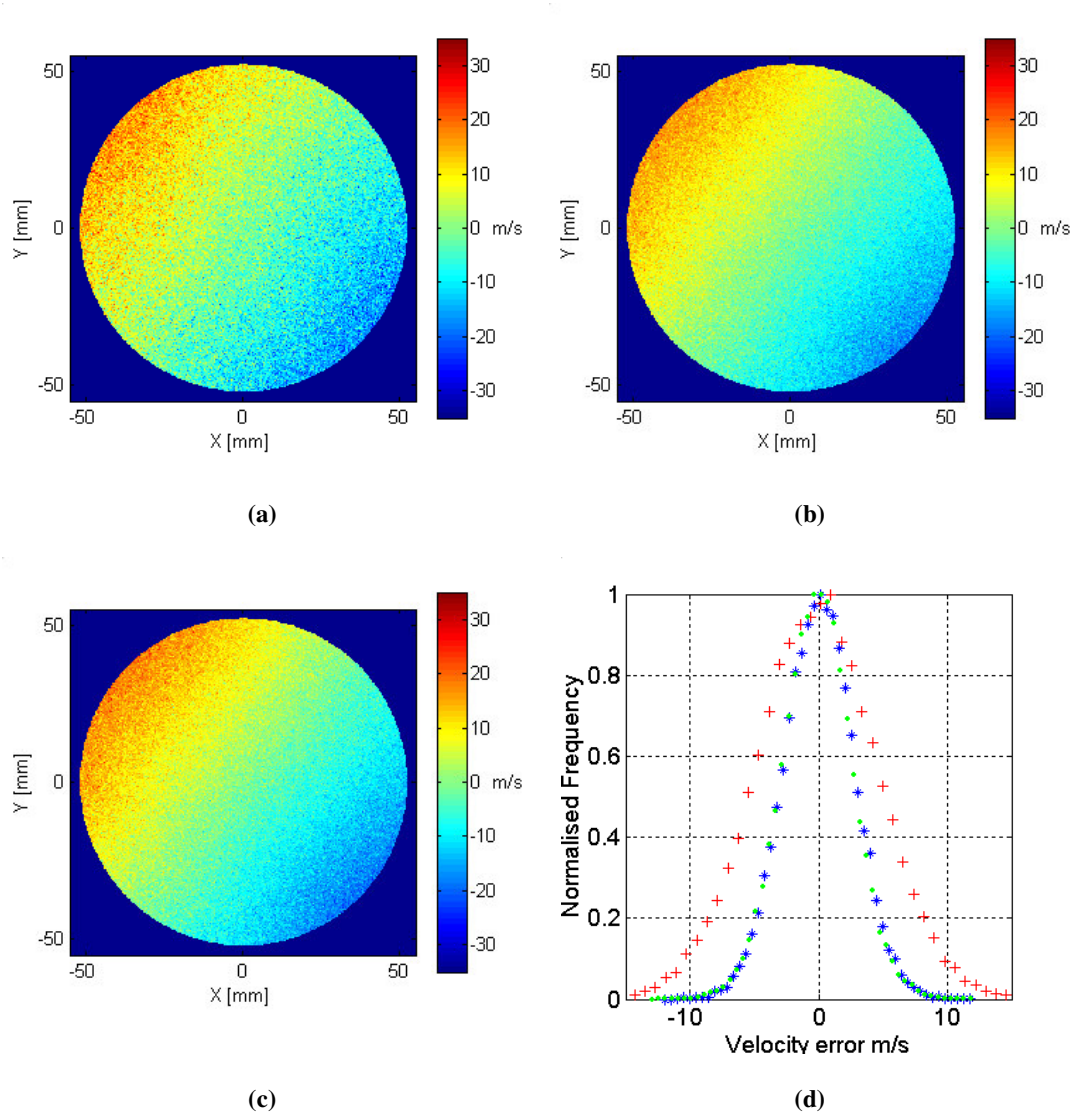

Figure 6-17 Computed measured velocity component for configuration B, view 1 calculated using

(a) Normal sensitivity 2ν-PDV method; (b) Increased sensitivity 2ν-PDV (linear approximation) method; (c) Increased sensitivity 2ν-PDV (look-up table) method. (d) Histogram of the error residual (difference between calculated and theoretical velocity component) where:

+Normal sensitivity 2ν-PDV technique;

***Increased sensitivity 2ν-PDV technique (linear approximation);**

·Increased sensitivity 2ν-PDV (look-up table)

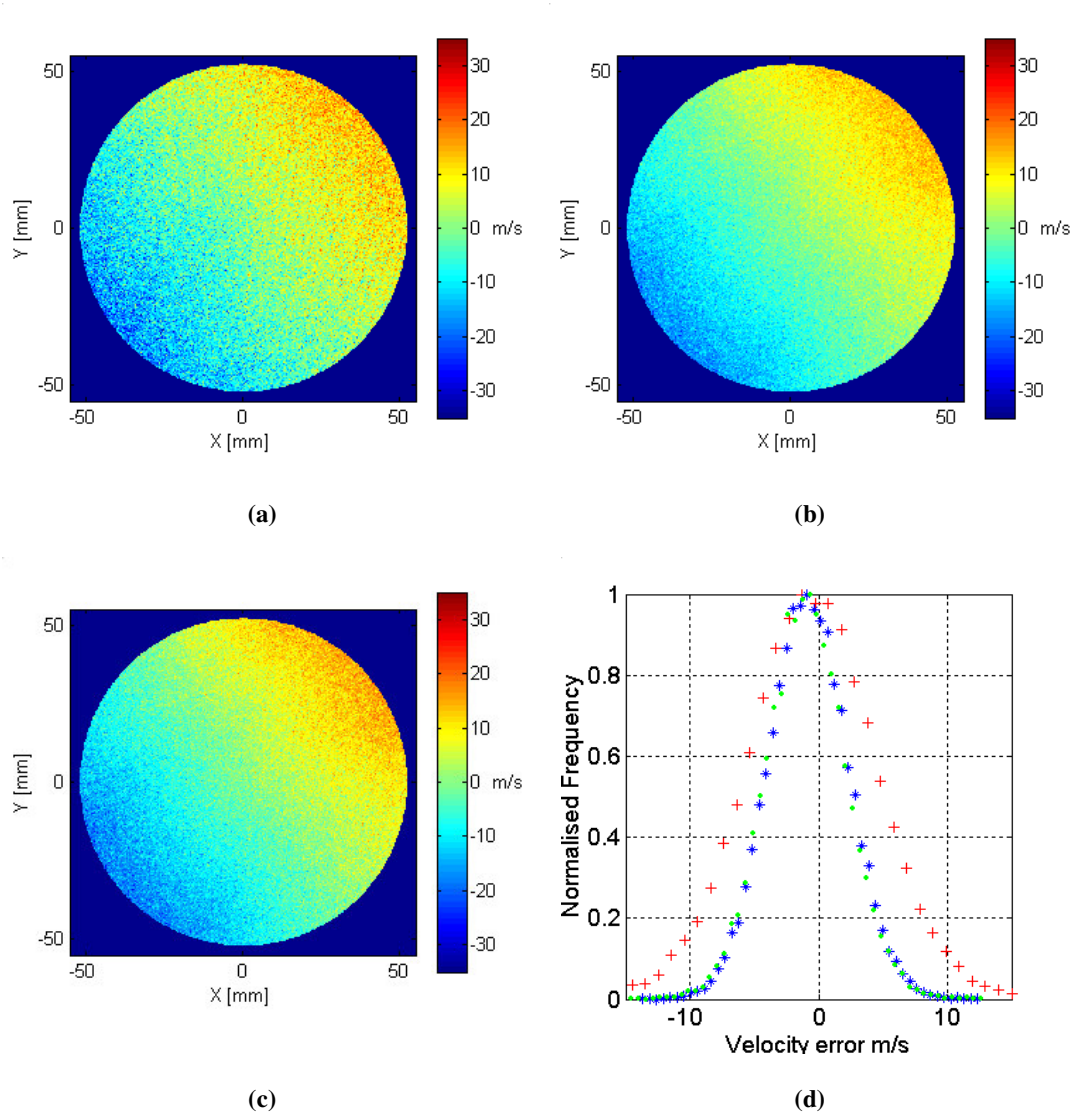

Figure 6-18 Computed measured velocity component for configuration B, view 2 calculated using

(a) Normal sensitivity 2ν-PDV method; (b) Increased sensitivity 2ν-PDV (linear approximation) method; (c) Increased sensitivity 2ν-PDV (look-up table) method. (d) Histogram of the error residual (difference between calculated and theoretical velocity component) where:

+Normal sensitivity 2ν-PDV technique;

***Increased sensitivity 2ν-PDV technique (linear approximation);**

·Increased sensitivity 2ν-PDV (look-up table)

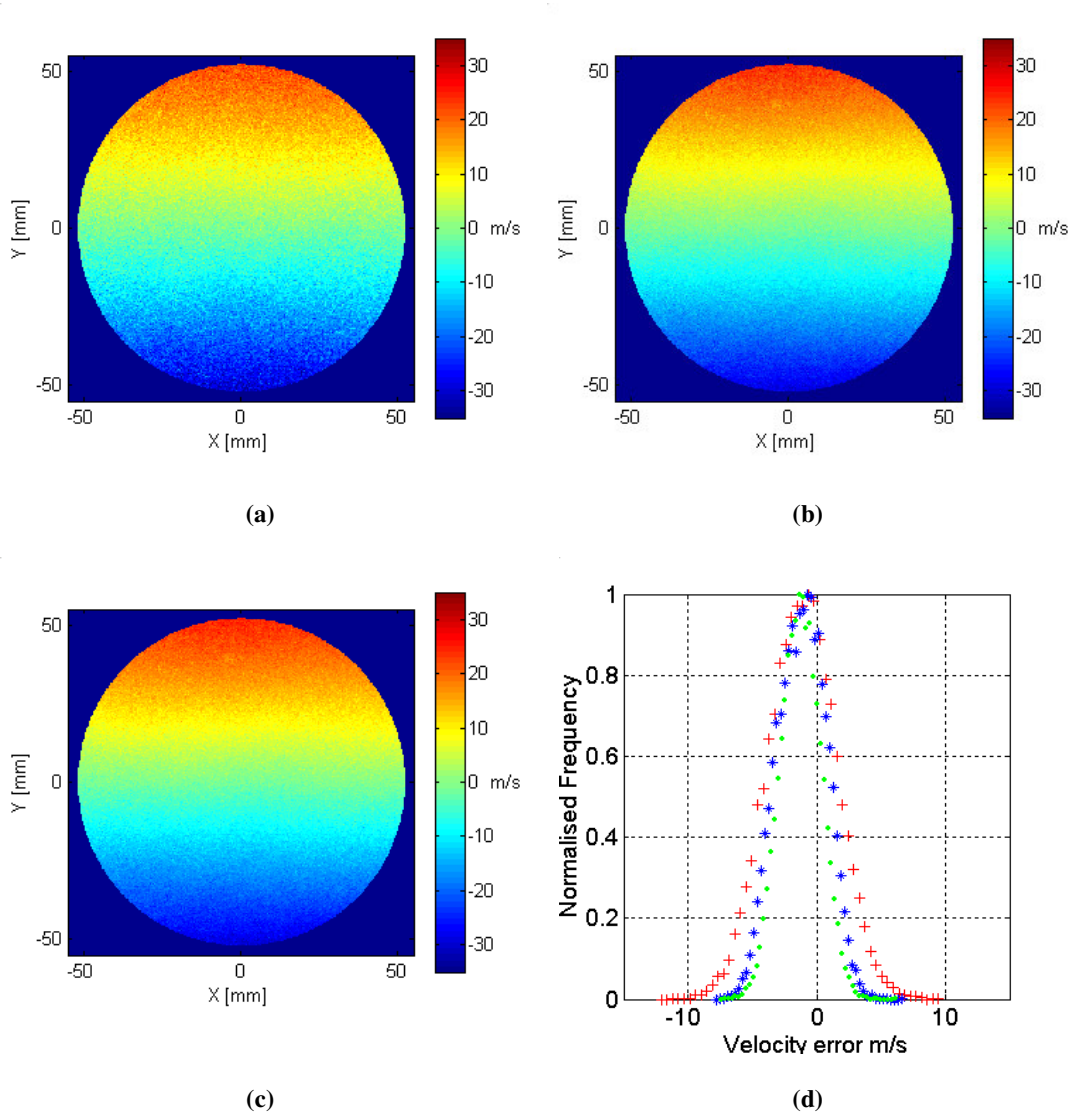

Figure 6-19 Computed measured velocity component for configuration B, view 3 calculated using

(a) Normal sensitivity 2ν-PDV method; (b) Increased sensitivity 2ν-PDV (linear approximation) method; (c) Increased sensitivity 2ν-PDV (look-up table) method. (d) Histogram of the error residual (difference between calculated and theoretical velocity component) where:

+Normal sensitivity 2ν-PDV technique;

***Increased sensitivity 2ν-PDV technique (linear approximation);**

·Increased sensitivity 2ν-PDV (look-up table)

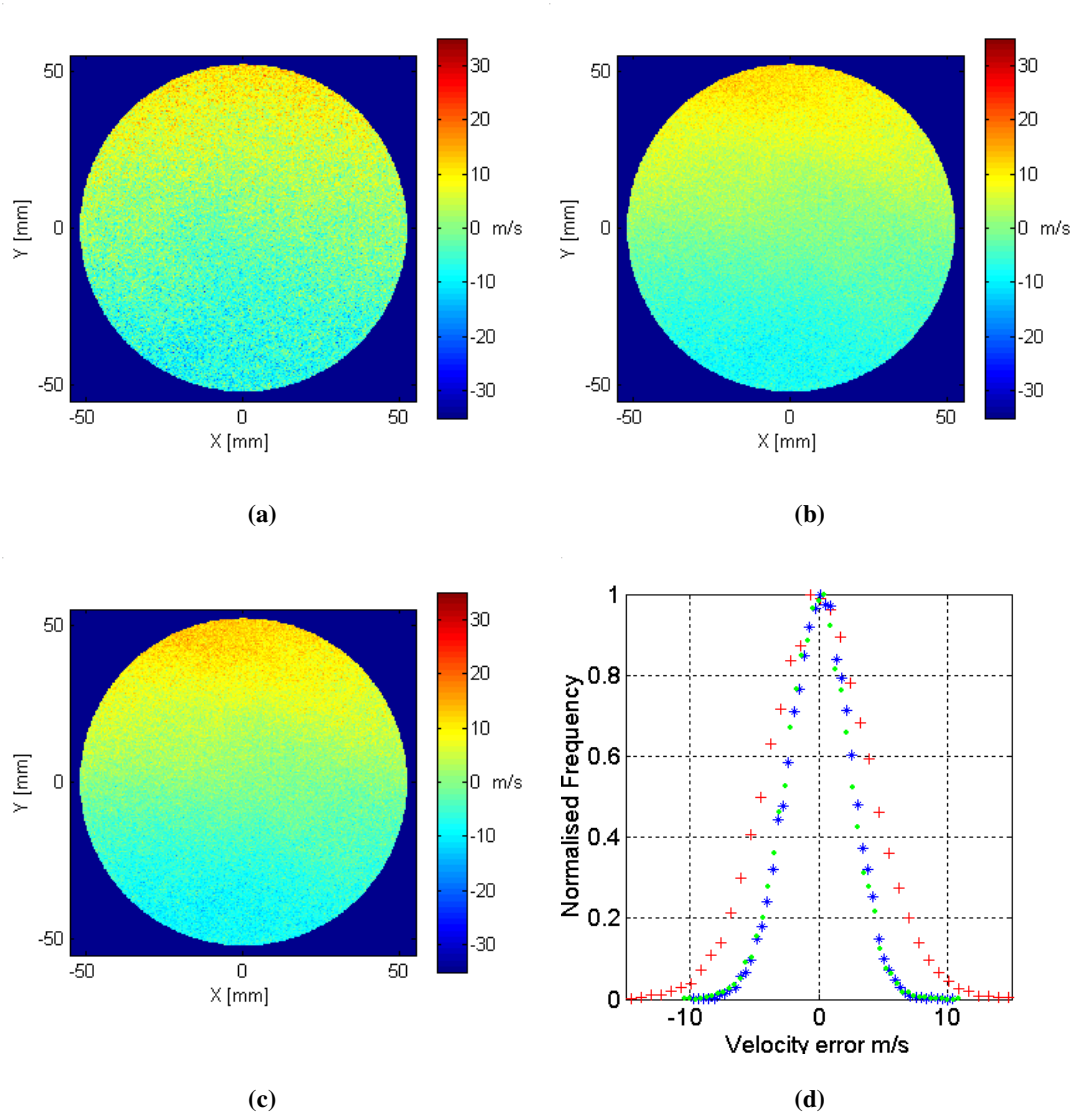

Figure 6-20 Computed measured velocity component for configuration B, view 4 calculated using

(a) Normal sensitivity 2ν-PDV method; (b) Increased sensitivity 2ν-PDV (linear approximation) method; (c) Increased sensitivity 2ν-PDV (look-up table) method. (d) Histogram of the error residual (difference between calculated and theoretical velocity component) where:

+Normal sensitivity 2ν-PDV technique;

***Increased sensitivity 2ν-PDV technique (linear approximation);**

·Increased sensitivity 2ν-PDV (look-up table)

Table 6-2 Standard deviations of the variation between the measured and theoretical velocity components (configuration A), and the calculated reduction in error when using the increased sensitivity scheme.

Standard deviation	View 1	View 2	View 3	View 4
Normal sensitivity	3.7 ms^{-1}	3.9 ms^{-1}	2.6 ms^{-1}	3.9 ms^{-1}
Increased sensitivity (Linear approximation)	2.1 ms^{-1}	2.2 ms^{-1}	1.5 ms^{-1}	2.2 ms^{-1}
% Reduction over normal sensitivity	43.2%	43.6%	42.3%	43.6%
Increased sensitivity (Look-up table)	2.1 ms^{-1}	2.2 ms^{-1}	1.7 ms^{-1}	2.2 ms^{-1}
% Reduction over normal sensitivity	43.2%	43.6%	34.6%	43.6%

Table 6-3 Standard deviations of the variation between the measured and theoretical velocity components (configuration B), and the calculated reduction in error when using the increased sensitivity scheme.

Standard deviation	View 1	View 2	View 3	View 4
Normal sensitivity	4.8 ms^{-1}	5.1 ms^{-1}	2.7 ms^{-1}	4.0 ms^{-1}
Increased sensitivity (Linear approximation)	2.7 ms^{-1}	3.1 ms^{-1}	1.9 ms^{-1}	2.4 ms^{-1}
% Reduction over normal sensitivity	43.8%	39.2%	29.6%	40.0%
Increased sensitivity (Look-up table)	2.7 ms^{-1}	3.1 ms^{-1}	1.6 ms^{-1}	2.5 ms^{-1}
% Reduction over normal sensitivity	43.8%	39.2%	40.7%	37.5%

The measured velocity components are then converted to the orthogonal velocity components U, V and W, representing the vertical, horizontal and out-of-plane components. Figure 6-21, Figure 6-22 and Figure 6-23 show a comparison between the sensitivity schemes for the orthogonal velocity components, U, V and W respectively, for configuration A. Likewise Figure 6-24, Figure 6-25 and Figure 6-26 show the same for configuration B. The improved sensitivity can also be seen in these calculated orthogonal components, shown in parts (a), (b) and (c), with the increased sensitivity results again being visibly smoother.

The calculated orthogonal components were compared, using the process shown in Figure 6-12(b), with the theoretical orthogonal velocity components for the rotating disc and histograms made of this variation. These are shown as part (d) in Figure 6-21 to Figure 6-26. Again the increased sensitivity schemes can be seen to make a considerable improvement in the level of error. The standard deviations of the error are shown in Table 6-4 (configuration A) and Table 6-5 (configuration B), are typically 40 to 50% smaller for the increased sensitivity scheme compared with the normal sensitivity scheme. This would be expected from the improvement in the measured velocity components although this is a larger reduction than for the individual measured components, the method for assessing errors for a measured component is less certain than for the orthogonal components. This is because when calculating the non-orthogonal theoretical components an assumption as to the view location has to be made, the calculation of the orthogonal theoretical components however is simpler and does not depend upon the view locations. It is therefore possible that the errors on individual measured velocity components have been calculated by comparison with an incorrect theoretical component.

As before slight differences in the error level exist between the results of the two increased sensitivity methods, with the look-up table appearing to produce marginally better results suggesting that the system may have been operating outside of the linear portion of the two slopes.

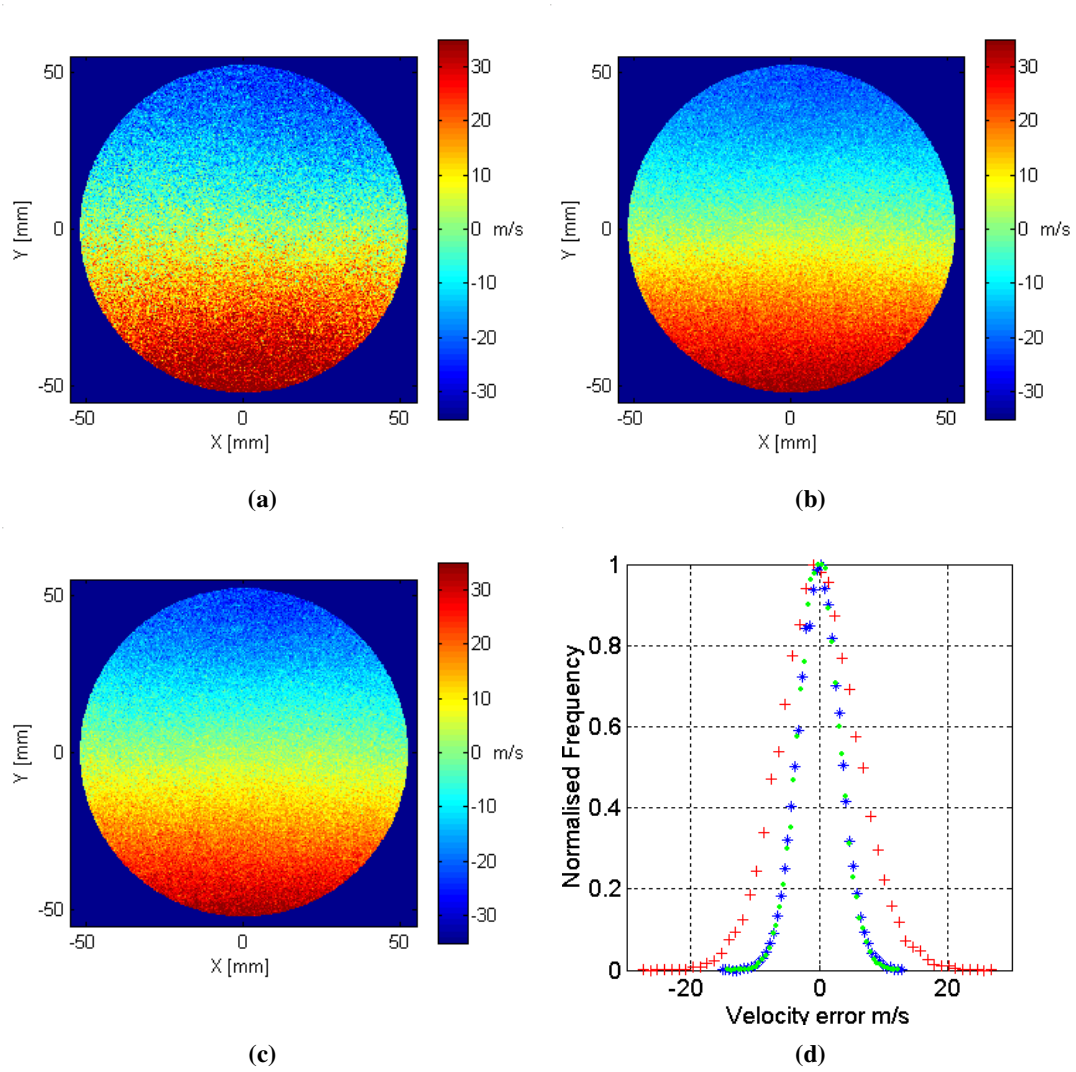

Figure 6-21 Computed U (horizontal) velocity components for configuration A calculated using:

(a) Normal sensitivity 2ν-PDV method; (b) Increased sensitivity 2ν-PDV (linear approximation) method; (c) Increased sensitivity 2ν-PDV (look-up table) method. (d) Histogram of the error residual (difference between calculated and theoretical velocity component) where:

+Normal sensitivity 2ν-PDV technique;

***Increased sensitivity 2ν-PDV technique (linear approximation);**

·Increased sensitivity 2ν-PDV (look-up table)

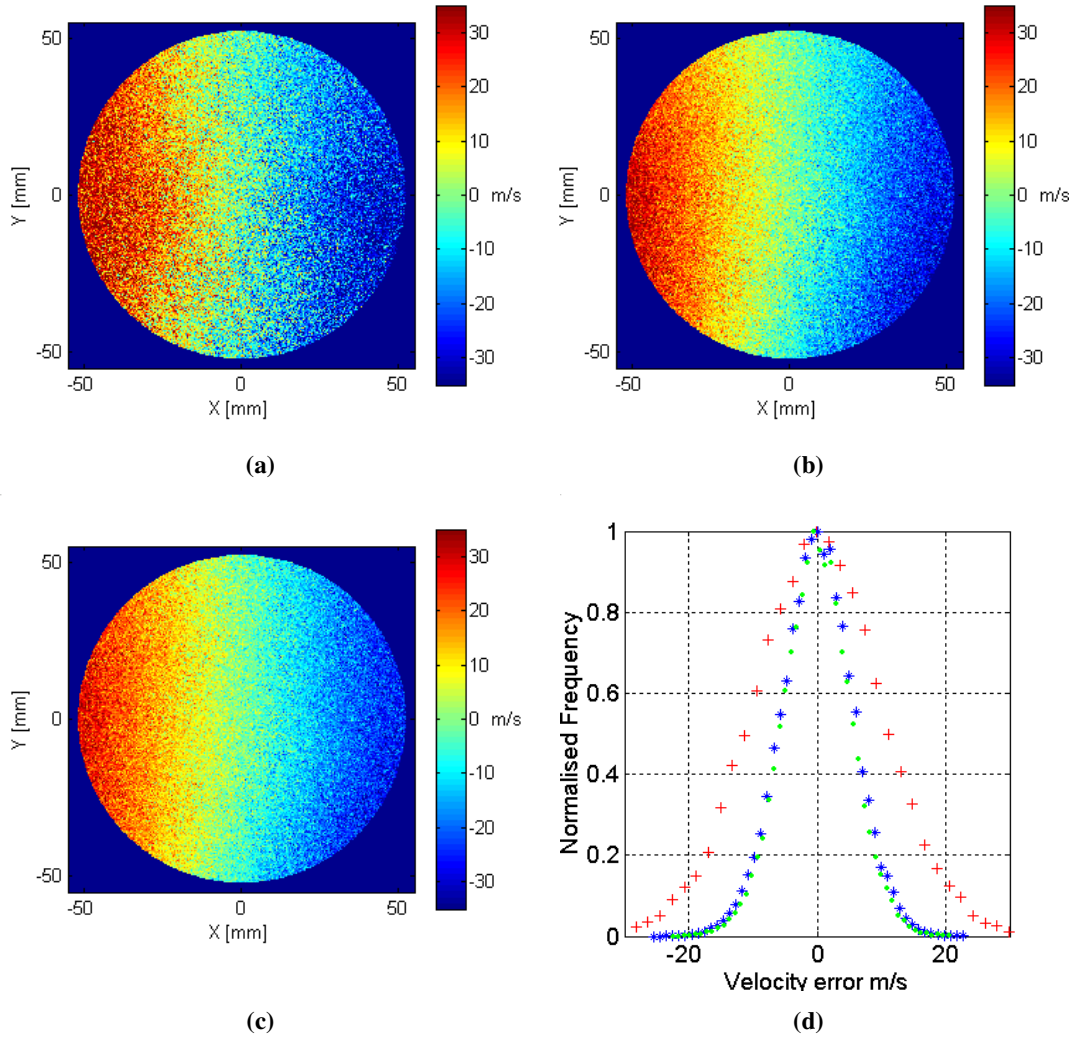

Figure 6-22 Computed V (vertical) velocity components for configuration A calculated using:

(a) Normal sensitivity 2ν-PDV method; (b) Increased sensitivity 2ν-PDV (linear approximation) method; (c) Increased sensitivity 2ν-PDV (look-up table) method. (d) Histogram of the error residual (difference between calculated and theoretical velocity component) where:

+Normal sensitivity 2ν-PDV technique;

***Increased sensitivity 2ν-PDV technique (linear approximation);**

·Increased sensitivity 2ν-PDV (look-up table)

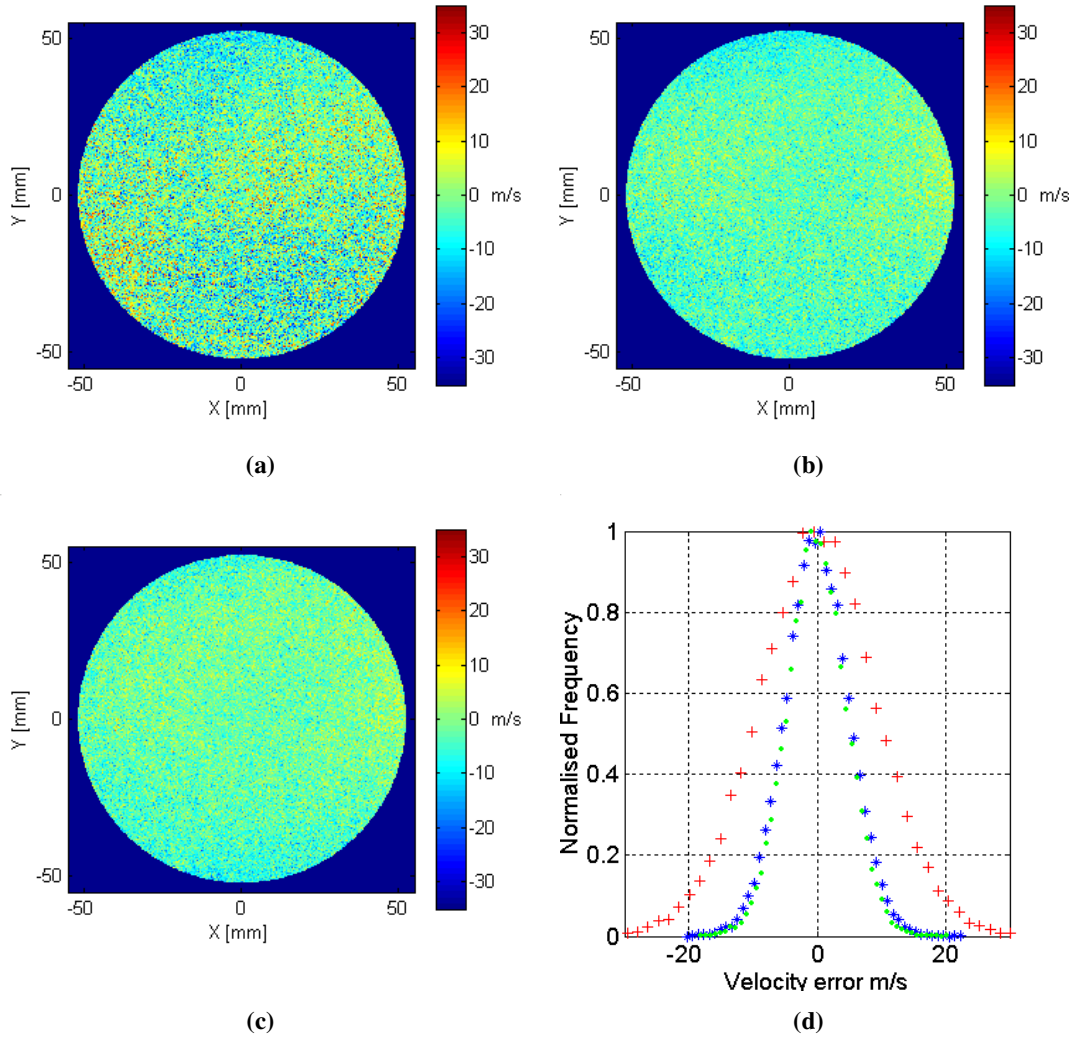

Figure 6-23 Computed W (out-of-plane) velocity components for configuration A calculated using:

(a) Normal sensitivity 2ν-PDV method; (b) Increased sensitivity 2ν-PDV (linear approximation) method; (c) Increased sensitivity 2ν-PDV (look-up table) method. (d) Histogram of the error residual (difference between calculated and theoretical velocity component) where:

+Normal sensitivity 2ν-PDV technique;

***Increased sensitivity 2ν-PDV technique (linear approximation);**

·Increased sensitivity 2ν-PDV (look-up table)

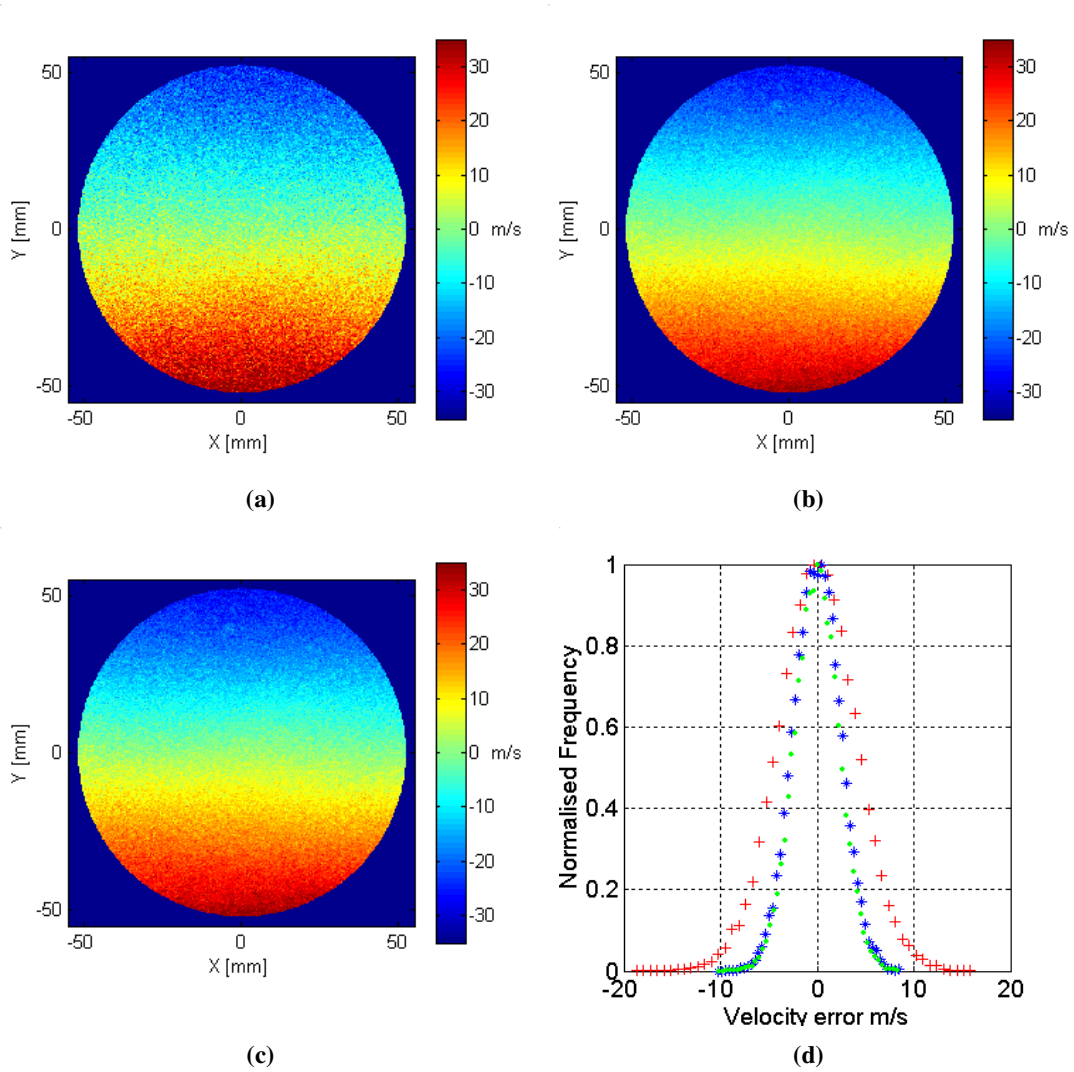

Figure 6-24 Computed U (horizontal) velocity components for configuration B calculated using:

(a) Normal sensitivity 2ν-PDV method; (b) Increased sensitivity 2ν-PDV (linear approximation) method; (c) Increased sensitivity 2ν-PDV (look-up table) method. (d) Histogram of the error residual (difference between calculated and theoretical velocity component) where:

+Normal sensitivity 2ν-PDV technique;

***Increased sensitivity 2ν-PDV technique (linear approximation);**

·Increased sensitivity 2ν-PDV (look-up table)

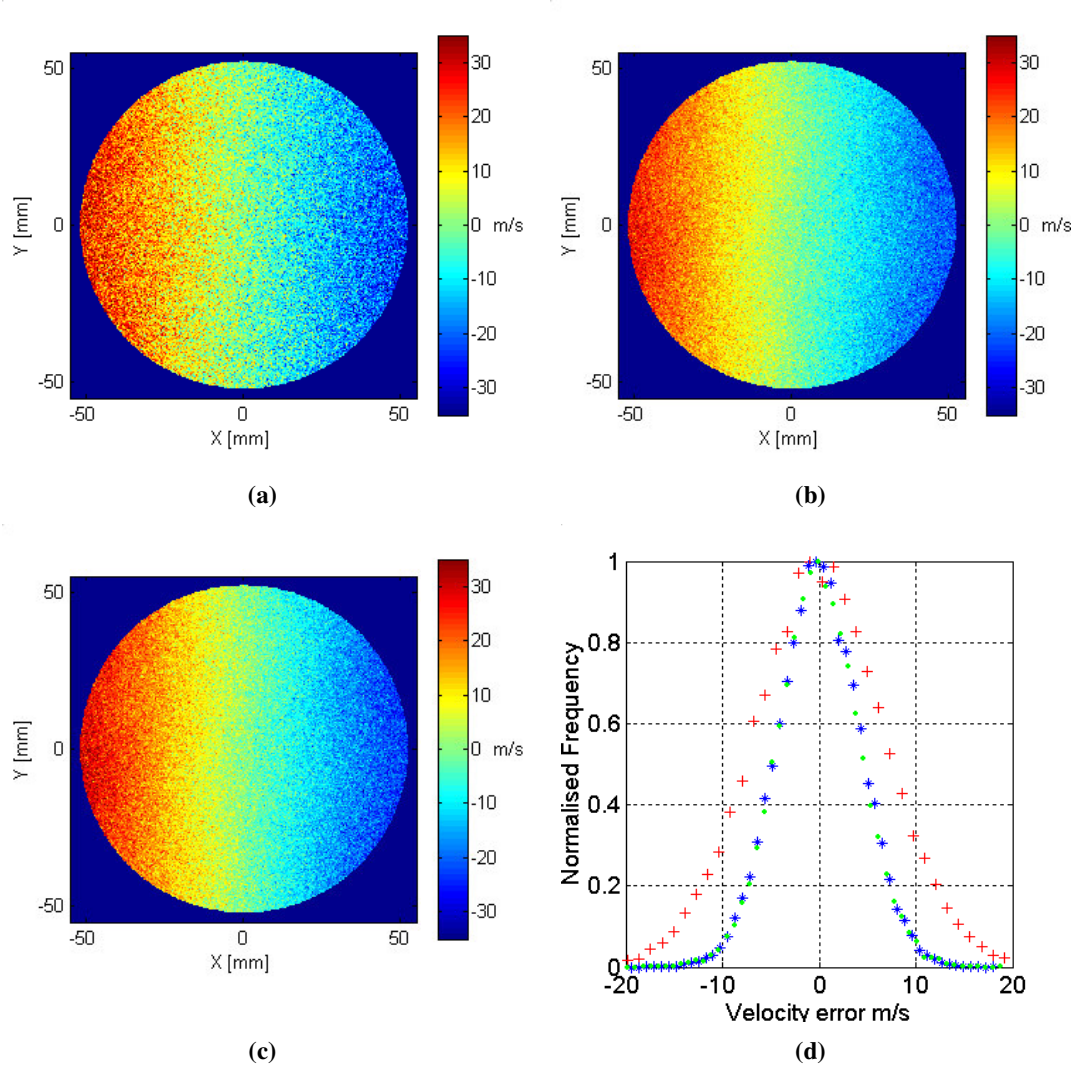

Figure 6-25 Computed V (vertical) velocity components for configuration B calculated using:

(a) Normal sensitivity 2ν-PDV method; (b) Increased sensitivity 2ν-PDV (linear approximation) method; (c) Increased sensitivity 2ν-PDV (look-up table) method. (d) Histogram of the error residual (difference between calculated and theoretical velocity component) where:

+Normal sensitivity 2ν-PDV technique;

***Increased sensitivity 2ν-PDV technique (linear approximation);**

·Increased sensitivity 2ν-PDV (look-up table)

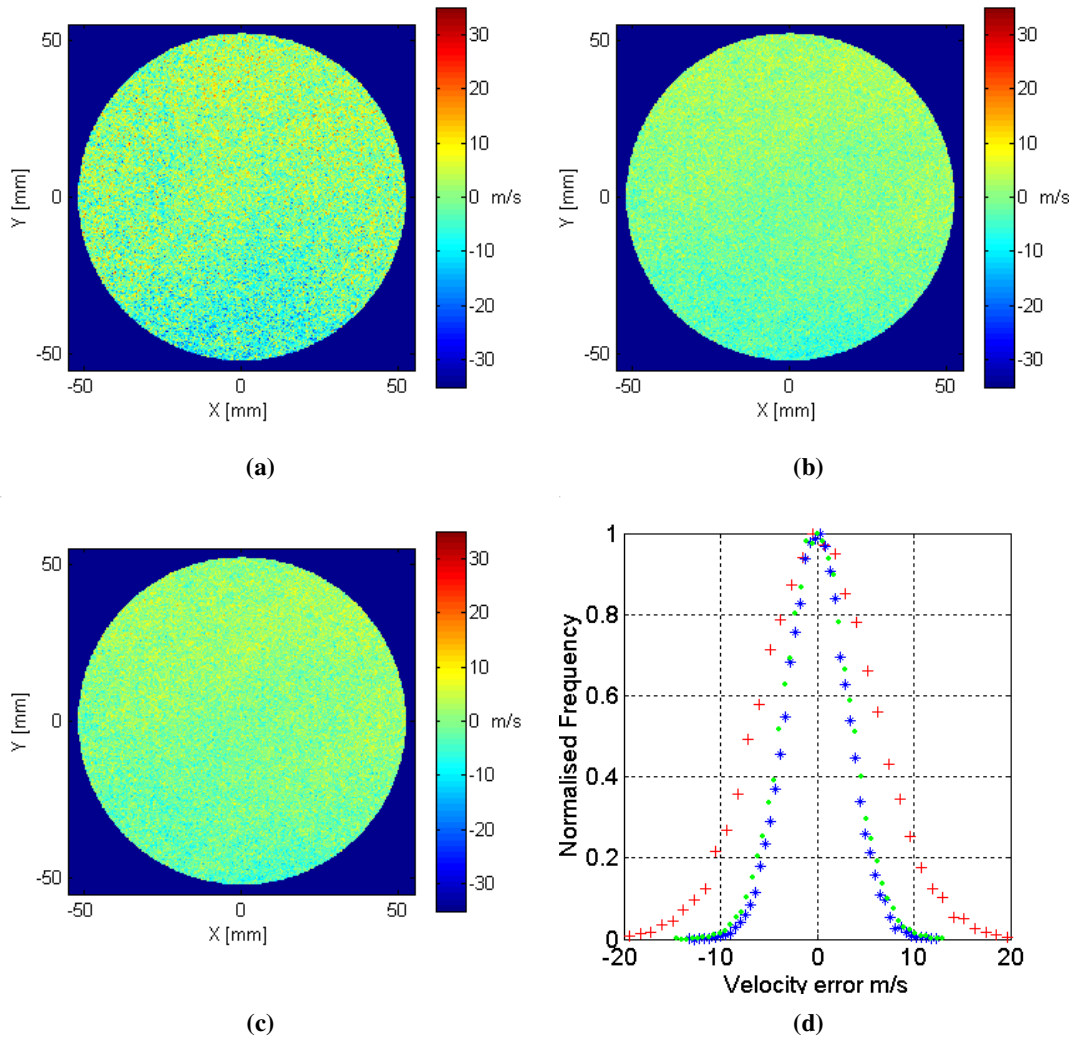

Figure 6-26 Computed W (out-of-plane) velocity components for configuration B calculated using:

(a) Normal sensitivity 2ν-PDV method; (b) Increased sensitivity 2ν-PDV (linear approximation) method; (c) Increased sensitivity 2ν-PDV (look-up table) method. (d) Histogram of the error residual (difference between calculated and theoretical velocity component) where:

+Normal sensitivity 2ν-PDV technique;

***Increased sensitivity 2ν-PDV technique (linear approximation);**

·Increased sensitivity 2ν-PDV (look-up table)

Table 6-4 Standard deviations of the variation between the calculated and theoretical orthogonal velocity components (configuration A), and the calculated reduction in error when using the increased sensitivity scheme.

Standard deviation	U	V	W
Normal sensitivity	6.1 ms^{-1}	10.2ms^{-1}	9.3 ms^{-1}
Increased sensitivity (Linear approximation)	3.3 ms^{-1}	5.6 ms^{-1}	5.0 ms^{-1}
% Reduction over normal sensitivity	45.9%	45.1%	46.2%
Increased sensitivity (Look-up table)	3.2 ms^{-1}	5.3 ms^{-1}	4.6 ms^{-1}
% Reduction over normal sensitivity	47.5%	48.0%	50.5%

Table 6-5 Standard deviations of the variation between the calculated and theoretical orthogonal velocity components (configuration B), and the calculated reduction in error when using the increased sensitivity scheme.

Standard deviation	U	V	W
Normal sensitivity	4.0 ms^{-1}	6.9 ms^{-1}	6.0 ms^{-1}
Increased sensitivity (Linear approximation)	2.4 ms^{-1}	4.2 ms^{-1}	3.2 ms^{-1}
% Reduction over normal sensitivity	40.0%	39.1%	46.7%
Increased sensitivity (Look-up table)	2.3 ms^{-1}	4.2 ms^{-1}	3.4 ms^{-1}
% Reduction over normal sensitivity	42.5%	39.1%	43.3%

6.5 3D Velocity measurements on an axis-symmetric air jet.

To further demonstrate the technique measurements were made on a seeded air jet. This was an axis-symmetric air jet, with a 20mm diameter smooth contraction nozzle. The air intake to the jet was seeded using a Concept Engineering ViCount compact smoke generator, which produces particles in the 0.2-0.3μm diameter range. The jet has a theoretical exit velocity of $94ms^{-1}$, which was calculated by measuring the nozzle pressure ratio.

6.5.1 Experimental arrangement

Two different experimental arrangements were used to make measurements on this air jet, in the first the jet was positioned vertically with the main flow direction in the positive Y direction. The laser sheet cut vertically through the flow in the X-Y plane this is shown in Figure 6-27 and the view angles are defined in Table 6-6 as configuration C.

In the second set of measurements the jet nozzle was rotated so that the main flow was in the out-of-plane direction and a 'swirler' was introduced into the nozzle in an attempt to create more in-plane flow velocities. The tripods used to support the SLR lenses and fibre bundles in the previous measurements only allowed limited variation in the elevation/depression (view angle P) also some arrangements were not possible due to the tripods obstructing views. To overcome this the tripods were modified to allow more flexibility in the view positioning. The modified tripods are shown in Figure 6-28. Using the new mounting system the viewing configuration was changed in an attempt to optimise the positioning of the views and increase the sensitivity to in-plane velocities. The new viewing angles are shown in Table 6-6 as configuration D.

Table 6-6 Definitions of viewing angles used for measurements on an axis-symmetric air jet.

Configuration	View Angles	1	2	3	4
C	T (^{o})	180	180	168	45
	P (^{o})	36	-25	4	3.7
D	T (^{o})	45	45	225	225
	P (^{o})	39	-39	39	-39

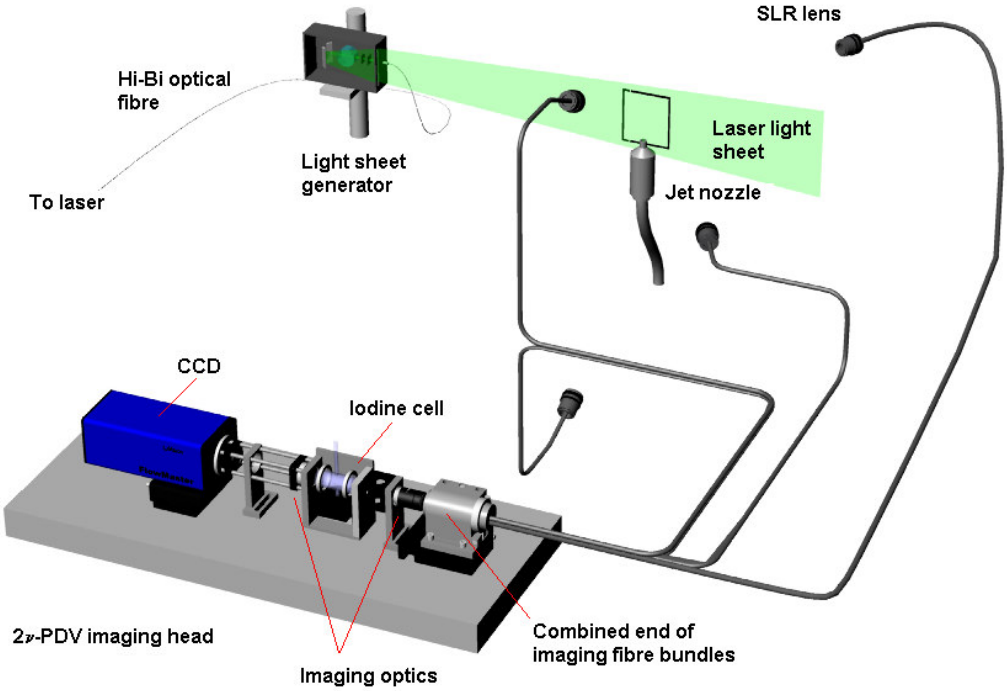

Figure 6-27 Diagram showing the experimental arrangement for 3D measurements made on an axis-symmetric air jet.

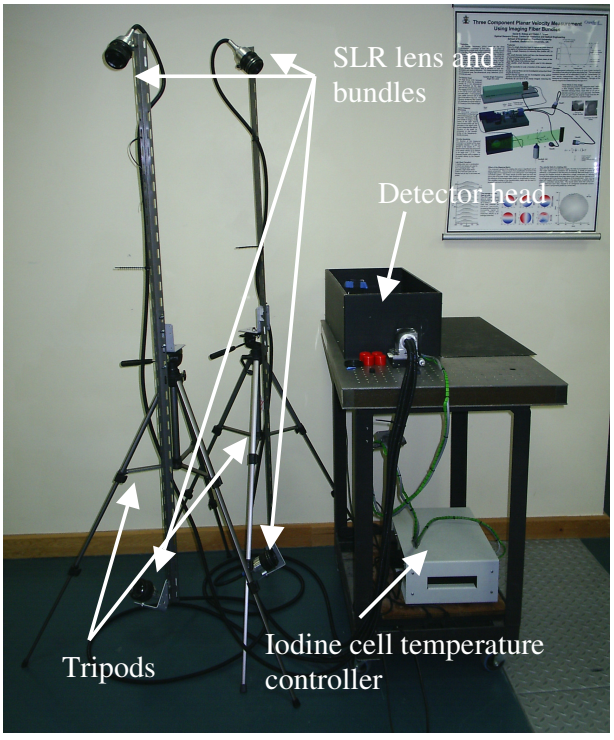

Figure 6-28 Photograph of modified tripod mounting system allowing increased elevation / depression of the view angle.

6.5.2 Results

An example of a measurement made using configuration C, is shown in Figure 6-29. In plane velocities are shown as vectors and the out-of-plane component by the colour coding. The density of measurement data is greater than shown with only every 40^{th} row and every 8^{th} point on each row shown. As for the single velocity component measurements, discussed in chapter 5, the jet was seeded through the air intake; seeding levels outside of the jet were low resulting in low levels of scattered light for these regions. As any velocity measurements for these regions would be unreliable a threshold has been applied to the data. As with the single velocity component measurements in chapter 5, no 'white card' correction was needed. Here a single pass of 3x3 pixel smoothing filter was applied to remove high frequency noise. It can be seen that the measurements show the expected development of the jet, in the main flow direction, with minimal out-of-plane velocities.

A second set of measurements was made with the jet nozzle rotated using the second experimental arrangement. The nozzle was then positioned at various distances from the sheet between 60 and 120mm and measurements of the flow velocity on these slices across the jet were made. This is shown in Figure 6-30 and an example of a single slice at 120mm downstream from the nozzle is shown in Figure 6-31. Again the in plane velocities are shown as vectors and the out-of-plane velocities represented by colour and the number of vectors has been reduced so that only every 12^{th} vector is shown.

Less useful conclusions can be drawn from these jet measurements than was possible from the rotating disc measurements, as no comparison could be made with independent measurements of the jet's velocity field which in principle could be made using PIV or LDV. However the main flow component has an empirically correct form with the profiles shown in Figure 6-30, following the formula described in section 5.6.2. Also although an attempt was made to introduce swirl into the jet and increase the magnitude of the in-plane velocities in the second experimental arrangement, these velocities were still very small and could be expected to be around the size of the velocity uncertainty in these components. The vectors shown in Figure 6-31 suggest that the jet was mainly entraining air from the top and bottom of the jet and this was in fact observed during the experiment from stray seeding in the light sheet.

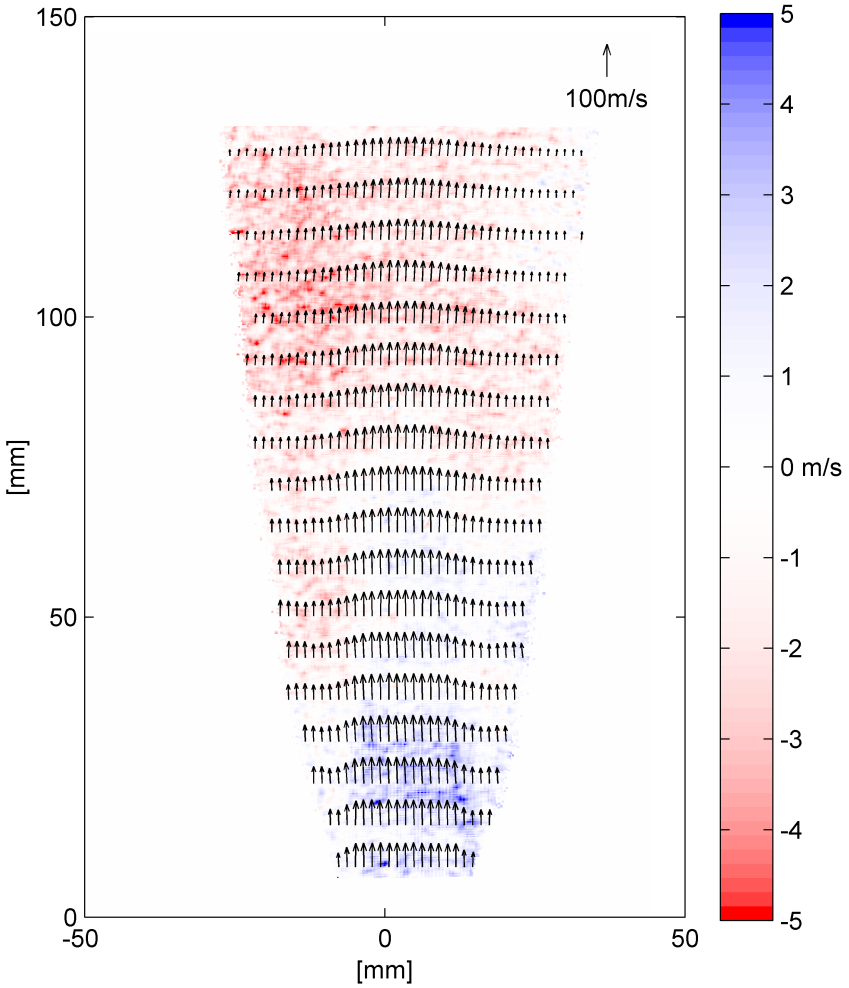

Figure 6-29 Example of a 3D 2ν-PDV measurement made on a seeded air jet. Vectors show the in plane velocities (every 8th and 40th vector show in the horizontal and vertical directions respectively) and colour the out of plane velocity.

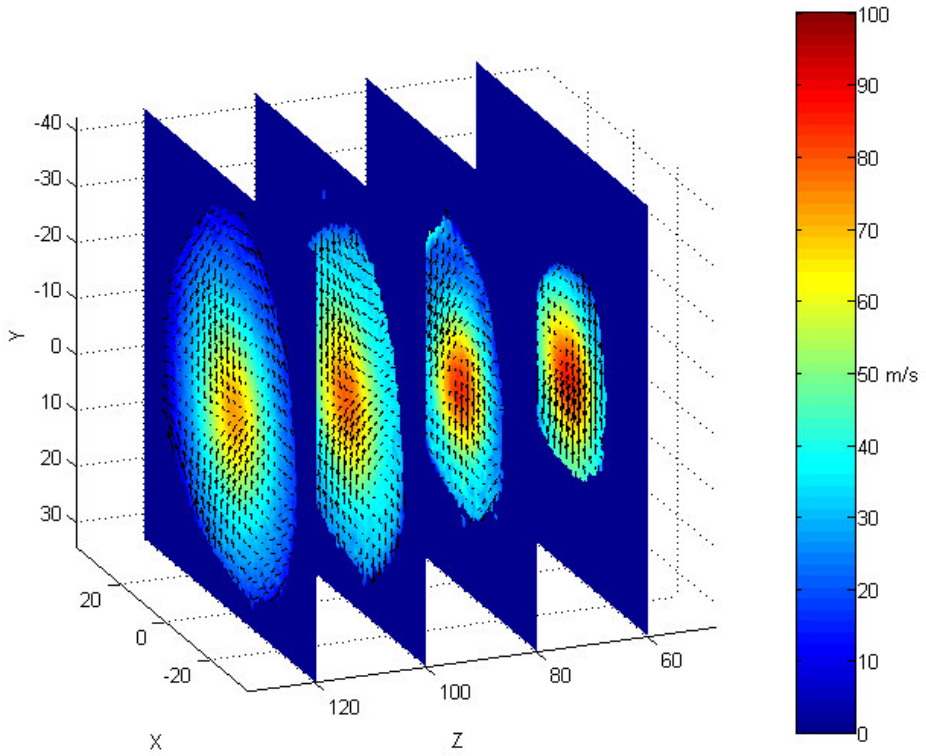

Figure 6-30 3D 2ν-PDV cross section measurements on a seeded air jet. Vectors represent the in plane velocities (12x12 skip) and colour the out-of-plane velocity. Cross sections were measured at 60,80,100 and 120mm distances from the jet nozzle.

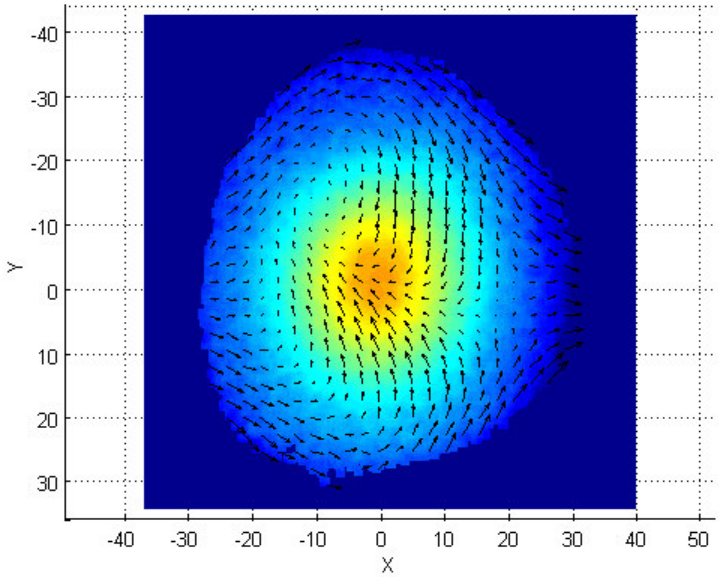

Figure 6-31 3D 2ν-PDV cross section measurements on a seeded air jet at 120mm downstream from the nozzle. Vectors represent the in plane velocities (12x12 skip) and colour the out-of-plane velocity.

6.6 Summary

A 2ν-PDV system was constructed using the temperature-controlled etalon of an argon ion laser to produce the required illumination frequencies. The PDV imaging head used multiple arm imaging fibre bundles to measure multiple components of the velocity simultaneously and allow the calculation of 3D velocities and consisted of only a single CCD camera and iodine cell.

The 2ν-PDV system has been demonstrated by making 3D velocity measurements on the velocity field of a rotating disc and a seeded axis-symmetric air jet with a maximum velocity of ~94ms^{-1}. The system was used to make 3D velocity measurements using both the normal and increased sensitivity 2ν-PDV methods.

By comparing the measured velocity field of a rotating disc with the theoretical velocity field an estimate of the error level in these measurements was possible. Two alternative processing schemes were used to calculate the velocity using the increased sensitivity method data, with these methods reducing the error in the computed orthogonal velocity components by ~40-50% over the normal sensitivity scheme measurements.

The use of a single mode fibre to transport the light to the sheet forming optics removed the differences in the output beam power distributions between the frequencies. This meant that there were no longer significant differences in the laser light sheets at each frequency, because of this the 'white card' correction, used in chapter 5 when making measurements on a rotating disc was no longer necessary.

6.7 References

1. Ford, H.D., Nobes, D.S., and Tatam, R.P., "Acousto-optic Frequency Switching with Fibre-optic Delivery for Single Camera Planar Doppler Velocimetry", 2003, *16th International Conference on Optical Fiber Sensors*, Nara, Japan, Tu3-5, pp 226-229.

2. Nobes, D.S., Ford, H.D., and Tatam, R.P., "Instantaneous, Two Camera, Three Dimensional Planar Doppler Velocimetry using Imaging Fiber Bundles", 2001, *SPIE Proceedings, Optical Diagnostics for Fluids, Solids and Combustion*, San Diego, Vol. 4448, pp 72-83.

3. Nobes, D.S., Ford, H.D., and Tatam, R.P., "Planar Doppler Velocimetry Measurements of Flows using Imaging Fiber Bundles", 2003, *Proc. SPIE*, 5191, pp 122-133.

4. Nobes, D.S., Ford, H.D., and Tatam, R.P., "Three Component Planar Doppler Velocimetry Using Imaging Fibre Bundles", 2004, *Experiments in Fluids*, Vol. 36, No. 1, pp 3-10.

5. Willert, C., Stockhausen, G., Beversdorff, M., Klinner, J., Lempereur, C., Barricau, P., Quest, J., and Jansen, U., "Application of Doppler Global velocimetry in cryogenic wind tunnels", 2005, *Experiments in Fluids*, Vol. 39, pp 420-430.

6. Meyers, J.F., "Private communication".

7. Hawkes, G., " Three-component instantaneous Doppler Global Velocimetry", 2004, *SET fro Britain presentations*, House of Commons, UK,

8. Schott AG website", 2005, http://www.schott.com.

9. Nobes, D.S., Wieneke, B., and Tatam, R.P., "Determination of View Vectors from Image Warping Mapping Functions", 2004, *Optical Engineering*, Vol. 43, No. 2, pp 407-414.

10. Chehura, E. and Tatam, R.P., "In-line Laser Doppler Velocimeter using fibre-optic Bragg grating interferometric filters", 2003, *Measurement Science and Technology*, Vol. 14, pp 724-735.

7 Factors influencing the selection of viewing configurations for 3D PDV systems

7.1 Introduction

In order to make 3D PDV measurements it is necessary to measure multiple components of the flow velocity, which are then transformed to an orthogonal coordinate system aligned with the experiment. At least three different measured velocity components are necessary to calculate the three orthogonal velocity components, U, V and W; hence at least three different observation directions are needed when making 3D PDV measurements. This chapter discusses the factors that should be taken into consideration when selecting a viewing configuration for use when making 3D PDV measurements.

There are two main considerations that will affect the level of error in the calculated orthogonal velocity components. The first of these is the magnitude of the errors on each of the individual measured velocity components. This will vary with the observation direction and is discussed in section 7.2. The second is how the errors will propagate through the transformation from measured velocity components to orthogonal velocity components. This is addressed in section 7.3, while other considerations that will affect the selection are summarized in section 7.4.

As in chapter 6, each observation direction has been defined using two view angles, rotation (T) and elevation (P). These are shown in Figure 7-1, with the rotation being the angle measured around from the Z-axis in the XZ plane (0-360^o) and the elevation being the angle from the XZ plane, (±90^o). The Cartesian components of the sensitivity vectors, the observation vector minus the laser illumination vector, are given by *X*, *Y* and *Z* as defined in section 4.10.

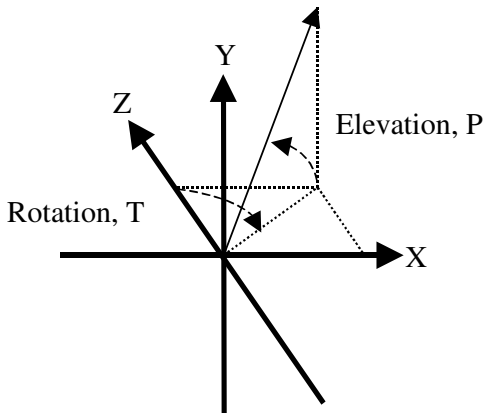

Figure 7-1. Diagram showing the definition of the viewing angles; Rotation, T (0-360^o) and elevation, P (±90^o)

7.2 Variation of the uncertainty in the measured velocity components with viewing direction.

The first consideration when selecting a viewing geometry is related to the magnitude of the uncertainty in each of the measured components. If a configuration converts to the orthogonal components better than another but the errors are larger to start with this benefit is negated.

The uncertainty of individual measured velocity components will vary depending upon the observation direction for two main reasons. The first of these is due to the uncertainty in determining the observation and the laser illumination directions. The second is due to how errors in the measurement of the Doppler shift translate to errors in the measured velocity components.

7.2.1 Error due to uncertainty in determining the sensitivity vector (ô - î)

Uncertainty in how the position of the view and the direction of the illumination light are measured leads to an uncertainty in the measured velocity component. Elliott and Beutner[1] give a derivation for the level of this error from the Doppler equation as:

$$\Delta U_n = \frac{\partial U_n}{\partial \phi}\Delta\phi = \frac{-U_n}{2\tan(\phi/2)}\Delta\phi$$

Equation 7-1

Where ϕ is the angle between $\hat{o}$ and $\hat{i}$, $\Delta\phi$ is the error in this angle, and U_n is the measured velocity component. The error increases as ϕ approaches 0^o (the observation direction moves into forward scatter) until the system is insensitive to velocity when $\hat{o}$ and $\hat{i}$ are equal. Figure 7-2 shows this variation of the uncertainty in the measured velocity component as the observation direction is varied calculated using Equation 7-1. The position on the surface represents the observation direction, which is varied between ±60 degrees from the normal to the sheet. The colour represents the level of uncertainty in the measured velocity component for that observation direction. The values were calculated using a velocity field of (50,50,50) ms^{-1} and the uncertainty in the measurement of the view angles, defining the observation direction, was assumed to be 1^o. From Equation 7-1 it can be seen that the magnitude of the uncertainty will also be dependent upon the magnitude of the flow velocity being measured.

The error in this angle, ϕ, can arise for several reasons:

Measurement / calculation of the observation direction – If the viewing angles are measured then there will be an uncertainty in the accuracy of these measurements. Alternatively the de-warping algorithm can be used to calculate the positions of the views from images of a target[2], as is the case in the PDV system developed at Cranfield. The observation direction will also vary across the image, which can be significant depending upon the collection optics used. This is automatically taken into

account when using the de-warping algorithm to calculate viewing direction as the calculation is performed for each pixel in the image[2].

Measurement / assumption of the laser illumination direction – As for the measurement of viewing angle there will be an uncertainty in the laser illumination direction. This uncertainty comes about for three reasons; the first is a measurement uncertainty in the bulk illumination direction; the second is due to a variation in illumination direction due to the divergence of the laser sheet in the measurement plane; and the third is convergence/divergence of the laser sheet thickness. It is possible to correct to a certain extent for the last two of these effects when processing the PDV data; however there will still be a degree of uncertainty in the laser illumination direction.

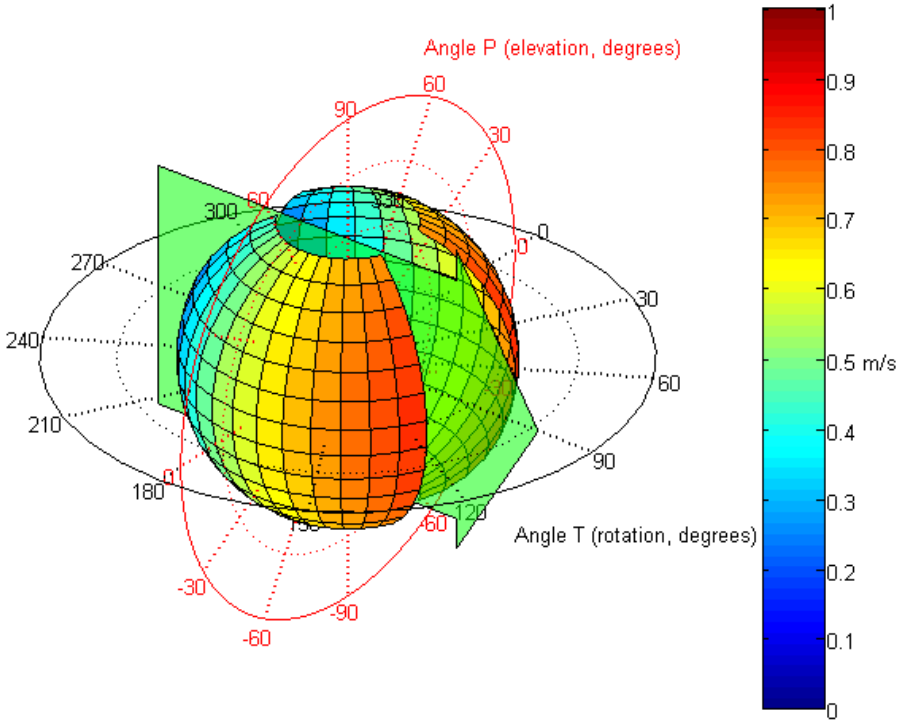

Figure 7-2 Variation of the uncertainty in the velocity component due to the uncertainty in the angle ϕ (between $\hat{o}$ and $\hat{i}$) calculated using Equation 7-1. Positions on the surface represent the observation direction and the colour the magnitude of the velocity uncertainty. The illumination direction is indicated, the velocity field used in the calculations was (50,50,50) m/s and the uncertainty in the angle ϕ was assumed to be 1^{o}.

7.2.2 Error due to uncertainty in the measurement of Doppler shift

There will be a contribution to the error on a measured velocity component that can be described by an uncertainty in the measurement of the Doppler shift. This will result from the components of the PDV system used to determine the Doppler shift, with contributions for example from the camera noise, the error in determining the transmission line and laser frequency uncertainty.

Following the method used above with the Doppler equation written in the form of Equation 7-2, then the measured velocity component uncertainty, ΔU_n, can be found from Equation 7-4.

$$U_n = \frac{\lambda}{\sin(\phi/2)}\Delta\nu$$

Equation 7-2

$$\Delta U_n = \frac{\partial U_n}{\partial(\Delta\nu)}\Delta(\Delta\nu)$$

Equation 7-3

$$\Delta U_n = \frac{\lambda}{\sin(\phi/2)}\Delta(\Delta\nu)$$

Equation 7-4

Where $\Delta\nu$ is the Doppler shift, $\Delta(\Delta\nu)$ is the uncertainty in the Doppler shift, λ is the wavelength of the illuminating light, ϕ is the angle between the observation and illumination vectors and U_n is the magnitude of the measured velocity component.

The magnitude of the uncertainty in Doppler shift, $\Delta(\Delta\nu)$, will be constant for all viewing directions and will depend upon the individual PDV system. However the resulting uncertainty in the velocity component will not be constant and is dependent upon viewing direction. The variation in the measured velocity component uncertainty, ΔU_n, is shown in Figure 7-3 for a 5MHz Doppler shift uncertainty.

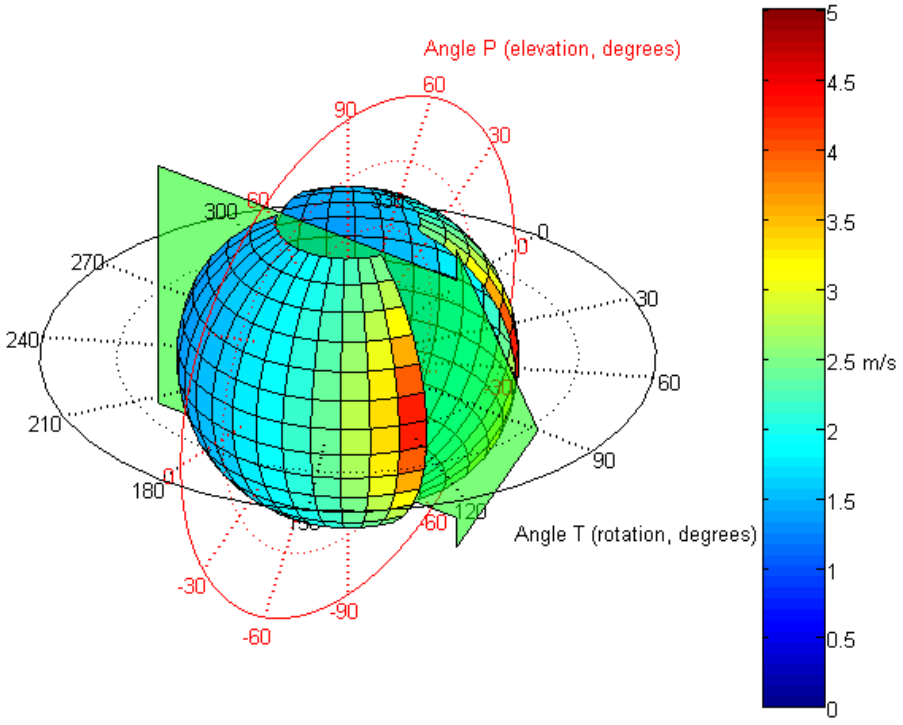

Figure 7-3 Variation of the uncertainty in the velocity component due to the uncertainty in Doppler shift measurement calculated using Equation 7-3. Positions on the surface represent the observation direction and the colour the magnitude of the velocity uncertainty. The view angles are varied between ±60° from the normal to the sheet. The illumination direction is indicated, and the uncertainty in the measurement of Doppler shift was assumed to be 5MHz.

7.2.3 Experimental observation of the variation in error with viewing direction

Using the 3D 2ν-PDV system described in chapter 6, the four channels of the imaging fibre bundle were arranged to measure four components of the velocity field of a rotating disc. Each arm of the bundles was located so that the view angles were increasingly positioned into forward scatter, so that the values of ϕ were 90,70,50 and 30° respectively.

Images of a target were used to calculate the observation directions for each view[2] and determine the position scaling of the image. This was then used to calculate theoretical velocity components, based upon the calculated scaling, observation direction information and the frequency of rotation of the disc. These theoretical velocity components were then subtracted from the experimental measured velocity components, and a histogram taken of the remaining values, giving a measure of the level of error in each component.

Figure 7-4 shows that the magnitude of the error increases as the view moves into forward scatter as would be expected. Also this variation of error between measured components is significant, the error approximately doubling between when the view is normal to the light sheet and when located predominantly in forward scatter. This suggests that this will have a strong influence in the choice of viewing configuration.

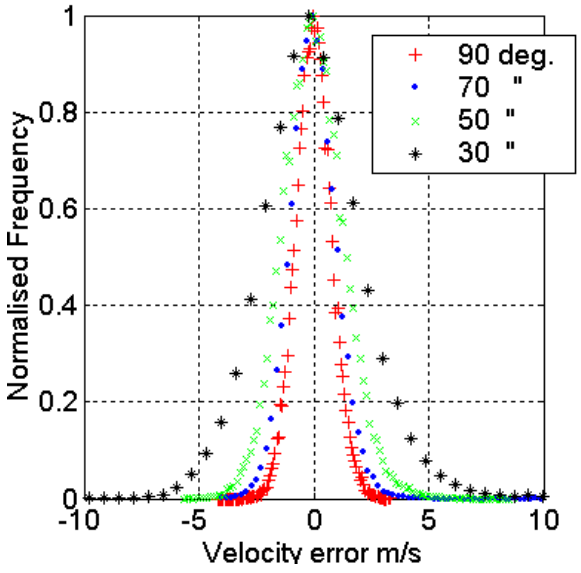

Figure 7-4 Measured error in the velocity components of a rotating disc for various values of ϕ (the angle between ô and î) from 30° to 90°, showing the increasing uncertainty as the view moves into forward scatter.

7.3 Influence of the transformation matrix upon the error level in the computed orthogonal velocity components

The second main consideration when selecting a viewing geometry for 3D PDV measurements involves how well the uncertainty in the measured velocity components will translate to the orthogonal velocity components.

7.3.1 Condition number

How well the measured velocity components can be mapped to the orthogonal Cartesian co-ordinate system can be described by the value of the conditioning number of the transformation matrix. The conditioning number, $\kappa(A)$, of a matrix can be used as a measure of the sensitivity of the solution of the system of linear equations defined by the matrix to errors in the data and is defined as [3]:

$$\kappa(A) = \|A\| \|A^{-1}\|$$

Equation 7-5

Here, A, is the transformation matrix and $\|A\|$ is the norm of the matrix and can be defined in several different forms. In this paper four definitions of the condition number are used based on four different definitions of the norm of the matrix.

κ_1 The norm is based on the largest column sum in *A*

κ_2 The norm is based on the largest column value in *A*

κ_3 The norm is based on Frobenius-norm of matrix *A*, $\sqrt{\sum diag(A'.A)}$

κ_4 The norm is based on the largest row sum in *A*.

The computed condition number for the ideal case, where the three sensitivity vectors are aligned with the axes of the Cartesian co-ordinate system, is given in Table 7-1. The closer the value of $\kappa(A)$ to this ideal case the better conditioned the matrix is for transforming measured results to the orthogonal coordinate system.

Table 7-1 The sensitivity vectors of the ideal case configuration, and the computed matrix conditioning numbers for the different definitions.

	Cartesian components of the measured velocity components / sensitivity vectors			Condition Numbers			
	X	Y	Z	κ_1	κ_2	κ_3	κ_4
$(\hat{o}_1 - \hat{t}_1)$	1.000	0.000	0.000				
$(\hat{o}_2 - \hat{t}_2)$	0.000	1.000	0.000	1.000	1.000	3.000	1.000
$(\hat{o}_3 - \hat{t}_3)$	0.000	0.000	1.000				

Although the condition number provides a useful measure of how well a set of measured non-orthogonal velocity components will convert to the orthogonal velocity components, it assumes that the error is constant on all these components which we know is unlikely to be the case from section 7.2. This means that although one configuration may have a lower condition number than another it may not have lower uncertainty levels in the orthogonal components due to greater uncertainties in the measured components. This is discussed further in chapter 8.

7.3.2 The effect of uncertainty in the viewing angles on the transformation to orthogonal velocity components

Another consideration that needs to be taken into account is that the co-ordinate system (aligned with the measured components) that is being transformed is assumed to be correct. This is not the case as uncertainty exists in the definition of each of the observation directions and hence the sensitivity vectors for each measured velocity component. This will lead to an associated level of uncertainty in the computed orthogonal velocity components.

Reinath[4] gives expressions for the uncertainty in the orthogonal transformation for the 3C method, discussed in section 4.10.1, as:

$$\Delta^2 U = \left(\frac{\partial U}{\partial |U_1|}\Delta |U_1|\right)^2 + \left(\frac{\partial U}{\partial |U_2|}\Delta |U_2|\right)^2 + \left(\frac{\partial U}{\partial |U_3|}\Delta |U_3|\right)^2 + \left(\frac{\partial U}{\partial X_1}\Delta X_1\right)^2 + \left(\frac{\partial U}{\partial X_2}\Delta X_2\right)^2 + \left(\frac{\partial U}{\partial X_3}\Delta X_3\right)^2 + \left(\frac{\partial U}{\partial Y_1}\Delta Y_1\right)^2 + \left(\frac{\partial U}{\partial Y_2}\Delta Y_2\right)^2 + \left(\frac{\partial U}{\partial Y_3}\Delta Y_3\right)^2 + \left(\frac{\partial U}{\partial Z_1}\Delta Z_1\right)^2 + \left(\frac{\partial U}{\partial Z_2}\Delta Z_2\right)^2 + \left(\frac{\partial U}{\partial Z_3}\Delta Z_3\right)^2$$

Equation 7-6

$$\Delta^2 V = \left(\frac{\partial V}{\partial |U_1|}\Delta |U_1|\right)^2 + \left(\frac{\partial V}{\partial |U_2|}\Delta |U_2|\right)^2 + \left(\frac{\partial V}{\partial |U_3|}\Delta |U_3|\right)^2 + \left(\frac{\partial V}{\partial X_1}\Delta X_1\right)^2 + \left(\frac{\partial V}{\partial X_2}\Delta X_2\right)^2 + \left(\frac{\partial V}{\partial X_3}\Delta X_3\right)^2 + \left(\frac{\partial V}{\partial Y_1}\Delta Y_1\right)^2 + \left(\frac{\partial V}{\partial Y_2}\Delta Y_2\right)^2 + \left(\frac{\partial V}{\partial Y_3}\Delta Y_3\right)^2 + \left(\frac{\partial V}{\partial Z_1}\Delta Z_1\right)^2 + \left(\frac{\partial V}{\partial Z_2}\Delta Z_2\right)^2 + \left(\frac{\partial V}{\partial Z_3}\Delta Z_3\right)^2$$

Equation 7-7

$$\Delta^2 W = \left(\frac{\partial W}{\partial |U_1|}\Delta |U_1|\right)^2 + \left(\frac{\partial W}{\partial |U_2|}\Delta |U_2|\right)^2 + \left(\frac{\partial W}{\partial |U_3|}\Delta |U_3|\right)^2 + \left(\frac{\partial W}{\partial X_1}\Delta X_1\right)^2 + \left(\frac{\partial W}{\partial X_2}\Delta X_2\right)^2 + \left(\frac{\partial W}{\partial X_3}\Delta X_3\right)^2 + \left(\frac{\partial W}{\partial Y_1}\Delta Y_1\right)^2 + \left(\frac{\partial W}{\partial Y_2}\Delta Y_2\right)^2 + \left(\frac{\partial W}{\partial Y_3}\Delta Y_3\right)^2 + \left(\frac{\partial W}{\partial Z_1}\Delta Z_1\right)^2 + \left(\frac{\partial W}{\partial Z_2}\Delta Z_2\right)^2 + \left(\frac{\partial W}{\partial Z_3}\Delta Z_3\right)^2$$

Equation 7-8

Similar expressions can be found for the 4C method (section 4.10.2) with the added contributions from the fourth measured velocity component and the fourth sensitivity vector.

$$\Delta^2 U = \left(\frac{\partial U}{\partial |U_1|}\Delta|U_1|\right)^2 + \left(\frac{\partial U}{\partial |U_2|}\Delta|U_2|\right)^2 + \left(\frac{\partial U}{\partial |U_3|}\Delta|U_3|\right)^2 + \left(\frac{\partial U}{\partial |U_4|}\Delta|U_4|\right)^2$$
$$+ \left(\frac{\partial U}{\partial X_1}\Delta X_1\right)^2 + \left(\frac{\partial U}{\partial X_2}\Delta X_2\right)^2 + \left(\frac{\partial U}{\partial X_3}\Delta X_3\right)^2 + \left(\frac{\partial U}{\partial X_4}\Delta X_4\right)^2$$
$$+ \left(\frac{\partial U}{\partial Y_1}\Delta Y_1\right)^2 + \left(\frac{\partial U}{\partial Y_2}\Delta Y_2\right)^2 + \left(\frac{\partial U}{\partial Y_3}\Delta Y_3\right)^2 + \left(\frac{\partial U}{\partial Y_4}\Delta Y_4\right)^2$$
$$+ \left(\frac{\partial U}{\partial Z_1}\Delta Z_1\right)^2 + \left(\frac{\partial U}{\partial Z_2}\Delta Z_2\right)^2 + \left(\frac{\partial U}{\partial Z_3}\Delta Z_3\right)^2 + \left(\frac{\partial U}{\partial Z_4}\Delta Z_4\right)^2$$

Equation 7-9

$$\Delta^2 V = \left(\frac{\partial V}{\partial |U_1|}\Delta|U_1|\right)^2 + \left(\frac{\partial V}{\partial |U_2|}\Delta|U_2|\right)^2 + \left(\frac{\partial V}{\partial |U_3|}\Delta|U_3|\right)^2 + \left(\frac{\partial V}{\partial |U_4|}\Delta|U_4|\right)^2$$
$$+ \left(\frac{\partial V}{\partial X_1}\Delta X_1\right)^2 + \left(\frac{\partial V}{\partial X_2}\Delta X_2\right)^2 + \left(\frac{\partial V}{\partial X_3}\Delta X_3\right)^2 + \left(\frac{\partial V}{\partial X_4}\Delta X_4\right)^2$$
$$+ \left(\frac{\partial V}{\partial Y_1}\Delta Y_1\right)^2 + \left(\frac{\partial V}{\partial Y_2}\Delta Y_2\right)^2 + \left(\frac{\partial V}{\partial Y_3}\Delta Y_3\right)^2 + \left(\frac{\partial V}{\partial Y_4}\Delta Y_4\right)^2$$
$$+ \left(\frac{\partial V}{\partial Z_1}\Delta Z_1\right)^2 + \left(\frac{\partial V}{\partial Z_2}\Delta Z_2\right)^2 + \left(\frac{\partial V}{\partial Z_3}\Delta Z_3\right)^2 + \left(\frac{\partial V}{\partial Z_4}\Delta Z_4\right)^2$$

Equation 7-10

$$\Delta^2 W = \left(\frac{\partial W}{\partial |U_1|}\Delta|U_1|\right)^2 + \left(\frac{\partial W}{\partial |U_2|}\Delta|U_2|\right)^2 + \left(\frac{\partial W}{\partial |U_3|}\Delta|U_3|\right)^2 + \left(\frac{\partial W}{\partial |U_4|}\Delta|U_4|\right)^2$$
$$+ \left(\frac{\partial W}{\partial X_1}\Delta X_1\right)^2 + \left(\frac{\partial W}{\partial X_2}\Delta X_2\right)^2 + \left(\frac{\partial W}{\partial X_3}\Delta X_3\right)^2 + \left(\frac{\partial W}{\partial X_4}\Delta X_4\right)^2$$
$$+ \left(\frac{\partial W}{\partial Y_1}\Delta Y_1\right)^2 + \left(\frac{\partial W}{\partial Y_2}\Delta Y_2\right)^2 + \left(\frac{\partial W}{\partial Y_3}\Delta Y_3\right)^2 + \left(\frac{\partial W}{\partial Y_4}\Delta Y_4\right)^2$$
$$+ \left(\frac{\partial W}{\partial Z_1}\Delta Z_1\right)^2 + \left(\frac{\partial W}{\partial Z_2}\Delta Z_2\right)^2 + \left(\frac{\partial W}{\partial Z_3}\Delta Z_3\right)^2 + \left(\frac{\partial W}{\partial Z_4}\Delta Z_4\right)^2$$

Equation 7-11

Here ΔU, ΔV and ΔW are the uncertainty in the U, V and W components respectively, $\Delta|U_n|$ is the uncertainty in the nth measured velocity component, likewise

$\Delta X_1, \Delta Y_1$ and ΔZ_1 are the uncertainty in the nth sensitivity vectors *X*, *Y* and *Z* components The partial derivatives are evaluated using the expression for *U*, *V* and *W* given by equations 4-11,4-12 and 4-13 for the 3C method and equation 4-20 for the 4C method. It can be seen from these expressions that the level of uncertainty will include contributions from the uncertainty in the Cartesian components of the sensitivity vectors. Also it should be noted that the magnitude of the uncertainty would also be dependent upon the magnitude of the flow velocity being measured.

7.4 Other considerations

As well as considering the level of error in the final computed orthogonal velocity components, the choice of viewing configuration may be limited by other considerations. These are summarised below:

Limitations of optical access – For many experimental arrangements the optical access will be limited, meaning that certain viewing configurations, for example those that optimise the error propagation, may not be possible.

Scattered light intensity – It may be necessary to locate views in forward scatter to increase the amount of scattered light detected, even though this will increase the level of error due to uncertainty in the angle φ (between ô and $\hat{\imath}$). Increased light intensities would however lead to an improved signal-to-noise ratio, potentially counteracting the disadvantages.

Laser frequency fluctuations cancellation effects – Fluctuations in the laser frequency will cause an uncertainty in the measured Doppler shift leading to an error in the measured velocity components. If only this source of Doppler shift measurement error is considered this would be equivalent to adding a Doppler shift equally to each component. However the viewing direction dictates how this additional shift will convert to an error in the velocity component. Clancy[5] and Elliot et al[6] suggest that by careful selection of three viewing directions any effect of this laser frequency variation can be eliminated from two of the three orthogonal velocity components in the transformation stage. It is also suggested this can be extended to allow all three components to be independent of any frequency variation, by adding a fourth measured component which can be used to eliminate any laser frequency variation from the remaining orthogonal velocity component. However due to viewing constraints in an experiment it may not be possible to select this special case viewing geometry. Also if the uncertainty introduced by laser fluctuations is less significant than other sources, smaller errors in the final result could well be achieved with a configuration where the laser fluctuations will not be eliminated but the condition number for the transformation is better.

7.5 Summary

In this chapter the following factors have been identified that will have an influence in the selection of a viewing configuration for use when making 3D PDV measurements:

- The magnitude of the uncertainty in measured non-orthogonal velocity components is variable depending upon the viewing direction.

    - This variation in measured velocity component uncertainty is due to two effects; the uncertainty in determining direction of the observation and illumination vectors and hence the sensitivity vector, and the propagation of Doppler shift uncertainty in the calculation of the velocity components.
    - The uncertainty in the velocity component due to uncertainty in determining the observation and illumination vectors is dependent upon the magnitude of the flow velocity being measured.
    - The variation in measured velocity component error has been demonstrated experimentally using the 2ν-PDV described in chapter 6.

- The process of transforming from a system of non-orthogonal velocity components to an orthogonal system aligned with the experiment will also cause errors to be propagated.

    - The condition number of the transformation matrix can be used, as a measure of how well these errors will propagate.
    - The uncertainty in the observation and illumination vectors will also cause an uncertainty in this transformation process. This will also be dependent upon the flow velocity being measured.

- Other considerations identified are:

    - Limitations due to optical access in experiments.
    - Limitations due to the Mie scattering light intensity.
    - Potential to cancel out laser frequency fluctuations in the transformation to orthogonal velocity components by careful positioning of the views.

These influences of these factors in the selection of a viewing configuration will be discussed in Chapter 8 with the benefit of a computer model of these processes in the propagation of errors to the orthogonal velocity components.

7.6 References

1. Elliott, G.S. and Beutner, T.J., "Molecular Filter Based Planar Doppler Velocimetry", 1999, *Progress in Aerospace Sciences*, Vol. 35, pp 799-845.

2. Nobes, D.S., Wieneke, B., and Tatam, R.P., "Determination of View Vectors from Image Warping Mapping Functions", 2004, *Optical Engineering*, Vol. 43, No. 2, pp 407-414.

3. Kreyszig, E, " *Advanced Engineering Mathematics, 7th Edition*", 1993, Wiley, New York, ISBN

4. Reinath, M.S., "Doppler Global Velocimeter Development for the Large Wind Tunnels at Ames Research Center", 1997, *NASA*, Technical Memorandum 112210.

5. Clancy, P.S., Samimy, M., and Erskine, W.R., "Planar Doppler Velocimetry: Three Component velocimetry in Supersonic Jets", 1999, *AIAA Journal*, Vol. 37, No. 6, pp 700-707.

6. Elliott, G.S., Crafton, J., Beutner, T.J., Carter, C.D., Baust, H.D., and Tyler, C., "Evaluation and optimization of a Multi-component Planar Doppler Velocimetry System", 2005, *AIAA 43rd Aerospace Sciences Meeting and Exhibit*, Reno, Nevada, AIAA 2005-35.

8 Investigation into the selection of viewing configurations for 3D PDV measurements with the aid of an error propagation model

8.1 Introduction

In order to investigate how the various factors, identified in chapter 7, influence the selection of a viewing configuration for 3D PDV measurements, a model has been developed of how the errors will propagate through the PDV calculations to the computed orthogonal velocity components.

This chapter first describes the computer model that has been developed and then investigates how the two main factors; the variation of uncertainty with viewing direction and the transformation to orthogonal velocity components, affect the final level of uncertainty.

The results of the model are then used to investigate the benefits of using a fourth velocity component in the calculation of the orthogonal velocity components. Experimental results are then presented comparing results calculated using three or four measured velocity components.

Finally the results of the error model are compared with the experimental measurements of the velocity field of rotating disc made using the 2ν-PDV system described in chapter 6.

8.2 Description of the error propagation model

The computer model was written using the Matlab package, to take advantage of the built-in scientific and mathematical functions. The first part of the process followed in the model is shown in Figure 8-1.

The first stage is to define the viewing configuration, field-of- view, image size, imaging range of the collection optics and the velocity field to be simulated.

The viewing configuration is defined as a set of bulk view angles (from the centre of the field of view to the centre of the collection optics) defining the rotation, T and elevation P for each view. The laser sheet was assumed to be in the XY plane with the rays within the sheet assumed to be parallel, not diverging.

The field of view was assumed to be 100mm by 100mm, and the collection optics positioned 1.5m away from the region of interest. The image size used was 400x400 pixels. These are typical of conditions found in current experimental set-ups. Scaling information is then determined giving the X and Y co-ordinates for each pixel in an image using the defined field of view and distance from the collection optics.

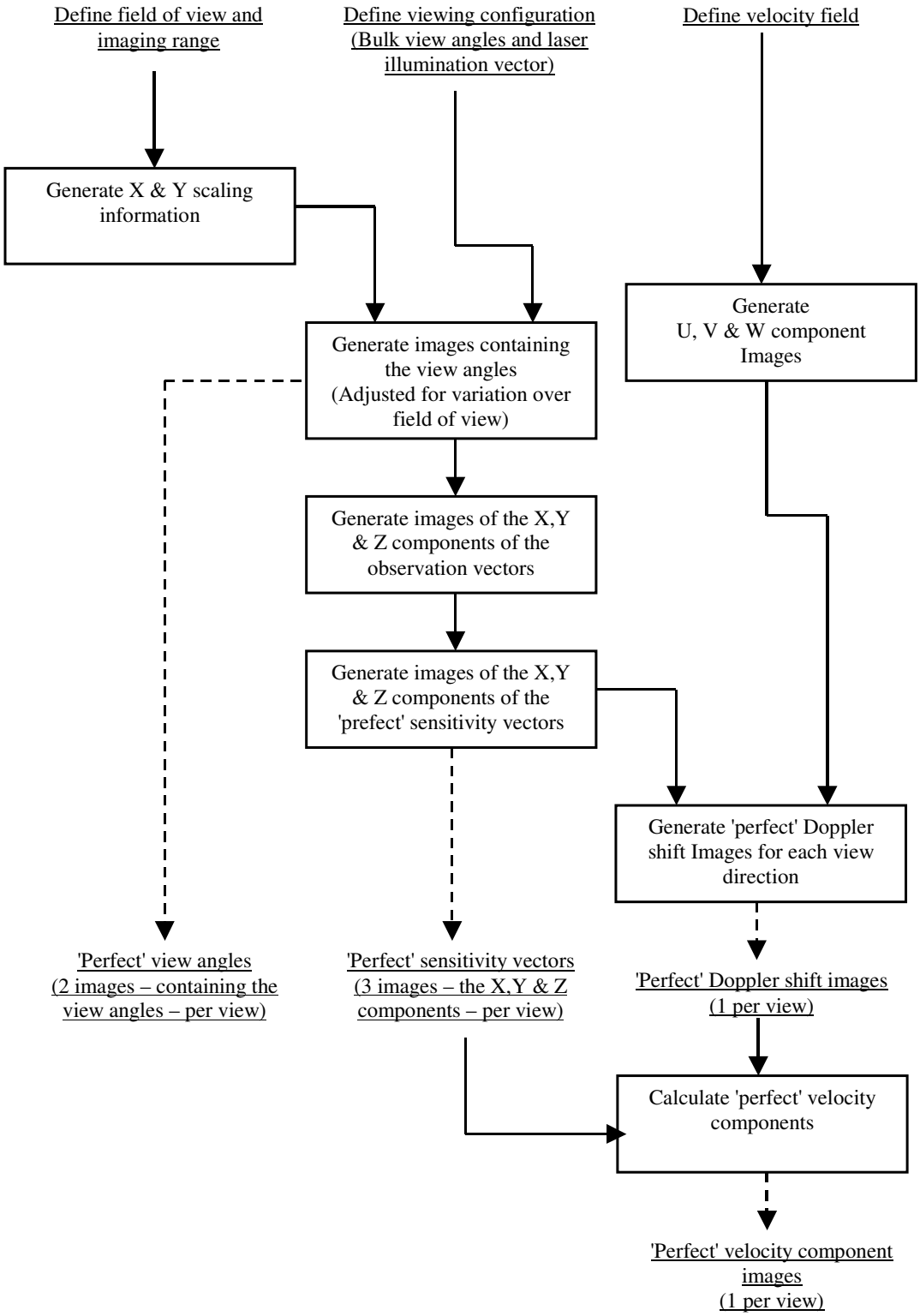

Figure 8-1 Flow diagram detailing the first stage of the computer model – generating the theoretical / 'perfect' measurement data.

The velocity field used is defined either as a constant velocity field or as that of a rotating disc in the XY plane. Three images are created containing the X, Y and Z components of this reference velocity field.

Images containing the view angles for each pixel in an image are generated from the bulk view vectors and corrected for the field-of-view using the scaling information calculated earlier. These are used to calculate the sensitivity vector components by finding the observation vector X,Y and Z components and subtracting the defined laser illumination vector.

From these sensitivity vectors and the defined velocity field, an image of the theoretical Doppler frequency shift is calculated using the Doppler formula. The wavelength of the illumination lights was assumed to be 514.5nm in this calculation. These images of the theoretical Doppler shift, one for each observation direction, can be thought of as being analogous to the Doppler shift that would be calculated in a 'perfect' PDV experiment containing no measurement uncertainty.

As no noise has been introduced in these calculations, the original defined velocity field will be recovered perfectly if the Doppler shift is converted back to the orthogonal velocity components. The only noise introduced will be rounding errors in the calculations. Therefore to simulate a situation typically found in experimental data, it is necessary to introduce a quantity of noise before calculating the velocity components.

From chapter 7, we know that there are two main error sources that we wish to emulate; the first of these is the uncertainty in the measurement of the Doppler shift. This will include error sources that do not depend upon the observation direction but only upon the PDV system components. For example the CCD camera noise, uncertainty in the iodine absorption spectrum and laser frequency uncertainty. The second is the uncertainty in the sensitivity vectors. This introduces error not only in the calculation of each measured velocity component but also when these measured velocity components are transformed to the orthogonal velocity components.

The second stage of the model, shown in Figure 8-2 involves adding measurement uncertainty to the data. Three methods of adding error to the data were used:

The first adds error to the Doppler shift. This is done by adding a random quantity of noise to each pixel in the Doppler shift image, from a normal distribution with a width specified according to the PDV system to be modelled. This is introduced after the calculation of the theoretical / perfect Doppler shift image, but before the calculation of the measured velocity components. The result is two sets of Doppler shift images, the first containing the perfect / theoretical calculated Doppler shift and the second containing the Doppler shift with added noise.

The uncertainty in the sensitivity vectors is introduced by adding a random quantity of noise, again taken from a normal distribution, to the images containing the view angles for each view. From this a new set of sensitivity vectors are calculated which includes this error.

The third method for introducing noise is to add noise directly to each measured velocity component. This is not physically accurate as the noise is present before this calculation is performed in PDV processing. This method of introducing error is used only when the effect of the transformation to orthogonal components is to be investigated and a constant error level is required on each velocity component.

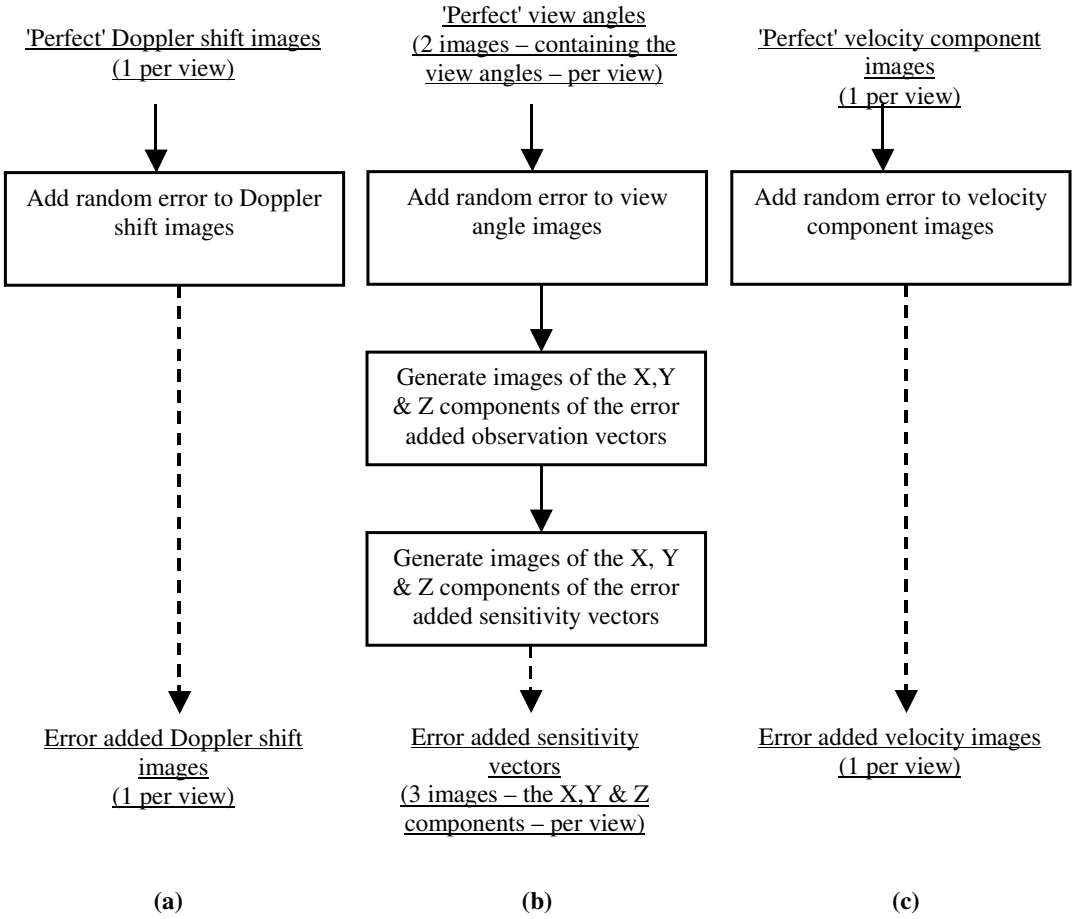

Figure 8-2 Flow diagram showing the second stage of the computer model – adding measurement uncertainty. (a) Simulating Doppler shift uncertainty (b) Simulating view angle uncertainty (c) Adding a constant level of error to each velocity component

The final stage of the processing proceeds in the same way as for experimental PDV measurements. Each of the Doppler shift images is converted to a velocity component using the Doppler formula and the sensitivity vector component images. These are then transformed to the orthogonal velocity components, using either the three component (3C) or four component (4C) methods defined in chapter 4. This yields three images containing the U, V and W velocity components of the velocity field.

Using the model it is possible to assess the level of error in the final calculated orthogonal velocity components for any viewing configuration for any defined velocity field. It is also possible to vary the sources and level of the noise added to the calculated velocity components. Just the effect of the transformation matrix can be assessed by adding a constant level of error to each velocity component as in Figure 8-2 (c). The more realistic method where variable noise determined by the viewing

direction is added can be modelled by adding error to both the Doppler shift images and the view angle images, Figure 8-2 (a) and (b). By transforming the non-orthogonal velocity components to the orthogonal components using the error added sensitivity vectors the effect this has can also be investigated, alternatively the perfect sensitivity vectors can be used to remove this effect. The final level of error in the calculated velocity can be determined by subtracting the initial defined velocity field from the calculated velocity field.

The influences these error sources have on the final level of error in the orthogonal velocity components is discussed further in section 8.3. Section 8.3.1 looks at the effect the variation in uncertainty in the velocity components has upon the selection of viewing configurations. Section 8.3.2 looks at the effect the uncertainty in the sensitivity vectors will have upon the transformation to U, V and W.

8.3 Investigation of the factors influencing the selection viewing configurations using computed results

Several viewing configurations, that could be used in experimental implementations, including two that have been previously reported, were investigated using the error propagation model described above. To allow the investigation of the benefits of using the four velocity components in the calculation of the velocity a fourth view has been added to each of the configurations. Where possible this view has been selected to have similar viewing angles to the other three. For the previously reported configurations no account was taken for possible obstruction of this additional view.

The viewing configurations used are defined in Table 8-1 using the viewing angles shown in Figure 8-3. The condition numbers, defined in chapter 7, for each configuration are shown in Table 8-2.

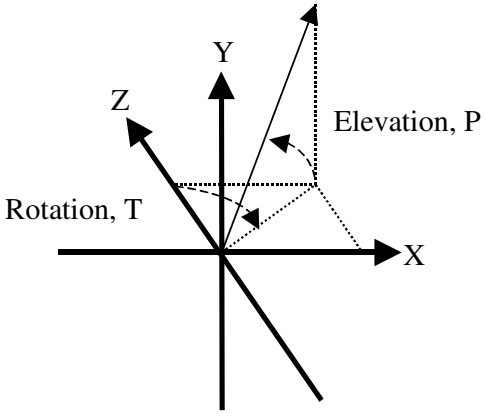

Figure 8-3 Definitions of viewing angles used to describe viewing geometries. Rotation, T (0-360^o) and elevation, P (±90^o)

Table 8-1 Definitions of the viewing configurations used in the investigation

Configuration	View angle (^{o})	View 1	View 2	View 3	View 4
A	T	180	180	225	180
	P	45	-45	0	0
B	T	135	135	225	135
	P	45	-45	0	0
C	T	135	135	45	135
	P	45	-45	0	0
D	T	225	225	-45	1350
	P	45	-45	0	
E	T	0	Four orthogonal laser sheets in the same		
	P	0	plane used sequentially		
F	T	144	144	26	144
	P	40	-40	0	0

Table 8-2 Condition numbers for the viewing configurations used in the investigation

Configuration	Condition Number			
	κ_1	κ_2	κ_3	κ_4
A	14.75	9.13	10.41	14.55
B	7.11	5.03	6.63	8.98
C	3.28	1.50	3.17	3.72
D	6.15	2.79	4.49	3.68
E	4.50	2.41	3.87	4.00
F	3.50	1.40	3.14	3.28

In configuration A, the views are aligned so that each of the view vectors, from the origin of the coordinate system to the cameras, are aligned such that the bulk view vector of each view is a function of only two of the Cartesian co-ordinate system variables. All view a laser light sheet in the positive x direction. The views are all on the same side of the laser sheet and as such will be poorly conditioned, demonstrated by the large values for the condition numbers.

Configuration B again has all four views on the same side of the light sheet. This configuration is similar to Configuration A however the set-up aims to increase the spread of the sensitivity vectors so as to improve the condition number.

Configuration C is similar to Configuration B except that one view has now been rotated, by 180°, about the y-axis. This results in a one view that views from the opposite side of the laser light sheet. All four views are in located in forward scatter with respect to the laser direction vector, which is again in the position x direction. The conditioning is much improved by having views located on both sides of the sheet.

Configuration D uses similar view angles to configuration C expect that now the first three views are all located in back scatter. Again the illumination direction remains unchanged.

Configuration E follows the configuration of Roehle et al[1], which consisted of a single view and three laser sheets in the same plane propagating from different orthogonal directions. The fourth measured component is added by including a fourth illumination direction. The sensitivity vectors all have a positive Z component and at the origin are a function of only two of the Cartesian co-ordinate variables.

The reported sensitivity vectors of Reinath[2] are used in configuration F. This is similar to Configuration D. The fourth view has been added between views 1 & 2, level with view 3. Again the illumination direction is in the positive x direction.

Low values of $\kappa(A)$ are achieved for configurations where the sensitivity vectors are well spread. This is evident for configurations where one of the sensitivity vectors is on the opposite sides to the light sheet (Configurations C, D & F) compared to the having all three sensitivity vectors on the same side (Configurations A & B). There is a small change in view direction vectors in Configuration A to Configuration B. This however leads to a halving of $\kappa(A)$. A further 50% reduction can be achieved on the value of Configuration B by moving one of the view directions to the other side of the light sheet as in Configuration C.

All definitions of $\kappa(A)$ show a similar trend in the magnitude of $\kappa(A)$ for the same configuration. Low values of $\kappa(A)$ are obtained for conditions where the sensitivity vectors are well spread or are close to orthogonal and are close to the directions of the Cartesian co-ordinate system of the experiment. High values of $\kappa(A)$ are determined where the sensitivity vectors have similar direction.

8.3.1 Computed effect of the variation in measured velocity component uncertainty with viewing direction

The first effect investigated was the result of no longer assuming a constant level of uncertainty in all the non-orthogonal velocity components, instead a variable level of error was added to each velocity component according to it's observation direction.
Figure 8-4 shows the remaining error in the calculated U, V and W components after the subtraction of the initial defined velocity field. Here histograms are shown for two configurations A and B for two cases; when a constant level of uncertainty is introduced to all views and when a variable level of uncertainty is introduced depending upon the observation direction of the view.

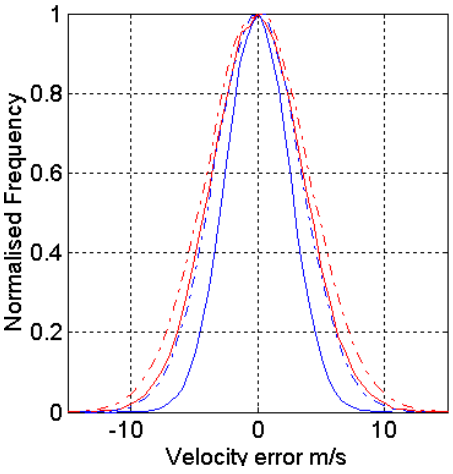

U

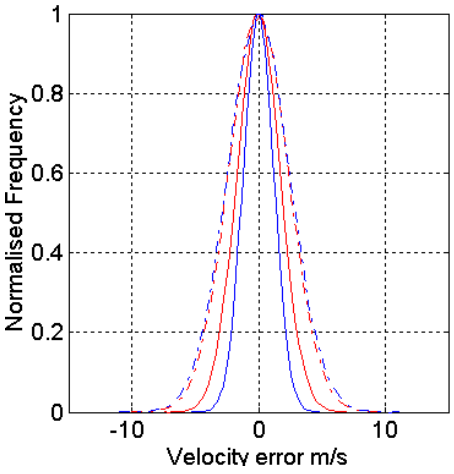

V

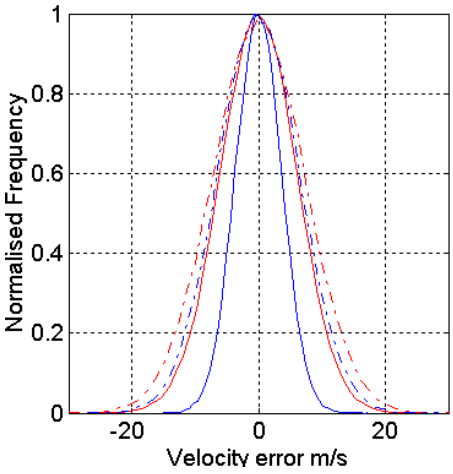

W

Figure 8-4 Histograms of the error in the orthogonal velocity components for configuration A (red) and configuration B (blue); Solid lines are for calculation with no variation in the errors on measured components; Dashed lines are for calculation with a variation in error with observation direction. A velocity field of (10,100,10) m/s was used.

As discussed in chapter 7 the level of uncertainty in a measured component is also dependent upon the velocity field being measured, for this calculation a velocity field of (10,100,10) ms^{-1} was assumed. For the calculation using a constant level of uncertainty in all of the velocity components, noise was added randomly from a normal distribution with a standard deviation of $1.2ms^{-1}$. This value was chosen to produce final error levels in the orthogonal velocity components that approximately matched the magnitude of the errors observed in a typical experimental set-up. When the uncertainty of each velocity component was determined according to it's observation direction, an uncertainty in the Doppler shift measurement of 4.5MHz was assumed as well as an uncertainty in each of the view angles of 1^o. The calculation of the orthogonal components was performed using only the first three non-orthogonal velocity components using the 3C method, described in chapter 4.

It can be seen that if a constant level of noise is added to each measured velocity component then configuration B will lead to smaller final errors in all three orthogonal components. This is because configuration B has better conditioning for the transformation (condition number $\kappa_1 \sim 7$) compared to configuration A (condition number $\kappa_1 \sim 14$).

However when the variation in error on the measured components is included the conditioning of the matrix becomes less important when considering the choice of viewing configuration. With this included in the calculation the errors in the orthogonal components for configuration B are still better for the U and W components, but this improvement is reduced. The error in the V component is now marginally worse than that for configuration A. This is due to configuration B having two views (views 1 & 2) positioned significantly into forward scatter and these measured components will have increased errors, as described in section 7.2. In configuration A however these views are not located in forward scatter, and therefore have smaller errors in the measured components.

Due to the dependency of the uncertainty in measured components upon the velocity field being measured, a particular viewing configuration may be better for one flow and worse for a different flow field. For example if the velocity field used in the calculations is increased five fold to (50,500,50) ms^{-1} then it is now better to select configuration A which had better levels of error for all three orthogonal components than for configuration B. This is shown in Figure 8-5, and the standard deviations of the orthogonal component residuals for this calculation as well as for the other configurations are shown in Table 8-3.

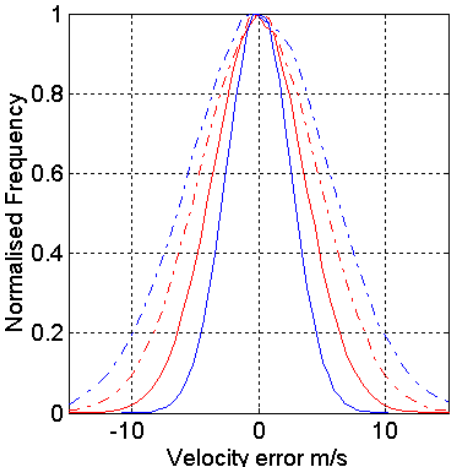

U

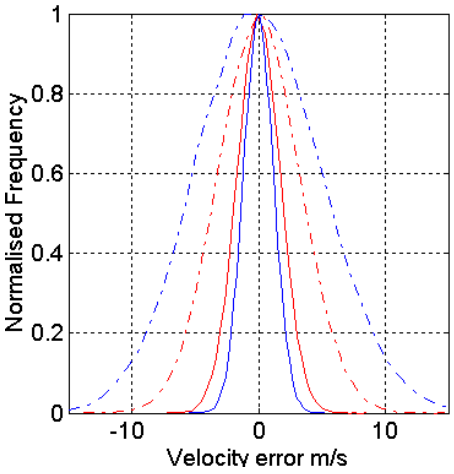

V

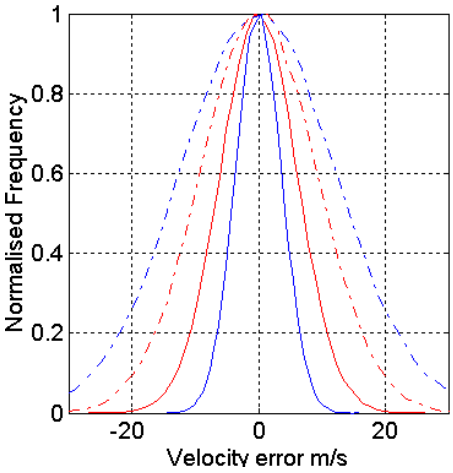

W

Figure 8-5 Histograms of the error in the orthogonal velocity components for configuration A (red) and configuration B (blue); Solid lines are for calculation with no variation in the errors on measured components; Dashed lines are for calculation with a variation in error with observation direction. A velocity field of (50,500,50) m/s was used.

Table 8-3 Computed standard deviation of orthogonal component residuals (computed values minus original values) for constant error and variable error on measured velocity components for a velocity field of (10,100,10) m/s

	Condition Number [1]	Standard deviation of computed orthogonal component residuals (m/s)					
		Constant error added to velocity components [2]			Variable error added depending upon observation direction [3]		
		U	V	W	U	V	W
A	14.75	3.6	1.7	6.0	4.0	2.4	7.3
A*	14.75	-	-	-	4.6	3.2	9.1
B	7.11	2.5	1.2	3.7	3.4	2.5	6.4
B*	7.11	-	-	-	5.5	5.0	12.2
C	3.28	1.5	1.2	1.1	3.4	2.5	2.5
D	6.15	0.8	2.1	2.2	0.9	2.3	2.3
E	4.50	1.2	2.1	1.2	1.6	3.0	1.6
F	3.50	1.3	1.4	1.0	2.5	2.7	1.9

[1] Condition number $\kappa 1$.

[2] Standard deviation $1.2ms^{-1}$.

[3] Errors calculated using a Doppler shift uncertainty of 4.5 MHz and uncertainty in view angles of 1^o.

*** Velocity field of (50,500,50) m/s used.**

8.3.2 Computed effect of the uncertainty in the sensitivity vectors on the transformation to orthogonal velocity components

As well as introducing a variation in the error on measured velocity components the uncertainty in the view angles will also introduce error into the transformation from the measured velocity components to the orthogonal velocity components. As discussed in section 7.3.2, the level of this uncertainty is related to the magnitude of the velocity components and will therefore also vary with flow velocity.

Table 8-4 shows the standard deviations of the residuals for each of the configurations for the two cases. In the first method variable error was added as described above, however no account of the angle uncertainty is made in the transformation from measured velocity components to orthogonal components as the perfect sensitivity vectors are used. The second method, again uses variable error depending upon observation direction and also uses the sensitivity vectors with uncertainty added, to both calculate the measured velocity components and to transform them to the orthogonal components.

Table 8-4 Computed standard deviation of orthogonal component residuals (computed values minus original values) when angle uncertainty is excluded / included in the transformation to orthogonal velocity components for a velocity field of (10,100,10) m/s

		Standard deviation of computed orthogonal component residuals (m/s)[2]					
	Condition Number [1]	No transformation error due to angle uncertainty [3]			Transformation error included [4]		
		U	V	W	U	V	W
A	14.75	4.0	2.4	7.3	4.9	2.6	8.6
A*	-	4.6	3.2	9.1	14.5	6.7	24.2
B	7.11	3.4	2.5	6.4	3.9	2.6	7.0
B*	-	5.5	5.0	12.2	11.2	6.7	18.5
C	3.28	3.4	2.5	2.5	3.9	2.6	3.1
C*	-	5.5	5.0	3.1	11.3	6.7	9.5
D	6.15	0.9	2.3	2.3	1.0	2.6	2.8
D*	-	1.0	2.8	2.5	3.0	6.7	8.3
E	4.50	1.6	3.0	1.6	2.1	3.6	2.1
E*	-	1.7	4.9	1.7	6.4	11.1	6.4
F	3.50	2.5	2.7	1.9	2.9	2.9	2.1
F*	-	3.8	4.9	2.6	8.6	7.9	6.8

[1] Condition number $\kappa 1$.

[2] The 3C method of calculating the orthogonal components was used – errors calculated using a Doppler shift uncertainty of 4.5 MHz and uncertainty in view angles of 1^o.

[3] Perfect sensitivity vectors used in transformation to orthogonal components.

[4] Sensitivity vectors containing uncertainty used in transformation to orthogonal components.

*** Velocity field of (50,500,50) m/s used.**

The inclusion of this error source in the calculation results in an increase in the overall level of error in all three orthogonal components, however the magnitude of this increase is not the same for all components and depends not only upon the particular viewing configuration but the magnitude of the flow velocity. The results shown in Table 8-4 were calculated using an uncertainty in view angles of 1^o. At this level of uncertainty it can be seen that this can be an important source of error in the calculation, especially for greater flow magnitudes where it greatly increases the overall error level. Although the estimate of 1^o is probably excessive it can be seen that for 3D PDV measurements minimising this source of error is important and can lead to greatly improved error levels.

8.3.3 Condition number as a measure of viewing configuration optimisation

To compare the relationship between the error levels in the orthogonal velocity components with the condition number of a viewing configuration these were plotted against each other for various viewing configurations. To generate multiple viewing configurations, the first two views were fixed, view 1 at 135^o and 45^o and view 2 at 135^o and 0^o for the view angles T and P respectively. The third view is varied over the possible view angles, $\pm 60^o$ from normal to the light sheet, in 10^o increments. This

generates 392 viewing configurations. The fixed views were chosen as an example of typically view angles found in PDV experiments. The error in the orthogonal components was then found for each configuration along with the condition number and this is shown in Figure 8-6.

From these results and from Table 8-3 and Table 8-4 it can be seen that typically the lower the value of the condition number the lower the level of uncertainty in the calculated orthogonal components. This is not however true in all cases, as demonstrated above this can also be seen in configuration D which has better computed error levels than for configurations C, E and F, which have lower condition numbers. The condition number can be used as an approximate guide to the suitability of a viewing configuration, but should not be the only factor considered when attempting to optimise a viewing configuration.

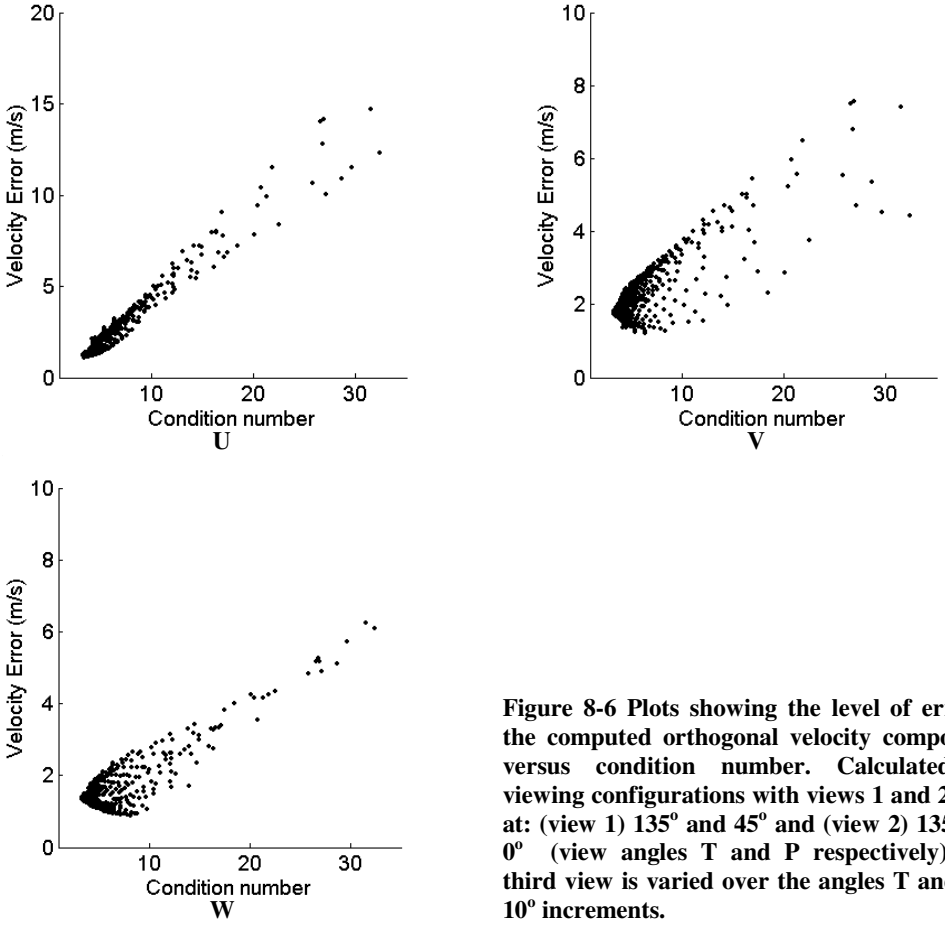

Figure 8-6 Plots showing the level of error in the computed orthogonal velocity components versus condition number. Calculated for viewing configurations with views 1 and 2 fixed at: (view 1) 135^o and 45^o and (view 2) 135^o and 0^o (view angles T and P respectively). The third view is varied over the angles T and P in 10^o increments.

8.4 Investigation into the effect of using additional velocity components in the transformation to orthogonal velocity components

To make 3D PDV measurements it is necessary to measure at least three components of the velocity in order to calculate the orthogonal velocity components. A method of using additional velocity components (to the three needed) was proposed in chapter 4, in this section the possible benefits of using this additional data in the transformation are assessed.

8.4.1 Computed effect of using an additional velocity component in the calculation of the orthogonal velocity components

Using the error propagation model described in section 8.2 the viewing configurations defined in Table 8-1 were processed using the first three components (3C method) and all four components (4C method) to calculate the orthogonal velocity components. The theoretical velocity field was then subtracted from these computed results and the difference found. The error added to each velocity component was calculated depending upon its observation direction, with contributions from the Doppler shift uncertainty (estimated previously as 4.5MHz) and the uncertainty in the view angles (estimated previously as 1^o). The uncertainty in the view angles was also included in the transformation to orthogonal velocity components. These errors were added as described in section 8.2. The velocity field used in the calculations was (10,100,10) ms^{-1}. As the level of error in the measured components depends upon the flow velocity a velocity field of (50,500,50) ms^{-1} was also used for each configuration to allow a comparison for higher flow velocities. For these configurations no attempt was made to optimise the positioning of the fourth view, rather it was placed so that the viewing angles were similar to the original three views.

Figure 8-7 shows the histograms of the remaining error for two of the configurations, A and B, for both methods of calculating the orthogonal components using a velocity field of (10,100,10) ms^{-1}. Here the solid lines represent the error when the orthogonal components are calculated using the 3C method and the dashed lines when calculated using the 4C method. It can be seen that the addition of a fourth measured component significantly decreases the level of error in two (U and W) of the three orthogonal components while the third (V) remains unchanged for both configurations.

Similar histograms are shown for configurations C and D in Figure 8-8 and configurations E and F in Figure 8-9. Similar improvements in the error level can be seen for the other configurations with one or two components having improved error levels with the remaining components unchanged or slightly degraded. The standard deviation of the error for all these configurations is shown in Table 8-5 for calculations using the 3C method and the 4C method with and without weighting. The weighting used here for a component was found by the ratio of the smallest error of all the velocity components, over the error on that velocity component. Table 8-6 shows the percentage change in the standard deviation of the error when the orthogonal velocity components are calculated using four components or four components with weighting (4Cw method) instead of three components.

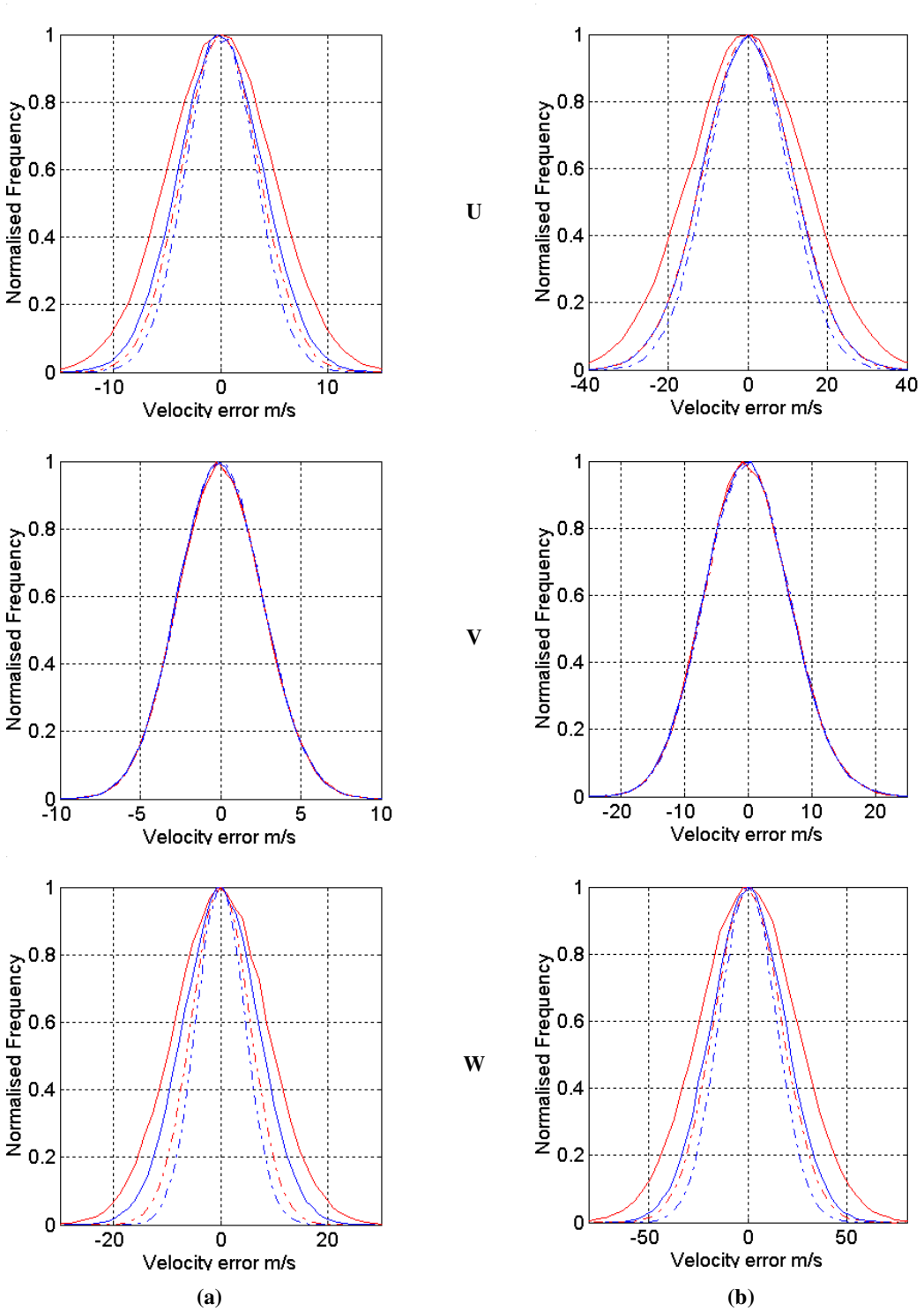

Figure 8-7 Histograms of error in orthogonal components for configuration A (red) and configuration B (blue). Solid lines show the error using the 3C method of calculating the orthogonal velocity components and the dashed lines show the error using the 4C method for (a) a velocity field of (10,100,10) ms^{-1} and (b) a velocity field of (50,500,50) ms^{-1}.

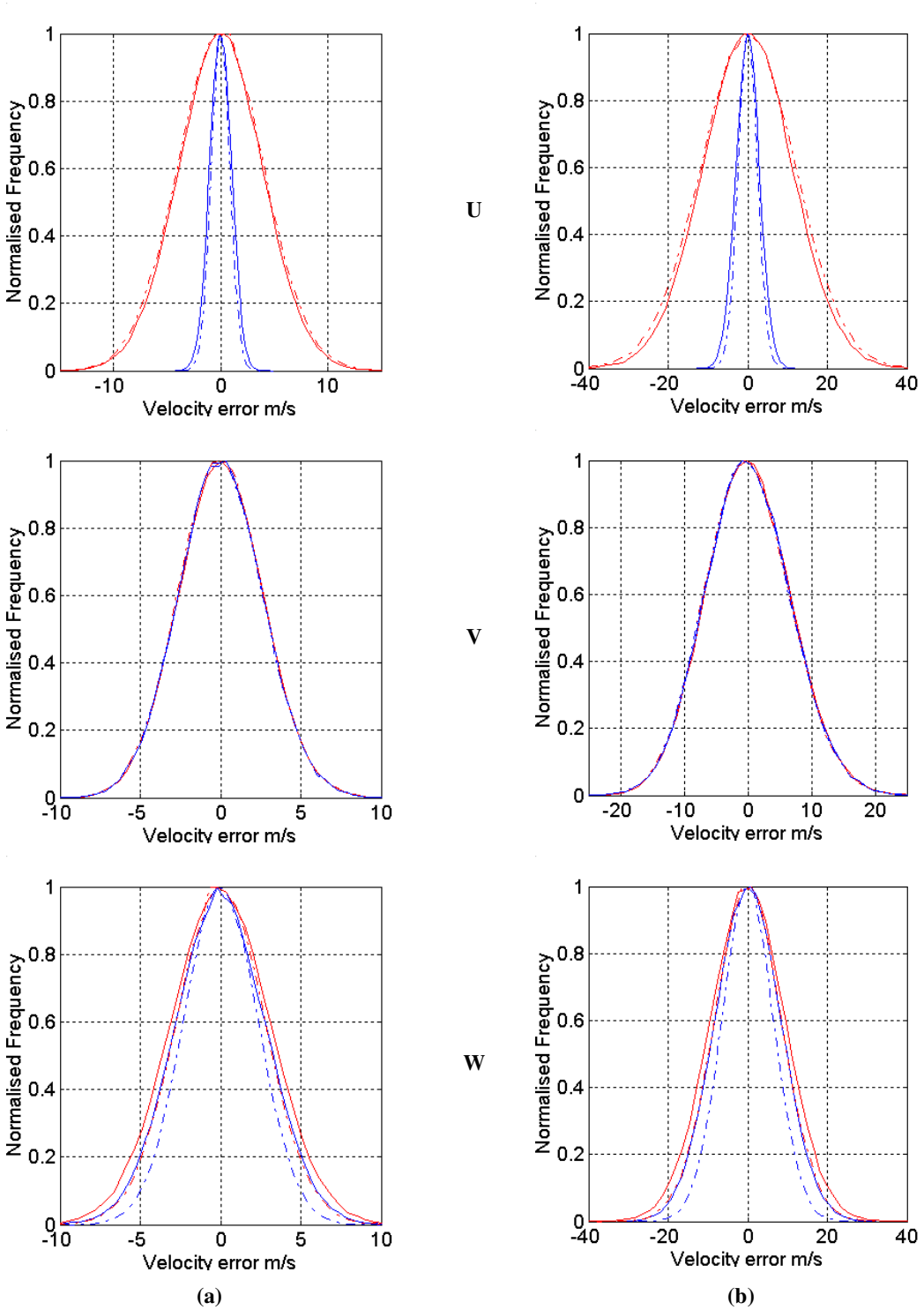

Figure 8-8 Histograms of error in orthogonal components for configuration C (red) and configuration D (blue). Solid lines show the error using the 3C method of calculating the orthogonal velocity components and the dashed lines show the error using the 4C method for (a) a velocity field of (10,100,10) ms^{-1} and (b) a velocity field of (50,500,50) ms^{-1}.

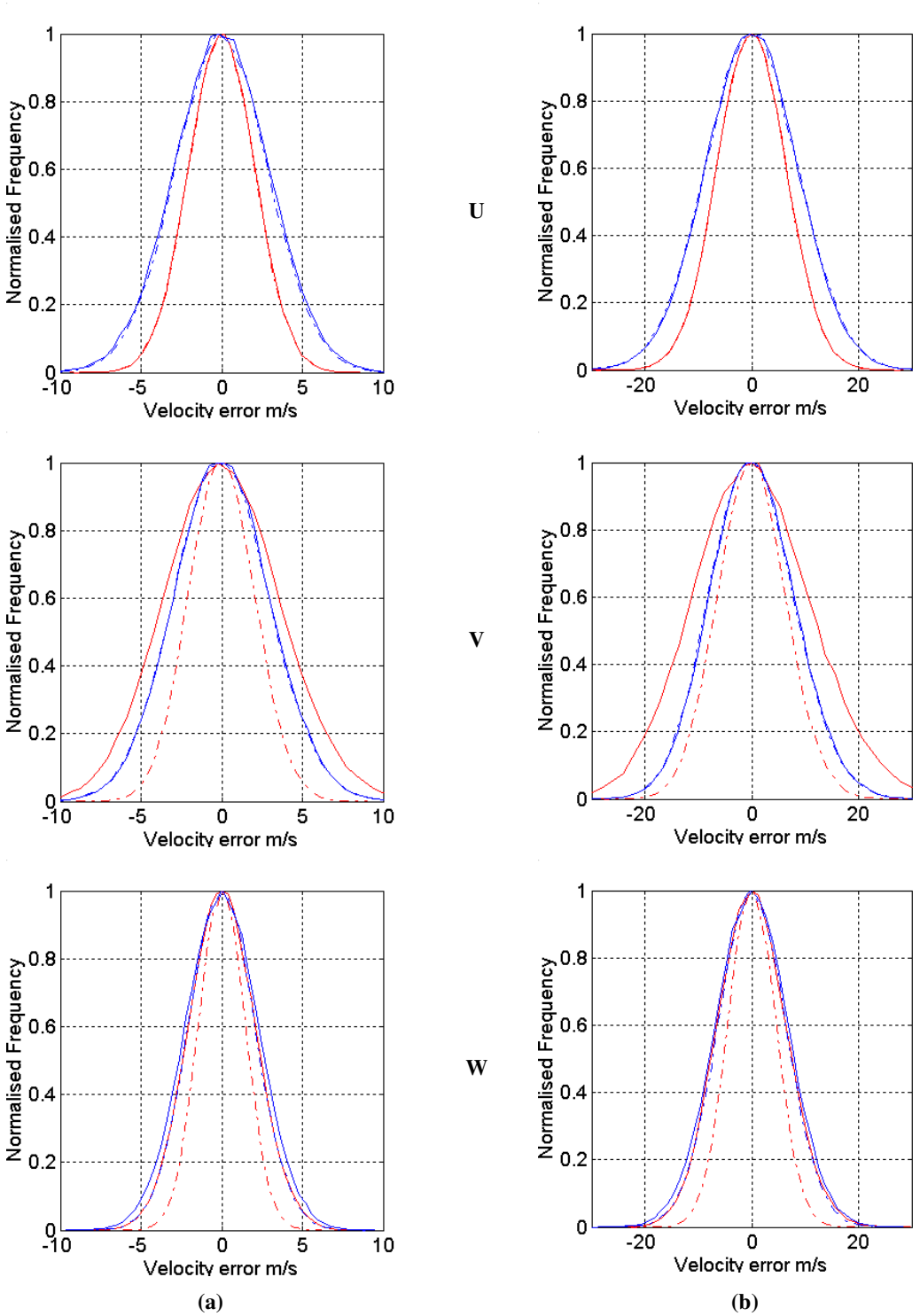

Figure 8-9 Histograms of error in orthogonal components for configuration E (red) and configuration F (blue). Solid lines show the error using the 3C method of calculating the orthogonal velocity components and the dashed lines show the error using the 4C method for (a) a velocity field of (10,100,10) ms^{-1} and (b) a velocity field of (50,500,50) ms^{-1}.

Table 8-5 Computed standard deviation of orthogonal component residuals (computed values minus original values) for a velocity field of (10,100,10) m/s.

	Standard deviation of computed orthogonal component residuals (m/s)								
	3C method			4C method			4Cw method		
	U	V	W	U	V	W	U	V	W
A	4.9	2.6	8.6	3.6	2.6	5.5	3.6	2.6	5.5
A*	14.5	6.7	24.3	11.2	6.7	17.1	11.1	6.7	17.1
B	3.9	2.6	7.0	3.2	2.6	4.6	2.9	2.6	4.4
B*	11.2	6.7	18.5	10.1	6.7	14.4	9.1	6.7	14.1
C	3.9	2.6	3.1	4.0	2.6	2.7	4.0	2.6	2.7
C*	11.2	6.7	9.4	12.0	6.7	8.5	12.9	6.7	8.5
D	1.0	2.6	2.8	0.9	2.6	2.3	0.9	2.6	2.3
D*	2.9	6.7	8.2	2.4	6.7	6.6	2.4	6.7	6.6
E	2.1	3.6	2.1	2.1	2.1	1.5	2.1	2.1	1.5
E*	6.4	11.2	6.4	6.4	6.4	4.5	6.4	6.5	4.8
F	2.9	2.9	2.3	2.9	2.9	2.1	2.9	2.9	2.0
F*	8.6	7.9	6.8	8.7	7.9	6.4	9.1	7.9	6.4

* Velocity field of (50,500,50) m/s used.

Table 8-6 Showing the percentage change in standard deviation when the orthogonal velocity components are calculated using the 4C method over the 3C method.

	Condition Number (1)	% Change in standard deviation using 4C method			% Change in standard deviation using 4Cw method		
		U	V	W	U	V	W
A	14.75	-26.5	0.0	-36.0	-26.5	0.0	-36.0
A*	-	-22.8	0.0	-29.6	-23.4	0.0	-29.6
B	7.11	-17.9	0.0	-34.3	-25.6	0.0	-37.1
B*	-	-9.8	0.0	-22.2	-18.8	0.0	-23.8
C	3.28	2.6	0.0	-12.9	2.6	0.0	-12.9
C*	-	7.1	0.0	-9.6	15.2	0.0	-9.6
D	6.15	-10.0	0.0	-17.9	-10.0	0.0	-17.9
D*	-	-17.2	0.0	-19.5	-17.2	0.0	-19.5
E	4.50	0.0	-41.7	-28.6	0.0	-41.7	-28.6
E*	-	0.0	-42.9	-29.7	0.0	-42.0	-25.0
F	3.50	0.0	0.0	-8.7	0.0	0.0	-13.0
F*	-	1.2	0.0	-5.9	5.8	0.0	-5.9

(1) Condition number, κ_1

* Velocity field of (50,500,50) m/s used.

From these results it can be seen clearly that the addition of fourth velocity component in the calculation of the orthogonal velocity components can be used to improve the error in the results. For most configurations one or two of the three orthogonal components are improved, however for some configurations this is at the expense of the error in the remaining components. For example using the 4C with configuration C will lead to improved out-of-plane measurements at the expense of the in-plane measurements. This effect is greater for the higher velocity field where the U error is 15% higher than when using the 3C method. For configuration E, were multiple light sheets together with a single observation direction normal to the sheet are used, the improvement in error level by using a fourth sheet is very significant, with a 42% reduction in the V error and a 29% reduction in the W error. For this configuration the velocity components would be captured sequentially[1] so the measurement of a fourth component would be easy to implement. The improvement achieved using the 4C method seems to be reduced as the magnitude of the velocity field being measured increases, although this is not the case for configuration D were the percentage reduction in error is greater.

It can also be seen that the use of variable weighting leads to mixed results, with further improvements in the level of error for configurations B and F, with the remaining configurations having unchanged or slightly increased error levels. The weighting used here may not be the optimal weighting scheme to use and this would require further investigation.

However it may be that by selecting the 'best' three of the four views the reduction achieved using the 4C method can be obtained using the conventional 3C. This was investigated by calculating the U, V and W components using all four combinations of three views and the 3C method. The lowest achievable error level in each orthogonal component using the 3C method was found. This is shown in Table 8-7 along with the error levels found using the 4C method and the percentage change in standard deviation when changing from using the 'best' 3C method to the 4C method.

When the best three views are used to calculate each velocity component, the benefit of calculating the orthogonal velocity components using the 4C method is reduced. However when using the 4C method further improvement is possible in the uncertainty of out-of-plane component for all of the configurations. Configuration D also shows an improvement in the U component when this is calculated using the 4C method.

From this it can be seen that the actual benefit of calculating the orthogonal velocity components using additional velocity components will depend upon the viewing configuration used. Measuring a fourth velocity component will allow the calculation of the orthogonal velocity components with reduced uncertainty over the calculated using just three components. The optimal results will be achieved by using a combination of the two methods, selecting the optimal method for the calculation of each orthogonal component. For example if configuration C were used, the results of the model would suggest that the U component should be calculated using the 3C method using views 1,2 and 3. The V component should be calculated using the either the 3C or 4C methods but the W component should be calculated using the 4C method.

Table 8-7 Comparison of the computed standard deviation of orthogonal component residuals (computed values minus original values) using the best 3 of 4 views and the 4C method for a velocity field of (10,100,10) m/s.

	Standard deviation of computed orthogonal component residuals (m/s)								
	'Best' 3C method			4C method			% Change		
	U	V	W	U	V	W	U	V	W
A	3.6	2.6	5.8	3.6	2.6	5.5	0.0	0.0	-5.2
A*	11.1	6.7	18.0	11.2	6.7	17.1	0.9	0.0	-5.0
B	2.9	2.6	5.1	3.2	2.6	4.6	10.3	0.0	-9.8
B*	9.1	6.7	15.8	10.1	6.7	14.4	11.0	0.0	-8.9
C	3.9	2.6	2.9	4.0	2.6	2.7	2.6	0.0	-6.9
C*	11.2	6.7	9.1	12.0	6.7	8.5	7.1	0.0	-6.6
D	1.0	2.6	2.8	0.9	2.6	2.3	-10.0	0.0	-17.9
D*	2.9	6.7	8.2	2.4	6.7	6.6	-17.2	0.0	-19.5
E	2.1	2.1	2.1	2.1	2.1	1.5	0.0	0.0	-28.6
E*	6.4	6.4	6.4	6.4	6.4	4.5	0.0	0.0	-29.7
F	2.9	2.9	2.3	2.9	2.9	2.1	0.0	0.0	-8.7
F*	8.6	7.9	6.8	8.7	7.9	6.4	1.2	0.0	-5.9

* Velocity field of (50,500,50) m/s used.

8.4.2 Experimental observation of the benefits of using the 4C in the calculation of the orthogonal velocity components

To further demonstrate the benefit of using a fourth velocity component in the calculation of the orthogonal velocity components, results from the 3D 2ν-PDV system, described in chapter 6, were processed using the 3C and 4C methods. The measurements used were made on the velocity field of a rotating disc using the two different viewing configurations shown in Table 8-8. The two configurations are similar to configurations A and B defined in section 8.3 however due to physical limitations on the positioning of views less elevation than desired was possible. The disc used was rotating at a frequency of 105Hz and the common field of view after de-warping was approximately 100x100mm, giving a velocity range of $\pm 33 ms^{-1}$ in the field of view. For this set-up the view angle would vary by $\pm 2^o$ over the image.

Table 8-8 Approximate viewing angles used for experimental measurements on a rotating disc and for comparison with modelled results.

Configuration	View Angles (^{o})	1	2	3	4
A_{exp}	T	180 $\pm 2^o$	180 $\pm 2^o$	-135 $\pm 2^o$	167.7 $\pm 2^o$
	P	20.75 $\pm 2^o$	-20.75 $\pm 2^o$	0 $\pm 2^o$	0 $\pm 2^o$
B_{exp}	T	135 $\pm 2^o$	135 $\pm 2^o$	-135 $\pm 2^o$	144 $\pm 2^o$
	P	21.9 $\pm 2^o$	-21.9 $\pm 2^o$	0 $\pm 2^o$	0 $\pm 2^o$

The measured velocity components for each viewing configuration were then processed using either the first three components only or all four components, to calculate the orthogonal velocity components. The error in these calculated orthogonal components is then found by subtracting the theoretical velocity component for the rotating disc. The standard deviations of the error for both the normal and increased sensitivity schemes are shown in Table 8-9 with the percentage change shown in Table 8-10. Histograms of the remaining error after the theoretical velocity has been subtracted can be seen in Figure 8-10.

The addition of a fourth measured velocity component improves the error level in at least two of the final orthogonal components. The use of weighting in the calculations (shown in Table 8-9 and Table 8-10) can be seen to have minimal effect on the propagated error levels as suggested by the computer model although alternative weighting schemes may have more effect. For configuration A the error of the U and W components respectively are reduced by around 15% and 25% when using a fourth velocity component. The reductions for configuration B are less but the U component error is still reduced by around 9% when using a fourth component while the W component is reduced by around 25%.

Table 8-9 Standard deviation of orthogonal component residuals (experimental values minus theoretical values) for a velocity field of a rotating disc when calculated using the 3C, 4C and 4Cw methods

	Standard deviation of the orthogonal component residuals (m/s)								
	3C method			4C method			4Cw method		
	U	V	W	U	V	W	U	V	W
A_{exp}[1]	6.1	10.2	9.3	5.3	10.2	7.0	5.2	10.2	6.9
A_{exp}[2]	3.3	5.6	5.0	2.8	5.5	3.7	2.8	5.5	3.6
B_{exp}[1]	4.0	6.9	6.0	3.6	6.9	4.4	3.6	6.9	4.4
B_{exp}[2]	2.4	4.2	3.2	2.2	4.2	2.4	2.2	4.2	2.4

[1] Normal sensitivity scheme, [2] Increased sensitivity scheme

Table 8-10 Showing the percentage change in standard deviation when the orthogonal velocity components are calculated using the 4C method over the 3C method.

	% Change in standard deviation using 4C method			% Change in standard deviation using 4Cw method		
	U	V	W	U	V	W
A_{exp}[1]	-13.1	0.0	-24.7	-14.8	0.0	-25.8
A_{exp}[2]	-15.2	-1.8	-26.0	-15.2	-1.8	-28.0
B_{exp}[1]	-10.0	0.0	-26.7	-10.0	0.0	-26.7
B_{exp}[2]	-8.3	0.0	-25.0	-8.3	0.0	-25.0

[1] Normal sensitivity scheme, [2] Increased sensitivity scheme

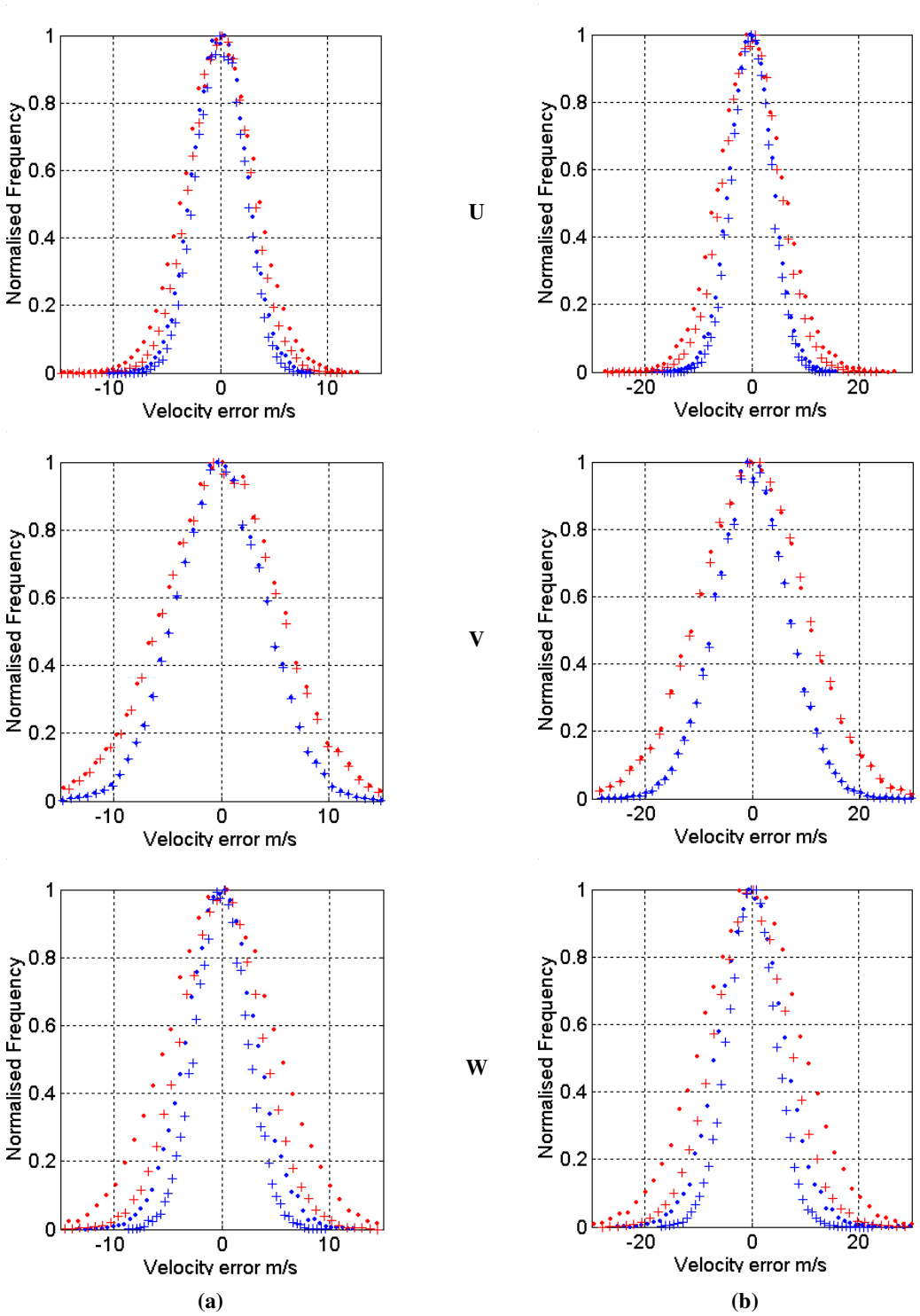

Figure 8-10 Histograms of the error in the experimental orthogonal velocity components for configuration A_{exp} (red) and Bexp(blue) when calculated using the 3C (dots), and 4C (crosses) methods. Experimental measurements are using (a) the increased sensitivity scheme and (b) the normal sensitivity scheme.

8.5 Comparison of the error propagation model with experimental results obtained using the 2ν-PDV system

To allow the model to be used in the future to predict the accuracy of viewing configurations the level of Doppler shift and view angle uncertainty for the experimental system being modelled must be determined. This was done by comparing the level of error found on experimental results with the level found via modelled results. As the error level has been shown to be dependent upon the velocity field being measured; the same velocity field must also be used as the input into the computer model as was measured experimentally.

In order to determine the level of error on experimental measurements a known velocity field has to be measured, in this case the velocity field of a rotating disc was used as in section 8.4.2. and the measurements used for this comparison where made using the viewing configurations described in Table 8-8.

Although these results were captured using the 3D 2ν-PDV system described in chapter 6, this analysis is non-specific to the 2ν-PDV technique and is equally applicable to a conventional 3D PDV system. However the use of the two-frequency technique removes the other potential error sources of pixel misalignment and polarisation effects from the beam splitter. The effect of low-pass filtering has not been investigated here, and all results, both modelled and experimental are presented without any filtering being applied in the processing.

The level of Doppler shift uncertainty was first determined for the increased sensitivity 2ν-PDV system used. This was estimated, for the increased sensitivity scheme, to be between 4.4 and 5.4MHz depending upon the received scattered light intensity for the measurements.

The values used for the uncertainty in viewing angles were then estimated so that the error level in the output of the computer model matched the level of error found in the experimental results. Values for the uncertainty in the view angles were selected by trial and error to provide a good fit between the total level of error on each measured velocity component and the modelled error on each velocity component. This was further complicated by the method used to calculate the observation direction in the experimental work. Here they were calculated using the results of the de-warping process[3] and it is known that this technique does not work as well for view angles that are close to perpendicular to the light sheet. For example values of T=0 or 180^o and values of P=0^o. To take account of this the uncertainty in the viewing angles was varied.
For view angles close to perpendicular a 0.8^o uncertainty was used, while a 0.1^o uncertainty in angle was used for all other observation directions as these provided a good fit between the experimental error and the modelled error. The level of error introduced in each view angle is shown in Table 8-11.

Table 8-11 Values of the view angle error introduced into the model.

Configuration		View 1	View 2	View 3	View 4
A_{exp}	Error in T	0.8	0.8	0.1	0.1
	Error in P	0.1	0.1	0.8	0.8
B_{exp}	Error in T	0.1	0.1	0.1	0.1
	Error in P	0.1	0.1	0.8	0.8

If the experimental results captured using the normal sensitivity 2ν-PDV method are compared to the model, it would be expected that the values used for the error in the view angles would remain constant while the uncertainty in Doppler shift would increase will the uncertainty in determining the view angles would remain the same. This is because the same method for determining observation direction is used in both sets of measurements, while the increased sensitivity method will allow a more accurate measurement of the Doppler shift. The Doppler shift uncertainty used to model the normal sensitivity scheme results was 1.8x that for the increased sensitivity scheme (between 7.8 and 9.7MHz) depending upon received scattered light intensity. If the values for uncertainty used in the model are reasonable then the model should predict error levels similar to those found on the experimental results for the normal sensitivity scheme if only the value of Doppler shift uncertainty is modified. Likewise the model should be able to predict error levels that are similar to the experimental levels when the U, V and W components are calculated using the 3C or 4C methods.

Table 8-12 shows a comparison between the total level of error on each measured velocity component for the experimental results and the level of noise added by the model. The values for the total error in the velocity components calculated using the model agree well with the experimentally measured velocity components, although there are slight discrepancies especially for configuration B_{exp} view 3, were the model under predicts the uncertainty level.

Table 8-12 Standard deviation of the error on experimental measured velocity components and the modelled velocity components

Configuration / sensitivity scheme		Standard deviation of error on measured components (ms^{-1})			
		View 1	View 2	View 3	View 4
A_{exp}	Increased sensitivity	2.1	2.2	1.5	2.2
	Modelled	2.0	2.0	1.5	2.2
A_{exp}	Normal sensitivity	3.7	3.9	2.6	3.9
	Modelled	3.5	3.5	2.7	4.0
B_{exp}	Increased sensitivity	2.7	3.1	1.9	2.4
	Modelled	2.7	2.7	1.2	2.5
B_{exp}	Normal sensitivity	4.8	5.1	2.7	4.0
	Modelled	4.8	4.8	2.2	4.4

Histograms of the remaining noise in each of the orthogonal components after the theoretical velocity field has been subtracted are shown in Figure 8-11 for configuration A_{exp} and Figure 8-12 for configuration B_{exp}. The left hand column shows the results for the increased sensitivity scheme and the right the normal sensitivity 2ν-PDV systems, with experimental results shown by the data points and the modelled results shown by the solid lines. Both histograms for the components calculated using three components and four components are shown. The standard deviations of the remaining noise in the U, V and W components can be seen in Table 8-13 that shows the standard deviation of the error in both the experimental and modelled results.

The result shown in Figure 8-11 and Figure 8-12 show that the error propagation model compare reasonably well with the experimental results when these values for the Doppler shift and view angle uncertainty are used. The model predicts the relative performance of the two viewing configurations as well as the magnitude of the error on each orthogonal velocity component. The values chosen for the view angle uncertainty work well in the model when using both the 3C and 4C methods of calculating the U, V and W components and for both sensitivity schemes, suggesting that these are reasonable approximations for the uncertainty in the 2ν-PDV system, although with these values the model does slightly over-estimate the error in the V component for the second configuration.

Table 8-13 Standard deviation of the error on experimental and modelled orthogonal velocity components

Configuration / sensitivity / method			Standard deviation of error (ms^{-1})		
			U	V	W
A_{exp}	Increased sensitivity	3C	3.3	5.6	5.0
	Modelled		3.3	5.6	4.9
A_{exp}	Increased sensitivity	4C	2.8	5.5	3.7
	Modelled		3.0	5.6	3.9
A_{exp}	Normal sensitivity	3C	6.1	10.2	9.3
	Modelled		6.0	10.0	8.8
A_{exp}	Normal sensitivity	4C	5.3	10.2	7.0
	Modelled		5.3	10.0	7.0
B_{exp}	Increased sensitivity	3C	2.4	4.2	3.2
	Modelled		2.1	4.3	3.2
B_{exp}	Increased sensitivity	4C	2.2	4.2	2.4
	Modelled		2.0	4.3	2.5
B_{exp}	Normal sensitivity	3C	4.0	6.9	6.0
	Modelled		3.8	7.6	5.8
B_{exp}	Normal sensitivity	4C	3.6	6.9	4.4
	Modelled		3.5	7.6	4.5

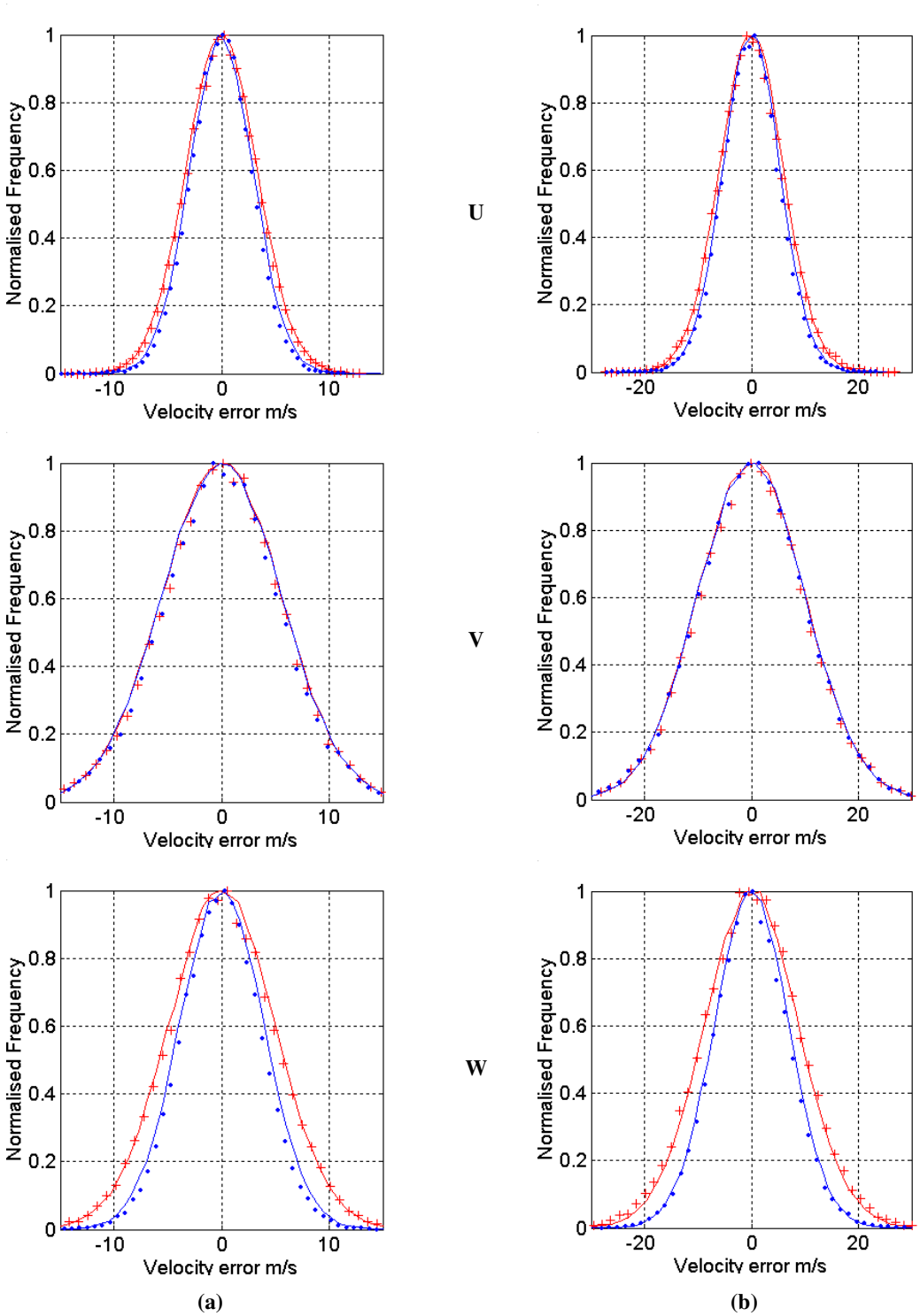

Figure 8-11 Histograms of the error in the orthogonal velocity components for configuration A_{exp}, when calculated experimentally (data points) and modelled (solid lines) using the 3C (red), and 4C (blue) methods. Experimental measurements are using (a) the increased sensitivity scheme and (b) the normal sensitivity scheme.

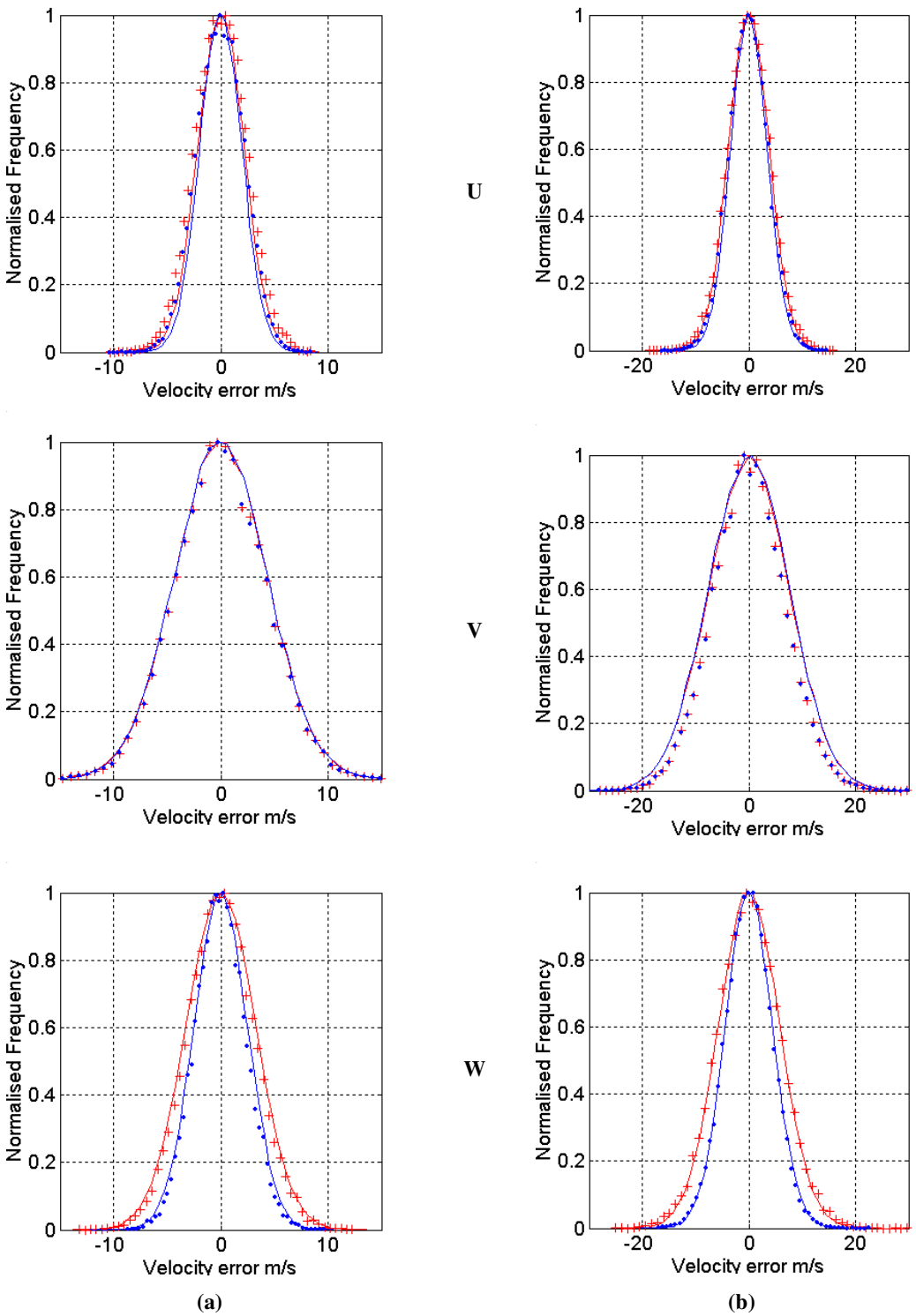

Figure 8-12 Histograms of the error in the orthogonal velocity components for configuration B_{exp}, when calculated experimentally (data points) and modelled (solid lines) using the 3C (red), and 4C (blue) methods. Experimental measurements are using (a) the increased sensitivity scheme and (b) the normal sensitivity scheme.

8.6 Summary

A computer model has been described that simulates propagation of errors through the measurement and processing of PDV data to the orthogonal velocity components.

The two sources of error identified in chapter 7, error in the measurement of the observation direction and error in the measurement of Doppler shift have been included in the model. The effect of error in the measurement of observation direction is included in both the calculation of the velocity component from the Doppler shift and in the transformation to orthogonal velocity components. The error in the Doppler shift is introduced before the calculation of the velocity components. This error is then propagated through the transformation to orthogonal velocity components.

The effect of a varying level of error with observation direction has been shown to have significant impact upon the selection of viewing configurations, with previously better configurations (when a constant error level is assumed) having larger errors when the errors are calculated based upon observation direction. This is especially important when the flow field being measured has higher velocity magnitudes.

The error propagation model was used to investigate the benefits of using an additional velocity component in the calculation of the U, V and W components. Using all four views and the 4C method can results in significant reductions in the error over using only three views. However calculating each orthogonal component using the best three out of the four views and the 3C method can result in similar improvements, although typically the 4C method will improve at least one orthogonal component further. In conclusion measuring a fourth component of velocity will allow an improvement in the error level, with the method used to calculate each component selected to give the best results.

Finally a comparison was made between the model and experimental results for two viewing configurations using a rotating disc as the velocity field. Estimates for the uncertainty in Doppler shift and view angles were made for the 2ν-PDV system, described in chapter 6, that was used. The uncertainty in view angles was estimated as 0.1 to 0.8^{o} depending upon the angle, with the de-warping process used to calculate them being known to break down under certain conditions. The uncertainty in the Doppler shift was estimated at between 4.4 and 5.4MHz for the increased sensitivity scheme and 7.8 and 9.7MHz for the normal sensitivity scheme.

The model predicted reasonably well the relative performance of the two viewing configurations used, when values for the Doppler shift and view angle uncertainty are estimated for 2ν-PDV system. The model also predicts the relative performance when the orthogonal velocity components are calculated using the 3C (three components) or 4C (four components) methods.

8.7 References

1. Roehle, I., Willert, C., Schodl, R., and Voigt, P., "Recent Developments and Applications of Quantitative Laser Light Sheet Measuring Techniques in Turbo machinery Components", 2000, *Measurement Science and Technology*, Vol. 11, pp 1023-1035.

2. Reinath, M.S., "Doppler Global Velocimeter Development for the Large Wind Tunnels at Ames Research Center", 1997, *NASA*, Technical Memorandum 112210.

3. Nobes, D.S., Wieneke, B., and Tatam, R.P., "Determination of View Vectors from Image Warping Mapping Functions", 2004, *Optical Engineering*, Vol. 43, No. 2, pp 407-414.

9 Conclusions and Future work

9.1 Introduction

The work presented in this thesis can be divided into two main sections, the development of the two-frequency Planar Doppler Velocimetry (2ν-PDV) technique and instrumentation, and the optimisation of viewing configurations for 3D PDV measurements. A summary of the work and the conclusion in each of these areas is given in the following sections. The final section outlines the possible directions that future work could take.

9.2 Conclusions – Two-frequency Planar Doppler velocimetry (2ν-PDV)

The main motivation behind the 2ν-PDV technique was the removal of image misalignment problems between the signal and reference cameras used in conventional PDV. This is a significant error source in conventional PDV measurements with an image misalignment of 0.1 pixels, giving an error of $\pm 5 ms^{-1}$[1]. The 2ν-PDV systems demonstrated in chapters 5 and 6, capture both images on a single CCD camera thus avoiding this problem. This resulted in the white-card correction, which is commonly applied to conventional PDV measurements, no longer being necessary.

The second motivation was the removal of the beam splitter used in conventional PDV imaging heads; this was removed completely from the 2ν-PDV imaging head used in chapter 6. This removes uncertainty introduced by the variation in split ratio for different polarisation states. For example non-polarizing beam splitters are often quoted as ±3% variation in the split ratio for S and P polarised light, leading to typical velocity errors of $\pm 7 ms^{-1}$. The use of only a single CCD camera and iodine cell significantly simplifies the set-up of the experiment.

In chapter 5, a single velocity component 2ν-PDV system was described with measurements made on a rotating disc with velocities errors of $\pm 2 ms^{-1}$. The system was also demonstrated by making measurements of the main flow component of an axisymmetric air jet. These measurements were compared with conventional PDV results, captured simultaneously, and with the theoretical velocity field of the jet, calculated from empirical equations, with good agreement between them. When compared to conventional PDV results the 2ν-PDV results agreed to within $\pm 5 ms^{-1}$ in the centre of the jet increasing towards the edges due to lower signal levels in these regions.

The frequency-switching set-up used in this system allowed the rapid acquisition of the two images necessary for the 2ν-PDV technique, however the components used resulted in a system that was light inefficient (~4-8mW from a laser output of 700mW). This resulted in exposure times of 5-10 seconds being necessary. However using alternative components in the construction of such a system could make significant improvements.

A significant amount of power is lost because the optical arrangement described in chapter 5, includes many surfaces, few of which are anti-reflection coated at 514nm. The major losses however occur in the acousto-optic modulators (AOM) used with a double pass through one AOM that had a small aperture and a first-order efficiency of less than 50% on each pass. The second order beam from the other AOM was used to increase the available frequency shift at the expense of optical efficiency. If acousto-optic modulators with higher frequency shift and efficiencies were used, then light efficiency could be improved significantly.

This system also provided insufficient frequency shift to use the increased sensitivity-tuning scheme described in chapter 2 (where both frequencies coincide with the absorption line, one on each slope). This would be possible if alternative higher shift acousto-optic devices were used.

In chapter 6, an alternative method of generating the two illumination frequencies required was used. Here the laser frequency was tuned using a temperature-controlled etalon and the two images acquired with an image separation of minutes rather than seconds. This allowed both sensitivity-schemes to be used when making measurements and increased the illumination power available.

When making single velocity component measurements on a rotating disc it was necessary to apply a white card correction, however when making measurements on the seeded air jet this was no longer necessary. This was found to be due to the coupling of the two beams into the fibre for delivery to the light sheet generator. The significantly different populations of propagating modes in the fibre gave different output beam power distributions. This was less noticeable when a small well-focussed sheet was used for real flows than for the poorly focussed sheet required to illuminate the face of the disc. When the system was expanded to measure multiple components of the velocity, in chapter 6, the multimode fibre used was replaced with a single mode polarisation maintaining fibre. This combined with the alternative method of generating the illumination frequencies, where both beams have the same optical path, prevented any differences in the light sheet used to illuminate the disc. This is turn meant that the white card correction, applied for single velocity component measurements on the disc was no longer necessary.

The alternative illumination arrangement, described in chapter 6, allowed both the normal and increased sensitivity schemes to be used for 2ν-PDV measurements. Measurements using both schemes were made on the velocity field of a rotating disc this allowed the error in the measured results for each sensitivity scheme to be compared with a theoretical velocity field. Using the increased sensitivity scheme resulted in a typical reduction in the error level of the measured velocity components of approximately 30-40% over the normal sensitivity scheme due to the increased sensitivity in the measurement of Doppler shift. The two alternative methods of processing the increased sensitivity scheme data produced similar results. The error level on each velocity component calculated using the normal sensitivity scheme was between 2.6ms^{-1} and 5.1ms^{-1} depending upon the observation direction, for a velocity field of ±34ms^{-1}. While those for the increased sensitivity scheme were between 1.5ms^{-1} and 3.1ms^{-1} depending upon observation direction for the same velocity field.

The error level in the calculated orthogonal velocity components should provide a more accurate estimate of the error. This is because the computed theoretical orthogonal velocity components are independent of the viewing direction, unlike the theoretical non-orthogonal velocity components that are calculated for the assumed viewing directions, which will not be precise. The error level in the calculated orthogonal velocity components was approximately 40-50% less for the increased sensitivity scheme than for the normal sensitivity scheme for the two viewing configurations, A and B, used. The error level in the orthogonal velocity components for configuration A using the normal sensitivity scheme were $6.1ms^{-1}$, $10.2ms^{-1}$ and $9.3ms^{-1}$ for the U, V and W components respectively, and $3.2ms^{-1}$, $5.3ms^{-1}$ and $4.6ms^{-1}$ when using the increased sensitivity scheme. For configuration B, these errors were $4.0ms^{-1}$, $6.9ms^{-1}$ and $6.0ms^{-1}$ for the normal sensitivity scheme and $2.3ms^{-1}$, $4.2ms^{-1}$ and $3.4ms^{-1}$ when using the increased sensitivity scheme. Configuration B has reduced errors due to having measured velocity components that are better conditioned for the transformation to the orthogonal velocity components, although both configurations are far from optimal as views can only be located on one side of the light sheet due to the disc. Therefore better final error levels could be anticipated in real flow measurements.

9.3 Conclusions – Optimisation of 3D PDV systems

In chapter 7, the factors that influence the selection of a viewing geometry were identified. The magnitude of the uncertainty in measured velocity components was shown to be dependent upon observation direction, due to two factors; the uncertainty in the measurement of the observation direction and how the uncertainty in Doppler shift propagates to the velocity component. This variation in measured velocity component uncertainty is dependent upon the magnitude of the flow being measured. This variation was also demonstrated experimentally using the 2ν-PDV system described in chapter 6.

The uncertainty in determining the observation directions also influences the process of transforming the measured velocity components to the orthogonal velocity components, with the uncertainty also dependent upon the flow velocity. Also the conditioning of the transformation matrix was demonstrated as a reasonable measure of how well errors will propagate through the transformation to the orthogonal velocity components.

Other considerations that could influence the selection of viewing geometry include potential limitations of optical access in experiments, variations in the Mie scattered light intensity and a potential method of cancelling out errors introduced by laser frequency fluctuations in the transformation[2,3].

A computer model was developed (described in chapter 8) simulating the propagation of errors through 3D PDV experiments. This was then used to investigate several viewing configurations.

The effect of a varying level of error in the measured velocity components with observation direction was shown to have significant impact upon the selection of viewing configurations. Viewing configurations that had previously better

uncertainties in the orthogonal velocity components, when a constant level of uncertainty in each measured component was assumed, are no longer better when this variation is introduced. This is especially important when the flow field being measured has higher velocity magnitudes as this variation in uncertainty with observation direction scales with the magnitude of the velocity.

The effect of introducing uncertainty in the sensitivity vector (via uncertainty in the view angles) to the transformation to orthogonal velocity components was shown to significantly increase the final error level. This effect is also dependent upon the magnitude of the flow velocity, so minimising the uncertainty in the view angles would greatly improve error levels. This would reduce the uncertainty in each measured velocity component and reducing uncertainty introduced in the transformation to the orthogonal velocity components.

To investigate the use of the condition number as a measure of the uncertainty in the orthogonal velocity components the model was used to test a number of viewing configurations. It was found that generally the condition number is a good first approximation as to the suitability of a viewing configuration, with the lower the value the lower the uncertainty levels in U, V and W. However the condition number should not be the only factor considered when attempting to optimise a viewing configuration, as a more suitable configuration may exist which has a higher condition number, but lower uncertainties.

The benefit of calculating the orthogonal velocity components, U, V and W using an additional measured velocity component (using four components rather than three) was also investigated using the error propagation model. By measuring a fourth velocity component for use in the transformation to the orthogonal velocity components, the propagated error can be significantly reduced over using only three measured components. The actual reductions achievable will depend upon the viewing configuration used and the location of the fourth view. However as four components are measured it may be preferable to use the 3C method using the best three of the four views. It was shown that the use of the 4C method could still reduce the level of uncertainty in the orthogonal velocity components. The optimum method would be to select the method (3C or 4C) and velocity components (three, best three or all four) that will give the lowest uncertainty for each orthogonal velocity component individually.

The results of the error propagation model were compared with the results of the 3D 2ν-PDV system described in chapter 6. The error level in the orthogonal velocity components was found from the measurements made on the rotating disc and the parameters of the model were then adjusted to find good agreement between the predicted error levels and those observed from experiment. This was done using both the 3C and 4C methods of calculating the orthogonal velocity components and for results captured using both sensitivity schemes. A good agreement between the predicted and observed error levels was found when a value for the total uncertainty in Doppler shift of between 4.4 and 5.4MHz was used for the increased sensitivity scheme. The value used varied depending upon the signal level in the images, which in turn depended upon the scattering intensity for each view. Estimating the view angle uncertainty was more complicated due to the method used in determining the view locations. This was done using the images of the de-warping target[4] with this

method known to break down at angles close to perpendicular to the light sheet, because of this the uncertainty in the view angle used for the model was varied between 0.1^o and 0.8^o depending upon the view location. When these values were used the model reasonably predicted the error seen in each measured velocity component, to within $0.2ms^{-1}$ for configuration A_{exp} and $0.7ms^{-1}$ for configuration B_{exp}. The predicted uncertainty level in the U, V and W components was within $0.3ms^{-1}$ of the observed error in the worst case.

When comparing the results of the normal sensitivity scheme with the model, it would be expected that the uncertainty in the views angles would remain the same, as they were calculated using the same method for both sensitivity schemes. The uncertainty in the measurement of Doppler shift would be expected to increase. The results of the model matched reasonably well when the Doppler shift uncertainty was approximately 1.8 times that for the increased sensitivity scheme, between 7.8 and 9.7MHz. Again the model predicted the level of uncertainty in each measured velocity component well, within $0.4ms^{-1}$ for configuration A_{exp}, and $0.5ms^{-1}$ for configuration B_{exp}. The predicted uncertainty level in the U, V and W components were within $0.7ms^{-1}$ in the worst case and most were within $0.2ms^{-1}$ of the observed error level.

9.4 Future work

9.4.1 Potential improvements to the two-frequency beam generator

Improvements could be made to the frequency-switching set-up that was originally employed to generate the two frequencies. The acousto-optic modulators (AOMs) used in this work were light inefficient, newer devices have better optical efficiency and larger frequency shifts. This would mean that the devices could be used in the more efficient single pass configurations and also using the second order beam would be unnecessary. This would allow greater illumination power resulting in higher scattered light levels and a better signal to noise ratio. The use of alternative AOMs would also allow greater frequency separation between the two illumination beams allowing the increased sensitivity scheme to be used for measurements using a rapid switching arrangement.

9.4.2 Extension of the 2ν-PDV technique to instantaneous measurements

The 2ν-PDV system developed to date is only capable of making time-averaged velocity measurements of the flow. Using dual pulse CCD cameras it is possible to capture closely spaced image pairs with separations down to 200ns. By using this camera for a pulsed 2ν-PDV system there would effectively be no shift in the flow. For example for a flow velocity of $100ms^{-1}$ a particle will have moved 20μm in the 200ns interval between the images. If the field of view is approximately 10cm x 10cm, resulting in an image reduction of a factor of 10 this will result in an equivalent movement of 2μm, a factor of 4 smaller than a pixel. A schematic of a proposed 2ν-PDV system is shown in Figure 9-1, here the outputs of two Nd:YAG laser cavities are combined and formed into the light sheet. This illuminates the flow and images are captured using the dual frame mode of the CCD camera with the pulse from each cavity in a separate exposure. The frequency of each pulse would be tuned to different

positions on the iodine absorption line providing the two illumination frequencies required by the 2ν-PDV technique.

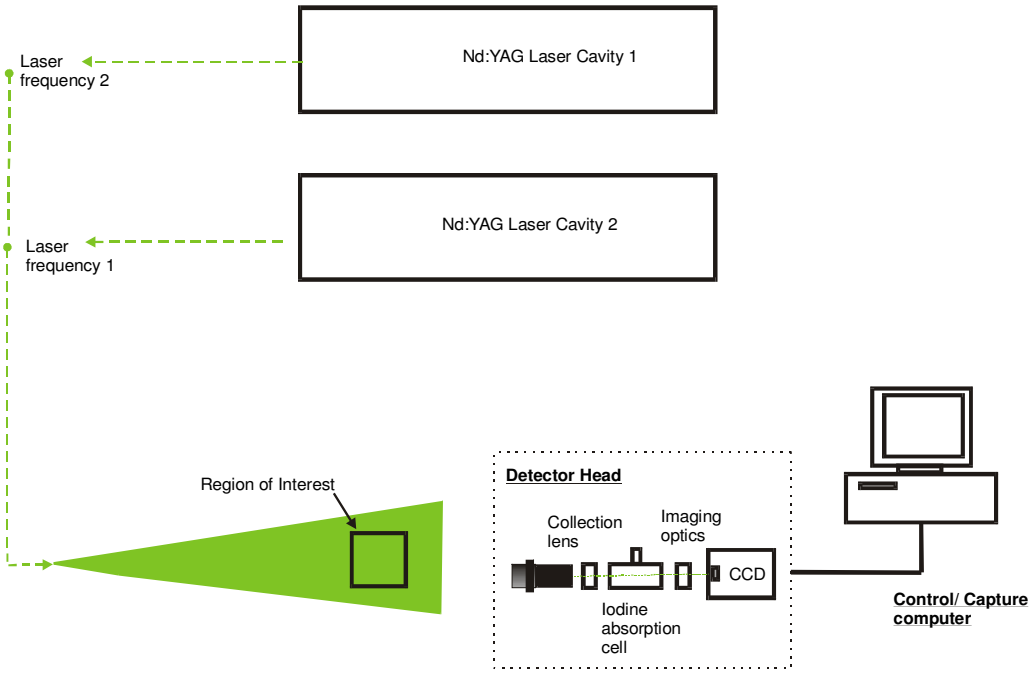

Figure 9-1 Schematic of the proposed pulsed 2ν-PDV system

This proposed system could then be easily expanded to make 3D measurements using the imaging fibre bundles described in chapter 6 using the existing imaging head. This is suitable for pulsed measurements as the cameras support both long exposure (used for time-averaged measurements) and dual frame modes. The may be issues related to the pulse-to-pulse frequency stability of the lasers however this can be overcome by measuring the frequency of each pulse using the fourth arm of the fibre bundles to view a small portion of each pulse as done by Nobes et al[5].

9.4.3 Combined PIV and 2ν-PDV

It could also be possible to implement a combined 2ν-PDV and PIV flow measurement technique, similar to the combined PDV and PIV approach implemented by Wernet[6,7]. However by using 2ν-PDV rather than PDV only a single CCD camera would be necessary to make 3D measurements. Two pulses illuminate the flow with a time separation set to allow PIV calculations of in plane velocities. As both laser cavities can also be injection seeded the pulses are tuned to the two laser frequencies required by the 2ν-PDV method, the out-of-plane component can then be found from the intensities in the two images. This would allow a hybrid velocimeter to be constructed using a single iodine cell and CCD and requiring only a single observation direction to measure all three components of the velocity. A potential problem with this approach could be the differences in seeding requirements for the two techniques, with PDV needing dense seeding to maximise scattered light and PIV require individual seed particles to be imaged. However Wernet[7] overcomes this problem by spatially averaging the PDV data over sub regions corresponding to the size of spacing between PIV measurements (in this case

16x16 pixels). This was achieved by pixel binning to obtain an estimate of the Doppler shift at the same spatial resolution as the PIV measurements.

9.4.4 Potential improvements in PDV processing

Future improvements to the 2ν-PDV system could be achieved with modifications to the processing. The method used to calculate the increased sensitivity 2ν-PDV images, could be improved currently these results are processed either using a linear approximation of each side of the absorption line, or using a look-up table generated from curves fitted to each side of the absorption line. The linear approximation is only valid on a limited range of Doppler shifts, while the look-up table approach can use a greater range of Doppler shifts. The current look-up table approach suffers from accuracy problems due to the curves fitted to each slope of the absorption line, either a better fitting method or a look-up table based upon the frequency/transmission scan of the absorption line could be implemented.

In the calculation of the orthogonal velocity component using the 4C method a weighting value can be used. An investigation to find the optimal weighting scheme would be useful. Likewise a study of the methods used in PDV processing would be useful to determine the best order to carry out the various stages for example when to apply low pass filtering - is it best to perform the image de-warping after the calculation of the velocity components or before?

Further improvements in the accuracy of 3D PDV systems could be achieved by improving the method used to calculate the observation directions. A method using a 3D calibration target to calculate the location of each view could be implemented. One such system has been developed at the French/German research institute at St Louis (ISL) in France[8]. An improved method of determining the observation direction for each view will reduced the measurement uncertainty in each measured velocity component as well as the propagated uncertainty in the calculated orthogonal velocity components.

9.4.5 Borescopes measurements on internal flows

The PDV imaging head arrangement combined with the use of multiple imaging fibre bundles allows the easy connection of different imaging optics, Figure 9-2. One particular application of this would be the use of borescopes to allow flow measurements to be made in internal flows. Preliminary work has been carried into the feasibly of making measurements on Cranfield University's low speed research compressor. The arrangement use to gain access, shown in Figure 9-3, consisted of a cartridge that can be mounted into the compressor and is used to support the borescopes. The imaging fibre bundles are then coupled to the borescopes and the views ported to the imaging head.
Initial measurements were made using the conventional PDV (two CCDs) imaging head using the borescopes mounted in the support cartridge to make measurements on the velocity field of a rotating disc. The region of the disc that was imaged is shown in Figure 9-4 (a) and the computed velocity field is shown in Figure 9-4 (b).

There are currently a number of problems with this approach. Using the borescopes results in low levels of collected light intensity leading to in low signal to noise levels. The process used to calculate the observation direction from the de-warping[4] does not perform well when used with the highly distorted images from the borescopes.

The analysis is chapters 7 and 8 shows that this uncertainty in the observation direction will lead to large errors in the calculated velocity, therefore an alternative method of determining the observation direction will be necessary. The third problem is that the choice of viewing configuration is very restricted leading to large errors being propagated to the computed orthogonal velocity components. This is unavoidable, however it should still be possible to make single component velocity measurements that are unaffected by this.

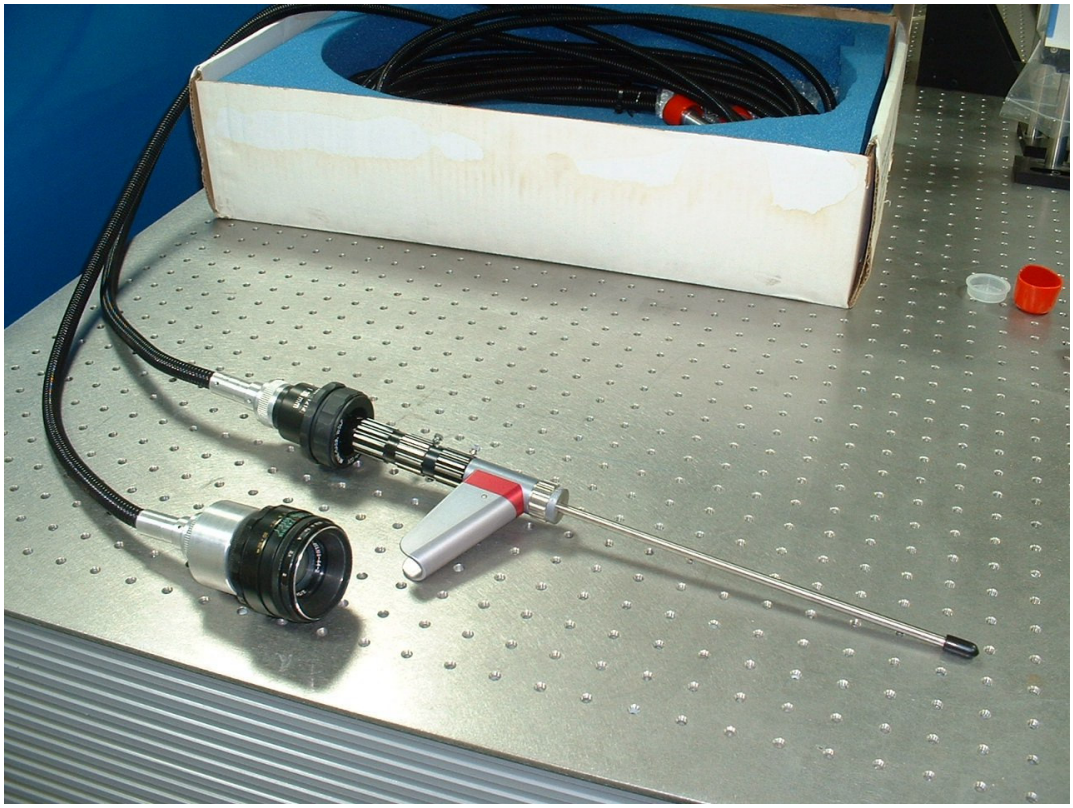

Figure 9-2 Photograph showing the imaging fibre bundles coupled to an SLR lens and a borescope.

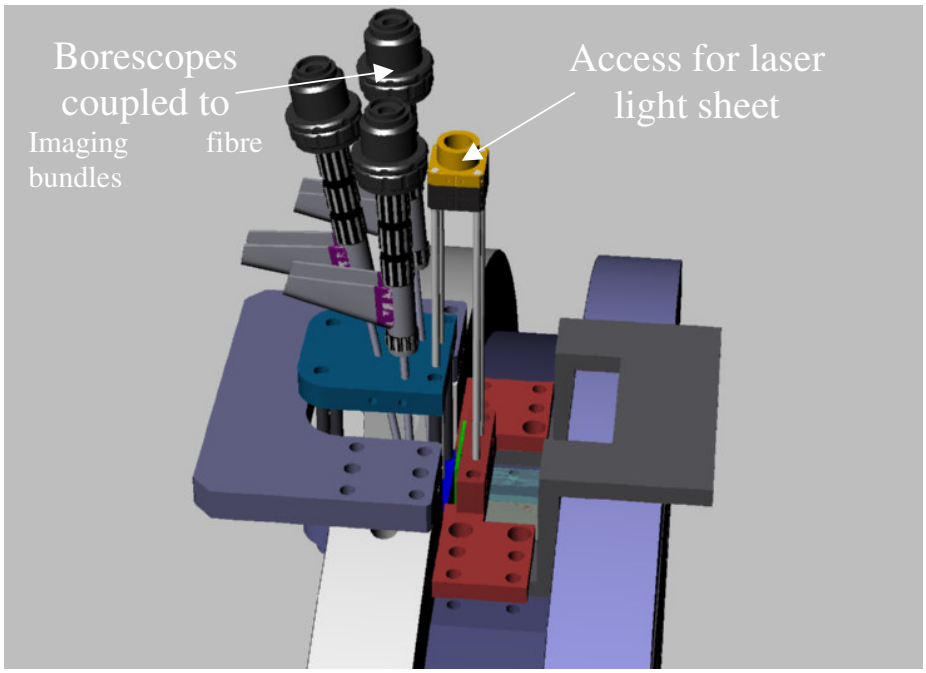

(a)

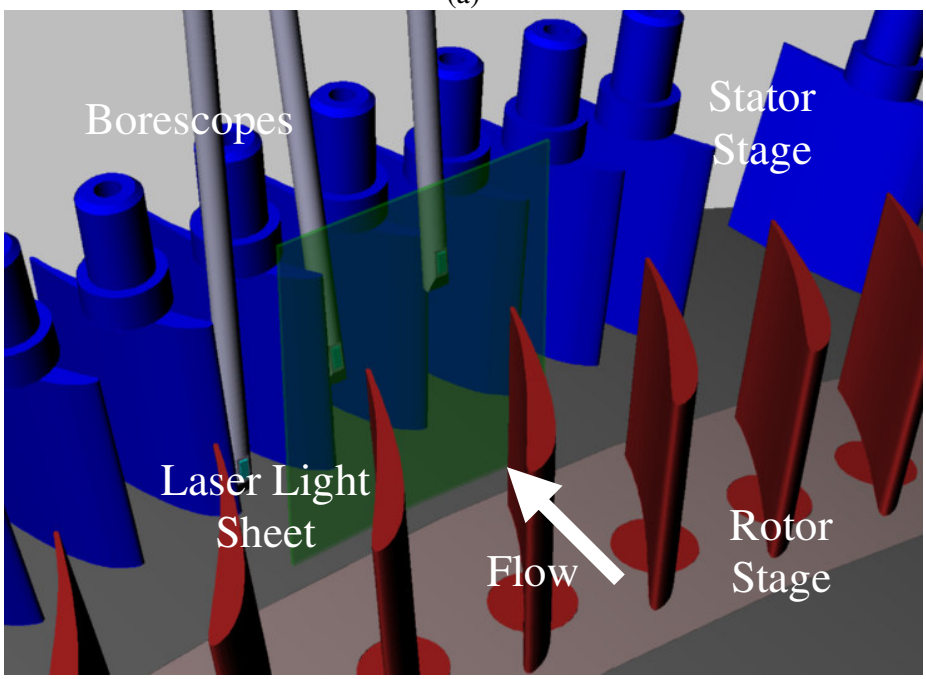

(b)

Figure 9-3 (a) A schematic showing the proposed arrangement of the borescopes for access for Cranfield University's low speed research compressor. (b) Showing the internal positioning of the borescopes and lights sheet.

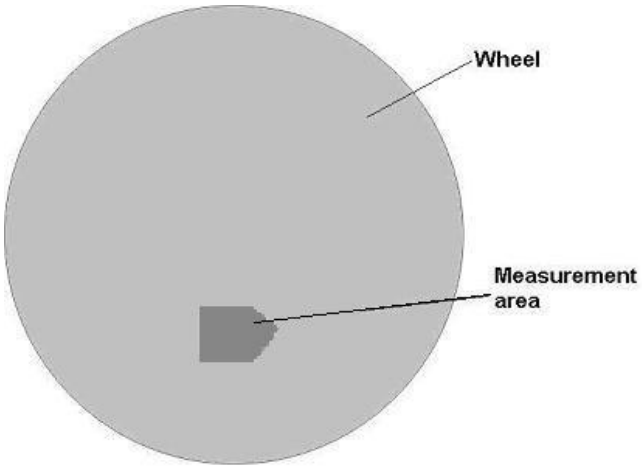

(a)

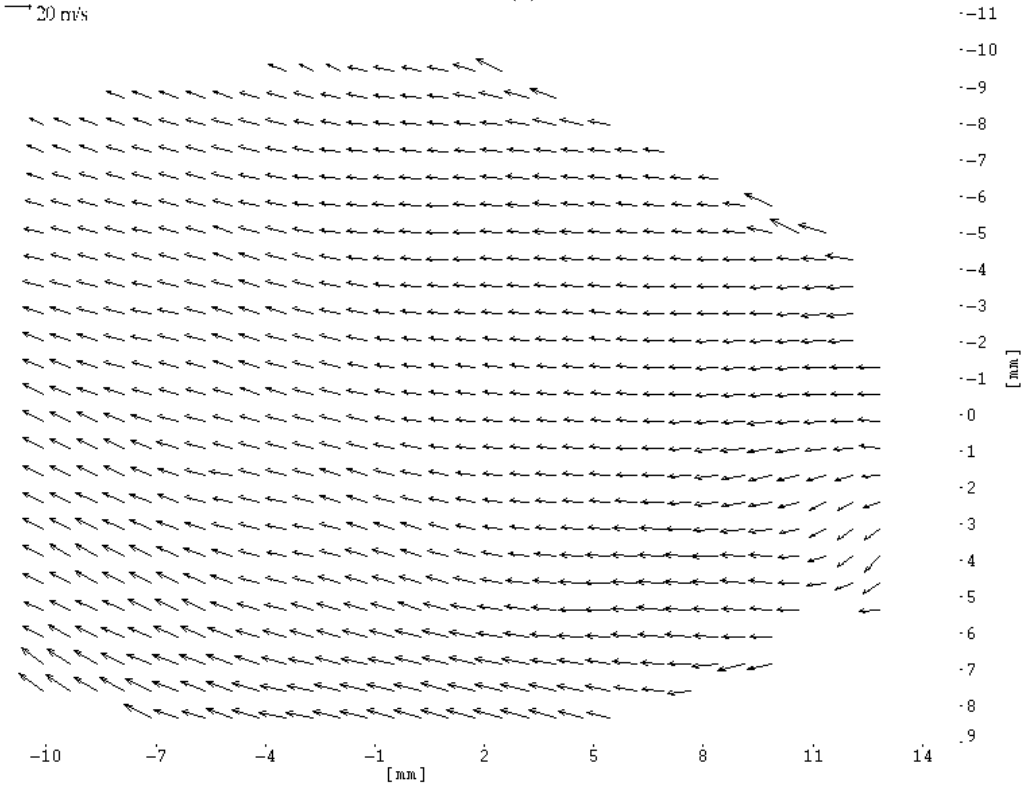

(b)

Figure 9-4 (a) Schematic showing the measurement region on the face of the wheel. (b) The computed velocity field made using the conventional PDV technique.

9.5 References

1. Thorpe, S.J., Ainsworth, R.W., and Manners, R.J., "The Development of a Doppler Global Velocimeter and its Application to a Free Jet Flow", 1995, *ASME / JSME Fluids Engineering and Laser Anemometry Conference and Exhibition*, Hilton Head, SC, USA,

2. Elliott, G.S., Crafton, J., Beutner, T.J., Carter, C.D., Baust, H.D., and Tyler, C., "Evaluation and optimization of a Multi-component Planar Doppler Velocimetry System", 2005, *AIAA 43rd Aerospace Sciences Meeting and Exhibit*, Reno, Nevada, AIAA 2005-35.

3. Clancy, P.S., Samimy, M., and Erskine, W.R., "Planar Doppler Velocimetry: Three Component velocimetry in Supersonic Jets", 1999, *AIAA Journal*, Vol. 37, No. 6, pp 700-707.

4. Nobes, D.S., Wieneke, B., and Tatam, R.P., "Determination of View Vectors from Image Warping Mapping Functions", 2004, *Optical Engineering*, Vol. 43, No. 2, pp 407-414.

5. Nobes, D.S., Ford, H.D., and Tatam, R.P., "Three Component Planar Doppler Velocimetry Using Imaging Fibre Bundles", 2004, *Experiments in Fluids*, Vol. 36, No. 1, pp 3-10.

6. Wernet, M.P., "Planar Particle Imaging Doppler velocimetry, A 3-Component Velocity Measurement Technique", 2004, *42nd AIAA Aerospace Sciences Meeting and Exhibit*, Reno, Nevada, AIAA 2004-22.

7. Wernet, M.P., "Planar Particle Imaging Doppler velocimetry, a hybrid PIV/DGV technique for three-component velocity measurements", 2004, *Measurement Science and Technology*, Vol. 15, pp 2011-2028 .

8. Martinez, B., "Multi component Doppler Global velocimetry in the ISL supersonic wind tunnel", 2006, *AIAA 44th Aerospace Sciences Meeting and Exhibit*, Reno, NV, AIAA-2006-046.

Publications

Journal papers

Charrett, T.O.H., Nobes, D.S. and Tatam, R.P., "Investigation into the selection of viewing configurations for 3D Planar Doppler Velocimetry (PDV) measurements", (submitted), *Applied Optics*.

Charrett, T.O.H. and Tatam, R.P., "Single camera three component planar velocity measurements using two frequency Planar Doppler Velocimetry (2ν-PDV) ", (In press), *Measurement Science and Technology*, OFS17 special issue.

Charrett, T.O.H., Ford, H.D., Nobes, D.S., and Tatam, R.P., "Two frequency Planar Doppler Velocimetry (2ν-PDV)", 2004, *Review of Scientific Instruments*, Vol. 75, No. 11, pp 4487-4496.

Conference papers

Charrett, T.O.H. and Tatam, R.P., "Instantaneous Two-frequency Planar Doppler Velocimetry using pulsed Nd:YAG lasers", to be presented, *13th International symposium on the application of Laser techniques to fluids*, Lisbon.

Charrett, T.O.H. and Tatam, R.P., "Single camera 3D planar Doppler velocity measurements, using two frequency Planar Doppler Velocimetry (2ν-PDV) and imaging fibre bundles", 2006, *44th AIAA Aerospace Sciences Meeting and Exhibit*, Reno, NV, AIAA 2006-0047.

Charrett, T.O.H., Ford, H.D., and Tatam, R.P., "Single camera three component planar velocity measurements, using two frequency Planar Doppler Velocimetry (2ν-PDV)", 2005, *International symposium on optical science and technology*, San Diego, USA, SPIE Proc. 5880.

Charrett, T.O.H., Ford, H.D., and Tatam, R.P., "Single camera 3D planar velocity measurements using imaging fibre bundles and two frequency Planar Doppler Velocimetry (2ν-PDV) ", 2005, *17th Conference on Optical Fibre Sensors (OFS)*, Bruges, Belgium, Proc SPIE 5855, pp924-927.

Charrett, T.O.H., Ford, H.D., and Tatam, R.P., "Single Camera 3D Planar Doppler Velocity Measurements using Imaging Fibre Bundles", 2005, *Second international conference on Optical and Laser Diagnostics (ICOLAD)*, City University, London.

Charrett, T.O.H., Ford, H.D., and Tatam, R.P., "Single camera three component planar velocity measurement using imaging fibre bundles", 2004, *SET for Britain presentations at the House of Commons*, London.

Charrett, T.O.H., Ford, H.D., and Tatam, R.P., "Two Frequency Planar Doppler Velocimetry", 2004, *Photon 04*, Glasgow.

Charrett, T.O.H., Ford, H.D., Nobes, D.S., and Tatam, R.P., "Two-Frequency Planar Doppler Velocimetry (2υ-PDV)", 2004, *12th International symposium on the application of Laser techniques to fluids*, Lisbon.

Charrett, T.O.H., Ford, H.D., Nobes, D.S., and Tatam, R.P., "Dual Illumination Planar Doppler Velocimetry using a Single Camera", 2003, *Optical Diagnostics for Fluids, Solids, and Combustions II, Proceedings of the Society of Photo-optical Instrumentation Engineers (SPIE)*, San Diego, CA, paper 5191, pp 113-121.